Sustaining Fracture Area and Conductivity of Gas Shale Reservoirs for Enhancing Long-Term Production and Recovery

08122-48.Final

May 15, 2012

Dr. Ahmad Ghassemi
Texas Engineering Experiment Station
Texas A&M University System
College Station, TX 77845
(405) 325-4347
Ahmad.Ghassemi@pe.tamu.edu

Dr. Roberto Suarez-Rivera
TerraTek, Inc.
A Schlumberger company
1935 S. Fremont Drive, Salt Lake City, UT 84104
(801) 584-2400
RSuarez-Rivera@slb.com

LEGAL NOTICE

This report is submitted by Texas Engineering Experiment Station as an account of work sponsored by the Research Partnership to Secure Energy for America, RPSEA. Neither RPSEA members of RPSEA, the National Energy Technology Laboratory, the U.S. Department of Energy, nor any person acting on behalf of any of the entities:

a. MAKES ANY WARRANTY OR REPRESENTATION, EXPRESS OR IMPLIED WITH RESPECT TO ACCURACY, COMPLETENESS, OR USEFULNESS OF THE INFORMATION CONTAINED IN THIS DOCUMENT, OR THAT THE USE OF ANY INFORMATION, APPARATUS, METHOD, OR PROCESS DISCLOSED IN THIS DOCUMENT MAY NOT INFRINGE PRIVATELY OWNED RIGHTS, OR

b. ASSUMES ANY LIABILITY WITH RESPECT TO THE USE OF, OR FOR ANY AND ALL DAMAGES RESULTING FROM THE USE OF, ANY INFORMATION, APPARATUS, METHOD, OR PROCESS DISCLOSED IN THIS DOCUMENT.

THIS IS A FINAL REPORT. THE DATA, CALCULATIONS, INFORMATION, CONCLUSIONS, AND/OR RECOMMENDATIONS REPORTED HEREIN ARE THE PROPERTY OF THE U.S. DEPARTMENT OF ENERGY.

REFERENCE TO TRADE NAMES OR SPECIFIC COMMERCIAL PRODUCTS, COMMODITIES, OR SERVICES IN THIS REPORT DOES NOT REPRESENT OR CONSTIITUTE AND ENDORSEMENT, RECOMMENDATION, OR FAVORING BY RPSEA OR ITS CONTRACTORS OF THE SPECIFIC COMMERCIAL PRODUCT, COMMODITY, OR SERVICE.

INTENTIAL BLANK PAGE

SIGNATURE AND DATE STAMP

Signature - Dr. Ahmad Ghassemi

Dr. Ahmad Ghassemi
Texas Engineering Experiment Station
Texas A&M University System
College Station, TX 77845
(405) 325-4347
Ahmad.Ghassemi@pe.tamu.edu

Date – May 15, 2012

ABSTRACT

The objective of this program was to understand the multiple causes of loss of fracture area and fracture conductivity, and define solutions to mitigate these for enhancing long-term reservoir production and recovery. To achieve this goal we conducted theoretical and experimental work, and anchored our analysis on a comprehensive evaluation of rock properties from the Marcellus, Barnett and Haynesville tight shale reservoirs in North America. These included understanding the drivers of hydraulic fracture networks, and determine the critical parameters to maintain productive fracture area and fracture conductivity—including optimal proppants, fracture fluids, and pumping schedules, all as they are related to the heterogeneous rock formations that are to be produced. The end product deliverable is an improved workflow for fracture design, rock characterization, and production of tight gas shales. The problem is difficult, but the potential for greatly improved production is real.

We conducted detailed material property characterization on reservoir and non-reservoir facies of each of these reservoirs. The effort included evaluation of petrology, mineralogy, reservoir properties, geochemical properties and mechanical properties, including time-dependent behavior (creep). We evaluated core fracture types and geometries, with particular attention to the interactions between coring induced fractures with mineralized fractures in the core and other planes of weakness (e.g., weak bedding). This allowed us to propose a conceptual model for generating large surface area per unit reservoir volume (i.e., fracture complexity) based on understanding the presence and orientation of planes of weakness in the reservoir rock. We proposed typical fracture geometries and used these to evaluate well production configurations and showed that knowledge of fracture surface area and fracture geometry are critical to understanding and predicting stage production.

We evaluated fracture conductivity on un-propped and propped fracture surfaces, as a function of confining stress, fluid type and proppant type. We also measured fracture conductivities to water and nitrogen gas. On tests with un-propped samples, we conducted measurements of surface hardness and fracture conductivity with and without shear displacement, to evaluate the impact of shear and rock hardness to preserve fracture conductivity. Results indicate that on soft facies (e.g., all Haynesville facies and most Marcellus facies) shear displacement does not contribute to the preservation of fracture conductivity, proppant does.

The effort included evaluation of reservoir geology, mechanical properties, in-situ stress, and rock-fluid interactions. This is required to predict how sparsely propped or self-propped fractures can have and maintain conductivity and to understand the rock fluid sensitivity which could adversely affect the movement of gas from the matrix into the fracture and the conductivity of the fracture. And, we must understand and be better able to predict the fracture connectivity—fracture conductivity alone is not enough; fractures must be connected.

The project team included Texas A&M University (prime contractor), TerraTek, A Schlumberger Company (subcontractor), and producers and cost sharing participants Shell,

EnCana Oil & Gas USA, and Pennsylvania General Energy Co. The participants brought critical, essential technology, unique laboratory and field experience, access to reservoir core, logs, completions information (including micro-seismic measurements), and production history, as well as cash and in-kind financial contributions. This was a strong team. The management of the project was led by Co-Principal Investigators, Dr. Ghassemi, Petroleum Engr. Dept. at Texas A&M University, and Dr. Suarez-Rivera, Schlumberger Advisor and Director of the Schlumberger Innovation Center, at TerraTek in Salt Lake City. Other team members included geologists and engineers, and most importantly, support from production companies.

TABLE OF CONTENTS

EXECUTIVE SUMMARY 18
1 MATERIAL PROPERTY CHARACTERIZATION 21
1.1 Introduction 21
1.2 Barnett Shale Properties 23
1.3 Haynesville Shale Properties 35
1.4 Marcellus Shale Properties 46
1.5 Creep Behavior 55
1.5.1 Sample Description 57
1.5.2 Experimental Procedures 58
1.5.3 Hydrostatic Creep 60
1.5.4 Deviatoric Creep 61
1.5.5 Creep Under Elevated Temperatures 67
1.5.6 Creep on Different Samples Under the Same Stress Conditions 69
1.5.7 Test Result and Interpretation of Uniaxial Creep 70
1.5.8 Comparison of Uniaxial and Triaxial Creep, Confining Pressure Dependence 72
1.5.9 Creep Mechanism 73
1.5.10 Discussion 74
1.6 Summary 74
2 LOSS OF SURFACE AREA IN FRACTURE NETWORKS 76
2.1 Introduction 76
2.2 Background 76
2.3 Fracture Characterization 77
2.4 Fracture Network Geometries 82
2.5 Created and Effective Surface Areas 83
2.6 Effective Fracture Surface Area 84
2.7 Numerical Simulations of Production through Complex Fractures 86
2.8 Near-Wellbore Flow Restrictions by Convergence 92
2.9 Summary 93
3 FRACTURE CONDUCTIVITY OF UN-PROPPED FRATURES ON CORE 95
3.1 Introduction 95
3.2 Testing Matrix 95

3.3 Observations on Experimental Protocol 96
3.4 Comparisons 99
3.5 Summary 116
4 FRACTURE CONDUCTIVITY OF PROPPED FRACTURES ON CORE 117
4.1 Introduction 117
4.2 Testing Matrix 117
4.3 Comparisons 119
4.3.1 Proppant Size and Distribution 119
4.3.2 Fluid Exposure 127
4.3.3 Proppant Concentration 132
4.4 Summary 133
5 INTEGRATION OF THE LOSS OF EFFECTIVE SURFACE AREA AND CONNECTIVITY IN FRACTURE NETWORKS AND THE DEGRADATION OF FRACTURE CONDUCTIVITY 135
5.1 Introduction 135
5.2 Background 135
5.3 Methods 135
5.4 Results 138
5.4.1 Wide Forked Fracture Simulation Results 138
5.4.2 Fishbone Fracture Simulation Results 140
5.5 Discussion 142
5.6 Summary 143
6 LARGE-SCALE SIMULATION OF FIELD PRODUCTION – BLOCK TESTING 144
6.1 Introduction 144
6.2 Large-scale Simulation (Block Test) Methodology and Results 145
6.2.1 Objectives 145
6.2.2 Testing Equipment 145
6.2.3 Sample Preparation and Quality Control 147
6.2.4 Experimental Set-up and Procedures 150
6.2.5 Test Results 152
6.2.6 Block Fracture and Proppant Placement Evaluation 175
6.2.7 AE Results During Hydraulic Fracturing of the Block 188
6.2.8 AE Results Registered during Proppant Injection 206
6.2.9 General Conclusions based on AE Analysis 211
6.3 Discussion and Summary 212

7 ROADMAP FOR RESERVOIR CHARACTERIZATION, AND PRODUCTION AND RECOVERY MAXIMIZATION 215
7.1 Introduction 215
7.2 Far-wellbore Region 216
7.3 Near-wellbore Region 220
7.4 The Connection between the Wellbore and Fracture System 223
7.5 The Wellbore 225
7.6 Summary 227
7.7 Current Industry Practices and Concerns 228
7.7.1 Introduction 229
7.7.2 Evidence that fractures are losing conductivity and/or surface area 229
7.7.3 Potential mechanisms responsible for loss of fracture effectiveness 231
7.7.4 Best field practices currently implemented to combat loss of fracture area and fracture conductivity 232
7.8 Participants Current Practices 234
7.9 Integration 238
7.10 Recommendations 240
7.11 Summary 241
8 REFERENCES 242
9 BIBLIOGRAPHY 244
10 LIST OF ACRONYMS AND ABBREVIATIONS 252
11 APPENDICES 253

LIST OF TABLES

Table 1.1 Barnett rock classes and corresponding reservoir quality Index 25
Table 1.2 Summary of Barnett Petrophysical Properties 28
Table 1.3 Summary Barnett Geochemical Properties 28
Table 1.4 Summary of Barnett Geomechanical Properties - Static 29
Table 1.5 Summary of Barnett Geomechanical Properties - Dynamic 29
Table 1.6 Summary of Barnett XRD Mineralogy 30
Table 1.7 Summary of Barnett RockEval Properties 30
Table 1.8 Summary of Barnett Surface Hardness and Strength Measurements 30
Table 1.9 Barnett Petrologic Summary 31
Table 1.10 Abbreviations for Barnett Images and Tables 34
Table 1.11 Haynesville rock classes and corresponding reservoir quality index 37
Table 1.12 Summary of Haynesville Petrophysical Tables 39
Table 1.13 Summary of Haynesville Geochemical Properties 39
Table 1.14 Summary of Haynesville Geomechanical Properties – Static 40
Table 1.15 Summary of Haynesville Geomechanical Properties - Dynamic 40
Table 1.16 Summary of Haynesville XRD Mineralogy 41
Table 1.17 Summary of Haynesville RockEval Properties 41
Table 1.18 Summary of Haynesville Surface Hardness and Strength Properties 41
Table 1.19 Haynesville Petrologic Summary 42
Table 1.20 Abbreviations for Haynesville Images and Tables 45
Table 1.21 Marcellus Rock classes and corresponding reservoir quality index 47
Table 1.22 Summary of Marcellus Petrophysical Properties 49
Table 1.23 Summary of Marcellus Geochemical Properties 49
Table 1.24 Summary of Marcellus Geomechanical Properties – Dynamic 50
Table 1.25 Summary of Marcellus XRD Mineralogy 50
Table 1.26 Summary of Marcellus RockEval Properties 51
Table 1.27 Summary of Marcellus RockEval Properties 51
Table 1.28 Marcellus Petrologic Summary 52
Table 1.29 Abbreviations for Marcellus Images and Tables 54
Table 1.30 Mineral contents of four shale samples 57
Table 1.31 Loading path of the six samples used I the program 59
Table 1.32 Burger creep parameters 63
Table 1.33 Power law creep parameters 64
Table 2.1 Sand volume balance per stage for numerical simulations 86
Table 3.1 Testing Matrix for Un-propped Samples 96
Table 3.2 Properties of Synthetic Water 96
Table 4.1. Testing Matrix for Propped Samples 118
Table 4.2. Properties of Synthetic Water 119
Table 6.1. Test details and conditions for test 154
Table 6.2. Details of loading history for the lower completion are shown below 155
Table 6.3. Applied stress conditions, measured differential pressure, an approximate flow rate and calculated Fracture conductivity at each stress state for un-propped fracture conductivity measurements are listed 161

Table 6.4. Applied stress conditions, measured DeltaP, an approximate flow rate and calculated Fracture conductivity at each stress state for propped fracture conductivity measurements are listed 169
Table 6.5: Distribution of proppant in grams, at defined locations on the fracture surface, and average proppant diameter at each of these locations 185
Table 6.6: Surface area measurements using 200x and 300x for the eleven locations on the block 188

LIST OF FIGURES

Figure 1.1 HRA classification of two wells in the Barnett play indicating the presence and distribution of 12 rock classes within the cored section of these wells. 24
Figure 1.2 Distribution of gas filled porosity (GFP), pressure-decay permeability and total organic carbon (TOC) for each rock class. 25
Figure 1.3 Petrologic overview of three rock classes in the Barnett shale. 26
Figure 1.4 Petrologic overview of four rock classes in the Barnett shale. 27
Figure 1.5 Representative thin section (top) and SEM (bottom) of the best reservoir quality rock class of the Barnett shale. The image shows show detrital clay minerals that originally composed the matrix in best reservoir intervals of the Barnett intimately admixed with diagenetic silica, and extensively coated with highly degraded kerogen. SEM shows a heterogeneous microfabric in the matrix where favorable gas-filled porosity and matrix permeability occurs. 34
Figure 1.6 HRA classification of two wells in the Haynesville play indicating the presence and distribution of 9 rock classes within the cored section of these wells. 36
Figure 1.7 Petrologic overview of three reservoir rock classes in the Haynesville shale..... 37
Figure 1.8 Petrologic overview of additional three poor reservoir to non-reservoir rock classes in the Haynesville shale. 38
Figure 1.9 Representative thin section (top) and SEM (bottom) of the best reservoir quality rock class of the Haynesville shale include moderate amounts of detrital clay minerals, significantly high amounts of microcrystalline calcite, and widespread fine kerogen. SEM depicts microtextural features such as fecal pellets that are defined by increased amounts of calcite and highly degraded kerogen, hosting the best gas-filled porosity and matrix permeability. 45
Figure 1.10 HRA classification of one well in the Marcellus play, indicating the presence and distribution of 6 rock classes within the cored section of this well. 47
Figure 1.11 Petrologic overview of three rock classes in the Marcellus shale. 48
Figure 1.12 Representative thin section (top) and SEM (bottom) of the best reservoir quality rock class of the Marcellus shale which includes a clay-dominated matrix that hosts relatively high amounts of diagenetic pyrite in framboidal form and variably degraded kerogen, commonly coating clay particles. SEM reveals that the associated microtextural features contributes to enhanced gas-filled porosity and matrix permeability. 54
Figure 1.13 Time-dependent behavior associated to spring and dashpot mechanical systems. 55
Figure 1.14 Strain-time creep function: The example shows the strain-time relationship of a typical creep test. 55
Figure 1.15 Visco-elastic creep behavior as defined by the Burgers model. The strain-time dependence is shown. 56
Figure 1.16 Examples of four shale samples used for creep testing. 58
Figure 1.17 The multistage loading path & the axial strain of Marcellus 09-30, confining pressure is 2755 psi. 59
Figure 1.18 The confining pressure and deviatoric stress path of Haynesville 07-11, stress drop is for strain recovery. 60

Figure 1.19 Haynesville 05-22: Strain-time response, under hydrostatic creep compression, at three pressure stages. 61
Figure 1.20 Results from Marcellus tests, sample 09-30. Top-left: First two stages of creep. Bottom-left: Third to seventh stages of creep. Top-right: Deviatoric stress and lateral strain, versus axial strain during the 3rd to 7th stages of creep. Bottom-right: Axial creep strain and strain rate versus time. 62
Figure 1.21 Strain rate-stress relation, confining pressure 2755 psi, Marcellus-09-30. 63
Figure 1.22 Comparisons between experimental creep strain and Burger creep reaction to five stresses, confining pressure 2755psi. 64
Figure 1.23 Results from Barnett tests, sample 03-20. Top-left: Five stages of triaxial compression creep conducted at a constant confining pressure of 2320 psi. Top-right: Axial strain rate versus deviatoric stress. Bottom -left: Best fit of the experimental data to the Burgers model. Bottom-right: Best fit of the experimental data to the Power law model. 65
Figure 1.24 Results from Haynesville tests, sample 05-22. Top-left: Three stages of triaxial compression creep conducted at a constant confining pressure of 2320 psi. Top-right: Axial strain rate versus deviatoric stress. Bottom -left: Best fit of the experimental data to the Burgers model. Bottom-right: Best fit to the Power law model. 66
Figure 1.25 Creep strain versus time at different deviatoric stresses for Haynesville samples 07-11 and 07-12. 66
Figure 1.26 Creep strain and pseudo-steady strain rate versus deviatoric stress for Haynesville samples 07-11 (left) and 07-12 (right). 67
Figure 1.27 Haynesville sample 07-12: Hydrostatic creep strains under 60 psi hydrostatic pressure and at 3 different temperature levels. 67
Figure 1.28 Sample Haynesville 07-12 : Hydrostatic (left) and deviatoric (right) creep strains under 3 hydrostatic levels, 5 deviatoric stress levels and 4 temperatures levels. 68
Figure 1.29 Deviatoric creep strain comparison between room temperature and elevated temperatures, Haynesville 07-12. 69
Figure 1.30 Comparisons between creep strains under the same confining pressure 2320 psi, and the same deviator stress 7975 psi. 70
Figure 1.31 Multistage uniaxial (unconfined) creep test of sample Barnett 03-20. Left figure represents results for a deviatoric stress of 6742.5 pasi, right figure represents that of 10585 psi. 71
Figure 1.32 Multistage uniaxial (unconfined) creep test of sample Mancos 7v. The magnitude of the deviatoric stress increased from 4495psi to 5365 psi and 6090 psi. A linear increase in creep strain rate with deviatoric stress was found. 72
Figure 1.33 Comparisons of creep strain under two conditions of confining (2320 MPa) and unconfined stress, and under the same deviatoric stress of 6525 psi, 7830 psi, 9135 psi and 10585 psi, and 12035 psi. 73
Figure 1.34 Thin sections of typical Barnett, Haynesville, and Marcellus shale. 74
Figure 2.1 Fracture analysis on core. Examples of coring- and handling-induced petal, centerline and bedding partings are shown. Also shown are interactions between mineralized fractures and the rock fabric, and between mineralized fractures and coring induced fractures. 78
Figure 2.2 The continuous strength measurement is used to quantify fracture density, per unit length, on a rock class by rock class basis. 78

Figure 2.3 Fracture density per unit length in the Barnett shale (Well-1), evaluated over the length of the cored section. Results are integrated with borehole imaging observations. FMI of conductive fractures (Dark Blue), FMI resistive fractures (Light Blue), drilling induced fractures (Yellow), core open fractures (Dark Green) and core filled fractures (Light Green) are shown. 79
Figure 2.4 Stereographic projection of fracture poles for core sections of the Barnett Well-1. The approximate direction of the maximum horizontal stress is also shown. 79
Figure 2.5 Fracture type and orientation overlaying the distribution of rock classes for Barnett Wells 1 and 2. The analysis is extended to the logged section. 80
Figure 2.6 Influence of the spatial distribution of material properties on deformation and stress distribution. Three systems are considered: homogeneous, layered and heterogeneous. The regions colored red are local regions of high tensile stress and high propensity for tensile fracturing. Regions colored blue are local regions of high compression (from Burghardt et. al., 2012). 82
Figure 2.7 Typical fracture geometries and fracture interactions observed in core (left three images) and mine back experiments (right image). 83
Figure 2.8 Conceptual fracture model (top) based on fracture observations on core, outcrops, and mine back experiments. Simplified fracture model (bottom) for numerical simulations. 83
Figure 2.9 Required surface area, in million square feet, for production rates of 1 MMscf/D (red) and 5 MMscf/D (blue) for reservoir permeability in the range of 0.1 to 100 nano-Darcy (left) and 100 to 500 nano-Darcy (right). For example, production at 5 MMscf/D by a 400 nano-Darcy reservoir requires a surface area of 5.8×10^6 ft^2 86
Figure 2.10 Geometrical model. Except for the base case, all fracture case scenarios have identical surface area, identical distribution of fracture conductivity, in the primary and secondary fractures, and are contained in a medium with identical matrix permeability. The only difference is their geometry. Production results after 30 days to 2 years are investigated. 87
Figure 2.11 Results after the initial 30 days of production. The red background color represents the original reservoir pressure and the decrease in reservoir pressure is presented as changes in colors from red (representing virgin reservoir pressure) to dark blue (representing full depletion). 88
Figure 2.12 Results after 90 days. 88
Figure 2.13 Results after 180 days. The cumulative production in each of these cases is remarkably different from the others. These effects are initially observed via changes after 30 to 180 days production. 89
Figure 2.14 Results after one year. The cumulative production in each of these cases is remarkably different from the others. These results become considerably more pronounced after 1 or 2 years of production. 90
Figure 2.15 Results after two years. Some fracture geometries results in a more uniform depletion and consequently higher cumulative production. Others exhibit localized depletion and consequent lower cumulative production. 90
Figure 2.16 Cumulative production from all cases. The geometry with the highest cumulative production is the "fork fracture' with long and well spaced secondary fractures. 91

Figure 2.17 This figure shows the hierarchical order in production, from best (left) to worst (right) and from early production (top) to long-term production (bottom). 91
Figure 2.18 3D grid model showing the increased grid concentration along the locations of the wellbore and the plane of the fracture. 92
Figure 2.19 3D simulations including the wellbore, a fracture stage, and the associated depletion from a single fracture, during production, and including convergent flow at the wellbore. 92
Figure 2.20 Results indicate that well cumulative production and production rate are more sensitive to the overall fracture conductivity than to flow restrictions associated to near-wellbore convergence. In the above, the green and yellow lines show comparisons with and without convergence flow. Differences between the two are small. 93
Figure 3.1 Conductivity data for flow through two steel halves in contact. 98
Figure 3.2 Baseline steel billets separated by two shims. The steel plates have some degree of roughness. 98
Figure 3.3 Photograph of a mechanically split sample showing bedding plane fractures that accepted the very small amounts of fluid injected at low rate and without backpressure. These fractures are usually a consequence of unloading during sample recovery and desiccation. 99
Figure 3.4 Schematic of laboratory flow paths showing the consequences of stress-relief and sample preparation difficulties. 100
Figure 3.5 Barnett test results with water. 102
Figure 3.6 Haynesville test results with water. 102
Figure 3.7 Marcellus test results with water. 103
Figure 3.8 Barnett test results with gas. 104
Figure 3.9 Haynesville test results with gas. 105
Figure 3.10 Marcellus test results with gas. 106
Figure 3.11 Composite of data for saw cut samples for water. Data for nitrogen could be generated. Does anything show up for the different lithologies and reservoir qualities? Possibly, it can be remarked that there is early depletion accelerated reduction in conductivity for the Haynesville shales. 107
Figure 3.12 A common feature of the un-propped, mechanically split data is the loss of fracture conductivity to water with increasing stress, asperity failure at an effective confining pressure that is well within what would be encountered during depletion of the three characteristic plays. 108
Figure 3.13 shows the results for high temperature conductivity tests for Barnett, Haynesville and Marcellus. The drop in conductivity at higher temperatures could be attributable to increasing viscosities of flowing fluid. 109
Figure 3.14 This is a comparison of fracture conductivity for two discrete Barnett (best reservoir quality) shale measurements, the relatively low values for the gas, in comparison with most other measurements made in the program, suggest that the data for gas in this plot may be unreliable. 110
Figure 3.15 Within the range of reliable prediction, these two curves – absolute fracture conductivity for each fluid, are nominally the same. Differences will arise with more than one fluid in the fracture (relative permeability) and with Reynolds' numbers that are substantially greater than 1. 111

Figure 3.16 Within the range of reliable prediction, these two curves – absolute fracture conductivity for each fluid, are nominally the same. Differences will arise with more than one fluid in the fracture (relative permeability) and with Reynolds' numbers that are substantially greater than 1. 111
Figure 3.17 Creep data from one Barnett shale sample. All measurements were carried out at an effective closure stress of 5,000 psi. The reservoir quality was "best," and the flowing fluid was the synthetic water. 112
Figure 3.18 Barnett shear displacement test results. 113
Figure 3.19 Haynesville shear displacement test results. 114
Figure 4.1 Barnett different proppant size tests with water. 120
Figure 4.2 Haynesville different proppant size tests with water. 121
Figure 4.3 Marcellus different proppant size tests with water. 122
Figure 4.4 Barnett different proppant size tests with gas. 123
Figure 4.5 Haynesville different proppant size tests with gas. 124
Figure 4.6 Marcellus different proppant size tests with gas. 125
Figure 4.7 Barnett, Haynesville and Marcellus samples for different proppant size tests with water. 126
Figure 4.8 Barnett fluid exposure tests with water. 127
Figure 4.9 Barnett fluid exposure with gas. 128
Figure 4.10 Haynesville fluid exposure tests with water. 129
Figure 4.11 Haynesville Fluid exposure tests with gas. 130
Figure 4.12 Marcellus fluid exposure tests with water. 131
Figure 4.13 Conductivity tests with higher proppant concentrations for Barnett, Haynesville and Marcellus shales. 132
Figure 5.1 Fracture geometries used in the production simulations in this chapter. 137
Figure 5.2 Fracture conductivity versus stress for Haynesville shale samples representative of a good reservoir quality facies. Changes in fracture conductivity with increasing stress and without proppant are compared to various proppant configurations, including discontinuous proppant placement (channel). The black and yellow dotted lines represent a reduction in fracture conductivity of 2 and 3 decades per 10,000 psi. 138
Figure 5.3. The pressure distribution within the reservoir for the wide forked fracture geometry after 1 month, 12 months, and 24 months of production. The top plots are for simulations with monolayer propped secondary fractures and the bottom plots are for simulations with un-propped secondary fractures. Red indicates high pore pressure and blue indicates low pore pressure. 139
Figure 5.4. Production rate (left) and cumulative gas production (right) for various production simulations through the wide forked fracture geometry. 140
Figure 5.5. The pressure distribution within the reservoir for the fishbone fracture geometry after 1 month, 12 months, and 24 months of production. The top plots are for simulations with monolayer propped secondary fractures and the bottom plots are for simulations with un-propped secondary fractures. Red indicates high pore pressure and blue indicates low pore pressure. 141
Figure 5.6. Production rate (left) and cumulative gas production (right) for various production simulations through the fishbone fracture geometry. 141

Figure 5.7. Cumulative gas production from the wide forked fracture with various values of secondary fracture conductivity. 142
Figure 6.1. A photograph of TerraTek's large multi-axial stress frame is shown. 146
Figure 6.2. The approximate location of the Niobrara quarry is shown. 147
Figure 6.3. Niobrara boulder acquired from the quarry. The surfaces are painted for preventing changes in humidity during transport and storage. 148
Figure 6.4. Photographs of all faces of the block showing calcite inclusions. 149
Figure 6.5. OMS dabbed on the block surfaces highlight the texture of the rock fabric. 149
Figure 6.6. A drawing of the sample configuration is shown. 150
Figure 6.7. AE sensor pockets drilled on the south face of the block. 151
Figure 6.8. AE sensor pockets drilled on the west face of the block. 151
Figure 6.9. Block pressurization history prior to wellbore injection is shown in a graphical format. 155
Figure 6.10. The change in flatjack volumes, as a function of applied stress, versus time is shown for the period preceding borehole fluid injection. The nonlinearities in the traces up to approximately 37 minutes reflect the stiffening up of the system as the flatjacks seat and the compliance of the system is reduced. Differing injected fluid volumes over each loading period are reflective of the rock anisotropy. 156
Figure 6.11. Bore pressure, bore volume and applied stresses versus time from the beginning of borehole fluid injection. 156
Figure 6.12. Bore pressure, and flatjack volumetric deformation versus time commencing with borehole fluid injection. 157
Figure 6.13. Borehole pressure and flatjack volumetric deformation measurements closer to the breakdown are shown. 157
Figure 6.14. Post hydraulic fracturing stress down phase is shown. 158
Figure 6.15. Diagram of the test setup is shown. 159
Figure 6.16. Borehole pressure and applied stresses during first two stages glycerol flushing phase are shown. 159
Figure 6.17. Borehole pressure, bead pack (pore) pressure and applied minimum stresses during the third stage of glycerol flushing phase are shown. 160
Figure 6.18. Pressure drop across the un-propped fracture (DeltaP), applied flatjack stresses and measured flow rate are shown for repeat of stage 1. 162
Figure 6.19. Flow rate vs. differential pressure across the fracture for the four measurements made during stage 1 of the un-propped fracture conductivity measurement. The slope of the linear regression curve was used to calculate the best-fit conductivity value at this value of closure stress. 162
Figure 6.20. Pressure drop across the un-propped fracture (DeltaP), applied flatjack stresses and measured flow rate are shown for stage 2. 163
Figure 6.21. Flow rate vs. differential pressure across the fracture for the four measurements made during stage 2 of the un-propped fracture conductivity measurement. The slope of the linear regression curve was used to calculate the best-fit conductivity value at this value of closure stress. 163
Figure 6.22. Pressure drop across the un-propped fracture (DeltaP), applied flatjack stresses and measured flow rate are shown for stage 3. 164

Figure 6.23. Flow rate vs. differential pressure across the fracture for the four measurements made during stage 3 of the un-propped fracture conductivity measurement. The slope of the linear regression curve was used to calculate the best-fit conductivity value at this value of closure stress. 164
Figure 6.24. Pressure drop across the un-propped fracture (DeltaP), applied flatjack stresses and measured flow rate are shown for stage 4. 165
Figure 6.25. Flow rate vs. differential pressure across the fracture for the four measurements made during stage 4 of the un-propped fracture conductivity measurement. The slope of the linear regression curve was used to calculate the best-fit conductivity value at this value of closure stress. 165
Figure 6.26. An example of the finite-element results that were used to invert for the effective conductivity from the block test measurements. Fluid flows from the 7" open-hole section of the wellbore (left-hand side of plot), through the fracture at out the edge of the block (right-hand side of plot). Red indicates high pressure and blue indicates low pressure and the red arrows are the fluid velocity vectors. 166
Figure 6.27. Stress ramp down phase after un-propped fracture conductivity measurements is shown. 167
Figure 6.28. Bore Pressure, pressure in the bead pack (pore pressure) and applied flatjack stresses versus time are shown. 168
Figure 6.29. Pressure drop across the propped fracture (DeltaP), applied flatjack stresses and measured flow rate are shown for stage 1. 170
Figure 6.30. Flow rate vs. differential pressure across the fracture for the four measurements made during stage 1 of the propped fracture conductivity measurement. The slope of the linear regression curve was used to calculate the best-fit conductivity value at this value of closure stress. 170
Figure 6.31. Pressure drop across the propped fracture (DeltaP), applied flatjack stresses and measured flow rate are shown for stage 2. 171
Figure 6.32. Flow rate vs. differential pressure across the fracture for the four measurements made during stage 2 of the propped fracture conductivity measurement. The slope of the linear regression curve was used to calculate the best-fit conductivity value at this value of closure stress. 171
Figure 6.33. Pressure drop across the propped fracture (DeltaP), applied flatjack stresses and measured flow rate are shown for stage 3. 172
Figure 6.34. Flow rate vs. differential pressure across the fracture for the four measurements made during stage 3 of the propped fracture conductivity measurement. The slope of the linear regression curve was used to calculate the best-fit conductivity value at this value of closure stress. 172
Figure 6.35. Pressure drop across the propped fracture (DeltaP), applied flatjack stresses and measured flow rate are shown for stage 4. 173
Figure 6.36. Flow rate vs. differential pressure across the fracture for the four measurements made during stage 4 of the propped fracture conductivity measurement. The slope of the linear regression curve was used to calculate the best-fit conductivity value at this value of closure stress. 173
Figure 6.37. Un-propped and Propped fracture conductivity as a function of confining stress. 174

Figure 6.38: Large block faces North (left) and South (right) with screens still on. 175
Figure 6.39: Block exterior with screens removed displaying the fracture face (North and South faces of the block respectively). 176
Figure 6.40: The en echelon fracture found on the North side of the block. 177
Figure 6.41: Exterior of the South face of the block displaying proppant bound to the fracture face. 177
Figure 6.42: The top of the block displaying the fracture radiating from the wellbore. The South face of the block is at the top of the picture and the North is at the bottom. En echelon fractures are found along the fracture from the wellbore to the edge of the North face. 178
Figure 6.43: The top surface of the block displaying the wellbore and fracture. The North face of the block is to the left of the photo and to the right is the South face of the block. . 179
Figure 6.44: The fracture on the top of the block displaying 5-6 layers of proppant..... 179
Figure 6.45: Images of the open fracture displaying the proppant placed on the fracture surface (East and West faces respectively). A representative drawing of the open hole section of the casing along with the stress concentrator is displayed towards the center of the block image..... 180
Figure 6.46: Top image of block (left) before casing and fracturing of the block. The pre-existing calcite healed fracture can be seen. The image on the right displays the post image of the hydraulic fracture (Yellow) interacting with a pre-existing fracture (Red). 181
Figure 6.47: Left image: En echelon fractures are observed along the top north section of the block (Red) and a large stepover, with other smaller stepovers, occurr on the north face (Blue). Right image: The Red line is used to delineate the location of the preexisting fracture and the Green arrows are used to display how the en echelon material broke in thin sheet along the rock surfaces. 182
Figure 6.48: A large stepover fracture on the North face of the block is observed to have continued on for several inches after passing a stepover fracture deviation. 182
Figure 6.49: En echalon fracture stacking observed on the upper portion of the East face of the block. The material separating these factures from one another was less than 1.0mm thick. 183
Figure 6.50: A goniometer device used to map the fracture surface. 183
Figure 6.51: Images of the fracture surface and the locations where proppant samples were collected to evaluate particle grain size distribution and crushing. 184
Figure 6.52: Digital microscope images of proppant grain quality and diameters being measured..... 186
Figure 6.53: Acoustic emissions on the East/West face of the block at fracture closure following the placement of proppant. The image displays acoustic events of proppant embedding and consolidation around one another. 186
Figure 6.54: The embedment on the facture surface (Red) was measured using the Green lines to determine the overall surface height change. In this instance a total of 0.059 mm height change occurred. Additionally no clear signs of embedded particles were found. . 187
Figure 6.55. Variation of triaxial stresses (pink, green and blue curves) and bead pack (pore) pressure (red curve) applied to the block during testing. Labels UT_0, UT_1 and UT_2 indicate moments of auto-calibrations performed to estimate P-wave velocity of the rock. 189

Figure 6.56. Photo of cables broken during block pressurization. 190
Figure 6.57. Velocity (km/s) of P-wave propagation along multiple paths inside the testing vessel. a) unstressed condition (UT_0); b) E-W Stress 2450 psi (UT_1); and c) E-W Stress 1000 psi (UT_2). 190
Figure 6.58. a) and d) Variation of P-wave velocities measured along 10 selected traces during the stressing of the block; b) and e) synoptic pictures demonstrating North View of selected traces; c) and f) synoptic pictures demonstrating Top View of selected traces. Upper row: sensors 3, 8 and 11 are transmitters; lower row: sensors 12 and 13 are transmitters of elastic waves. 191
Figure 6.59. Distance between sensors versus observed onset time. The slope characterizes the mean value of homogenized velocity. 192
Figure 6.60. Bore pressure (red), cumulative number of localized AE (black), East-West flat jack volume (green), North-South flat jack volume (pink) and Top-Bottom Actuator volume (blue). All parameters are plotted versus loading time, separation of loading stages (a)-(e) is shown by vertical dash lines. 193
Figure 6.61. (a)-(c) Three orthogonal projections of AE hypocenters; d) Loading history recorded during Stage (a) of injection. The color of the dots corresponds to the time sequence of AE events appearance according to the color bar at the bottom of the figure. 194
Figure 6.62. (a)-(c) Three orthogonal projections of AE hypocenters; d) Loading history recorded during Stage (a) of Injection. Original AE hypocenter data are the same as presented in Figure 6.61 (a)-(c). 195
Figure 6.63. (a)-(c) Three orthogonal projections of AE hypocenters; d) Loading history recorded during stage (b) of injection. The color of the dots corresponds to the time sequence of AE events appearance according to the color bar at the bottom of the figure. 196
Figure 6.64. Three orthogonal projections of AE hypocenter normalized density calculated for the stage (b) of injection. Original AE hypocenter data are the same as presented in Figure 6.63 (a)-(c). 196
Figure 6.65. (a)-(c) Three orthogonal projections of AE hypocenters; d) Loading history recorded during Stage (c) of Injection. The color of the dots corresponds to the time sequence of AE events appearance according to the color bar at the bottom of the figure. 197
Figure 6.66. Three orthogonal projections of AE hypocenter normalized density calculated for the stage (b) of injection. Original AE hypocenter data are the same as presented in Figure 6.65 (a)-(c). 198
Figure 6.67. Top view photo of fractured sample. 199
Figure 6.68. (a)-(c) Three orthogonal projections of AE hypocenters; d) Loading history recorded during Stage (d) of Injection. The color of the dots corresponds to the time sequence of AE events appearance according to the color bar at the bottom of the figure. 199
Figure 6.69. Three orthogonal projections of AE hypocenter normalized density calculated for stage (d) of injection. Original AE hypocenter data are the same as presented in Figure 6.68 (a)-(c). 200

Figure 6.70. (a)-(c) Three orthogonal projections of AE hypocenters; d) Loading history recorded during Stage (e) of Injection. The color of the dots corresponds to the time sequence of AE events appearance according to the color bar at the bottom of the figure. 200
Figure 6.71. Three orthogonal projections of AE hypocenter normalized density calculated for stage (e) of injection. Original AE hypocenter data are the same as presented in Figure 6.70 (a)-(c). 201
Figure 6.72. (a)-(c) Three orthogonal projections of AE hypocenters; d) Loading history recorded during Stage (f) of Injection. The color of the dots corresponds to the time sequence of AE events appearance according to the color bar at the bottom of the figure. 202
Figure 6.73. Three orthogonal projections of AE hypocenter normalized density calculated for the stage (f) of injection. Original AE hypocenter data are the same as presented in Figure 6.72 (a)-(c). 203
Figure 6.74. (a)-(c) Three orthogonal projections of AE hypocenters; d) Loading history recorded during Stage (g) of Injection. The color of the dots corresponds to the time sequence of AE events appearance according to the color bar at the bottom of the figure. 203
Figure 6.75. Three orthogonal projections of AE hypocenter normalized density calculated for the stage (g) of injection. Original AE hypocenter data are the same as presented in .. 204
Figure 6.76. a) Time history of mechanical parameters and amplitude of localized AE events (pink color dots); b) P-wave velocity measured by using sensor 8 as transmitter and sensors 17, 19, 20, 21, 23 and 24 as receivers; c) P-wave first motion amplitude vs time. 205
Figure 6.77. Bore pressure (red), amplitude of localized AE (blue), East-West flat jack volume (green), North-South flat jack volume (pink) and East-West stress (black). All parameters are plotted versus loading time, separation of loading stages (a)-(c) is shown by vertical dash lines. 207
Figure 6.78. Representative example of waveforms recorded during the stage (a) at the moment of ultrasonic transmission by channel 8. 207
Figure 6.79. (a)-(c) Three orthogonal projections of AE hypocenters; d) Loading history recorded during Stage (b) of proppant injection. The color of the dots corresponds to the time sequence of AE event appearances according to the color bar at the bottom of the figure. 209
Figure 6.80. (a)-(c) Three orthogonal projections of AE hypocenters; d) Loading history recorded during Stage (b) of proppant injection. The color of the dots corresponds to the time sequence of AE event appearances according to the color bar at the bottom of the figure. 209
Figure 6.81. (a)-(c) Three orthogonal projections of AE hypocenters; d) Loading history recorded during Stage (c) of proppant injection. The color of the dots corresponds to the time sequence of AE event appearances according to the color bar at the bottom of the figure. 210
Figure 6.82. (a)-(c) Three orthogonal projections of AE hypocenters; d) Loading history recorded during Stage (c) of proppant injection. The color of the dots corresponds to the time sequence of AE event appearances according to the color bar at the bottom of the figure. 211

Figure 7.1 Conceptual fracture model (top), based on fracture observations on core, outcrops, and mine back experiments and simplified fracture model (bottom) for use in numerical simulations. 215
Figure 7.2 Typical morphology of far-wellbore fractures: (1) Conceptual model. (2) Mineralized fractures in sandstone away from the source. (3) Closely spaced fracturing in laminated sandstone. Fracture propagates in multiple sub-parallel directions and minimal width. 217
Figure 7.3 Fracture morphology and heterogeneous distribution of proppant transport during hydraulic fracturing in Niobrara shale. Regions with visual evidence of proppant in the fracture are highlighted with red rectangles (top). Closely spaced fracture branches and stepovers are commonly observed (center, bottom). These observations are recorded at the block surfaces, away from the wellbore and correspond to the far-wellbore region. 218
Figure 7.4 Proppant embedment results from rock failure due to stress concentrations and the proppant/rock interface. Proppant crushing results if the failure stress for embedment is higher than the crushing strength of the proppant. In both cases the result is fines generation, fracture closure and loss of fracture conductivity. 219
Figure 7.5 Tensile failure, at the unsupported fracture face, arises from high drawdown during production. This results in solids production (i.e., generation rock fragments and fines) that may enter the wellbore or plug the hydraulic fracture. The problem is controlled by understanding the failure envelope to drawdown, as a function of time. 220
Figure 7.6 Conceptual morphology of the near-wellbore fracture region (left, center). Experimental results show the fracture face arises from high drawdown during production. This results in solid production (i.e., generation rock fragments and fines) that may enter the wellbore or plug the hydraulic fracture. The problem is controlled by understanding the failure envelope to drawdown, as a function of time. 221
Figure 7.7 Microscope images of proppant embedment, plastic flow at the rock/proppant interface and associated extrusion of the surface around the proppant. The bulged region may be dispersed and mobilized by the flow. The surface of the rock in contact with the proppant is a plastified surface of highly reduced permeability. 222
Figure 7.8 Schlumberger's HiWAY* fracturing proposes to control the distribution of proppant, create proppant pillars and high conductive channels and as a consequence facilitate the passage of solids and precipitants from the far-wellbore region. It also proposes to reduce the area of contact and thus the damage to the fracture-face permeability. 223
Figure 7.9 Examples of connectivity between the wellbore and the near-wellbore fracture. The conceptual representation of this region and the frequent use of perforations to facilitate fracture initiation are shown in the upper section. Photographs of this region from real experiments on tight shales are shown below. The fracture complexity in this region could be high. The opposite is the desired outcome. 225
Figure 7.10 Effect of creep deformation (i.e., time dependence) on the stress concentrations around the wellbore. The hoop stress and fracture initiation pressure decrease considerably as a function of time. 226

Figure 7.11 List of dominant dependence (Red= Bad, Yellow = Intermediate, Green = Neutral, White = No dependence) of critical properties along the various regions of a fracture. 228
Figure 7.12 Graphical representation of the various contribution to the preservation of fracture surface area and fracture conductivity, and to the preservation of well production. 239

EXECUTIVE SUMMARY

This project consisted of theoretical and experimental work, to understand the multiple causes of loss of fracture area and fracture conductivity, and to define solutions to mitigate the resulting loss of production. To accomplish this we endeavored to understand both the simpler and the often complex hydraulic fracture networks, and determine the critical parameters to maintain productive fracture area and fracture conductivity—including optimal proppants, fracture fluids, and pumping schedules, all as they are related to the heterogeneous rock formations that are to be produced. The end product deliverable is an improved workflow for fracture design, rock characterization, and production of tight gas shales. The problem is difficult, but the potential for greatly improved production is real.

The components of this effort included the evaluation of reservoir geology, mechanical properties, in-situ stress, and rock-fluid interactions on three representative tight shale plays in North America: Barnett, Marcellus and Haynesville shales. Results include evaluation of loss of fracture conductivity and loss of fracture surface area. Fracture conductivity measurements were conducted under various conditions of propped and un-propped fractures, flowing with water and gas, as well as evaluating the effects of temperature, creep, and water interaction prior to fracture conductivity measurements.

Results were subsequently compared to a large-scale fracture conductivity experiment, to understand the effect of scale on the measurements. Results of loss of surface area included numerical simulations using fracture networks of complex geometries, and allowing the second and third tier fractures in the network to be disconnected from the main fracture, by insufficient connectivity or insufficient conductivity. In addition, and for a reference to the above work, the effort included an extensive discussion of the current (best) practices by the industry and the best practices by the operator participants to this project. The project also included a thorough discussion of the various regions of the fracture system needed for adequate characterization. It is by understanding and integrating the above that the workflow proposes production improvement.

Results for material property characterization provided a strong reference for comparing the reservoir, geochemical, petrologic and mechanical behavior of the various rock facies in the Barnett, Marcellus and Haynesville rocks.

Results of fracture surface area characterization indicated that the fracture geometry and the total surface area are both important to well production. We show that fractures with identical first tier fracture length and fracture conductivity, and multiple realizations of the secondary fracture geometry, under conditions of constant surface area, results in considerable differences in daily production and cumulative production. We found that some fracture network geometries promote high early productivity, where as other network geometries promote long term productivity at the expense of early productivity. We also show that the contribution of the second and third tier fracture networks to production depends strongly on the transport of proppant to these fractures. It also depends on their mechanical properties (e.g., hardness, creep) and rock-fluid sensitivity.

A considerable component of this report was the characterization of fracture conductivity on laboratory samples under multiple conditions. For consistent analysis and interpretation, fracture conductivities of 0.01 mD-ft or lower were assumed to be too low for production. Results show that smooth fractures without proppant do not retain sufficient conductivity to be of relevance to production. In contrast, fractures with natural asperities are important to production, and particularly so when the closure stress is below 4000 to 6000 psi. The sensitivity with stress for these is approximately 2 decades per 10,000 psi. There is a great deal of consistency on the measured data between samples, and at high closure stress, there is no rock type differentiation. The sensitivity to temperature and time dependence, creep, was also investigated. Temperature appears to introduce a dramatic decrease in fracture conductivity at some critical stress. Creep introduces high initial stress dependence, at low confining stress. Thus, laboratory conditions for fracture conductivity may need to include temperature and creep to be more representative of field conditions.

Results also show that in all cases, adding proppant to the fractures resulted in a considerable increase in fracture conductivity, by several orders of magnitude, and a considerable reduction of the stress sensitivity. Typical reductions of fracture conductivity with stress for un-propped and propped fractures are 3 to 2 decades per 10,000 psi. A great deal of consistency on the measured data between samples was found, and in general, there is no rock type differentiation. When there is, this is most apparent at low closure stress.

The effect of water soaking the fracture surfaces prior to fracture conductivity testing showed a clear softening of the rock surface hardness and an associated loss in both fracture area and fracture conductivity with stress. Results of tests with increased proppant concentration (3 monolayers) show a consistent and strong increase in fracture conductivity and a reduction in stress sensitivity from 2 decades to 1 decade per 10,000 psi, compared to proppant concentrations of a single monolayer.

Large scale laboratory tests on a rock block of approximately 36 inches x 36 inches x 36 inches, provided a strong insight in to the development of fracture geometry and fracture conductivity, and the scaling of measurements on small samples. Results show that the laboratory data on small samples is conservative and represents an over-estimation of the large-scale change in fracture conductivity with stress. It also shows that fracture complexity is inevitable, particularly along the far-wellbore fracture region, and is associated to the textural complexity of the medium.

Results of this program indicate that there is no simple solution for alleviating the loss of surface area and fracture conductivity during production, and consequently there is no simple solution for alleviating the loss of productivity with time. The solution is complex. It requires understanding of multiple reservoir and completion quality properties affecting the characteristic regions of the fracturing system. These are the wellbore, wellbore/fracture connector, near wellbore fracture region and far-wellbore fracture region. Because each of these regions may require different conditions of optimization, the

solution also requires understanding the conflicting requirements and needed compromises to obtain an optimum overall solution. Unconventional tight shale reservoirs are geologic plays and understanding their geologic complexity is a fundamental prerequisite. The observed heterogeneous distribution of rock properties and in-situ stress are a direct reflection of their geologic complexity. Because of their low permeability, production depends on the creation of surface area in contact with the high reservoir quality sections of the play, and on the long-term retention of surface area and fracture conductivity. As indicated, however, it also depends on selecting the adequate landing point for improving the conditions of fracture initiation and depends critically on the wellbore/fracture connectivity.

Although this report and the experimental effort addressed primarily the loss of fracture surface area and loss of fracture conductivity in the far-wellbore region (i.e., region with no proppant or low proppant concentration), it is clear from the discussion that defining a workflow for improving well productivity requires the integration and optimization of the various components of the fracturing system. This includes:

- Understanding the geologic system,
- Understanding the distribution of material properties in the system,
- Understanding the combination of these rock properties, to define critical conditions of reservoir quality and completion quality,
- Understanding the implication of the distribution of reservoir quality and completion quality properties on the four fracture regions of: wellbore, wellbore fracture connector, near wellbore region and far-wellbore region, and
- Understanding the combined contribution of these regions to well production.

1 MATERIAL PROPERTY CHARACTERIZATION

1.1 Introduction

The objective of material property characterization is to provide a summary of fundamental petrophysical, petrological, geochemical, and mechanical properties of all formations included in the study: Barnett, Haynesville, and Marcellus tight shale plays. This includes defining in a quantitative and non-subjective manner the presence and distribution of unique facies in each of these plays, and sampling these adequately to obtain a representative assessment of their properties.

Key components of this effort are as follows:

(i) Define average reservoir petrophysical properties following the Tight Rock Analysis (TRA) methodology, including porosity, gas-filled porosity, permeability, and pore fluid saturations (mobile oil, water and gas).

(ii) Define average petrological and mineralogical properties via thin section, Scanning Electron Microscope (SEM) and X-ray diffraction (XRD) testing. This includes mudstone type classification by age, depositional texture, matrix composition, and organic content and type.

(iii) Define average geochemical properties of organic content, type and maturation.

(iv) Define average anisotropic mechanical properties (including static and dynamic anisotropic elastic moduli and strength). This will cover the matrix features as well as the properties of the characteristic discontinuities, as determined by direct or triaxial shear testing.

For analysis of heterogeneity and optimal selection of laboratory sample locations for testing, we used advanced n-dimensional heterogeneous rock analysis (HRA) of well log measurements, to define distinct rock classes, and maximize representations of their variability while optimizing the number of samples taken. The analysis provides a mathematically precise method for identifying patterns of bulk log responses and for finding small but consistent variations in texture and composition along the length of the region of interest (including reservoir and non-reservoir rocks). HRA identifies rock classes with similar texture and composition, and with corresponding similar material properties, and discriminates those with different texture and composition, thus identifying the building blocks of the heterogeneous medium. The analysis results in a color-coded representation of the distinct rock classes along the region of interest and provides a quantitative assessment of the distribution, stacking patterns and relative abundance of the various units. This allows us to define the dominant reservoir and non-reservoir units. Sample locations for laboratory testing are then selected within each of these rock classes and the resulting characterization is representative of the various realizations of these classes, along the core tested, and outside the cored section, along the well.

HRA also allows identification of these rock classes from log responses of other wells in the basin by comparison to log responses defined in the reference well (with core and with adequate laboratory measurements of geologic, petrologic, reservoir, geochemical and mechanical properties). This process facilitates the propagation of laboratory data via logs to other locations in the play without core data. Propagation of the knowledge gained in this study to multiple wells was, however, not part of this study.

Laboratory properties were measured using the Tight Rock Analysis (TRA) method for laboratory characterization of tight, organic-rich mudstone systems, on core samples. The TRA method was specifically developed to accurately resolve petrophysical properties on nano-darcy permeability and ultra-low porosity rocks. Laboratory measurements include pore fluid saturations (oil, water and gas), effective porosity, total porosity, and matrix permeabilities in tight reservoirs. It includes organic content, degree of maturation, as well as canister desorption and adsorption measurements for assessment of adsorbed gas, gas composition and adsorption capacity. It includes core geologic descriptions and detailed petrology and X-ray diffraction (XRD) analysis. It includes fluid sensitivity analysis and the evaluation of anisotropic mechanical properties for completion design.

The data presented below summarizes the TRA characterization for dominant facies of the Barnett, Haynesville, and Marcellus tight gas shale plays. Reservoir and non-reservoir units were characterized. Results provide a good reference data set for evaluation of the variability in properties from facies to facies and between plays. It also provides a good data set for defining the type of property combinations resulting in good reservoir quality and poor reservoir quality. Furthermore, the data provides the opportunity for relating the set of properties representative of good or poor quality reservoir rocks to the corresponding rock mechanical behavior, which controls the loss in fracture conductivity and surface area. Data are presented in groups representative of each HRA rock class and denoted by a particular color. This color labeling allows us to associate these properties to rock classes identified with logs with similar colors throughout the play. Subsequently each rock class is also classified according to its respective reservoir quality index (RQI) into one of the following five groups: Best, good, fair, poor, and worst. RQI evaluation is based on the combined evaluation of gas filled porosity, permeability, total organic content and pore pressure. The latter is considered constant for each of these plays.

1.2 Barnett Shale Properties

The Barnett Shale is a geological formation located in the Bend Arch-Fort Worth Basin. It consists of sedimentary rocks of Mississippian age (354–323 million years ago) in Texas. The formation underlies the city of Fort Worth and underlies 5,000 mi^2 (13,000 km^2) and at least 17 counties. The Barnett shale stratigraphic section consists of limestone and organic-rich shales. The Barnett Shale, in particular, consists of dense, organic-rich, soft, thin-bedded, petroliferous, fossiliferous shale and hard, black, finely crystalline, petroliferous, fossiliferous limestone. In the northeastern portion of the basin, the Barnett is divided into informal upper and lower shale members by the presence of the intervening Forestburg Limestone Member. In addition, the shale members themselves contain a significant volume of interbedded limestone and minor dolomite in the north. Over the Bend Arch the lower Barnett passes laterally into the Chappel Limestone, a crinoidal limestone with local buildups up to 300 ft. The upper shale is usually thinner than the lower member and not divided. The middle Forestburg Member ranges up to 300 ft, but thins to a feather edge in southernmost Wise and Denton Counties Where the Forestburg is absent. (Wikipedia, 2012; Bruner and Smosna, 2011).

Two wells representative of the Johnston County of this play were selected for this study. Petrologic evaluation conducted on selected Barnett shale from the Barnett Well 1 include siliceous mudstones, mixed siliceous/calcareous mudstones, mixed siliceous/phosphatic mudstones, and mixed siliceous/argillaceous mudstones. Overall reservoir quality is high with a high average measured porosity (7.8%), average gas-filled porosity (6.9%), and average calculated permeability (473 nanodarcies). The lithotype that exhibits the best quality is the siliceous mudstone with an average gas-filled porosity of 7.4% and average calculated permeability of 530 nanodarcies. Recrystallized silica is the dominant authigenic mineral in the cored interval and imparts a high reservoir quality zone by lining pore throats and providing rigidity to compressive stress. Amorphous kerogen is admixed with silica cement creating organic matter that typically has a high surface area and propensity to adsorb various gas species. A very slight reduction in reservoir quality is noted at the base of the cored interval where detrital clays are more common. Clay species are dominated by illite and mixed-layer illite-smectite, with only trace amounts (<1%) of chlorite and kaolinite. Overall fresh water sensitivity is considered very low; total expandable clay content is variable and ranges from 0-2% (XRD data). Reservoir sensitivity to acid-based completion fluids is regarded as low with total iron bearing mineral species present such as pyrite, ferroan dolomite/ankerite, and siderite ranging from 3-7%.

Samples selected for petrologic study from samples from the second core, Barnett Well 2, include predominantly siliceous and siliceous/argillaceous facies of the Barnett Shale. These are characterized by pervasive microcrystalline silica cement in the matrix and variable, but generally common to abundant ferroan dolomite, disseminated organic matter, and phosphatic grains, and represent the best reservoir quality units in the sampled interval. Reservoir sensitivity to fresh water is moderate to high, particularly in, but not restricted to, argillaceous samples. Illite-smectite makes up to 31% of clays present and expandability is as high as 35%. Due to the presence of ferroan dolomite and pyrite,

sensitivity to acid-based completion fluids is considered moderate to high. Rock property characterization for selected units present in these cores is described below.

Figure 1.1 shows the HRA classification of two wells in the Barnett play and show the presence and distribution of 12 rock classes within the cored section of these wells. We noticed that Barnett Well 1 exhibits a significant amount of vertical heterogeneity with representation of all the rock classes. In contrast, Barnett Well 2 exhibits a high degree of vertical homogeneity and is predominantly represented by a single rock class (orange). To the right side of the well log classification along the length of the cored sections, are histograms showing the distribution and preponderance of the various rock classes within each of the cores. This information is important for identifying the sampling strategy and the degree of redundancy between wells. Eight rock classes representative of reservoir and non-reservoir units were selected for characterization. These are the Dark Blue, Yellow, Red, Brown, Purple, Olive, Orange and Gray classes.

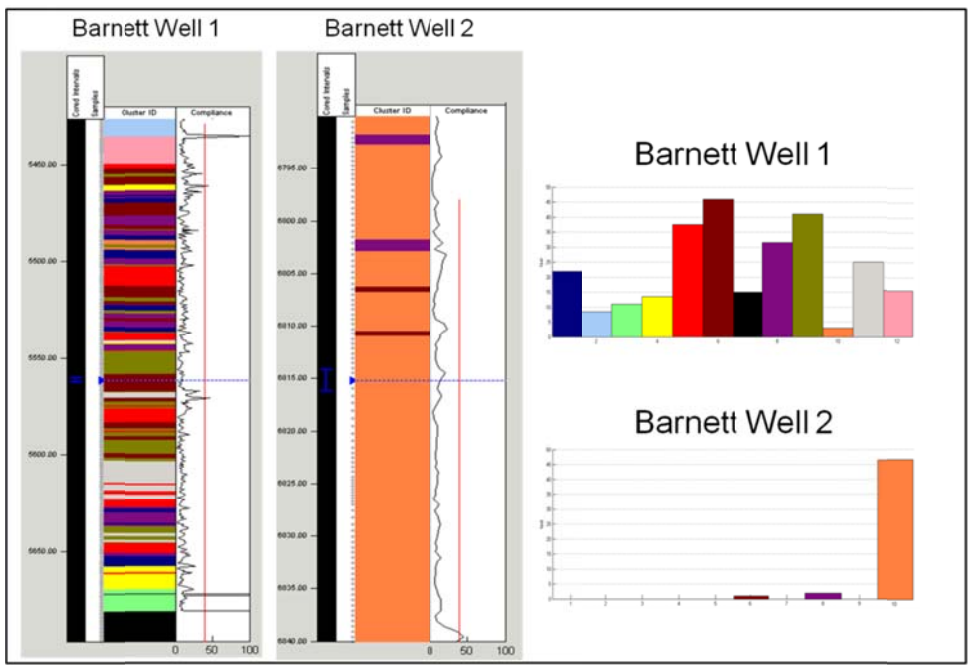

Figure 1.1 HRA classification of two wells in the Barnett play indicating the presence and distribution of 12 rock classes within the cored section of these wells.

Table 1.1 Barnett rock classes and corresponding reservoir quality Index

Barnett Rock Classes	RQI	Petrophysical	Petrologic	Geochemical	Geomechanical Static	Geomechanical Dynamic	XRD
Dark Blue	Poor	✓	✓	✓	✓	✓	✓
Yellow	Poor	✓	✓	✓			✓
Red	Poor	✓	✓	✓	✓	✓	✓
Brown	Good	✓	✓	✓	✓	✓	✓
Purple	Good	✓	✓	✓			✓
Olive	Fair	✓	✓	✓	✓	✓	✓
Orange	Best	✓	✓	✓	✓	✓	✓
Gray	Fair	✓	✓	✓			✓

Figure 1.2 shows the distribution of gas filled porosity (GFP), pressure-decay permeability and total organic carbon (TOC) for each rock class. These values define the reservoir quality of the individual units. The distribution of properties is color coded in accordance with the rock class colors. The units within the section with pink background indicate the reservoir units (highest GFP, permeability and TOC). The units within the section with blue background indicate the non-reservoir units (lowest GFP, permeability and TOC). Clearly, the orange class is the class with highest reservoir quality and highest RQI.

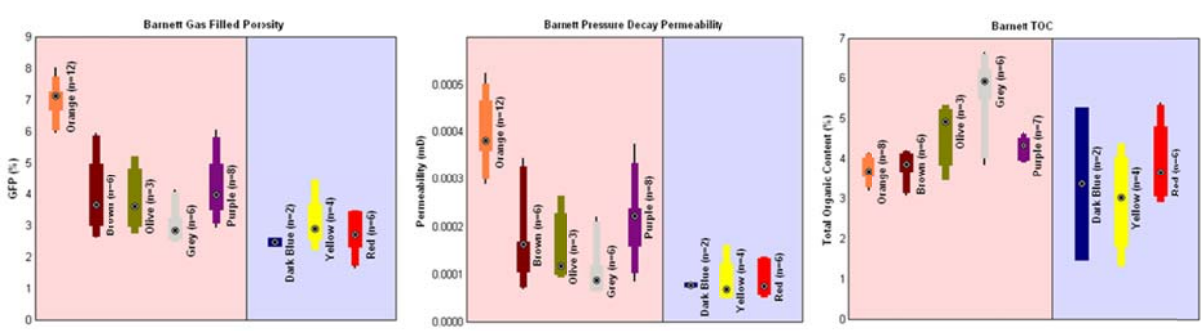

Figure 1.2 Distribution of gas filled porosity (GFP), pressure-decay permeability and total organic carbon (TOC) for each rock class.

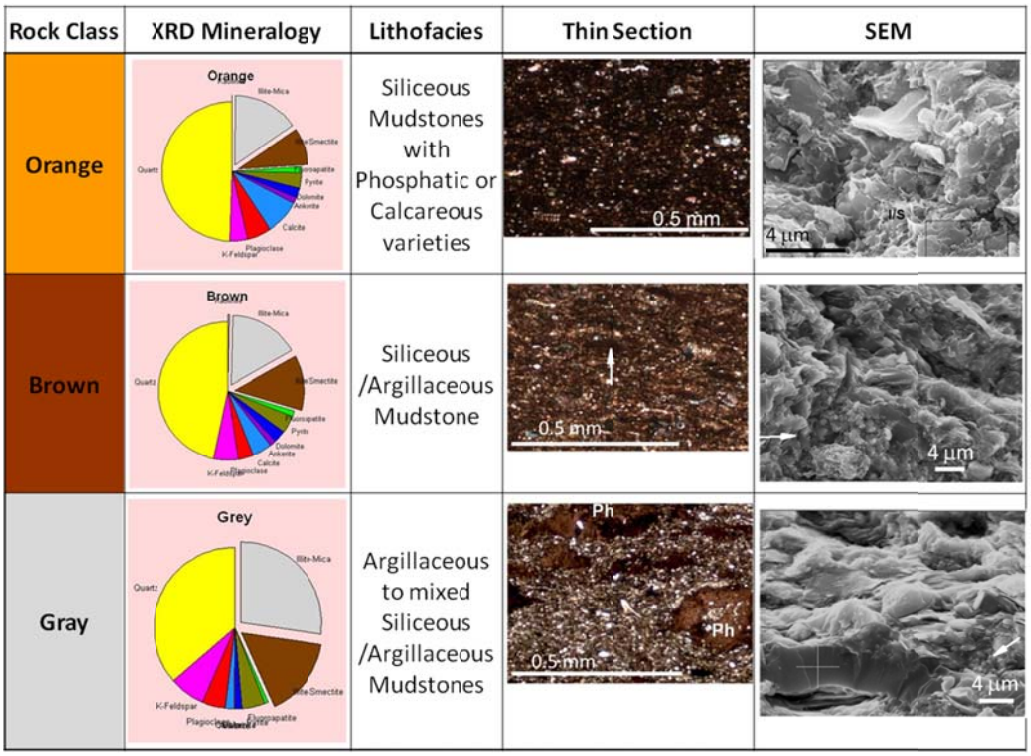

Figure 1.3 Petrologic overview of three rock classes in the Barnett shale.

Figure 1.3 and Figure 1.4 show a petrologic overview of the selected rock classes representative of the Barnett shale. The Orange, Brown, Gray, and Purple class are reservoir units. The Dark Blue, Yellow and Red classes are non-reservoir units. Mineral composition, lithologic denomination, thin section micrographs and SEM photographs are included for each rock class. These provide a good description of the dominant matrix minerals, the bulk mineral distribution, the fossil and detrital distribution and the micro texture of each rock class.

Rock Class	XRD Mineralogy	Lithofacies	Thin Section	SEM
Dark Blue	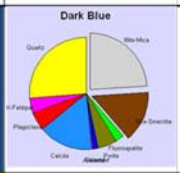	Silty, Argillaceous Mudstone	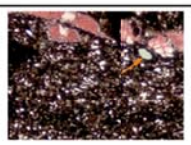	
Yellow	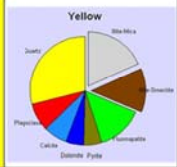	Phosphatic to Siliceous Argillaceous Mudstones	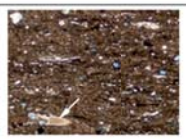	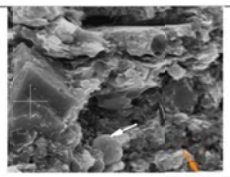
Red	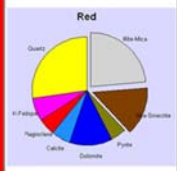	Argillaceous to Calcareous and Dolomitic Mudstones	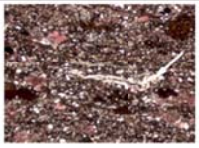	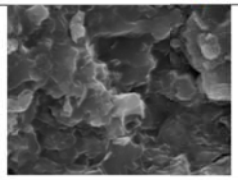
Purple	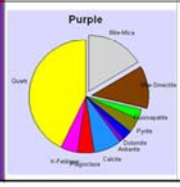	Siliceous, commonly with mixed Argillaceous and locally Phosphatic	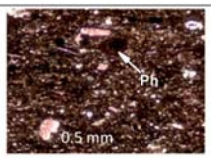	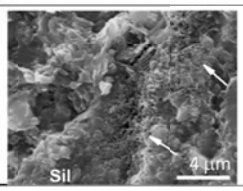

Figure 1.4 Petrologic overview of four rock classes in the Barnett shale.

Table 1.2 Summary of Barnett Petrophysical Properties

Rock class	No of Samples	Bulk Density		Grain Density		Dry Gas Density		Effective Porosity		Water Saturation		Gas Saturation	
		(g/cc)		(g/cc)		(g/cc)		(% BV)		(% PV)		(% PV)	
		Avg	STD	Avg	STD	Avg	STD	Avg	STD	Avg	STD	Avg	SRD
DarkBlue	2	2.59	0.05	2.65	0.04	2.67	0.03	3.54	1.03	11.92	13.04	71.54	14.93
Yellow	4	2.54	0.10	2.62	0.08	2.66	0.07	5.09	1.63	26.97	7.81	61.81	8.20
Red	6	2.52	0.02	2.59	0.02	2.62	0.02	4.62	0.74	21.25	8.12	57.65	8.84
Brown	6	2.47	0.05	2.58	0.04	2.61	0.04	5.86	1.22	14.50	9.19	66.25	8.65
Purple	8	2.48	0.03	2.59	0.03	2.62	0.03	6.06	0.95	13.35	3.73	68.93	7.99
Olive	3	2.48	0.01	2.57	0.03	2.60	0.03	5.34	1.43	12.95	6.67	71.17	4.34
Orange	12	2.45	0.03	2.64	0.01	2.65	0.01	7.88	0.50	6.04	2.04	88.48	2.80
Grey	6	2.49	0.04	2.56	0.04	2.59	0.05	4.62	0.86	12.58	5.34	65.13	7.62

Summary of Barnett Petrophysical Properties (continued …)

Rock class	No of Samples	Mobile Oil Saturation		Gas Filled Porosity		Bound Hydrocarbon Saturation		Clay Bound water		Pressure Decay Permeability	
		(% PV)		(% BV)		(% BV)		(% BV)		(nD)	
		Avg	STD	Avg	STD	Avg	STD	Avg	STD	Avg	STD
DarkBlue	2	16.54	1.89	2.46	0.20	0.62	0.20	4.01	2.94	76	6.79
Yellow	4	11.22	4.66	3.10	0.94	0.64	0.57	6.07	1.12	86	52.64
Red	6	21.10	5.19	2.69	0.71	0.74	0.39	6.48	1.11	87	38.81
Brown	6	19.25	4.04	3.95	1.28	0.84	0.20	5.53	1.59	168	95.64
Purple	8	17.72	5.05	4.22	1.04	0.83	0.33	5.32	0.75	211	85.34
Olive	3	15.88	3.15	3.84	1.25	1.08	0.37	5.65	0.23	157	93.17
Orange	12	5.48	1.09	6.98	0.60	0.70	0.57	4.22	1.00	400	74.32
Grey	6	22.29	4.85	3.00	0.61	0.82	0.53	6.75	0.78	106	59.46

Table 1.3 Summary Barnett Geochemical Properties

Rock class	No of Samples	Total Organic Content	
		(% Wt)	
		Avg	STD
DarkBlue	2	3.56	1.95
Yellow	4	2.92	1.39
Red	6	3.76	1.03
Brown	6	3.83	0.39
Purple	8	4.17	0.32
Olive	3	4.20	1.10
Orange	12	3.72	0.33
Grey	6	5.21	1.51

Table 1.4 Summary of Barnett Geomechanical Properties - Static

Rock class	No of Samp.	Bulk Density		Effective Confining Stress		Peak Strength (V)		Peak Strength (H)		Young's Mod (V)		Young's Mod (H)	
		(g/cc)		(psi)		(psi)		(psi)		(psi x E6)		(psi x E6)	
		Avg	STD	Avg	STD	Avg	STD	Avg	STD	Avg	STD	Avg	STD
Dark Blue	2	2.51	0.087	2509	364	30636	11035	26340	1627	3.99	2.33	5.4	0.16
Red	1	2.54	---	2204	---	19883	---	23590	---	2.90		4.03	
Brown	1	2.45	---	2553		24164	---	24790	---	3.27		4.33	
Olive	3	2.52	0.016	2562	273	16988	3364	21546	470	2.88	0.39	4.53	0.43
Orange	5	2.50	0.046	3030	320	25909	828	30758	3624	3.86	0.26	5.60	0.36

Summary of Barnett Geomechanical Properties – Static (continued …)

Rock class	No of Samples	Poisson's Ratio (V)		Poisson's Ratio (H)	
		Avg	STD	Avg	STD
Dark Blue	2	0.219	0.047	0.190	0.008
Red	1	0.156	---	0.143	---
Brown	1	0.153	---	0.183	---
Olive	3	0.131	0.026	0.162	0.008
Orange	5	0.201	0.017	0.256	0.058

Table 1.5 Summary of Barnett Geomechanical Properties - Dynamic

Rock class	No of Samples	Bulk Density		Mean Stress		P-Wave Vel (V)		P-Wave Vel (H)		S-Wave Vel (V)		S-Wave Vel (H)	
		(g/cc)		(psi)		(ft/s)		(ft/s)		(ft/s)		(ft/s)	
		Avg	STD	Avg	STD	Avg	STD	Avg	STD	Avg	STD	Avg	SRD
Dark Blue	2	2.59	0.086	4196	844	16296	2702	17003	1312	9015	962	9589	128
Red	1	2.56	---	4553	---	13000	---	16091	---	7756	---	9402	---
Brown	1	2.46	---	3226	---	13070	---	15342	---	7887	---	9162	---
Olive	3	2.53	0.021	3559	325	13562	797	16216	626	8132	516	9350	353
Orange	5	2.51	0.05	3729	328	13088	799	15123	873	7849	608	8775	871

Summary of Barnett Geomechanical Properties – Dynamic (continued…)

Rock class	No of Samples	Bulk Density		Young's Mod (V)		Young's Mod (H)		Poisson's Ratio (V)		Poisson's Ratio (H)	
		(g/cc)		(psi x E6)		(psi x E6)					
		Avg	STD	Avg	SRD	Avg	STD	Avg	STD	Avg	STD
Dark Blue	2	2.59	0.086	7.53	2.07	8.16	0.59	0.258	0.058	0.257	0.083
Red	1	2.56	---	4.53		7.37		0.24	---	0.193	---
Brown	1	2.46	---	4.84		6.81		0.211	---	0.206	---
Olive	3	2.53	0.021	5.05	0.72	7.43	0.68	0.234	0.005	0.226	0.018
Orange	5	2.51	0.05	4.68	1.25	6.43	1.31	0.240	0.065	0.208	0.086

Table 1.6 Summary of Barnett XRD Mineralogy

Rock class	No of Samples	QUARTZ		CALCITE		TOTAL CLAY		OTHER	TOTAL
		%		%		%		%	%
		Avg	STD	Avg	STD	Avg	STD		
DarkBlue	2	26	---	16	---	39	---	19	100
Yellow	4	29	---	6.9	---	31	---	33.1	100
Red	6	27	---	5.5	---	38	---	29.5	100
Brown	6	47	13	4.6	3.9	30	10	18.4	100
Purple	8	43	12	7.9	2.7	29	9.7	20.1	100
Olive	3	31	---	12	---	41	---	16	100
Orange	12	50	4.1	8.1	2.5	24	4	17.9	100
Grey	6	36	12	1.8	2.5	43	11	19.2	100

Table 1.7 Summary of Barnett RockEval Properties

Rock Class	Tmax	Calc. Ro
Orange	472	1.33
Brown	473	1.35
Olive	469	1.28
Red	254	0.98

Table 1.8 Summary of Barnett Surface Hardness and Strength Measurements

Rock Class	No of Samples	BHN kgf/mm^2		UCS ksi	
		Avg	STD	Avg	STD
Red	7	28	7.0	13.1	1.1
Brown	12	29	10.6	12.1	1.4
Olive	8	33	1.1	10.5	2.4
Orange	11	33	8.9	13.8	2.0

Table 1.9 Barnett Petrologic Summary

Rock Class	DarkBlue	Yellow	Red
Lithology	silty, Argillaceous mudstone	phosphatic to siliceous argillaceous	argillaceous to calcareous and Dolomitic mudstone
Detrital Grains	very common; Q > F; maximum grain, size coarse silt	minor to abundant; Q > F; maximum grain size ranges from coarse silt to very fine sand	fairly to very common; Q > F; maximum grain size ranges from medium silt to very fine sand
Dominant Matrix Composition	argillaceous	argilalcoeus & silcieous or phosphatic	argilalcoeus & silcieous or calcaroeus
Clay Minerals	IL > I/S	IL ≈ I/S	IL > I/S
Biotic Grains	calcareous shell fragments abundant; conodonts fairly common	calcareous shell fragments uncommon to common; conodonts rare to uncommon; radiolaria rare; sponge spicules locally abundant	calcareous shell fragments common to abundant; conodonts rare to common
Organic Components	stringers, blebs, & disseminated in matrix	stringers, blebs, & disseminated in matrix	algal macerals common; stringers, blebs, & disseminated in matrix
Accessory Grains	mica & glauconite	mica > glauconite	mica > glauconite
Authigenic Minerals	calcite abundant in recrystallized shell fragments & common in matrix; pyrite common; ferroan dolomite rare	calcite common in recrystallized shell fragments & common to fairly common in matrix; pyrite common; ferroan dolomite rare; silica replacing macerals and locally shell fragmetns; fluorapatite local	pyrite common to abundant; calcite locally common in recrystallized shell fragments & matrix; ferroan dolomite locally common replacing fossils and in matrix; silica minor replacing macerals and some shell fragmetns
Pore Types	micropores intercrystalline within the matrix	micropores intercrystalline within the matrix	micropores intercrystalline within the matrix
Petrographic Comments	matrix very opaque; laminations defined by large shell fragments and calcite-cemented layers; clay- and silt-filled burrows common; phosphatic pellets common; pyrite as few large concretions	matrix moderately to highly opaque; phosphatic pellets common to abundant; pyrite local; intraparticle porosity in sponge spicules and phosphatic pallets locally filled with cements including phoshate and calcite, respectively; stress-release cracks locally abundant	matrix locally highly opaque; phosphatic pellets rare to common; pyrite locally replacing macerals and shells alongside silica and ferroan dolomite

Barnett Petrologic Summary (Continued …)

Rock Class	Brown	Purple	Olive
Lithology	siliceous/argilalceous mudstone	siliceous mudstone commonly with mixed argilaceous and locally phosphatic	siliceous/argill mudstone
Detrital Grains	minor to common; Q > F; maximum grain size ranges from medium silt to fine sand	minor to very common; Q > F; maximum grain size ranges from medium silt to fine sand	Q > F minor to fairly common
Dominant Matrix Composition	argilalcoeus & silcieous	argilalcoeus & silcieous	silcieous/ argillaceous
Clay Minerals	IL > I/S	IL > I/S	ILL > I/S
Biotic Grains	sponge spicules ucommon to abundant; calcareous shell fragments rare to common; conodonts rare to uncommon	sponge spicules rare to common; calcareous shell fragments rare to fairly abundant; radiolaria rare to very common; conodonts rare	shell fragments fairly abundant; rare spicules, radiolarians, & forams; possible calcispheres
Organic components	algal macerals common; stringers, blebs, & disseminated in matrix	algal macerals locally common; stringers, blebs, & disseminated in matrix	stringers, blebs, & disseminated in matrix
Accessory Grains	mica > glauconite	mica > glauconite	phosphate grains/pellets
Authigenic Minerals	silica commonly in matrix and replacing organic particles; pyrite common; calcite and ferroan calcite locally abundant in recrystallized shell fragments & matrix; ferroan dolomite rare to uncommon; fluorapatite local	silica in matrix, recrystalized microfossils, and replacing macerals; pyrite common; calcite common to abundant in recrystallized shell fragments & matrix; ferroan dolomite uncommon; fluorapatite local	Cal, Fe-cal, & Py common in matrix & recryst. fossils; Fe-dol & fluorapatite nodules uncommon; chert replacing macerals
Pore Types	micropores intercrystalline within the matrix	micropores intercrystalline within the matrix	micro intercrystalline within the matrix
Petrographic Comments	matrix commonly opaque; laminations locally defined by calcite-cemented layers; phosphatic pellets common to fairly abundant; pyrite locally replacing macerals alongside silica and ferroan dolomite; some burrows filled with silt and some kerogen	pyrite locally replacing macerals and radiolaria alongside silica, ferroan dolomite, and ferroan calcite; patches of calcite cement; amorphous phosphate locally encrusts calcareous and siliceous fossils as well as older phosphatic pellets, which are fairly common to abundant	spherical calcite grains may be shell frags, recryst. spicules, or calcispheres; authigenic f-spar occurs in microcrystalline patches of cal cement; tends to have anomalous concentration of phosphatic particles

Barnett Petrologic Summary (Continued …)

Rock Class	Orange	Gray
Lithology	siliceous mudstones including phosphatic or calcareous varieties	argillaceous to mixed siliceous/argilalceous mudstones
Detrital Grains	niderate to abundant; Q & F; maximum grain size, medium silt	fairly common to common; Q > F; maximum grain size, coarse silt
Dominant Matrix Composition	silcieous & phosphatic or calcareous	argilalcoeus & silcieous
Clay Minerals	IL & I/S	IL > I/S
Biotic Grains	sponge spicules; radiolaria; ostracode; foraminifera; bivalve, thin-shelled	conodonts uncommon to fairly common; sponge spicules uncommon and local
Organic components	stringers, blebs, & disseminated in matrix	algal macerals uncommon to abundant; stringers, blebs, & disseminated in matrix
Accessory Grains	mica	mica > glauconite
Authigenic Minerals	phoshatic nodules sparse to very common; silica in matrix & recrystalized microfossils; pyrite; calcite local as recrystallized fossils & in matrix; dolomite & ferroan dolomite	pyrite common; silica replacing macerals and locally in the matrix; ferroan dolomite minor to common
Pore Types	micropores intercrystalline within the matrix	micropores intercrystalline within the matrix
Petrographic Comments	faintly laminated; rare bioturbation including burrows	opaque matrix; common organic-poor lenses representing possible burrows; pyrite and ferroan dolomite local as nodules; common phosphatic pellets

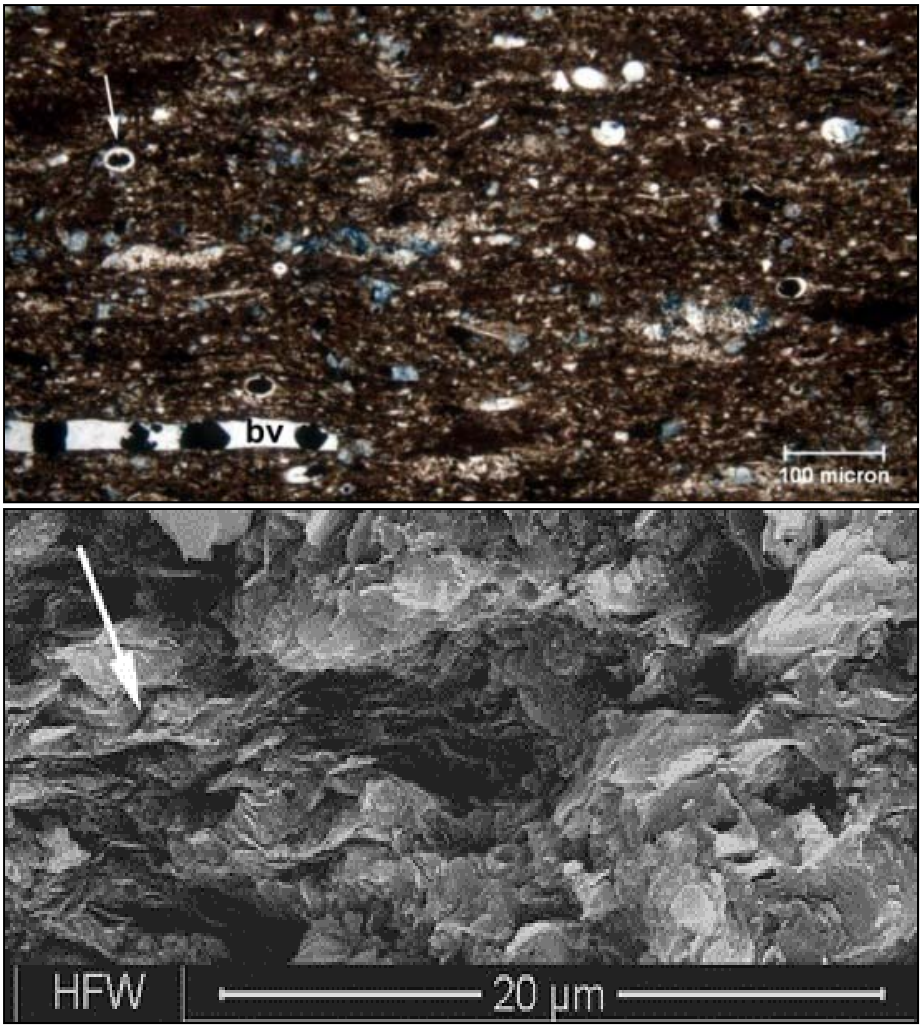

Figure 1.5 Representative thin section (top) and SEM (bottom) of the best reservoir quality rock class of the Barnett shale. The image shows show detrital clay minerals that originally composed the matrix in best reservoir intervals of the Barnett intimately admixed with diagenetic silica, and extensively coated with highly degraded kerogen. SEM shows a heterogeneous microfabric in the matrix where favorable gas-filled porosity and matrix permeability occurs.

Table 1.10 Abbreviations for Barnett Images and Tables

Argill = argillaceous	cal = calcite	Calc = calcareous
dissem = disseminated	dol = dolomite	F = feldspar
Fe-cal = ferroan calcite	Fe-dol = ferroan dolomite	fos = fossil tests
frag or frags = fragment(s)	interg = intergranular	intxln = intercrystalline
IL = illite	I/S = mixed-layer illite-smectite	lam or lams = laminations
m-mica = micromica	mpor = micropore(s)	phos = phosphate
por = pore(s)	py = pyrite	Q = quartz
silic = siliceous	XRD = X-ray diffraction	

1.3 Haynesville Shale Properties

The Haynesville Shale (also known as the Haynesville/Bossier shale) is a Late Jurassic Kimmeridgian shale accumulation underlying an area of approximately 9,000 square miles extending to parts of southwestern Arkansas, northwest Louisiana, and east Texas. It lies at depths of 10,500 to 13,000 feet and is overlain by sandstone of the Cotton Valley Group and underlain by limestone of the Smackover Formation. This Haynesville shale represents a transgressive flooding event in a restricted shelfal basin following the deposition of the Smackover formation. Laterally this shale grades into Haynesville, or Cotton Valley limestone build-ups along the margins of the basin. Thicknesses approaching 300 feet are common in the northern area and 130 to 150 feet is common in the south. Above the Haynesville, the Bossier shale is present with less organic facies preserved and represents shallower more oxygenated shelfal conditions (Wikipedia, 2012).

Two cored wells representative of the Haynesville and Bossier sections of this play were selected for this study. Haynesville Well 1 represents an extended vertical section that includes the Late Jurassic Age Bossier Shale, and the Haynesville Shale. Thin horizons of dolostones and dolomitic mudstones are interbedded throughout the upper cores representing the Bossier Shale. Samples here primarily represent argillaceous mudstones and silty, argillaceous mudstones. A large influx of terrigenous silt and calcareous fecal pellets are observed in the samples from the lower core, representing predominantly the Haynesville Shale. Silty argillaceous mudstones and silty, calcareous mudstones are the dominant lithotypes. The base of this core is represented by a silty, dolomitic mudstone and one a wackestone variation of limestone at the base of the Haynesville shale and representative of the Smackover formation. The best potential reservoir quality with favorable gas-filled porosity and permeability exists in silty, argillaceous and silty, calcareous mudstones of the Haynesville Shale, as well as select argillaceous mudstones and silty, argillaceous mudstones of the middle Bossier Shale. Calcite is in the form of recrystallized biotic grains and fecal pellets composed of degraded organic material and coccolith plates is observed in the Haynesville shale section. Organic material is also observed as particles similar to the overlying Bossier Shale and as amorphous kerogen thickly coating the matrix. Clay minerals throughout the well consist primarily of illite and expandable mixed-layer illitesmectite. The clay presents a marginal risk of reservoir sensitivity to freshwater completion fluids.

Haynesville Well 2 also represent the Bossier and Haynesville shale sections. However, samples for laboratory testing represented primarily the argillaceous mudstones and intercalated dolomitic mudstones of the Bossier section. Textural development here varied from non-laminated to well-defined laminae consisting of silt, biotic grains, authigenic minerals, and/or admixed layers of organic material and pyrite. Organic material occurs as both smooth and degraded particles and as disseminated kerogen in the matrix. Detrital clay minerals that predominantly compose the matrix are illite and mixed-layer illitesmectite. Authigenic chlorite flakes are commonly associated with other authigenic minerals such as albite and calcite. According to X-ray diffraction analyses based on the amounts of expandable smectite interlayers within mixed-layer illite-smectite clays,

sensitivity to fresh-water is moderate in the Bossier Formation and low in the Haynesville Formation. In addition, moderately high amounts of iron bearing chlorite in the Bossier and common pyrite throughout the sampled interval may result in moderate sensitivity to acid-based completion fluids. Rock property characterization for selected units present in these cores is described below.

Figure 1.6 shows the HRA classification of the two wells with core studied in Haynesville play. They show a distribution of 9 rock classes defined within the cored section of these wells. Well 1 is presented in two sections, upper and lower, which correspond to the sections represented by the core. Well 2 is represented by a continuous core section representative of most of the rock classes, not all, that were identified along the length of the well. To the right side of the well log classification, are box and whiskers plots showing the distribution of gas filled porosity (GFP), total organic carbon (TOC) and pressure decay permeability (perm), for each of the rock classes (indicated by numbers). The relationship between the rock class color and the number sequence is also provided. This information is used to define the reservoir quality index for each rock class. The Dark Blue, Light Blue and Brown classes are classes with good to best reservoir quality. Red and Purple are non-reservoir classes. Table 1.11 shows the corresponding testing matrix for these units and their relative reservoir quality index (RQI).

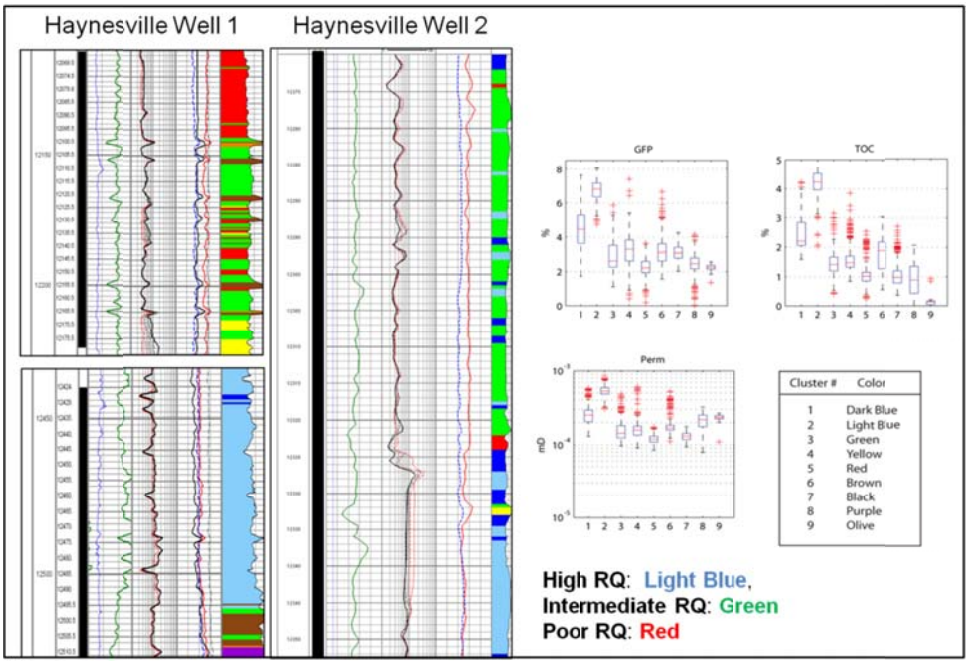

Figure 1.6 HRA classification of two wells in the Haynesville play indicating the presence and distribution of 9 rock classes within the cored section of these wells.

Table 1.11 Haynesville rock classes and corresponding reservoir quality index

Haynesville Rock Classes	RQI	Petrophysical	Petrologic	Geochemical	Geomechanical Static	Geomechanical Dynamic	XRD
Dark Blue	Good	✓	✓	✓	✓	✓	✓
Light Blue	Best	✓	✓	✓	✓	✓	✓
Yellow	Fair	✓	✓	✓			✓
Red	Poor	✓	✓	✓	✓		✓
Brown	Good	✓	✓		✓	✓	✓
Purple	Poor	✓	✓		✓	✓	✓
Green	Fair	✓	✓	✓	✓	✓	✓

Figure 1.7 and Figure 1.8 show a petrologic overview of the selected rock classes representative of the Haynesville shale. The Dark Blue, Light Blue and Brown rock classes are good reservoir quality units. The Green, Red and Yellow classes are non-reservoir units. Mineral composition, lithologic denomination, thin section micrographs and SEM photographs are included for each rock class. These provide a good description of the dominant matrix minerals, the bulk mineral distribution, the fossil and detrital distribution and the micro texture of each rock class.

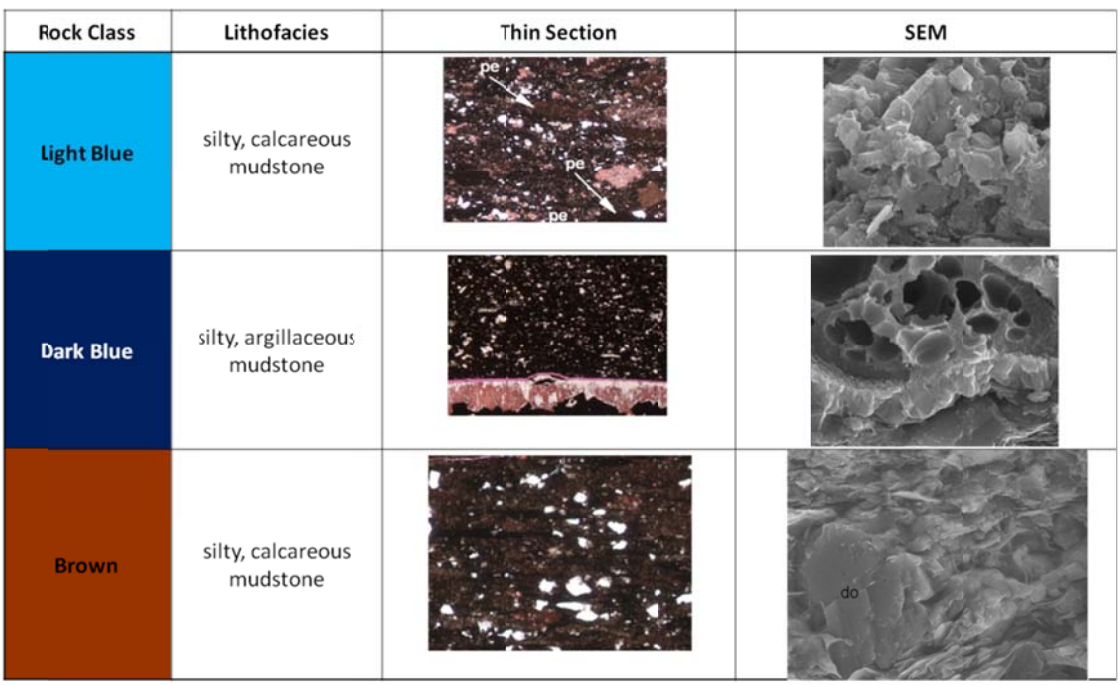

Figure 1.7 Petrologic overview of three reservoir rock classes in the Haynesville shale.

Rock Class	Lithofacies	Thin Section	SEM
Green	dolomite, argillaceous mudstone	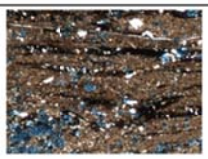	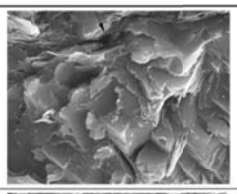
Red	Dolomitic mudstone	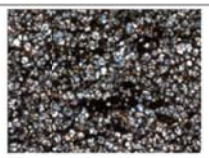	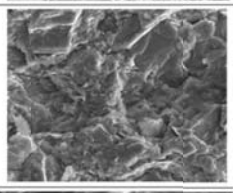
Yellow	silty, argillaceous mudstone	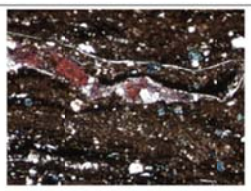	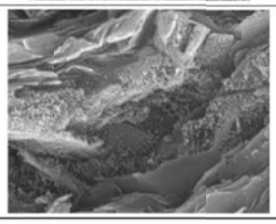

Figure 1.8 Petrologic overview of additional three poor reservoir to non-reservoir rock classes in the Haynesville shale.

Table 1.12 Summary of Haynesville Petrophysical Tables

Rock class	No of Samples	Bulk Density		Grain Density		Dry Gas Density		Effective Porosity		Water Saturation		Gas Saturation	
		(g/cc)		(g/cc)		(g/cc)		(% BV)		(% PV)		(% PV)	
		Avg	STD	Avg	STD	Avg	STD	Avg	STD	Avg	STD	Avg	SRD
DarkBlue	3	2.489	0.080	2.637	0.041	2.661	0.030	6.830	2.360	8.77	5.68	82.80	4.90
Light Blue	22	2.469	0.039	2.648	0.033	2.669	0.030	7.820	0.880	4.89	2.84	86.70	7.60
Yellow	1	2.568	---	2.665	---	2.673	---	4.060	---	7.93	---	90.00	---
Red	6	2.651	0.020	2.703	0.015	2.718	0.017	2.770	0.398	26.90	8.00	69.80	8.10
Brown	8	2.601	0.061	2.718	0.041	2.715	0.043	4.500	0.980	4.94	0.98	92.00	5.20
Purple	5	2.713	0.070	2.789	0.092	2.795	0.097	3.001	1.250	1.420	1.340	91.90	5.10
Green	29	2.618	0.030	2.692	0.018	2.706	0.021	3.550	0.870	18.490	11.080	78.60	11.10

Summary of Haynesville Petrophysical Tables (Continued …)

Rock class	No of Samples	Mobile Oil Saturation		Gas Filled Porosity		Bound Hydrocarbon Saturation		Clay Bound Water		Pressure Decay Permeability	
		(% PV)		(% BV)		(% BV)		(% BV)		(nD)	
		Avg	STD	Avg	STD	Avg	STD	Avg	STD	Avg	STD
DarkBlue	3	8.410	7.000	5.630	1.860	0.321	0.131	7.39	2.25	397	212
Light Blue	22	8.380	5.380	6.760	0.800	0.456	0.156	4.92	0.91	509	108
Yellow	1	2.100	---	3.650	---	0.151	---	8.23	---	235	---
Red	6	3.300	1.600	1.930	0.370	0.160	0.073	10.60	0.70	105	20
Brown	8	3.020	2.020	4.180	1.100	0.304	0.144	5.01	1.27	294	104
Purple	5	6.650	3.800	2.730	1.050	0.152	0.052	2.960	0.960	143	24
Green	29	2.940	1.610	2.780	0.820	0.134	0.085	9.600	1.340	150	69

Table 1.13 Summary of Haynesville Geochemical Properties

Rock class	No of Samples	Total Organic Content	
		(% Wt)	
		Avg	STD
DarkBlue	7	1.830	0.610
LightBlue	4	2.150	0.120
Yellow	1	1.860	---
Red	1	1.580	---
Green	10	1.700	0.550

Table 1.14 Summary of Haynesville Geomechanical Properties – Static

Rock class	No of Samples	Bulk Density		Effective Confining Stress		Peak Strength (V)		Peak Strength (H)	
		(g/cc)		(psi)		(psi)		(psi)	
		Avg	STD	Avg	STD	Avg	STD	Avg	SRD
Dark Blue	2	2.47	0.01	2364	1	---	---	---	---
Light Blue	10	2.49	0.04	2370	4	18047	2016	18853	2596
Red	1	2.67	---	2310	---	19223	---	23012	---
Brown	6	2.27	0.99	2340	37	28083	7699	30654	9497
Purple	3	2.81	0.01	2300	2	---	---	---	---
Green	7	2.61	0.02	2300	4	20118	1155	20620	1039

Summary of Haynesville Geomechanical Properties – Static Continued (continued …)

Rock class	No of Samples	Young's Mod (V)		Young's Mod (H)		Poisson's Ratio (V)		Poisson's Ratio (H)	
		(psi x E6)		(psi x E6)					
		Avg	STD	Avg	STD	Avg	STD	Avg	SRD
Dark Blue	2	2.14	0.198	5.01	0.036	0.14	0.006	0.235	0.008
Light Blue	10	2.57	0.612	4.27	0.911	0.176	0.035	0.217	0.071
Red	1	5.94		5.93		0.120	---	0.166	---
Brown	6	4.76	1.83	6.64	2.23	0.208	0.030	0.258	0.065
Purple	3	5.48	0.263	6.04	0.177	0.232	0.005	0.291	0.027
Green	7	2.39	0.199	4.96	0.558	0.184	0.034	0.223	0.056

Table 1.15 Summary of Haynesville Geomechanical Properties - Dynamic

Rock class	No of Samples	Bulk Density		Mean Stress		P-Wave Vel (H)		P-Wave Vel (V)		S-Wave Vel (V)		S-Wave Vel (H)	
		(g/cc)		(psi)		(ft/s)		(ft/s)		(ft/s)		(ft/s)	
		Avg	STD	Avg	STD	Avg	STD	Avg	STD	Avg	STD	Avg	SRD
DarkBlue	1	2.48	---	3250	----	12147	---	15136	---	7491	---	9161	---
LightBlue	4	2.50	0.040	3283	200	12016	1028	15428	949	7510	538	9475	309
Brown	2	2.70	0.018	3406	414	14733	1786	16701	995	9268	1464	9964	198
Purple	1	2.82	---	3503	---	17246	---	18836	---	10355	---	10340	---
Green	3	2.63	0.02	3322	344	12222	103	17101	462	7390	92	10698	197

Summary of Haynesville Geomechanical Properties – Dynamic (continued …)

Rock class	No of Samples	Bulk Density		Young's Mod (V)		Young's Mod (H)		Poisson's Ratio (V)		Poisson's Ratio (H)	
		(g/cc)		(psi x E6)		(psi x E6)					
		Avg	STD	Avg	STD	Avg	STD	Avg	STD	Avg	STD
DarkBlue	1	2.48	---	4.48	---	6.80		0.193	---	0.211	---
LightBlue	4	2.50	0.040	4.51	0.799	7.29	0.76	0.178	0.018	0.195	0.028
Brown	2	2.70	0.018	7.47	2.57	8.86	1.20	0.174	0.04	0.222	0.034
Purple	1	2.82	---	9.93		10.4		0.218	---	0.284	---
Green	3	2.63	0.02	4.68	0.06	9.55	4.36	0.211	0.015	0.178	0.023

Table 1.16 Summary of Haynesville XRD Mineralogy

Rock class	No of Samples	QUARTZ		CALCITE		TOTAL CLAY		OTHER	TOTAL
		Avg	STD	Avg	STD	Avg	STD		
Dark Blue	3	25.13	3.43	14.43	7.85	44.27	10.02	16.17	100.00
light Blue	15	25.42	4.02	23.44	12.96	33.45	7.80	17.69	100.00
Yellow	1	27.00	---	9.00	---	47.00	---	17.00	100.00
Red	4	20.98	0.6	4.85	1.33	59.70	2.74	14.47	100.00
Brown	4	22.55	3.47	27.05	10.96	33.20	3.81	17.20	100.00
Purple	3	16.73	7.38	32.13	31.39	22.93	8.08	28.21	100.00
Green	9	22.46	2.57	7.01	4.50	51.79	7.15	18.74	100.00

Table 1.17 Summary of Haynesville RockEval Properties

Rock Class	Tmax	Calc. Ro
Light Blue	529	2.37
Green	531.5	2.41
Red	514	2.09

Table 1.18 Summary of Haynesville Surface Hardness and Strength Properties

Rock Class	No of Samples	BHN kgf/mm^2		UCS ksi	
		Avg	STD	Avg	STD
Light Blue	6	17	1.5	9.5	1.3
Red	8	27	2.3	11.8	1.7
Green	7	25	3.8	9.8	1.0

Table 1.19 Haynesville Petrologic Summary

Rock Class	Dark Blue	Light Blue	Yellow
Lithology	silty, argillaceous mudstone	silty, argillaceous mudstone	silty, argillaceous mudstone
Detrital Grains	abundant Q & F silt	abundant Q & F silt	abundant Q & F silt
Dominant Matrix Composition	argillaceous, calcareous	argillaceous > calcareous	argillaceous
Clay Minerals	abundant IL + I/S, rare KA	abundant IL + I/S	abundant IL + I/S, rare KA
Biotic Grains	sparse indistinct siliceous forms, thin-shelled bivalve & ammonite frags, calc cysts common, coccoliths	indistinct siliceous forms, sparse foraminifera & cysts, thin-shelled bivalve and ammonite frags, indistinct calc hash, coccoliths	modest indistinct siliceous forms, abundant thin-shelled bivalve and ammonite frags, sparse brachiopod frags
Organic Components	very abundant carb particles (some partially silicified), stringers, lenses, dissem amorphous kerogen	abundant carb particles (some partially silicified), stringers, lenses, dissem amorphous kerogen	very abundant carb particles (most partially silicified), lenses, stringers, dissem amorphous kerogen
Accessory Grains	abundant mica, sparse CHL	abundant mica & peloids, fecal pellets, rare CHL	abundant mica & CHL
Authigenic Minerals	abundant cal (fos + matrix, pellets and peloids), silica (fos + matrix), py, dol	moderate cal (fos + matrix micrite), silica (fos + matrix), py, dol, Fe-dol, rare sph	abundant silica (forms + matrix), cal (fos), py, dol, Fe-dol, F (organic particles + frags)
Pore Types	intxln matrix mpor, sparse interg por within silt-filled burrows	intxln matrix mpor, sparse interg por within silt-filled burrows	intxln matrix mpor, interg por among silty lamina and silt-filled burrows
Petrographic Comments	very well lam defined by partially silicified organic particles, lenses, and stringers, silt is more common and closely associated with organic matter	subtly lam, abundant amount of micritized fecal pellets, thin calcite-filled fractures, very silty with abundant burrows	very well lam as defined partially silicified organic particles and stringers, increased silt content, F frequently replaces organic particles and biotic frags

Haynesville Petrologic Summary (continued …)

Rock Class	Red	Brown	Purple
Lithology	argillaceous mudstone	silty, dolomitic mudstone	dolostone
Detrital Grains	sparce Q & F silt	abundant Q & F silt	rare Q & F silt
Dominant Matrix Composition	argillaceous	calcareous > argillaceous	dolomitic
Clay Minerals	IL + I/S, sparce KA	abundant IL, sparce I/S	sparse IL + I/S, rare KA
Biotic Grains	sparse indistinct siliceous forms, sparse thin-shelled bivalve and ammonite frags	sparce thin shelled bivalve and ammonite frags, abundant, coccoliths, sparce siliceous forms	rare indistinct siliceous forms and thin-shelled bivalve frags
Organic Components	moderate carb particles (some partially silicified), stringers, lenses, & dissem amorphous kerogen	moderate carb particles (some partially silicified), stringers, dissem amorphous kerogen	moderate carb particles (some partially silicified), stringers , rare lenses, dissem amorphous kerogen
Accessory Grains	abundant mica & CHL	abundant mica, peloids & pellets, rare CHL	sparse mica, rare CHL
Authigenic Minerals	silica (matrix + forms), cal (fos + matrix), py, dol, Fe-dol, rare sph	very abundant cal (fos + matrix micrite, sparry), silica (fos + matrix), py, dol	pervasive dol & Fe-dol, sparse silica (matrix + forms), py, cal (fos)
Pore Types	intxln matrix mpor, rare interg por within silt-filled burrows	intxln matrix mpor, interg por among most silt grains	intxln matrix mpor, sparse intxln por around sparry dol & Fe-dol
Petrographic Comments	very well lam, sparse burrows - bioturbated, modest visual organic matter, rare anastomosing fractures filled with cal & fe-cal	subtly lam defined by pervasive micritized pallets aligned parallel to bedding and organic stringers, sparce silt-filled borrows-bioturbated	very subtly lam as defined by layer-parallel organic stringers.

Haynesville Petrologic Summary (continued …)

Rock Class	Green
Lithology	argillaceous mudstone
Detrital Grains	moderate Q & F silt
Dominant Matrix Composition	argillaceous
Clay Minerals	abundant IL + I/S, rare KA
Biotic Grains	modest indistinct siliceous forms, thin-shelled bivalve and ammonite frags more common, silicified cysts
Organic components	abundant carb particles (some partially silicified), stringers, lenses, dissem amorphous kerogen
Accessory Grains	abundant mica & CHL
Authigenic Minerals	silica (forms + matrix), cal (fos), dol, Fe-dol, py, rare sph
Pore Types	intxln matrix mpor, interg por in silty lamina and silt-filled burrows
Petrographic Comments	very well lam defined by abundant organic particles and stringers, abundant silt-filled burrows (bioturbated) frequent layer-parallel fractures filled with silica

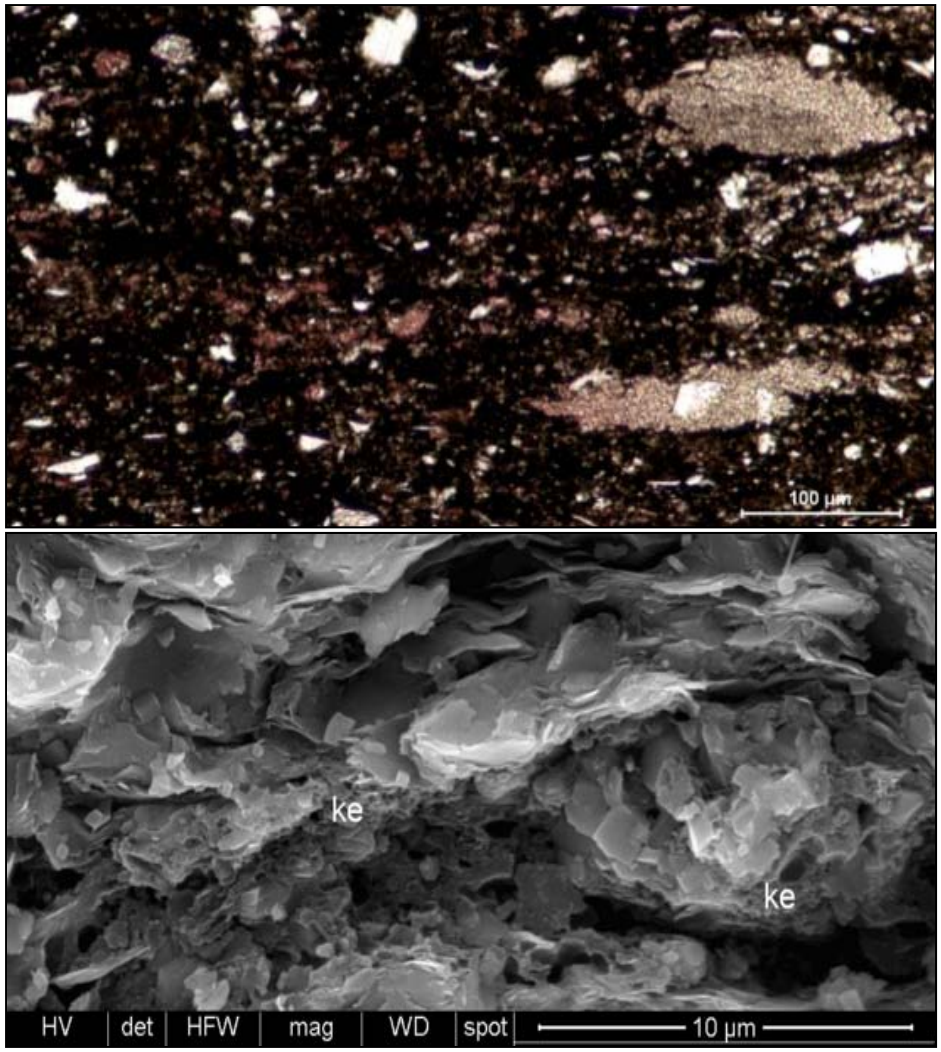

Figure 1.9 Representative thin section (top) and SEM (bottom) of the best reservoir quality rock class of the Haynesville shale include moderate amounts of detrital clay minerals, significantly high amounts of microcrystalline calcite, and widespread fine kerogen. SEM depicts microtextural features such as fecal pellets that are defined by increased amounts of calcite and highly degraded kerogen, hosting the best gas-filled porosity and matrix permeability.

Table 1.20 Abbreviations for Haynesville Images and Tables

cal = calcite	calc = calcareous	carb = carbonaceous
CHL = chlorite	dissem = disseminated	dol = dolomite
F = feldspar	Fe-cal = ferroan calcite	Fe-dol = ferroan dolomite
fos = fossils	frac = fracture(s)	frag or frags = fragment(s)
IL = illite	interg = intergranular	intrap = intraparticle
intxln = intercrystalline	I/S = mixed-layer illite-smectite	KA = kaolinite
lam = laminated	mpor = microporosity	por = porosity
py = pyrite	Q = quartz	sph = sphalerite

1.4 Marcellus Shale Properties

The Marcellus formation (also classified as the Marcellus Subgroup of the Hamilton Group, Marcellus Member of the Romney Formation, or simply the Marcellus Shale) is a unit of marine sedimentary rock found in eastern North America. Named for a distinctive outcrop near the village of Marcellus, New York in the United States, it extends throughout much of the Appalachian Basin. Stratigraphically, the Marcellus formation is the lowest unit of the Devonian age Hamilton Group, and is divided into several sub-units. Although black shale is the dominant lithology, it also contains lighter shales and interbedded limestone layers due to sea level variation during its deposition almost 400 million years ago. The organic-rich black shale was deposited in relatively deep water devoid of oxygen, and is only sparsely fossiliferous. Most fossils are contained in the limestone members, and the fossil record in these layers provides important paleontological insights on faunal turnovers (Wikipedia, 2012).

One cored well representative of the Pennsylvanian section of this play was selected for this study. The cored interval in Marcellus Well 1 consists of hard, fissile, pyritic black mudstones and shales of the Burkett and Marcellus Formations, overlying Carbonates of the Onondaga Limestone, and spiculitic chert of the Huntersville Formation. Organic-rich mudstones show excellent reservoir properties despite high clay contents. Clays include coarse grained illite, and micromicas; microporosity is observed as teepee-shaped voids in brittlely deformed clays. This relatively large grain size and brittle behavior preserves a system of micropores fostering good permeability and other reservoir properties. In addition, microcrystalline silica and authigenic feldspar cements prop open micropores, and preserve porosity and permeability. The best overall reservoir quality is exhibited in organic-rich mudstones with mixed siliceous/argillaceous matrices, present in both the upper and lower cored intervals. Rock property characterization for selected units present in this core is described below.

Figure 1.10 shows the HRA classification of one well in the Marcellus play showing the presence and distribution of 6 rock classes within the cored section. We noticed that the Marcellus Well 1 exhibits a significant amount of vertical heterogeneity with representation of all the rock classes. To the right side of the well log classification are box and whisker plots defining the distribution of gas filled porosity (GFP), total organic carbon (TOC) and pressure decay permeability (perm), for each of the rock class (indicated by numbers). The relationship between the rock class color and the number sequence is also provided. This information is used to define the reservoir quality index for each rock class. The Dark Blue, Light Blue classes are classes with good to best reservoir quality. The Red and Brown classes are non-reservoir classes. Table 1.21 shows the corresponding testing matrix for these units and their relative reservoir quality index (RQI).

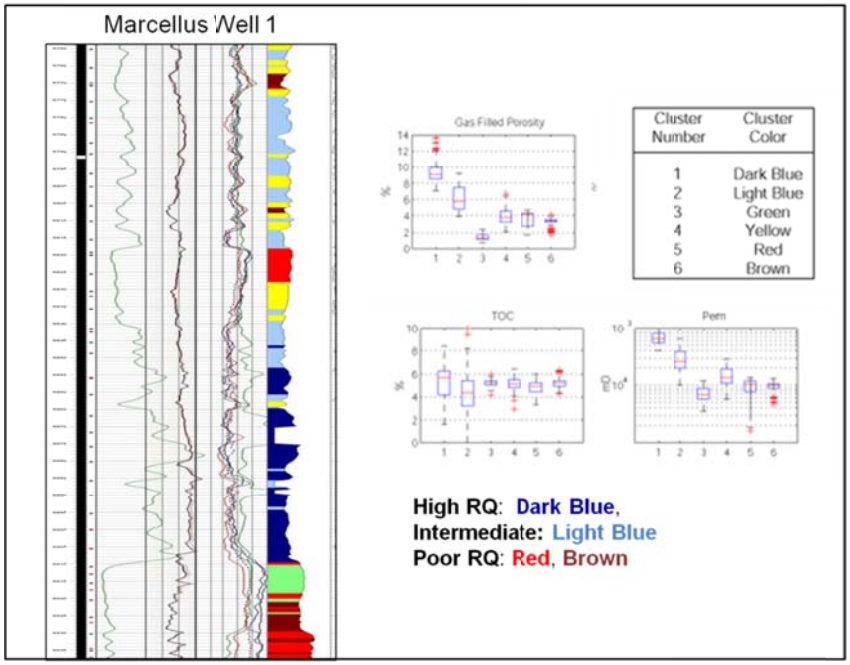

Figure 1.10 HRA classification of one well in the Marcellus play, indicating the presence and distribution of 6 rock classes within the cored section of this well.

Table 1.21 Marcellus Rock classes and corresponding reservoir quality index

Marcellus Rock Classes	RQI	Petrophysical	Petrologic	Geochemical	Geomechanical Static	Geomechanical Dynamic	XRD
Brown	Poor	✓	✓	✓	✓	✓	✓
Dark Blue	Best	✓	✓	✓	✓	✓	✓
Green	Worse	✓	✓	✓	✓	✓	✓
Light Blue	Good	✓	✓	✓	✓	✓	✓
Red	Poor	✓	✓	✓	✓	✓	✓
Yellow	Poor	✓	✓	✓	✓	✓	✓

Figure 1.11 show a petrologic overview of the selected rock classes representative of the Marcellus shale. The Light Blue and Dark Blue rock classes are reservoir units. The Brown rock class is a non-reservoir unit. Lithologic denomination, thin section micrographs and SEM photographs are included for selected rock classes. The information provides a good description of the dominant matrix minerals, the fossil and detrital distribution and the micro texture of each rock class.

Rock Class	Lithofacies	Thin Section	SEM
Light Blue	Siliceous/argillaceous mudstone	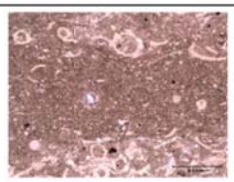	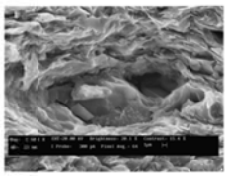
Dark Blue	silty, siliceous/argillaceous mudstone	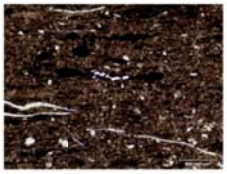	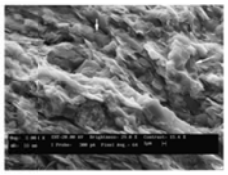
Brown	Wackestone	N/A	N/A

Figure 1.11 Petrologic overview of three rock classes in the Marcellus shale.

Table 1.22 Summary of Marcellus Petrophysical Properties

Rock class	No of Samples	Bulk Density		Grain Density		Dry Gas Density		Effective Porosity		Water Saturation		Gas Saturation	
		(g/cc)		(g/cc)		(g/cc)		(% BV)		(% PV)		(% PV)	
		Avg	STD	Avg	STD	Avg	STD	Avg	STD	Avg	STD	Avg	SRD
Brown	5	2.66	0.02	2.74	0.01	2.77	0.02	4.09	1.39	26.19	9.01	71.81	7.88
DarkBlue	12	2.43	0.06	2.64	0.06	2.67	0.07	9.56	1.45	13.17	2.89	86.07	2.79
Green	5	2.64	0.06	2.71	0.04	2.71	0.04	2.54	0.62	3.64	5.03	93.97	4.70
LightBlue	17	2.50	0.07	2.66	0.05	2.69	0.06	7.41	1.51	17.78	5.61	80.93	5.92
Red	5	2.63	0.06	2.71	0.05	2.73	0.07	4.07	1.73	17.46	18.03	81.16	18.33
Yellow	18	2.60	0.06	2.71	0.05	2.74	0.04	5.72	1.64	28.09	7.09	69.91	7.61

Summary of Marcellus Petrophysical Properties (continued …)

Rock class	No of Samples	Mobile Oil Saturation		Gas Filled Porosity		Bound Hydrocarbon Saturation		Clay Bound Water		Pressure Decay Permeability	
		(% PV)		(% BV)		(% BV)		(% BV)		(nD)	
		Avg	STD	Avg	STD	Avg	STD	Avg	STD	Avg	STD
Brown	5	2.00	1.23	2.90	0.99	0.31	0.15	5.96	2.99	94.00	32.99
DarkBlue	12	0.76	0.24	8.22	1.24	0.35	0.07	5.19	0.87	424.00	61.21
Green	5	2.39	1.24	2.39	0.58	0.06	0.03	1.00	0.45	75.00	63.69
LightBlue	17	1.29	0.70	5.99	1.23	0.29	0.12	5.85	1.02	272.00	87.07
Red	5	1.38	0.99	3.13	1.28	0.10	0.09	2.37	1.60	84.00	57.67
Yellow	18	2.01	1.23	4.04	1.33	0.30	0.11	5.84	1.65	165.00	69.41

Table 1.23 Summary of Marcellus Geochemical Properties

Rock class	No of Samples	Total Organic Content	
		(% Wt)	
		Avg	STD
Brown	5	0.602	0.385
DarkBlue	12	7.342	1.734
Green	5	0.928	1.566
LightBlue	17	3.779	1.722
Red	5	0.727	0.541
Yellow	18	1.758	1.374

Summary of Marcellus Geomechanical Properties – Static (continued …)

Rock class	No of Samples	Bulk Density		Poisson's Ratio (V)		Poisson's Ratio (H)	
		(g/cc)					
		Avg	STD	Avg	STD	Avg	SRD
Brown	5	2.68	0.02	0.224	0.019	0.295	0.02
DarkBlue	3	2.50	0.06	0.237	0.059	0.334	0.024
Green	2	2.68	0.01	0.284	0.036	0.356	0.063
LightBlue	4	2.54	0.06	0.179	0.057	0.276	0.096
Red	1	2.61	---	0.272	---	0.228	---
Yellow	3	2.62	0.03	0.217	0.026	0.296	0.046

Table 1.24 Summary of Marcellus Geomechanical Properties – Dynamic

Rock Class	No. of Samples	Bulk Density (g/cc)		Mean Stress (psi)		P-Wave Vel (V) (ft/s)		P-Wave Vel (45) (ft/s)		S-Wave Vel (V) (ft/s)		S-Wave Vel (45) (ft/s)	
		Avg	STD	Avg	STD	Avg	STD	Avg	STD	Avg	STD	Avg	STD
Brown	5	2.68	0.02	4583	643	14906	1504	16135	1555	8315	768	8998	624
Dark Blue	3	2.5	0.06	4222	403	13318	4020	12873	810	7790	1479	7954	306
Green	2	2.68	0.01	5898	640	18424	828	19423	43	9685	239	10141	70
Light Blue	4	2.54	0.06	4060	280	12610	1204	13273	870	7433	461	8125	477
Red	1	2.61	---	9657	---	18233	---	16990	0	10775	---	10302	---
Yellow	3	2.62	0.03	3964	53	12475	423	14825	258	7366	389	8804	46

Summary of Marcellus Geomechanical Properties – Dynamic (continued …)

Rock Class	No. of Samples	Bulk Density (g/cc)		Young's Mod (V) (psi x E6)		Young's Mod (45) (psi x E6)		Poisson's Ratio (V)		Poisson's Ratio (45)	
		Avg	STD	Avg	STD	Avg	STD	Avg	STD	Avg	STD
Brown	5	2.68	0.02	6.48	1.21	7.52	1.18	0.274	0.015	0.272	0.021
Dark Blue	3	2.5	0.06	5.43	2.57	5.08	0.52	0.223	0.040	0.187	0.025
Green	2	2.68	0.01	8.90	0.50	9.78	0.12	0.310	0.000	0.315	0.005
Light Blue	4	2.54	0.06	4.77	0.83	5.42	0.71	0.228	0.050	0.203	0.008
Red	1	2.61	---	10.39	---	8.79	---	0.230	0.000	0.210	0.000
Yellow	3	2.62	0.03	4.73	0.41	6.81	0.21	0.230	0.022	0.223	0.012

Table 1.25 Summary of Marcellus XRD Mineralogy

Rock class	No of Samples	QUARTZ		CALCITE		TOTAL CLAY		OTHER	TOTAL
		Avg	STD	Avg	STD	Avg	STD		
Brown	2	19.50	13.44	41.50	43.13	27.00	25.46	12.00	100.00
DarkBlue	4	28.25	8.06	8.50	12.34	39.50	10.97	23.75	100.00
Green	2	9.50	2.12	85.00	0.00	2.50	2.12	3.00	100.00
LightBlue	5	34.40	5.27	3.00	2.45	44.80	5.36	17.80	100.00
Red	3	35.33	37.31	35.00	45.92	15.00	17.32	14.67	100.00
Yellow	7	29.71	5.25	9.50	10.52	46.71	5.50	14.07	100.00

Table 1.26 Summary of Marcellus RockEval Properties

Rock Class	Tmax	Calc. Ro
Dark Blue	475	1.39
Light Blue	479	1.46

Table 1.27 Summary of Marcellus RockEval Properties

Rock Class	No of Samples	BHN kgf/mm^2		UCS ksi	
		Avg	STD	Avg	STD
Dark Blue	6	21	9.8	10.6	1.8
Light Blue	7	35	9.4	10.4	1.2

Table 1.28 Marcellus Petrologic Summary

Rock Class	Brown	Dark Blue	Green
Lithology	silty argillaceous mudstone	calcareous silic/argill mudstone	calcareous mudstone
Detrital Grains	feldspar	quartz	quartz
Dominant Matrix Composition	argillaceous	silica/argillaceous	silica/argillaceous
Clay Minerals	illite, I/S, CHL	illite, I/S	trace illite
Biotic Grains	silica-replaced microfossils, styliolinids, ostracodes	silica-replaced microfossils; conodonts	echinoderms, bryozoans
Organic Components	disseminated carbonaceous material + streaks, flecks, blebs	disseminated carbonaceous material, oil stain + streaks, flecks, blebs	oil stains
Accessory Grains	abundant micromicas, chlorite	few to abundant micromicas	none
Authigenic Minerals	silica, py, trace Fe-dol	silica, Fe-dol, pyrite	cal, fe-cal, silica, pyrite
Pore Types	matrix intercrystalline, induced	matrix intercrystalline visible under UV	matrix intercrystalline
Petrographic Comments	alternate, fine, muddy & silty laminae; truncated laminae, slightly bioturbated	dark matrix, abundant micromicas, disseminated carbon and particles	tightly crystalline; argillaceous matrix; well-preserved ostracodes

Marcellus Petrologic Summary (continued …)

Rock Class	Light Blue	Red	Yellow
Lithology	silty/argillaceous mudstone	calcareous or glauconitic mudstone	silty/argillaceous mudstone
Detrital Grains	quartz	quartz	quartz
Dominant Matrix Composition	silic/argillaceous	argillaceous or Siliceous	argillaceous
Clay Minerals	illite, I/S, CHL	illite, I/S, minor CHL	illite, I/S, CHL
Biotic Grains	silt-replaced microfossils; conodonts some with adherent micas	silica-replaced microfossils	calcareous hash, styliolinids, silica-replaced microfossils,
Organic Components	carbonaceous flecks, some py-replaced	carbonaceous streaks, flecks, some py-replaced	carbonaceous streaks, flecks; concentration varies in laminae
Accessory Grains	abundant micromicas, siliceous/illitic pods	abundant glauconite; phosphatic pellets; micromicas	abundant micromicas, illitic pods
Authigenic Minerals	silica, Fe-dol, Fe-cal, py	calcite, Fe-cal, minor silica, py	cal, Fe-cal, Fe-dol, py, minor silica
Pore Types	matrix intercrystalline visible under UV; induced	matrix intercrystalline	matrix intercrystalline; induced
Petrographic Comments	weakly laminated; abundant micromicas; mixed siliceous/argill matrix	bioturbated; pervasive glauconite pellets; pyrite-replaced carbonaceous material	laminated; organic streaks & laminae; illite pods, siderite-replaced microfossils

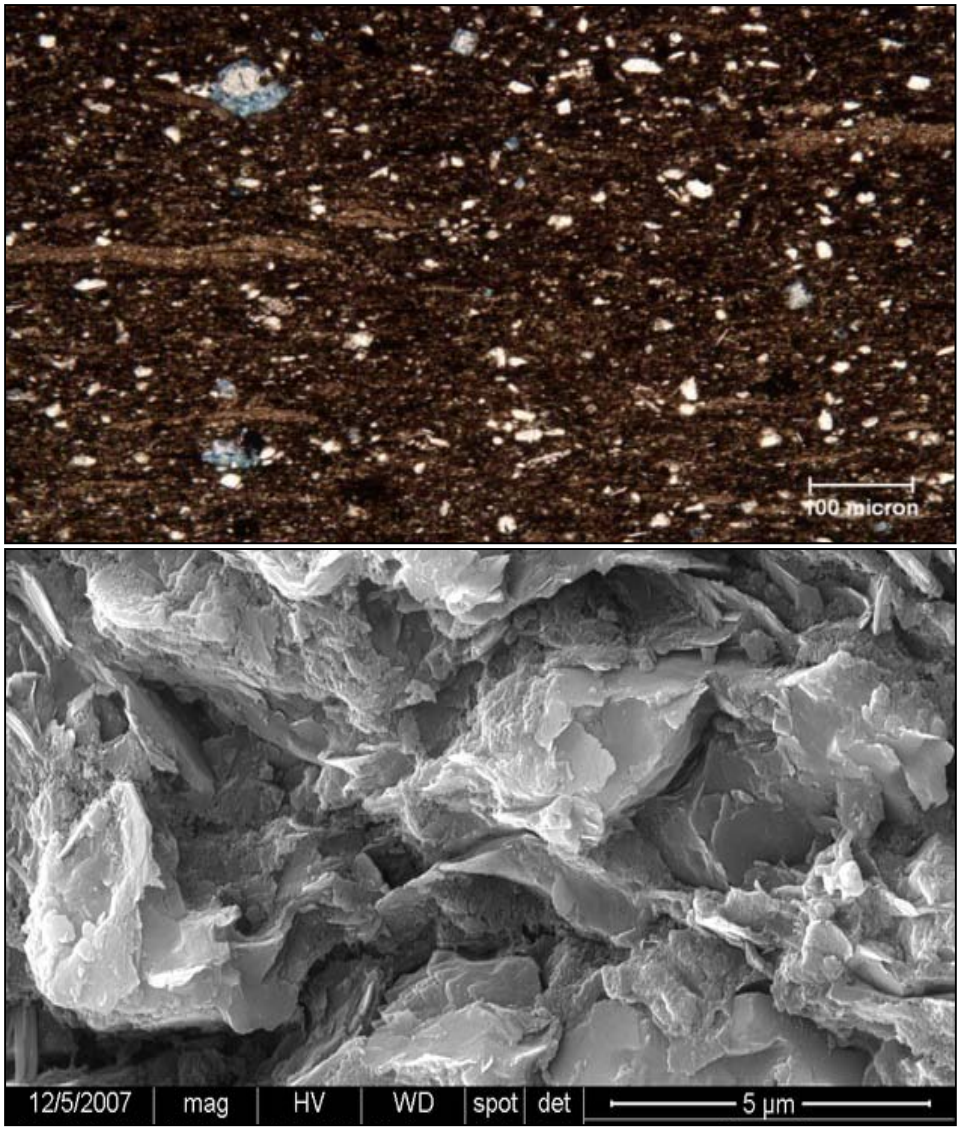

Figure 1.12 Representative thin section (top) and SEM (bottom) of the best reservoir quality rock class of the Marcellus shale which includes a clay-dominated matrix that hosts relatively high amounts of diagenetic pyrite in framboidal form and variably degraded kerogen, commonly coating clay particles. SEM reveals that the associated microtextural features contributes to enhanced gas-filled porosity and matrix permeability.

Table 1.29 Abbreviations for Marcellus Images and Tables

cal = calcite	calc = calcareous	carb = carbonaceous
CHL = chlorite	dissem = disseminated	dol = dolomite
F = feldspar	Fe-cal = ferroan calcite	Fe-dol = ferroan dolomite
fos = fossils	frac = fracture(s)	frag or frags = fragment(s)
IL = illite	interg = intergranular	intrap = intraparticle
intxln = intercrystalline	I/S = mixed-layer illite-smectite	KA = kaolinite
lam = laminated	mpor = microporosity	por = porosity
py = pyrite	Q = quartz	sph = sphalerite

1.5 Creep Behavior

Creep is a time-dependent deformation in response to a constant load. It is also the time-dependent relaxation in response to the removal of the load. In contrast to the elastic response that is instantaneous and time-independent, creep is time dependent and it reaches its final value over a period of time, often a considerable time. Because of an analogy with the time-delayed response of mechanical systems built with springs and dashpots, creep is also known as a visco-elastic behavior. This means that in practice, there is an instantaneous and time-independent component of deformation that is followed by a delayed response that stabilizes over time (Figure 1.13). Therefore, the total deformation obtained from applying a constant stress to the material is the sum of its elastic response and its creep response. The creep function (Figure 1.14) characterizes the rheological (viscous) properties of the material and is characterized experimentally for a given stress range, temperature, water content and lithology.

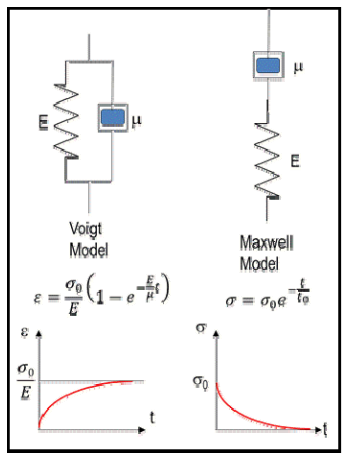

Figure 1.13 Time-dependent behavior associated to spring and dashpot mechanical systems.

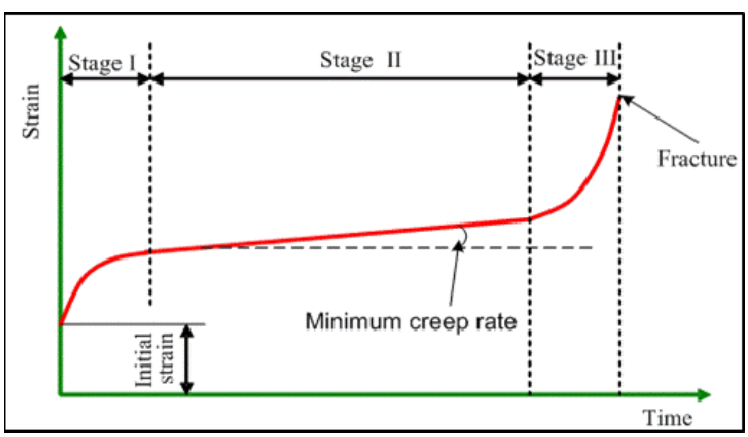

Figure 1.14 Strain-time creep function: The example shows the strain-time relationship of a typical creep test.

In this program, we conducted laboratory testing to evaluate the creep properties of six shale samples from the Barnett, Marcellus and Haynesville reservoirs. These were tested under hydrostatic and multistage triaxial compression testing conditions. Multistage creep tests facilitated the evaluation of creep parameters at different stress states, and different temperatures, using a single sample, by applying a step-wise loading path. Hydrostatic creep tests were conducted, to evaluate volumetric creep behavior.

The tested samples varied in mineralogical composition, total organic content, organic maturity and degree of diagenesis. Results show that, rocks with more biogenic cementation, less clay and less organic content have higher stiffness and higher strength. Creep strain, at a given time, correlates strongly with Young's modulus, clay and organic content. Higher confining pressure increased the amount of creep strain, at a given time, under the same deviatoric stress conditions. Under hydrostatic loading creep behavior can be described using a power-law strain-time model. Under deviatoric loading, creep behavior was better described by a Burgers model (Figure 1.15) but could also be described with a power law strain-time model. At higher deviatoric stresses, the visco-elastic deformation deviated considerably from a linear behavior and the sample eventually fails under tertiary creep (Figure 1.14).

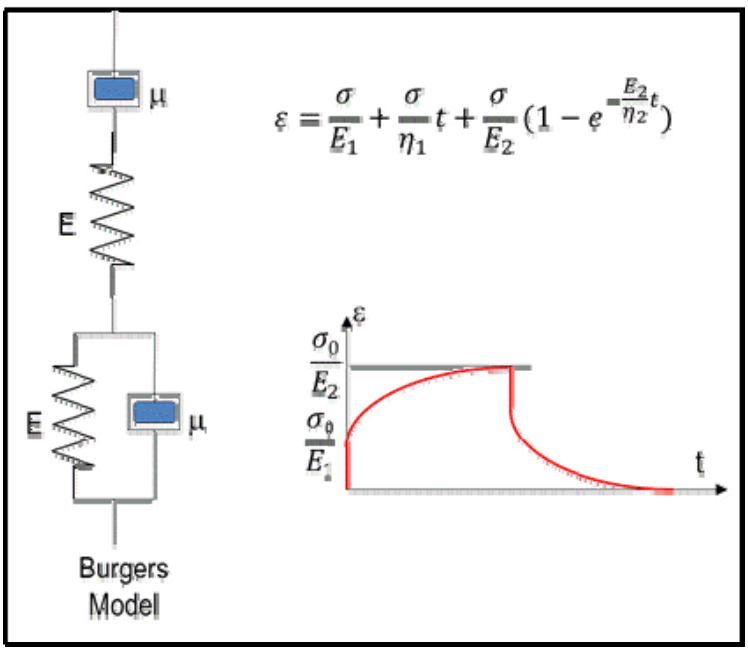

Figure 1.15 Visco-elastic creep behavior as defined by the Burgers model. The strain-time dependence is shown.

1.5.1 Sample Description

Table 1.30 shows sample identification, depths, mineral content and elastic moduli of the six samples used in this investigation. Prior to testing, these were wrapped in Teflon heat-shrink tube and kept at room condition. Tests were conducted under as-received conditions of saturation and under drained conditions. This allowed us to eliminate poroelastic effects and characterize the behavior of the rock frame. All samples had nominal dimensions of 1" diameter and 2" length, cylindrical shape, and axes oriented perpendicular to the bedding planes.

Table 1.30 Mineral contents of four shale samples

Sample Name (Depth)	Qtz/Feldspar %	Carbonate %	Clay %	Others %	TOC %	Confining Pressure psi	Young's modulus psi
Marcellus 09-30 (5,899.48 ft)	28	9	40	24		2755	2501320
						2320	2245619
						725	1840964
Barnett 3-20 (5,552.35 ft)	60	10	25	5		2320	4661077
						0	4036689
Haynesville 05-21 (12,424.75 ft)	25	23	33	18		0	2100146
Haynesville 05-22 (12,454.55 ft)	25	23	33	18		2320	2554549
Haynesville 07-11 (12,079.14 ft)							
Haynesville 07-12 (12,080.14 ft)							

Figure 1.16 shows examples of four shale samples used for creep testing. The second sample –from the left- was photographed after testing and still wrapped on its Teflon heat shrink isolation sleeve. This sleeve is used to isolate the sample from the hydraulic fluid used for applying confining pressure to the sample.

Figure 1.16 Examples of four shale samples used for creep testing.

1.5.2 Experimental Procedures

All of the creep tests were performed on GCTS triaxial rock test system and two additional Teledyne syringe pumps were used to provide constant confining pressure and axial load. The latter was applied to the samples via a hydraulic jack. Table 1.31 shows the loading paths for each of the six samples used.

Table 1.31 Loading path of the six samples used I the program

Sample name	Confining Pressure, psi	Deviatoric stresses, psi
Marcellus 09-30	2320.6032	3900-5220
	2755.7163	8000-9300-10450-11750-12900
	725.1885	9300
Barnett 03-20	2320.6032	6740-7760-9140-10590-12040
	0	6525-8000-9300-10450-11750
Haynesville 05-21	0	4930-6525-9210-10440
Haynesville 05-22	2320.6032	4930-6525-9210-10440
Haynesville 07-11	1450-2900-4350	0-0-0
	4350	2900-5800-2900-8700-11600-14500-17405-20305
Haynesville 07-12	1450-2900-4350	0-0-0
	4350	2900-5800-2900-5800-8700-11600-14500
Haynesville 07-12 (Elevated Temperature)	1450-2900-4350	0-0-0
	4350	2900-5800-8700-11600-14500

Figure 1.17 and Figure 1.18 illustrate the typical loading path of a multistage triaxial creep test for the Marcellus and Haynesville tests. After installing the sample and the strain sensor assembly in the confining cell, a constant confining pressure is applied. The sample is then loaded with the desired constant deviatoric stress, for a desired period of time. Subsequently, the deviatoric stress is increased to the next level and held constant for a specified time. During this process, the deformation of the sample is monitored continuously, and recorded.

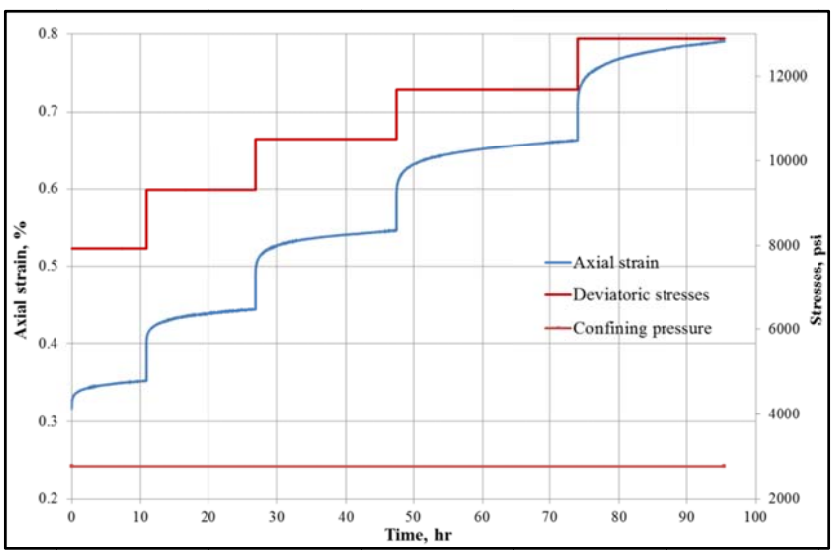

Figure 1.17 The multistage loading path & the axial strain of Marcellus 09-30, confining pressure is 2750 psi.

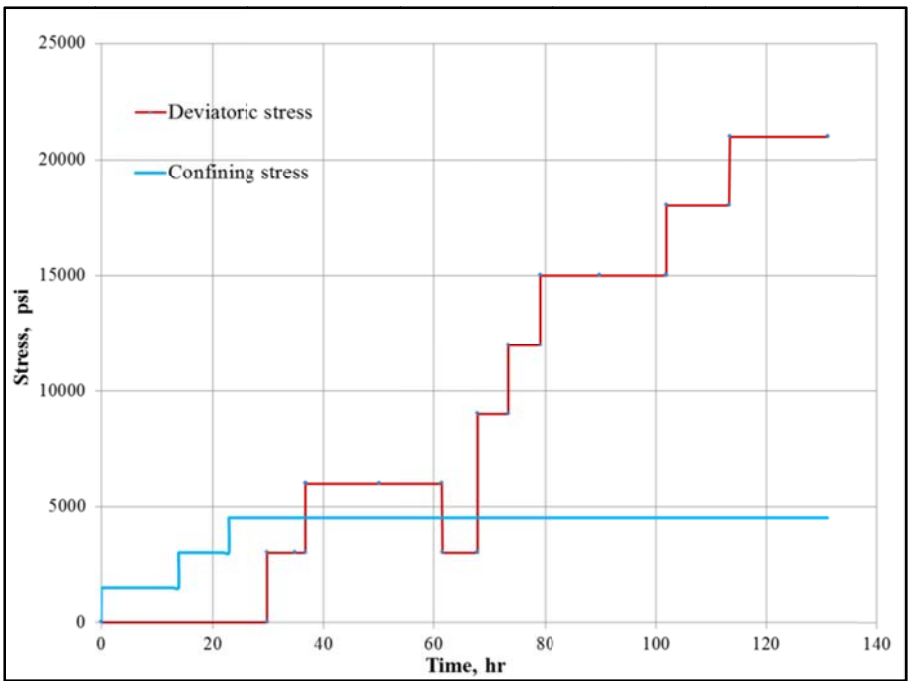

Figure 1.18 The confining pressure and deviatoric stress path of Haynesville 07-11, stress drop is for strain recovery.

1.5.3 Hydrostatic Creep

Figure 1.19 shows results from hydrostatic creep compression. Two Haynesville samples were tested and are compared. The left section of the plot shows results from sample 05-22 and the right side shows results from sample 07-12. Axial strain versus time, creep strain versus time and creep strain versus the logarithm of time are shown, at three pressure stages respectively. A best fit exponential creep function is also shown in both cases.

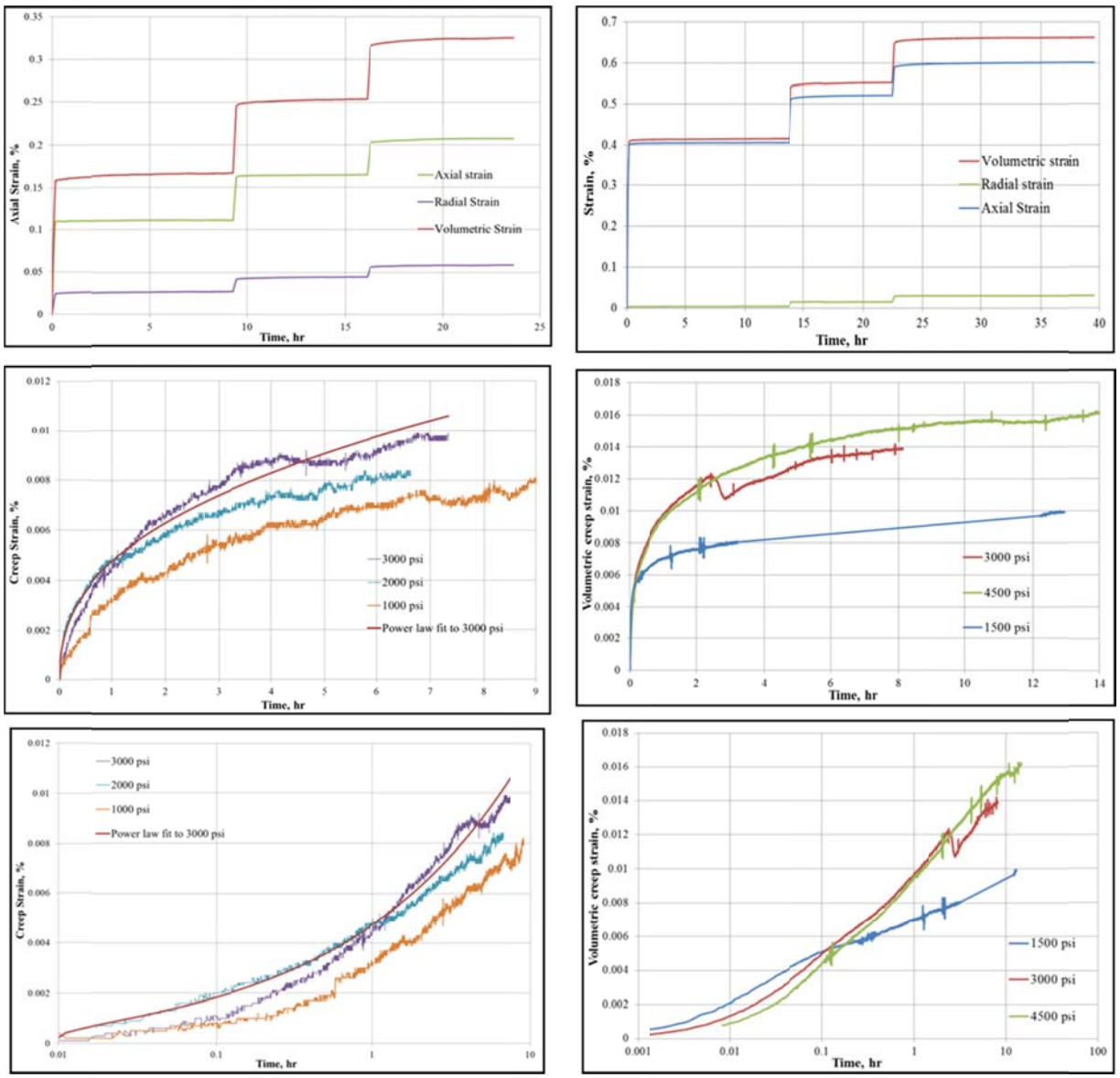

Figure 1.19 Haynesville 05-22: Strain-time response, under hydrostatic creep compression, at three pressure stages.

1.5.4 Deviatoric Creep

Figure 1.20 shows results from multistage triaxial creep compression. A Marcellus example (sample 09-30) is presented. The test was completed with seven stages of creep. Results from the first two stages are shown in the top-left section of the plot. The bottom-left section shows creep stages 3rd to 7th. The top-right section of the figure shows the relationship between the change in deviatoric stress and the change in axial strain, representing the axial stiffness of the sample, and the change in lateral strain and the chain in axial strain, representing the lateral stiffness of the sample. The Bottom-right section of

the figure shows the axial creep strain versus time (blue curve) and axial creep rate versus time (red curve).

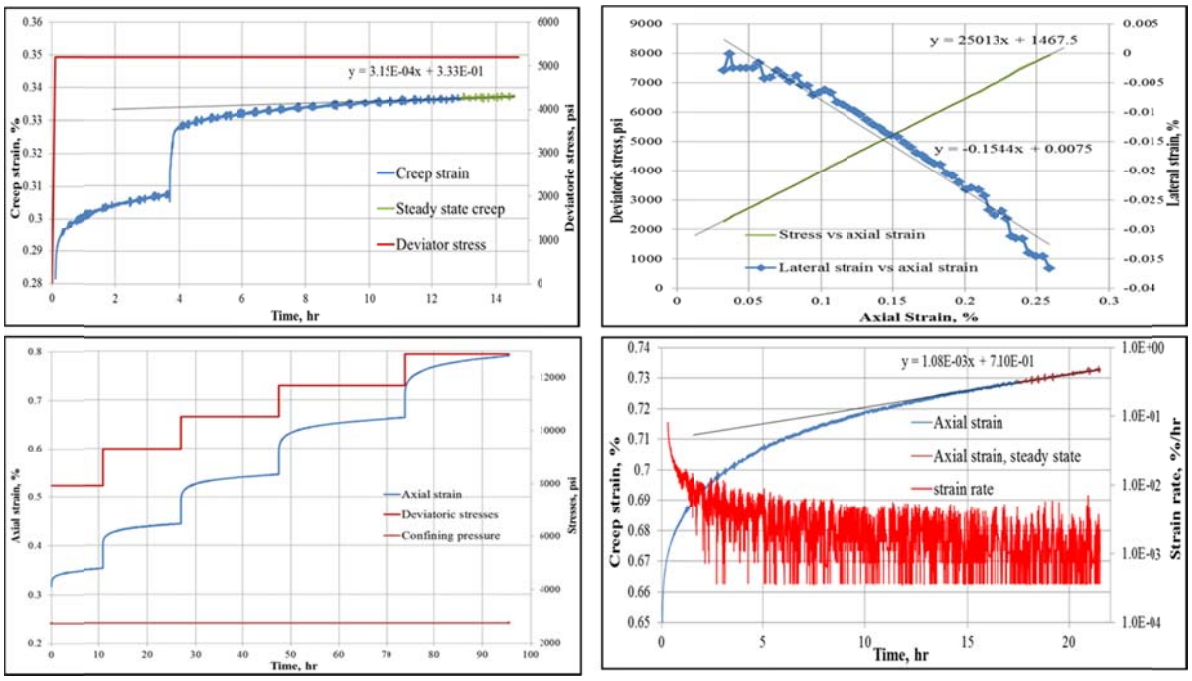

Figure 1.20 Results from Marcellus tests, sample 09-30. Top-left: First two stages of creep. Bottom-left: Third to seventh stages of creep. Top-right: Deviatoric stress and lateral strain, versus axial strain during the 3rd to 7th stages of creep. Bottom-right: Axial creep strain and strain rate versus time.

The steady state creep (i.e., secondary creep rate) was evaluated from the extrapolated linear portion of the curve (bottom-right section of Figure 1.20). This section reflects the portion of the strain rate $\frac{d\varepsilon_1}{dt}$ curve, where a reasonable constant value is reached.

Figure 1.21 shows the relationship between the secondary creep strain rate versus the applied deviatoric stress. The strain rates of the 3rd to 7th stages of the creep test were obtained by linear fitting to the last portion of the axial strain-time curves, as shown in Figure 1.20 (Bottom-right section).

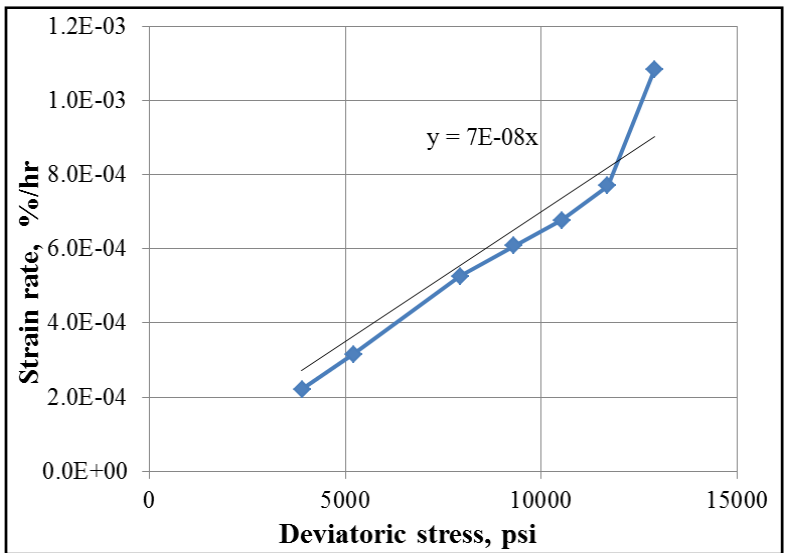

Figure 1.21 Strain rate-stress relation, confining pressure 2755 psi, Marcellus-09-30.

Results show a linear relationship with a constant slope up to a deviatoric stress of 11600 psi. This means that creep for this sample can be modeled using a linear viscoelastic Burgers model. Unfortunately, the confining stress during the first two creep stages changed from 2320 psi to 2755 psi, and we are consequently ignoring this in fitting the Burger's model to the measured data. Equation 1 describes the model and we used a least-square fitting method over the 3rd to 7th stage of creep, to model the measured data.

$$\varepsilon = \frac{\sigma}{E_1} + \frac{\sigma}{\eta_1} t + \frac{\sigma}{E_2}(1 - e^{-\frac{E_2}{\eta_2}t}) \quad (1)$$

$$\dot{\varepsilon} = \frac{\sigma}{\eta_1} + \frac{\sigma}{\eta_2} e^{-\frac{E_2}{\eta_2}t} \quad (2)$$

The two elastic and two viscous parameters (E_1, E_2, η_1, η_2) were obtained using the least-square fitting method. The burgers model gives a relatively good fit to the creep data with a least-square error of 0.040238.

Table 1.32 Burger creep parameters

	E_1 ,psi	E_2, psi	η_1, psi/s	η_2, psi/s
Marcellus 09-30 (2755 psi)	2556144	32059278	3364881.6	128648.71
Barnett0 3-20 (2320 psi)	4747809	354417895	13720594.8	1414120.5
Haynesville (2320 psi)	2508572	46731509	19725168.0	465572.0

The power law relationship for creep strain versus time is another widely used model to represent viscoelastic materials. It has the following form:

$$\varepsilon^c = k\sigma^p t^n \tag{3}$$

where ε^c is the creep strain excluding the instantaneous elastic strain. For this test, the quasi-strain rate increases almost linearly with the deviatoric stress (Figure 17), thus the exponent p is equal to 1, and the total strain of a constant stress creep test is:

$$\varepsilon = \frac{\sigma}{E} + k\sigma t^n \tag{4}$$

We evaluated the other two coefficients k and n by a least-square fitting to the data and obtained a least-square error of 0.023684. Figure 1.22 shows the multistage data (loading stages 3 to 7) fitted to the Burgers model (left) and the power law model (right). Both models fit the experimental data well.

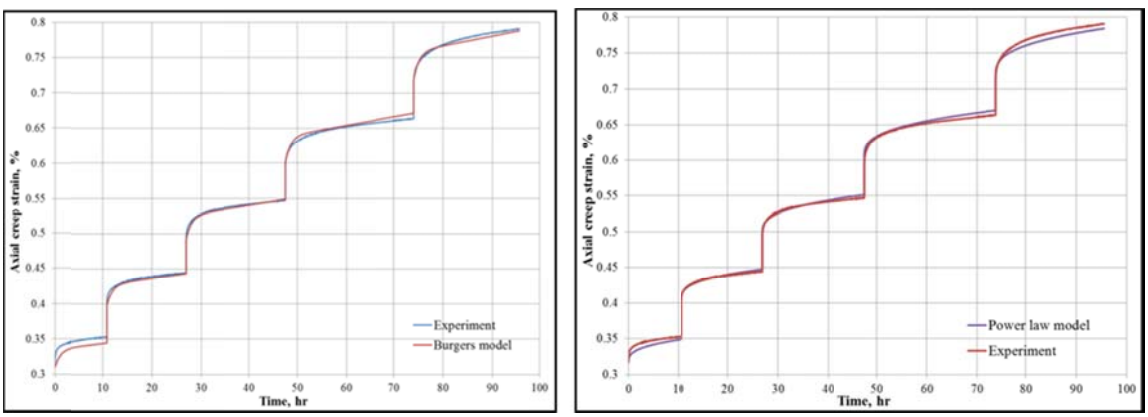

Figure 1.22 Comparisons between experimental creep strain and Burgers creep reaction to five stresses, confining pressure 2755 psi, Marcellus 09-30.

Table 1.33 Power law creep parameters

	E, psi	k	n
Marcellus 09-30 (2755 psi)	2501320	3.77E-8	0.17938
Barnett 03-20 (2320 psi)	4821920	1.29E-8	0.15937
Haynesville (2320 psi)	2521360	1.27E-8	0.47327

Figure 1.23 shows results from multistage triaxial creep compression on a Barnett sample (03-20). The test was completed with five triaxial stages of creep and at a constant confining pressure of 2320 psi. Results from all stages are shown in the top-left section of

the plot. The top-right section shows the axial strain rate as a function of the deviatoric stress. The bottom-left section shows the comparison of the experimental data to the Burgers model. The Bottom-right section shows the comparison between the experimental data and the power law model. Table 1.32 summarizes the coefficients defining the Burgers model. Table 1.33 shows the corresponding coefficients representing the Power Law model.

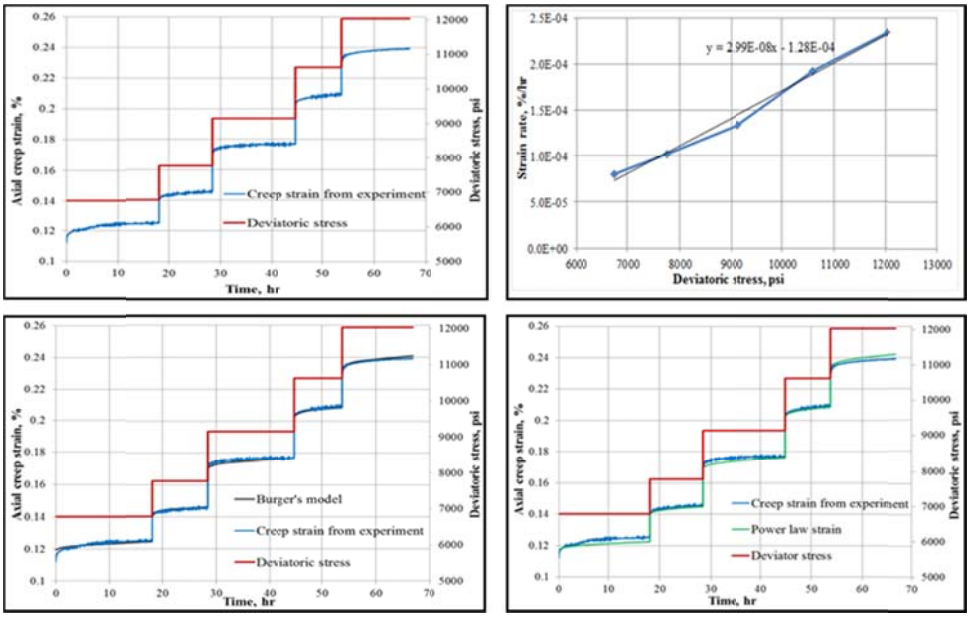

Figure 1.23 Results from Barnett tests, sample 03-20. Top-left: Five stages of triaxial compression creep conducted at a constant confining pressure of 2320 psi. Top-right: Axial strain rate versus deviatoric stress. Bottom -left: Best fit of the experimental data to the Burgers model. Bottom-right: Best fit of the experimental data to the Power law model.

Figure 1.24 shows results from multistage triaxial creep compression on a Haynesville sample (05-22). The test was completed with three triaxial stages of creep and at a constant confining pressure of 2320 psi. Results from all stages are shown in the top-left section of the plot. The bottom-left section shows the comparison of the experimental data to the Burgers model. The Bottom-right section shows the comparison between the experimental data and the power law model. Table 1.32 summarizes the coefficients defining the Burgers model. Table 1.33 shows the corresponding coefficients representing the Power Law model.

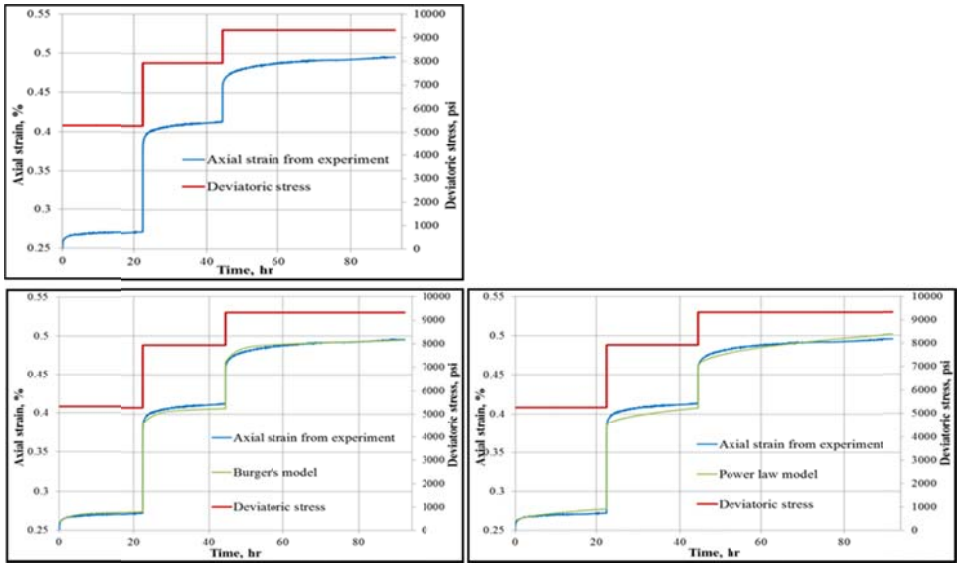

Figure 1.24 Results from Haynesville tests, sample 05-22. Top-left: Three stages of triaxial compression creep conducted at a constant confining pressure of 2320 psi. Top-right: Axial strain rate versus deviatoric stress. Bottom -left: Best fit of the experimental data to the Burgers model. Bottom-right: Best fit to the Power law model.

Figure 1.25 shows results of creep strains, for Haynesville samples 07-11 and 07-12, as a function of time, for different deviatoric stresses in the ranges from 3000 psi to 18,000 psi. Results show gradual increase in the creep strain with deviatoric stress up to 15,000 psi. At higher deviatoric stresses, the samples creep significantly and fail macroscopically.

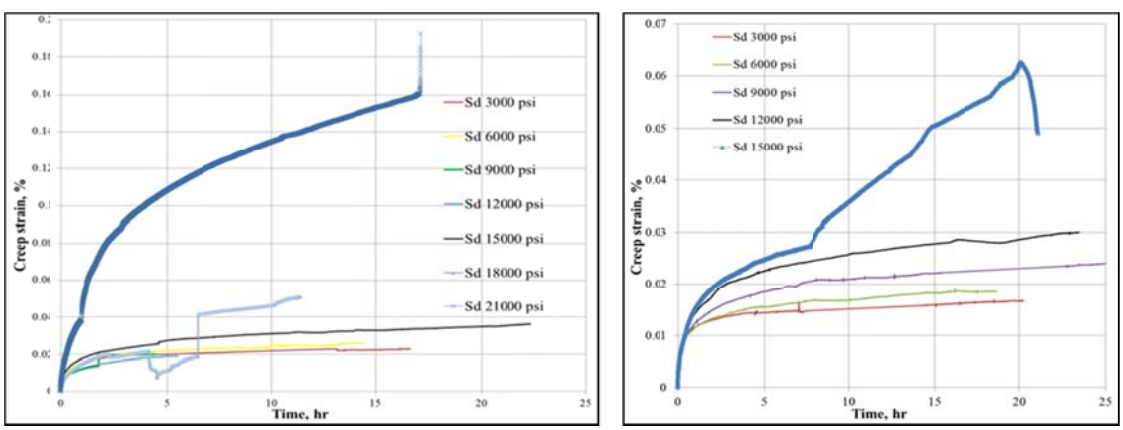

Figure 1.25 Creep strain versus time at different deviatoric stresses for Haynesville samples 07-11 and 07-12.

Figure 1.26 shows the corresponding plot of the steady state strain rate versus the deviatoric stress. Secondary and tertiary creep is apparent in the sample behavior. At lower deviatoric stresses, the sample exhibits a linear viscoelastic behavior. At higher

deviatoric stresses, the strain rate increases significantly until the sample fails macroscopically.

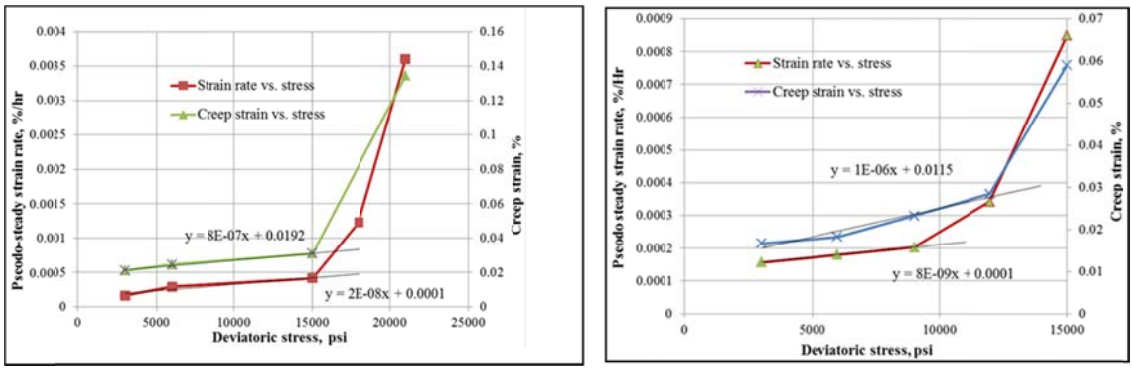

Figure 1.26 Creep strain and pseudo-steady strain rate versus deviatoric stress for Haynesville samples 07-11 (left) and 07-12 (right).

1.5.5 Creep Under Elevated Temperatures

Haynesville sample 07-12 was tested under low hydrostatic stress and three temperatures conditions of 60°, 40° and room temperature. Subsequently, the sample was subjected to three stages of hydrostatic stress, and hydrostatic creep, at a constant temperature. Finally, the sample was subjected to creep under deviatoric loading.

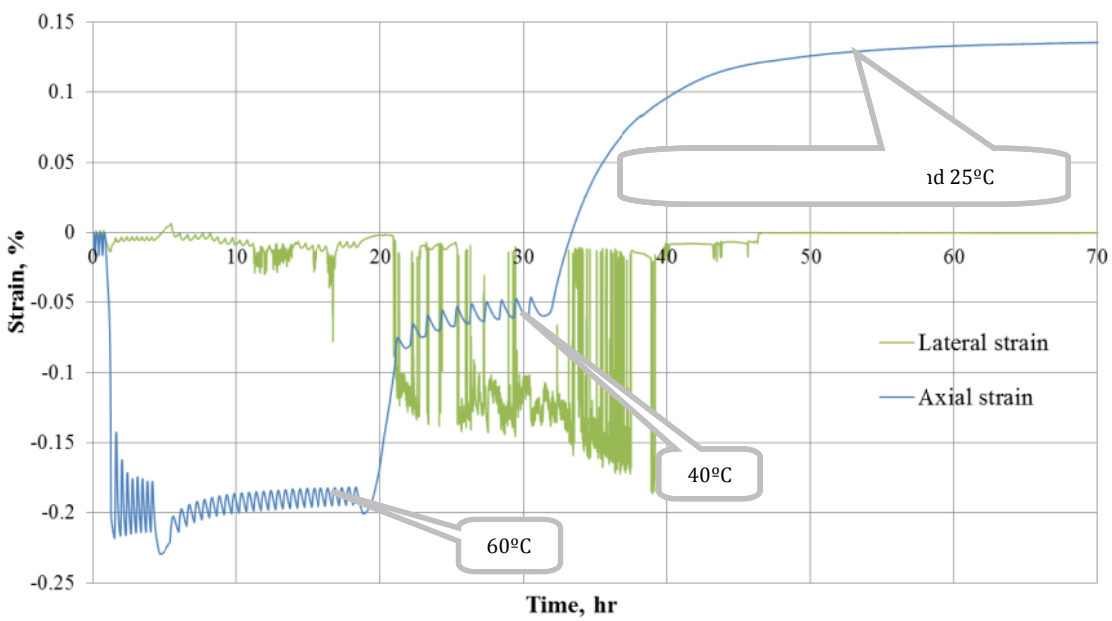

Figure 1.27 Haynesville sample 07-12: Hydrostatic creep strains under 60 psi hydrostatic pressure and at 3 different temperature levels.

Figure 1.27 shows results of this test and the effect of thermal expansion on the measurements. Under a small hydrostatic pressure of 60 psi, the lateral thermal strain is small compared to axial thermal strain. The temperature control system maintained the cell temperature constant to within a 3ºC range and the thermal oscillation associated to the control system resulted in axial and lateral strain oscillation.

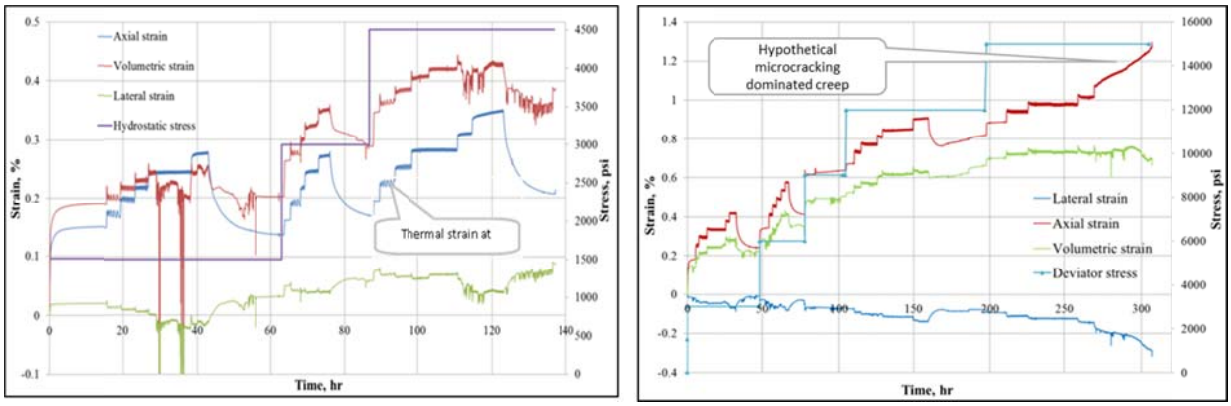

Figure 1.28 Sample Haynesville 07-12 : Hydrostatic (left) and deviatoric (right) creep strains under 3 hydrostatic levels, 5 deviatoric stress levels and 4 temperatures levels.

Additional creep tests were conducted under hydrostatic and deviatoric stress, with multiple stress cycles, and at 4 temperature levels, from 20ºC to 140ºC, and at 40ºC intervals. Figure 1.28 shows creeps results from hydrostatic (left) and deviatoric (right) loading. Results show that the temperature loading resembles stress loading; in addition, the axial strain oscillates with an oscillating temperature. For the test subjected to deviatoric loading, the lateral strain decreases with increasing temperature, which results from the volumetric dilation of the sample under temperature.

The deviatoric creep at elevated temperature was conducted for around 300 hours. During this time, the axial strain increased with temperature and oscillated with oscillations in temperature. The last temperature stage shows a fast creep strain rate, followed by tertiary creep and sample failure. In this case, the axial remains unchanged, while the radial strain increases at an increased rate, giving rise to the dilatational failure.

Figure 1.29 compares the creep strain at elevated temperatures (left) and room temperature (right), under various levels of deviatoric stress, for sample Haynesville 07-12. Al high temperature, the creep strain reduces with increasing deviatoric stress. At room temperature it increases with increasing deviatoric strain. We do not have an explanation for this behavior and more creep tests under elevated temperatures, assisted by ultrasonic test and acoustic emission test, may be needed to infer more information on this.

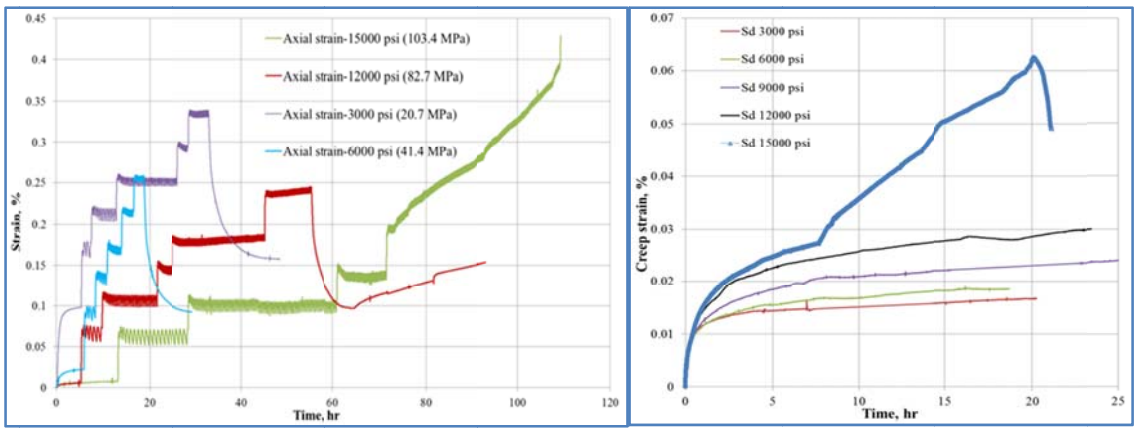

Figure 1.29 Deviatoric creep strain comparison between room temperature and elevated temperatures, Haynesville 07-12.

1.5.6 Creep on Different Samples Under the Same Stress Conditions

Creep deformation is also dependent on rock type, including clay content and organic content. Figure 1.30 compares the creep strain between Haynesville, Barnett and Marcellus samples. All samples were subjected to a confining stress of 2320 psi. The deviatoric stress varied from 7975 psi and 9135 psi on the Haynesville Barnett pair, to 5220 psi for the Haynesville, Marcellus pair. The Barnett sample has a high degree of microcrystalline silica mineralization, has high modulus and high surface hardness. The Haynesville shale has calcareous cementation, higher clay and lower surface hardness.

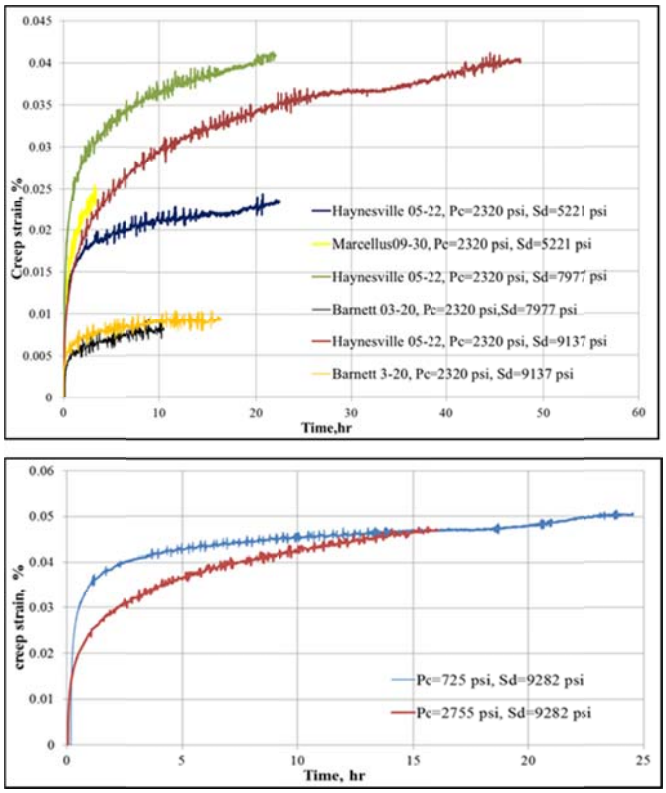

Figure 1.30 Comparisons between creep strains under the same confining pressure 2320 psi, and the same deviator stress 7975 psi.

The Marcellus sample has high organic content and high clay content and is the softest of the three. This contrast in properties is also reflected in the degree of creep strain. The Haynesville samples exhibit considerably higher creep strain than the Barnett samples, and the Marcellus sample exhibits slightly higher creep strain than the Haynesville.

1.5.7 Test Result and Interpretation of Uniaxial Creep

In this section we report uniaxial or unconfined compression stress creep tests using a Barnett sample 03-20. Three creep stages were monitored at increasing values of the axial stress (i.e., deviatoric stress). Figure 1.31 shows these results. The creep strain stabilizes after approximately 8 to 12 hours and remains constant thereafter. Subsequently, the creep strain rate is zero. However, at increasing axial stress, the creep strain and creep strain rate appears to increase marginally.

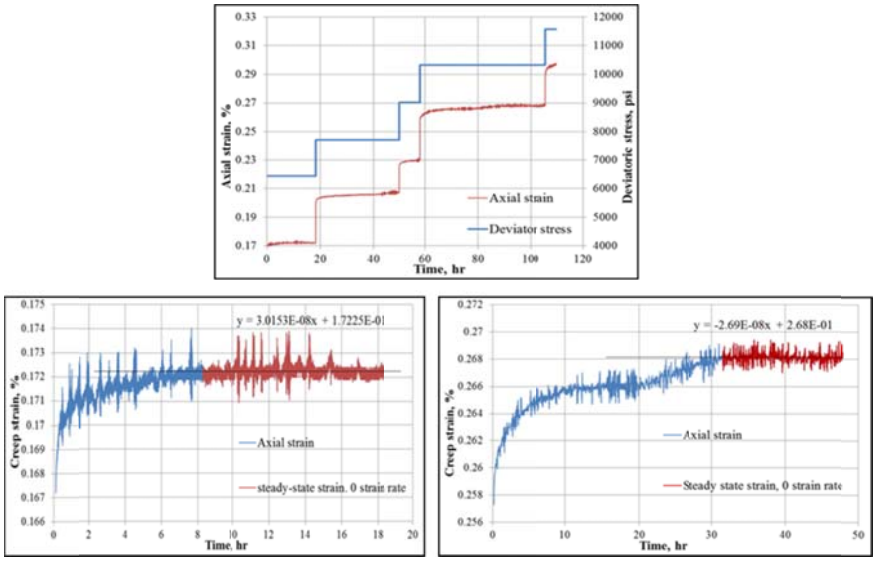

Figure 1.31 Multistage uniaxial (unconfined) creep test of sample Barnett 03-20. Left figure represents results for a deviatoric stress of 6742.5 psi, right figure represents that of 10585 psi.

Figure 1.32 shows similar results for Mancos shale. Here we observe a zero creep strain rate at the first deviatoric stage (4495 psi) and a linear increase in strain rate with deviatoric stress afterwards.

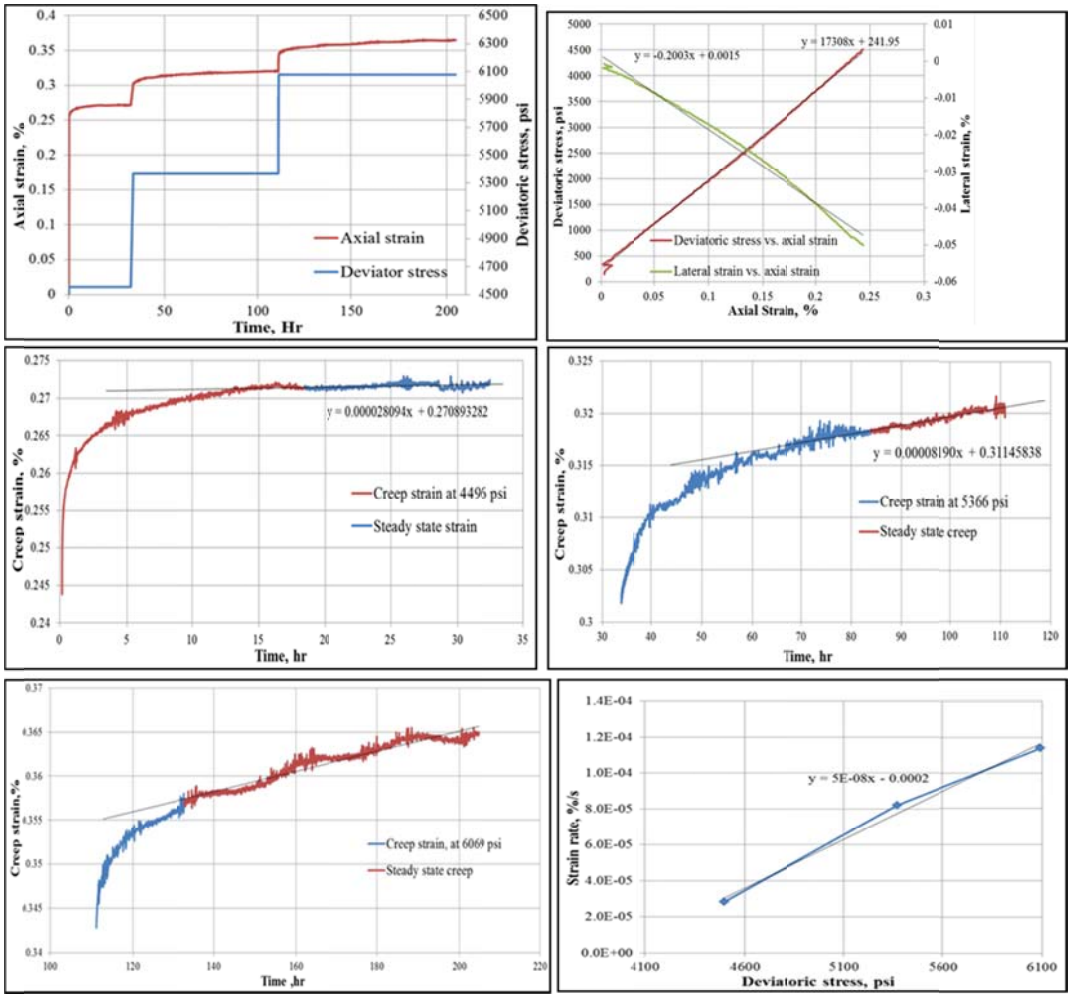

Figure 1.32 Multistage uniaxial (unconfined) creep test of sample Mancos 7v. The magnitude of the deviatoric stress increased from 4495 psi to 5365 psi and 6090 psi. A linear increase in creep strain rate with deviatoric stress was found.

1.5.8 Comparison of Uniaxial and Triaxial Creep, Confining Pressure Dependence

In this section we compare results from creep strain under two conditions of confined (2320 psi) and unconfined stress, and identical deviatoric stress conditions (6525 psi, 7830 psi, 9135 psi and 10585 psi, and 12035 psi), for Barnett samples. We observe that when the uniaxial deviatoric stress is lower than the creep stress threshold, the uniaxial creep strain smaller than the confined creep strain. However, when the uniaxial deviatoric stress is greater than the creep stress threshold, the uniaxial creep strain is larger than that the confined creep strain.

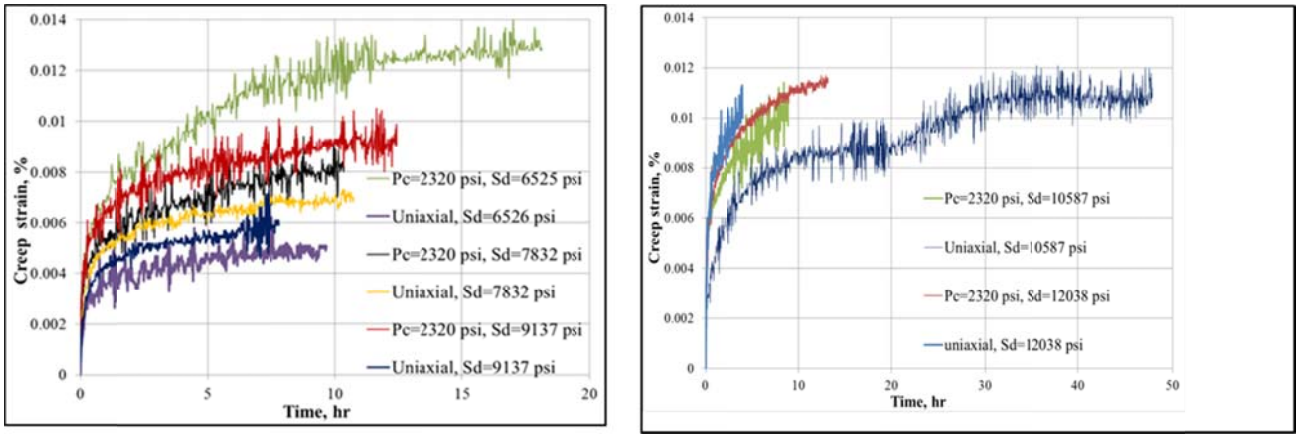

Figure 1.33 Comparisons of creep strain for Barnet 3-20 under two conditions of confining (2320 psi) and unconfined stress, and under the same deviatoric stress of 6525, 7830, 9135, 10585, and 12035 psi.

1.5.9 Creep Mechanism

For the samples tested, the creep strain in the radial direction is smaller than that in the axial direction. This implies that the sample loses volume during deviatoric creep stages. Because of the highly laminated nature of tight shales and their weak organic-mineral contacts, significant microcracking is created during coring and core retrieval. The volume loss measured is most likely accommodated by microcrack closure and potentially compaction of the organic matter. Future studies of creep on tight shales will require special consideration of the induced microcrack porosity and a workflow to minimize their effect. Previous studies of creep deformation in rocks (Lockner, 1993; Karner et al., 2003; Chester et al., 2005; Heap et al., 2009) have identified the creep mechanisms by direct observation of the deformation structure in the microscope. The colloidal size constituents in shales make it difficult to visually observe the resulting deformation at the microstructure level. Tight shales are also heterogeneous, consisting of multiple mineral and organic constituents and with multiple mechanisms responsible for the observed creep strain. Microstructural, SEM observations of tight shales (Loucks et al., 2009; Sondergeld et al., 2010; Curtis et al., 2010) has revealed that most of the pores are either mineral pores (intracrystalline between clay minerals) or organic pores (existing in the organic matter). Furthermore, the texture of the organic matter is generally laminated. Therefore, it is possible that shear compaction is likely responsible for creep deformation during deviatoric loading. This couldn only be verified once the effect of the microcracks is removed. As clay content increases, microcrystalline mineralization decreases, and thus the increase in clay content may also result in enhanced creep strain (Sone et al., 2010, Li et al, 2012). This may result because clay minerals have low frictional coefficients (Moore and Lockner, 2004) and facilitate grain rearrangement. At high deviatoric stresses, coring induced microcracks coalesce, and failure is induced by macroscopic shear fracturing.

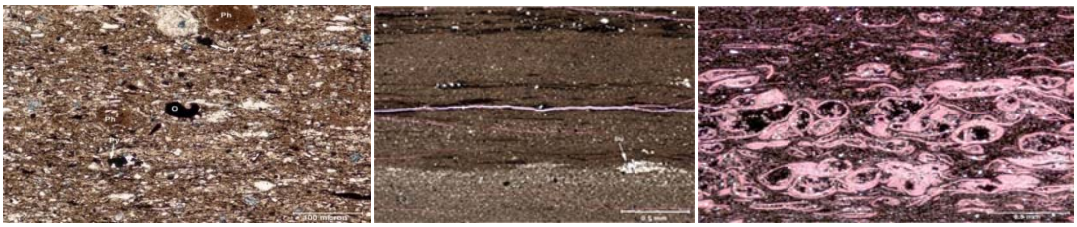

Figure 1.34 Thin sections of typical Barnett, Haynesville, and Marcellus shale.

1.5.10 Discussion

The above comparison and analysis suggests that Young's modulus, clay content, clay maturation and organic content are indicators for evaluating visco-elastoplastic properties of shales. Stiffer shale creeps less, shale with more clay content and less mature clay creep more. More organic rich and less mature shales also creep more. Quantitative characterization of the viscoelastic-plastic/ductility of tight shale reservoir rocks is important for long-term production. Creep deformation affects the effectiveness of hydraulic fracturing, and the long term reservoir response during depletion. Over geologic time scales, viscoelastic-plastic deformation also changes the regional stress state. Creep also affects the stress concentrations around wellbores and perforations. Previous studies of creep behavior on reservoir rocks have proposed constitutive laws describing their time-dependent effect. Among these, the Burger's and Power law models appear to describe one-dimensional creep behavior reasonably well. The volumetric creep behavior needs to be investigated further.

The behavior of axial creep strain caused by temperature step-loading is similar to that caused by stress-step loading. For the same elevated temperature, creep strain at higher deviatoric stress is smaller than that at lower deviatoric stress. This is opposite to results of deviatoric creep under room temperature. Additional studies on creep behavior of tight shales under in-situ conditions, minimizing the effects of induced microcracking, with temperature and humidity control, and monitored with ultrasonic and acoustic emission measurements are needed better understand this rock property.

1.6 Summary

In this section of material property characterization, we provide a comprehensive assessment of petrophysical, petrologic, geochemical, and mechanical properties for selected rock classes for the Barnett, Haynesville, and Marcellus shale plays. Samples were selected using the Heterogeneous Rock Analysis Method (HRA). The HRA defines rock classes in a quantitative and non-subjective manner based on pattern recognition of log responses. These classes, representing the building blocks of the heterogeneous shale system, are then cored and adequately sampled for laboratory measurements to obtain a representative distribution of each measured property. Results are then presented in the form of averaged values and standard deviations for each rock classes.

One advantage of the methodology is that HRA workflow allows identification of these rock classes on other wells in the basin, by comparison of their log responses in relation to log responses in the reference HRA model. This process facilitates the propagation of laboratory data via logs to other locations in the play without core data. However, propagation of the knowledge gained in this study to multiple wells was not part of this study.

The following summary of reservoir properties is noted for the best reservoir quality facies of the three rocks studied:

Barnett shale: Bulk density 2.45 ± 0.03 g/cc; effective porosity 7.88 ± 0.5%; water saturation 6.04 ± 2.04%; gas saturation 88.48 ± 2.80%; oil saturation 5.48 ± 1.09; gas filled porosity 6.98 ± 0.60%; clay bound water 4.22± 1.00; and permeability 400± 74.32 nD; and TOC 3.72 ± 0.33% (BW).

Haynesville shale: Bulk density 2.469 ± 0.039 g/cc; effective porosity 7.820 ± 0.880%; water saturation 4.89 ± 2.84%; gas saturation 86.70 ± 7.60%; oil saturation 8.380 ± 5.38%; gas filled porosity 6.760 ± 0.80%; clay bound water 4.92 ± 0.91%; permeability 509 ± 108 nD; and TOC 2.150 ± 0.120% (BW).

Marcellus shale: Bulk density 2.43 ± 0.06 g/cc; effective porosity 9.56 ± 1.45%; water saturation 13.17 ± 2.89%; gas saturation 86.07 ± 2.79%; oil saturation 0.76 ± 0.24%; gas filled porosity 8.22 ± 1.24%; clay bound water 5.19 ± 0.87%; permeability 424.00 ± 61.21nD; and TOC 7.342 ± 1.734% (BW).

The following summary of mechanical properties is also noted for the same units:

Barnett shale (Measured at a confining pressure of 2500 psi): Peak strength σ_V=25909 ± 828 psi and σ_H = 30758 ± 3624 psi; Young modulus E_V = 3.86 ± 0.26x10^6 psi, E_H = 5.60 ± 0.36x10^6 psi; Poisson's ratio ν_V = 0.201± 0.017, ν_H = 0.256± 0.058.

Haynesville shale (Measured at a confining pressure of 2370 psi): Young modulus E_V = 2.57± 0.612 x10^6 psi, E_H = 4.27± 0.911 x10^6 psi; Poisson's ratio ν_V = 0.176± 0.035, ν_H = 0.217± 0.071.

Marcellus shale: Measured at a confining pressure of 2160 psi): Peak strength σ_V=24348± 10592 psi, σ_H=11906 ± 2482 psi; Young modulus E_V =3.57 ± 2.84 x10^6 psi, E_H =2.17 ± 0.28 x10^6 psi; Poisson's ratio ν_V =0.237 ± 0.059, ν_H = 0.334 ± 0.024.

2 LOSS OF SURFACE AREA IN FRACTURE NETWORKS

2.1 Introduction

The objective of this section is to evaluate the loss of connectivity between fracture branches, in fracture networks and at junctions, by performing numerical modeling of fracture network geometries, and parametric study of the propensity for isolating branches and developing local restrictions.

Key components of this effort are as follows:

(i) Generate fracture networks based on comparisons with published micro-seismic measurements from representative reservoirs. Supplement this effort with structural geological considerations, delineating stratigraphic and structural fabric, as well as tectonic overprinting.

(ii) Conduct a numerical evaluation of well production through fracture networks with varying distributions of fracture conductivity within branches, using discrete fracture models (Eclipse or equivalent). The model is used primarily to estimate how the geometry of fracture branches (fracture tiers) affects well production and propensity of losing connectivity.

(iii) Evaluate well production through fracture networks numerically, as described above, but using measured values of fracture conductivity. Results help defining metrics to evaluate the potential loss of fracture surface area, for characteristic reservoir mudstone types (Marcellus, Haynesville, Barnett), and for different fracture network and depletion scenarios.

2.2 Background

Achieving economic production in nano-Darcy permeability gas-shale reservoirs requires creating a large surface area by hydraulic fracturing. In general, the more complex the created hydraulically fractured system, the more difficult it is to transport and place adequate proppant volumes; the un-propped branches are more susceptible to closing, particularly when unfavorably oriented in relation to the in-situ stresses, and the loss of effective surface area during production is more severe. Factors that contribute to the loss of productive fracture area are: complex rock fabric, the presence of fracture branches with connectors aligned unfavorably to the intermediate and maximum in-situ stress; poor proppant delivery and placement, low fracture surface hardness, and degradation of fracture surface hardness by fluid-rock interactions. In addition, and possibly less understood, is the loss of fracture surface area (and loss of fracture face permeability) at the proppant-fracture-face interface. The implication of this is that the higher the proppant coverage along the created fracture area, the lower may be the effective surface area for fluid flow to the fracture.

Loss of fracture area can take place rapidly (resulting in a rapid drop from IP), or over a longer time, (leading to lower stabilized gas flow rates and often to marginal or uneconomical production). The problem may be less severe in reservoirs with limited fabric, simpler hydraulic fractures, less fracture branches, less connectors, better cemented mudstones, higher surface hardness, moderate in-situ stress conditions (i.e., moderate depths and relatively low tectonic loading), and moderate rock-fluid sensitivity. Current operational experience in tight shale reservoirs indicates that retention of productive fracture area and fracture conductivity are major economic issues in these plays.

The objective here is to understand the multiple causes of loss of fracture area and define solutions to mitigate the resulting loss of production. To accomplish this goal one must understand complex hydraulic fracture networks and determine critical parameters to maintain productive fracture area, and fracture conductivity on these. One must also understand the geologic conditions affecting rock fabric, fracture complexity and fracture surface area development and preservation. The desirable end product is an improved methodology for production of tight gas shales.

2.3 Fracture Characterization

Natural fractures and fracture networks were studied via core fracture evaluation on the three plays under study (Barnett, Marcellus and Haynesville shales). We found that near-vertical, calcite- or other mineral-filled fractures were common on all cores. Interactions between these mineralized fractures and the rock fabric and mineralized fractures and coring induced fractures were also common. Petal fractures, centerline fractures, partings, interaction with the rock fabric were observed to be recurrent features. Examples of these observations are provided in Figure 2.1 through Figure 2.4. When available, core fracture characterization was compared with borehole imaging (e.g., FMI) fracture characterization. It was noted that some hair-line mineralized fractures, clearly visible in the core, may be interpreted as conductive fractures (non-mineralized) in the FMI. Calibration of the FMI fracture characterization with the core fracture characterization considerably improves the reliability of the interpretation.

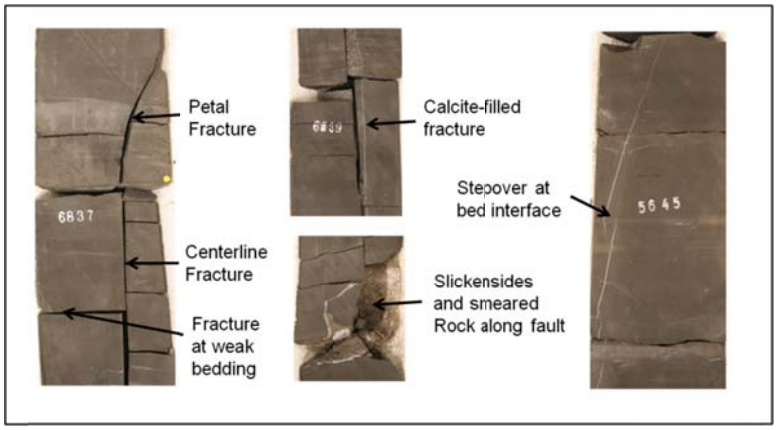

Figure 2.1 Fracture analysis on core. Examples of coring- and handling-induced petal, centerline and bedding partings are shown. Also shown are interactions between mineralized fractures and the rock fabric, and between mineralized fractures and coring induced fractures.

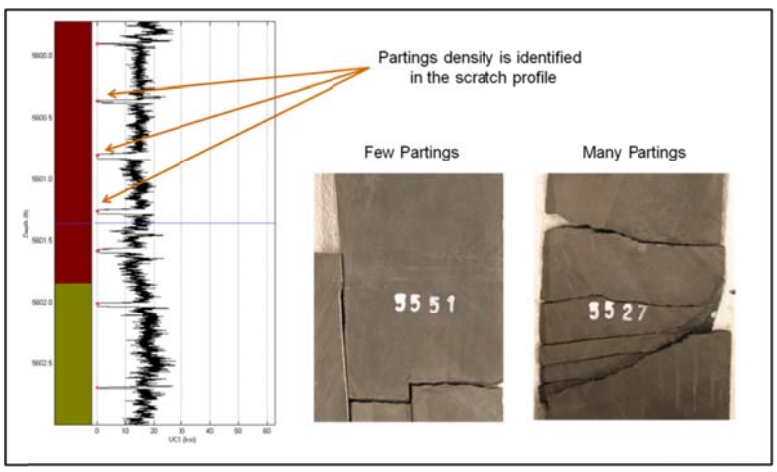

Figure 2.2 The continuous strength measurement is used to quantify fracture density, per unit length, on a rock class by rock class basis.

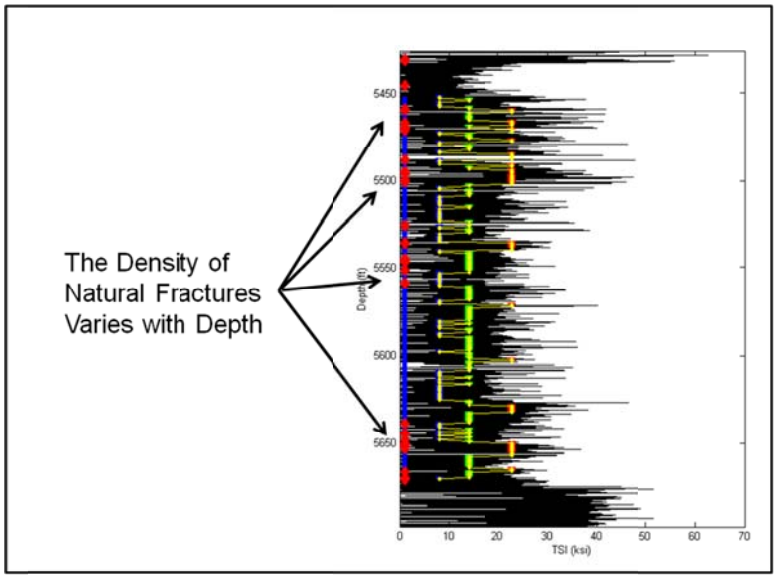

Figure 2.3 Fracture density per unit length in the Barnett shale (Well-1), evaluated over the length of the cored section. Results are integrated with borehole imaging observations. FMI of conductive fractures (Dark Blue), FMI resistive fractures (Light Blue), drilling induced fractures (Yellow), core open fractures (Dark Green) and core filled fractures (Light Green) are shown.

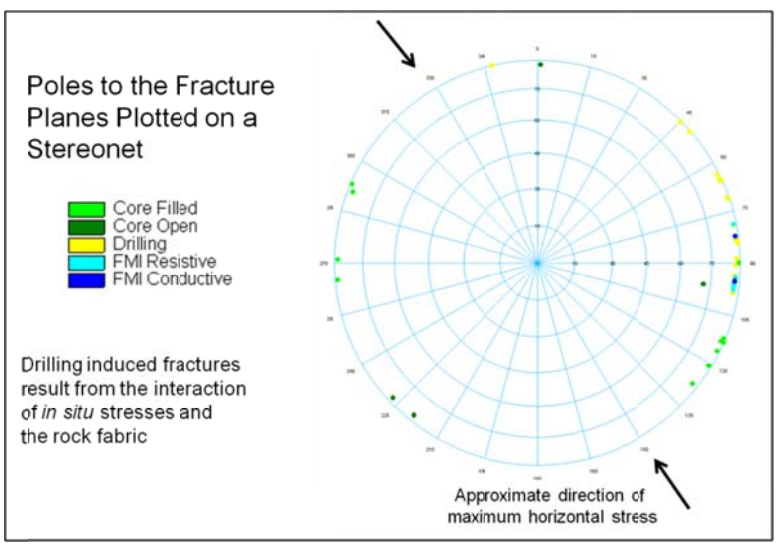

Figure 2.4 Stereographic projection of fracture poles for core sections of the Barnett Well-1. The approximate direction of the maximum horizontal stress is also shown.

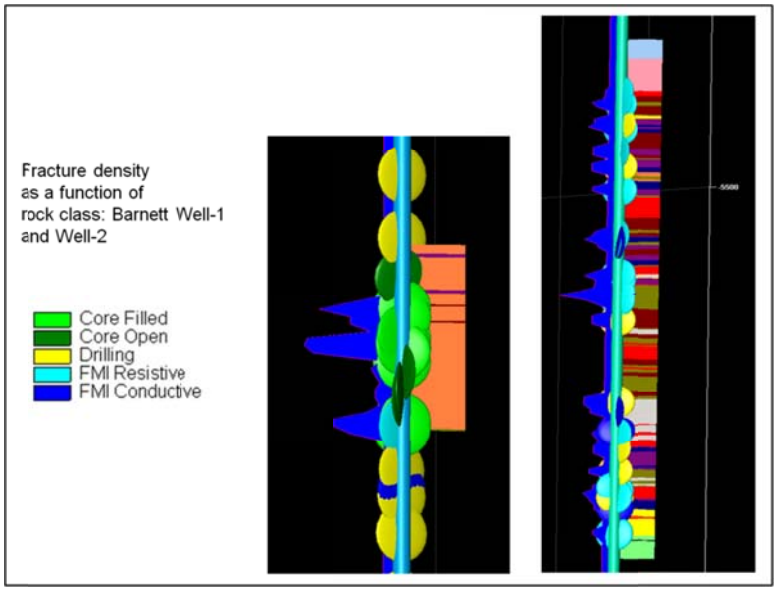

Figure 2.5 Fracture type and orientation overlaying the distribution of rock classes for Barnett Wells 1 and 2. The analysis is extended to the logged section.

Figure 2.1 shows results of fracture analysis on core. Core fracture analysis consists of evaluating all fractures observed in the core, including coring-induced fractures (e.g., petal, centerline and bedding partings) and natural fractures (e.g., mineralized, slickensides) are shown. The analysis also included the evaluation of interactions between mineralized fractures and the rock fabric, and between mineralized fractures and coring induced fractures. This allowed us to understand common geometric patterns between the various rock types. In addition, continuous measurements of strength along the core length were observed to be affected by the presence of fractures, open or mineralized, and the effect of fractures on these measurements allowed us to have a quantitative measure of their density per unit core length. Figure 2.2 and Figure 2.3 show examples of these results. Figure 2.2 shows an example of the partings that are seen in the core via continuous strength measurements and the difference in spacing between partings (e.g., weak bed boundaries) between rock facies. These are represented with the Olive and Brown colors in the figure. Figure 2.3 shows an evaluation of the fracture density per unit length in the Barnett shale (Well-1), conducted over the length of the cored section. These were integrated with borehole imaging results from FMI logs. In this example, we show FMI conductive fractures (Dark blue), FMI resistive fractures (Light blue), drilling induced fractures (Yellow), core open fractures (Dark green) and core filled fractures (Light green). Figure 2.4 shows the stereographic projection of fracture poles for the same core section. The approximate direction of the maximum horizontal stress is also shown. Figure 2.5 shows a graphical rendering of the type and orientation of the various fractures overlaying the distribution of HRA rock classes for Barnett Wells 1 and 2. Because of the different lithologic representation in these two wells, a comparison of the fracture distributions between rock types across wells could not be made. A significant higher number of

fractures (open and mineralized) were observed in Well 2 than in Well 1. A corresponding increase in the FMI detected fractures was also observed.

For the purposes of understanding the geometry of fracture networks and the relationship of these geometries with the rock fabric, evaluating fracture densities and fracture types is important for defining a criterion to select the most common fractures types. This is how the information was used. This, in turn, gave us information on geometrical interactions with the rock fabric and helped us developing simplified models of common fracture networks. The analysis was also considered for providing information on the effect of tectonic overprinting. This however, proved to be difficult.

In relation to tectonic overprinting, we analyzed the case of bending of geologic strata due to lateral tectonic deformation. Bending causes redistribution of strains within the formation and an associated redistribution of stresses. In locations where the change in stress (increase or decrease) exceeds the strength of the formation (compression or tension), failure occurs. Thus, estimates of local changes in strains associated to tectonic deformation, and the resulting changes in stresses, are critical to understanding fracture development. Geomechanical analysis of folded structures typically assumes isotropic and homogeneous rock behavior. Unfortunately, this is not an adequate representation for heterogeneous and anisotropic organic-rich mudstone systems (tight shales).

In tight shales, vertical and lateral heterogeneity develops as a result of depositional complexity and post-depositional diagenetic transformations. The result is the presence of spatial variability in properties. This has a strong influence on how the rock mass deforms, and more importantly, where the maximum and minimum stresses develop. For example, whereas in homogeneous media the location of high strains (extension and compression) is the same as the location of the maximum and minimum stresses (i.e., the material properties do not change with location), this is not the case in heterogeneous media.

Studies of folded structures (Burghardt et. al., 2012[1]) with various conditions of anisotropy and heterogeneity, including layering, indicate that understanding the distribution of rock properties within the structure is the most important condition to infer regions of high stress and potential presence of fractures. In complex, heterogeneous, distributions of properties, the distribution of fractures is difficult to predict. For example, zones with high strains are often located in regions of low stiffness and develop lower stresses than other regions with lower strains but higher stiffness. Similarly, the tectonic influence on fracturing is strongly affected by the distribution of material properties. Figure 2.6 summarizes these concepts.

[1] Burghardt, J, Suarez-Rivera, R., and C. Deenadayalu, Effect of Anisotropy and Heterogeneity on the Bending of Geologic Structures. Presented at the 46th US Rock Mechanics / Geomechanics Symposium held in Chicago, IL, USA, 24-27 June 2012.

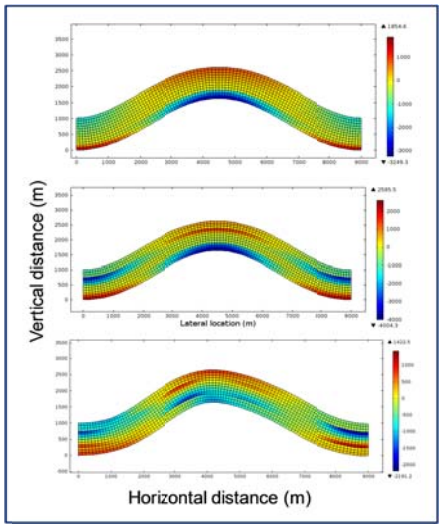

Figure 2.6 Influence of the spatial distribution of material properties on deformation and stress distribution. Three systems are considered: homogeneous, layered and heterogeneous. The regions colored red are local regions of high tensile stress and high propensity for tensile fracturing. Regions colored blue are local regions of high compression (from Burghardt et. al., 2012).

2.4 Fracture Network Geometries

Fracture geometries from core observations indicate branching at interfaces, veins or bed boundaries, and the emergence of closely spaced fracture propagation. Fracture geometries from mine-back observations indicate branching at interfaces, veins or bed boundaries, and the convergence of fractures into a single fracture. Figure 2.7 shows representative fracture geometries from core and mine back studies. Rock interfaces appear to play a strong role in the segmentation and branching of the propagating hydraulic fracturing. The branches that are generated at these interfaces are observed to propagate at relatively close proximity, for some distances, and eventually truncate or branch at the subsequent interface. These observations allowed us to propose four typical networks of fracture propagation. One of these type networks is the 'fish bone" structure (Figure 2.7). Here the secondary fractures emanate semi-perpendicular to the main fracture as this propagates. This structure can be complicated or simple, and is strongly dependent on the fabric of the rock. In the case of fracture propagation through a layered medium and perpendicular to the planes of weakness, the secondary fractures are associated to partings along the planes of weakness, and occur as the main fracture develops. Incidentally, this mechanism also promotes containment in the dominant fracture. Another typical network structure is the "fork fracture". This structure typically consists of a dominant fracture that reaches a plane of weakness and branches into secondary fractures that propagate in the direction of the original fracture. The complexity of this structure depends of the orientation of the interface, the number of branches that emanate from it and the distance between branches. Figure 2.7 shows a graphical description of these type networks. A simplified version of these fracture models are shown in Figure 2.8 .

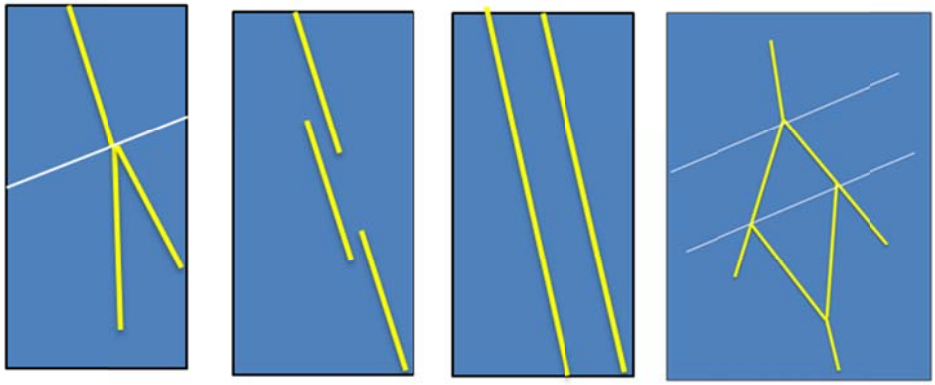

Figure 2.7 Typical fracture geometries and fracture interactions observed in core (left three images) and mine back experiments (right image).

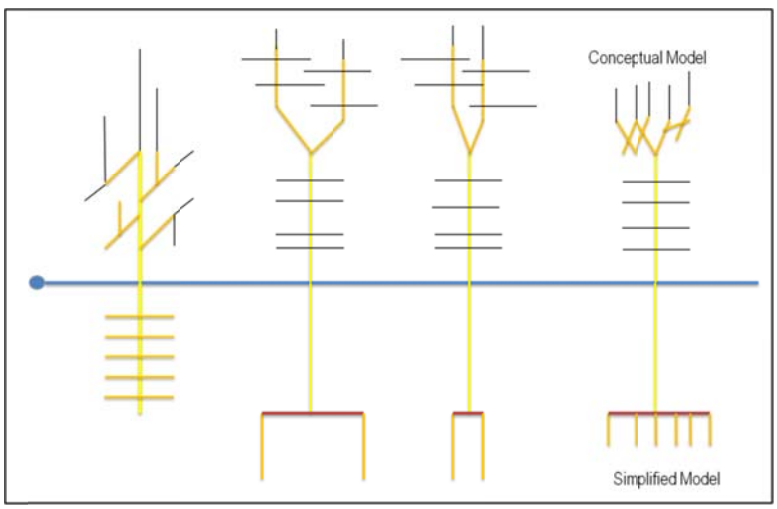

Figure 2.8 Conceptual fracture model (top) based on fracture observations on core, outcrops, and mine back experiments. Simplified fracture model (bottom) for numerical simulations.

The simplified geometrical models were used for numerical flow simulations using the Schumberger Eclipse reservoir simulator. The goal is to investigate reservoir production as a function of fracture geometry and as a function of fracture conductivity. The goal is also to understand single-phase gas flow through complex fracture geometries. The modeling is not intended as a history matching or forecasting model.

2.5 Created and Effective Surface Areas

For the purposes of this study, we estimated the created fracture surface area and the effective surface area based on fluid and proppant volume balance, field fracture design data, and microseismic measurements. We believe that the created surface area, during pumping, is reasonably well represented by the microseismic localization data. It is

understood, however, that during the fracturing process microseismic monitoring measures the combination of fracture generation as well as slippage failure of existing weak interfaces in the neighborhood of the fracture. These events, however, result from changes in stress and pore pressure during fracturing, and are currently perceived to occur close to the fractured region. That is, that the fracture geometry is not considerably altered by these events. In contrast, we believe that the effective surface area is defined during initial depressurization and early production, after the fracture connectors without proppant have closed, and after the fracture surface regions with low proppant concentration have also closed. As a result, the effective surface area is often considerably smaller than the created surface area. Comparison of field production with predictions of field production suggests that this could be decreased by as much as 90%.

After differentiating the created and effective surface areas, we also estimated realistic fracture network geometries based on fracture observations on core, outcrops and mine back studies. The goal was to obtain a reasonable representation of the fracture geometry and evaluate the effect of changes in fractured surface area and geometry on production. In addition to the above, production is also affected by matrix permeability, fracture conductivity, hydrocarbon filled porosity, pore pressure, hydrocarbon rheology, the effective surface for flow, and the fracture geometry. However, the effects of these parameters on production are, in general, better understood. In this study we focus on the role of effective fracture surface area and fracture geometry on hydrocarbon flow and stage production.

2.6 Effective Fracture Surface Area

Numerical simulations of reservoir production through a fracture, with single phase gas, were conducted to evaluate effective surface area requirements for attaining a desired production rate. Sensitivity analysis of input variables indicates that the reservoir pressure, reservoir permeability, and effective fracture surface area are the dominant input properties. By fixing reservoir pressure, to the normal pressure gradient of 0.45 psi/ft, it was possible to analyze effective surface area requirements, to attain a desired gas production rate, as a function of reservoir permeability alone. Results indicate a nonlinear increase in effective surface area with decreasing permeability.

Numerical modeling was conducted with production rate targets of 1 MMscf/D to 5 MMscf/D, and permeability ranges from 0.1 nD to 500 nD. Figure 2.9 summarizes the results from the modeling. For a given reservoir matrix permeability of 400 nano-Darcy, the figure indicates an effective surface area requirement of 5.8×10^6 ft^2 per well to achieve a 5MMscf/D production, and 1.0×10^6 ft^2 per well, to achieve a 1MMscf/D production. For wellbores with eighteen producing stages, and only six of these contributing to production, the required effective surface area and production rate per effective stage is 0.96×10^6 ft^2 and 0.83MMscf/D, for a well production of 5MMscf/D. Similarly, this requirement is 0.16×10^6 ft^2, and 0.16MMscf/D per stage, for a well production of 1MMscf/D. As a

reference, the effective surface area per stage corresponds to an equivalent fracture half-length of 1208.3 ft, and 200 ft respectively, on a 200 ft thick reservoir[2].

In comparison to these predictions, we considered typical volumes of slick water and sand per stage (e.g., 483,000 gal of slick water and 390,000 pounds of sand), and by assuming an average fracture width (0.15 in), we calculated a created fracture surface area of 10.7×10^6 ft^2, per stage, and 64.3×10^6 ft^2 for 6 stages. In relation to results presented in Figure 2.9, the above values indicate that significantly more fracture surface area is created than required for economic production, and the ratio of these two varies from 11:1 to 64:1. It is reasonable to assume that because of lack of containment and heterogeneous distribution of reservoir quality, a significant portion of the created surface area extends outside the reservoir. In addition, if the fracture geometry is complex, fracture branches have smaller fracture widths, and some of these are inaccessible by the proppant and become disconnected from the fractured system. It is also possible that some level of imbibition may take place, thus reducing the liquid volume available for creating surface area. Recent laboratory testing of water imbibition to various organic rich mudstones (Pagels et. al., 2011[3]) indicates an imbibition rate of approximately 650×10^{-6} $gal/ft^2/hr$. This corresponds to approximately 14,000 gal over 2 hours of pumping over an exposed surface area of 10.7×10^6 ft^2 and represents 2.9% of the total volume pumped.

The above calculations indicate that the bulk of the volume pumped contributes to the creation of surface area and that only a small fraction of this surface area contributes to production. It also suggests that while microseismic monitoring provides an indication of the total created surface area during pumping, it does not provide a measure of the effective surface area, in contact with good quality reservoir, and that remains open and conductive during production. The above calculations also indicate that the opportunity for improving the efficiency of the hydraulic fracturing process is high.

[2] In reality, the number of stages may be 10, 12, 18 or higher. However, the number of producing stages is approximately one third of this number. Thus, the above estimate with 6 effective stages is reasonable.

[3] Pagels, M, Willberg, D. M., Edelman, E., (2011) Chemo-mechanical Effects of Induced Fluid Invasion Into Ultralow Permeability Rocks, Abstract H21B 1091 presented at 2011 Fall Meeting, AGU, San Francisco, CA, USA, 5-9 Dec.

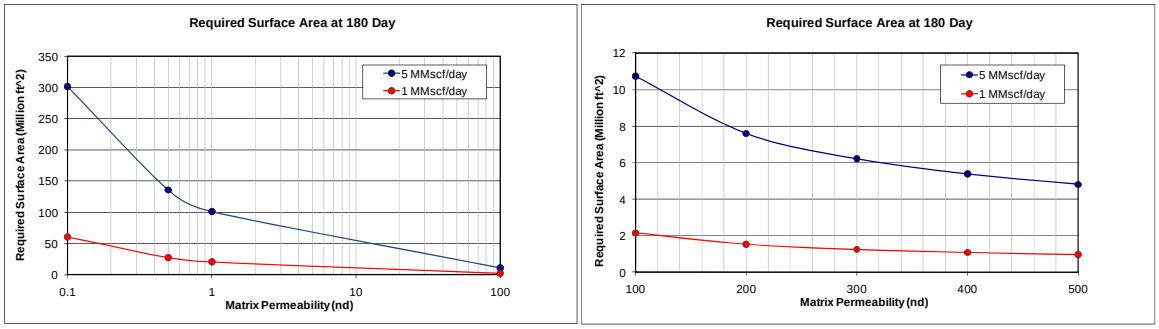

Figure 2.9 Required surface area, in million square feet, for production rates of 1 MMscf/D (red) and 5 MMscf/D (blue) for reservoir permeability in the range of 0.1 to 100 nano-Darcy (left) and 100 to 500 nano-Darcy (right). For example, production at 5 MMscf/D by a 400 nano-Darcy reservoir requires a surface area of 5.8×10^6 ft^2.

2.7 Numerical Simulations of Production through Complex Fractures

Numerical simulations of single-stage production with ideal gas, and single-phase flow were conducted in this study. Following the conceptual type geometries defined in the previous section, the reservoir height is 200 ft. The primary near-wellbore fracture is 200 ft high, 600 ft long (300 ft half length), has a surface area of 0.24×10^6 ft^2 and a fracture conductivity of 500 md-ft. This near-wellbore fracture is connected to a secondary set of fractures with a total surface area of approximately 12×10^6 ft^2. These secondary fractures are 200 ft high, 800 ft long (400 ft half length), and have a lower fracture conductivity of 0.2 md-ft. Tertiary and fourth tier fracture systems exist, however, have negligible fracture conductivity, and are ignored in these simulations. The reservoir matrix permeability is 400 nano Darcy, and the initial reservoir pressure is 5000 psi. These values correspond directly to measurements and field data from the Haynesville shale play.

The fracture surface area was calculated based on typical field pumping volumes of 11,500 Bbs slick water and 390,000 lbs of proppant. Table 2.1 shows the details of the proppant schedule, density and volume. The sand volume balance per stage is shown to be 2,375 ft^3. Given a total water volume of 11,500 bbl, the total volume of incompressible slurry in the fracture is 66,947 ft^3. The geometry represents a realistic field case where approximately 23% of the created surface area is effective surface area, 1% of the fracturing fluid volume is lost to imbibition and does not contribute to surface area generation, and 76% of the created surface area is disconnected or contacts rock units with poor reservoir quality rock.

Table 2.1 Sand volume balance per stage for numerical simulations

	Weight (1000 lb)	Density (gr/cc)	Volume (ft^3)
100 mesh sand	90	2.63	548
30/70 mesh sand	250	2.63	1522
30/50 mesh sand	50	2.63	304

Results of the simulation are provided in Figure 2.10 through Figure 2.17 . For comparison, a reference case of a primary near-wellbore fracture without secondary fractures is presented. All fracture case scenarios have identical surface area, identical distribution of fracture conductivity, in the primary and secondary fractures, and are contained in a medium with identical matrix permeability. The only difference is their geometry. Production results after 30 days to 2 years are investigated.

Figure 2.10 shows the geometrical configuration. As reference, the base case (Case 1) provides a representation of the near-wellbore, high conductivity, fracture with no secondary fractures. Case 2 and 3 are identical except for the larger separation between the secondary fractures in Case 2. Case 4 has a shorter but denser network of fractures. Figure 2.11 shows results after the initial 30 days of production. Here the red background color represents the original reservoir pressure and the decrease in reservoir pressure is presented as changes in colors from red (representing virgin reservoir pressure) to dark blue (representing full depletion). Near fracture depletion and subsequent interference, between the areas being drained between secondary fractures, are observed. Figure 2.12 shows results after 90 days and Figure 2.13 after 180 days. In all these cases, depletion occurs near the fracture face and fracture interaction at the secondary fracture level is seen in all cases except for Case 3.

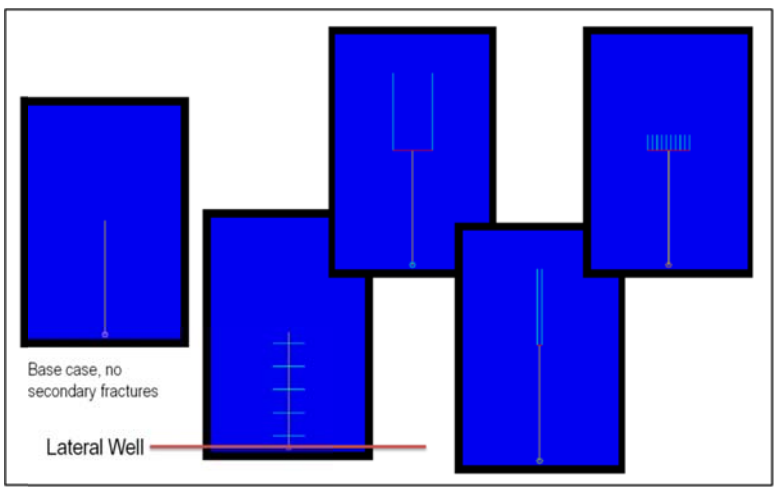

Figure 2.10 Geometrical model. Except for the base case, all fracture case scenarios have identical surface area, identical distribution of fracture conductivity, in the primary and secondary fractures, and are contained in a medium with identical matrix permeability. The only difference is their geometry. Production results after 30 days to 2 years are investigated.

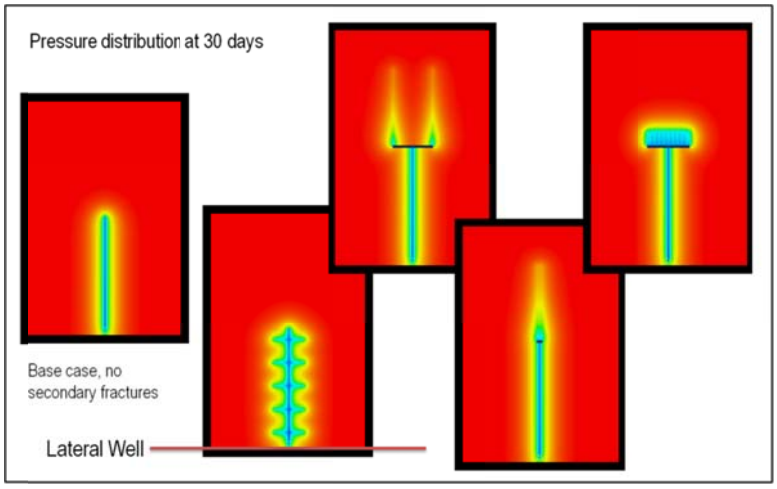

Figure 2.11 Results after the initial 30 days of production. The red background color represents the original reservoir pressure and the decrease in reservoir pressure is presented as changes in colors from red (representing virgin reservoir pressure) to dark blue (representing full depletion).

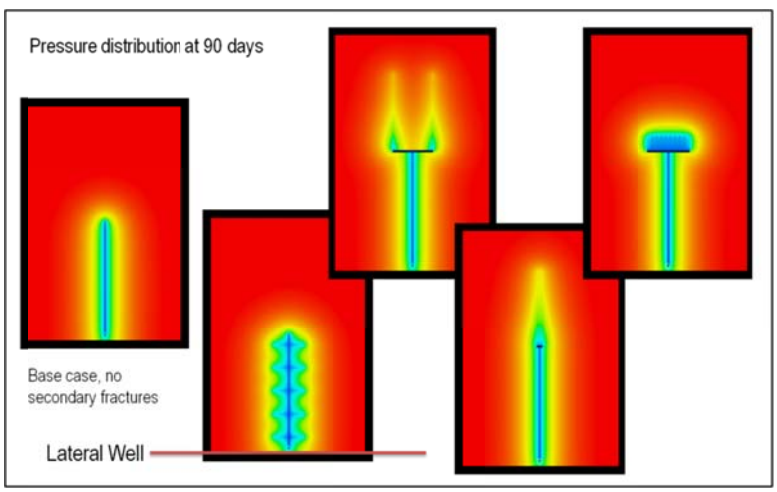

Figure 2.12 Results after 90 days.

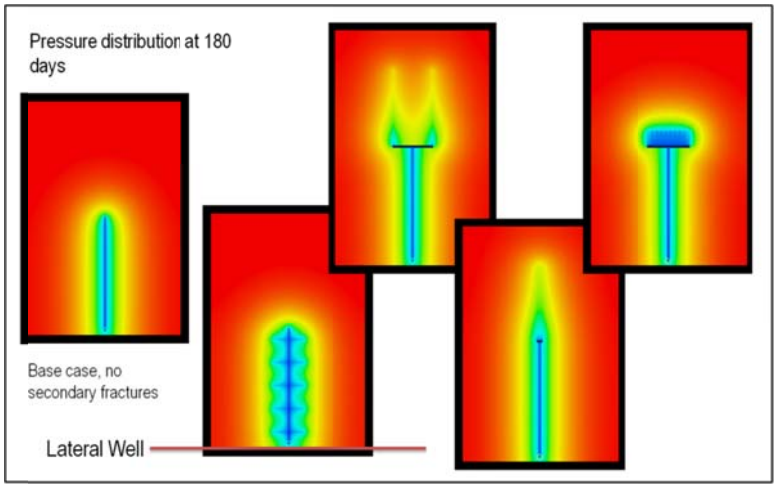

Figure 2.13 Results after 180 days. The cumulative production in each of these cases is remarkably different from the others. These effects are initially observed via changes after 30 to 180 days production.

Pressure depletion and net production, in these simulations, are affected by the fracture spacing and the geometry of the fracture network. Thus, despite their identical surface area, distribution of fracture conductivity and matrix permeability, the cumulative production in each of these cases is remarkably different from the others. These effects are initially observed via changes after 30 to 180 days production. However, these become considerably more pronounced after 1 or 2 years of production (Figure 2.14 and Figure 2.15). After 2 years (Figure 2.15) it is visually apparent that some fracture geometries results in a more uniform depletion and consequently higher cumulative production. Others exhibit localized depletion and consequent lower cumulative production. Figure 2.16 compares the cumulative production from all the cases. Here it is clear that the geometry with highest initial production (e.g., "fish bone" fracture) is overcome by all other geometries in the long-term. The geometry with the highest cumulative production is the "fork fracture' with long and well spaced secondary fractures. The other "fork fractures' produce better than the 'fish fracture' but not as well. It is also seen that the shortest the length of the secondary fractures, the lesser the long term benefit.

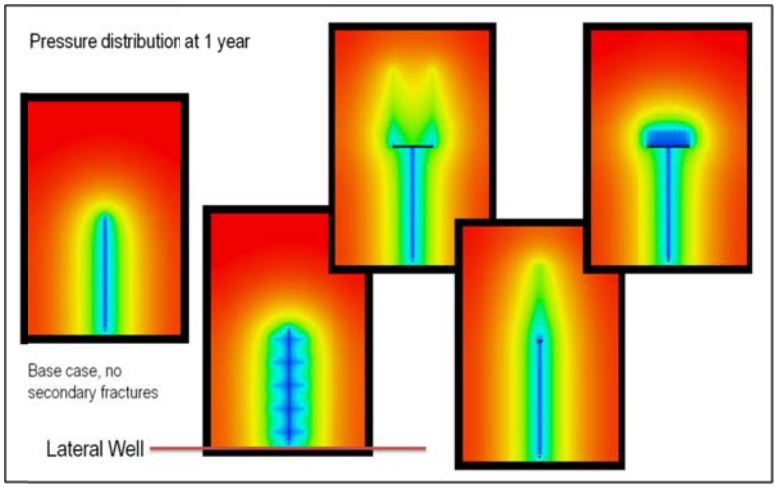

Figure 2.14 Results after one year. The cumulative production in each of these cases is remarkably different from the others. These results become considerably more pronounced after 1 or 2 years of production.

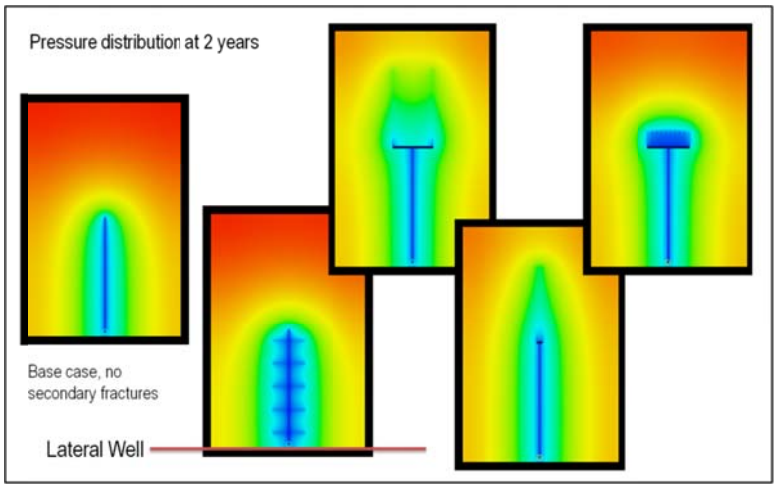

Figure 2.15 Results after two years. Some fracture geometries results in a more uniform depletion and consequently higher cumulative production. Others exhibit localized depletion and consequent lower cumulative production.

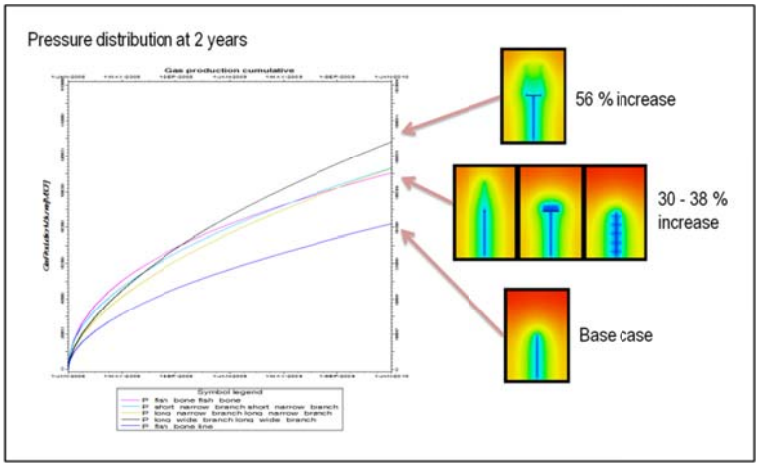

Figure 2.16 Cumulative production from all cases. The geometry with the highest cumulative production is the "fork fracture' with long and well spaced secondary fractures.

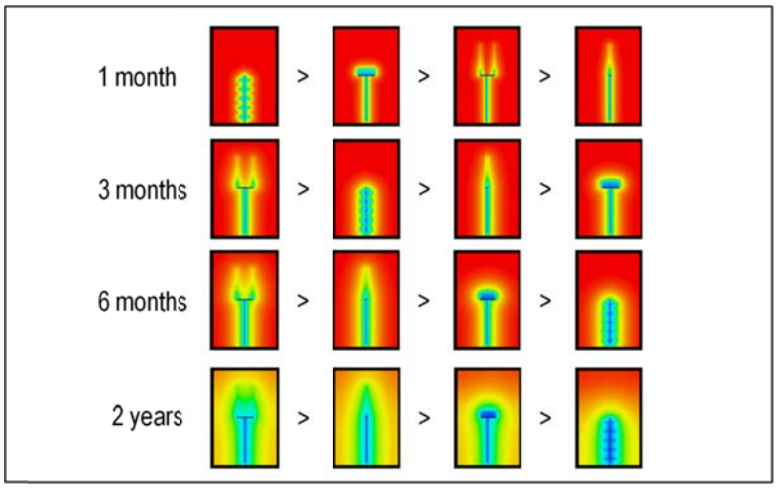

Figure 2.17 This figure shows the hierarchical order in production, from best (left) to worst (right) and from early production (top) to long-term production (bottom).

Figure 2.17 shows a matrix display of the hierarchical order in production, from best (left) to worst (right) and from early production (top) to long-term production (bottom). The figure shows that the "fish bone' fracture starts as the most productive and quickly (after six months) becomes the worst. The Figure also shows how the "fork fractures" with long secondary fractures start with the lowest production and become the geometries with best and second best production in the long-term.

Contrary to anticipated concepts based on analytical models, indicating that production is predominantly proportional to the square root of permeability and the surface area, these results show conclusively that the geometrical configuration of the effective surface area makes a considerable difference to production.

2.8 Near-Wellbore Flow Restrictions by Convergence

In addition to loss of fracture conductivity and loss of fracture area, the near-wellbore region is subjected to convergent flow and consequently to flow restrictions associated to convergent flow. In this section, we present additional numerical simulations that evaluate the magnitude of loss of productivity by convergence in horizontal wellbores. This was done using 3D models.

Figure 2.18 shows the details of the geometric model, including the grid design to capture small changes in pressure near the wellbore region and along the plane of the hydraulic fracture. Figure 2.19 show results of the simulation. Notice that the model includes the wellbore and a single stage fracture.

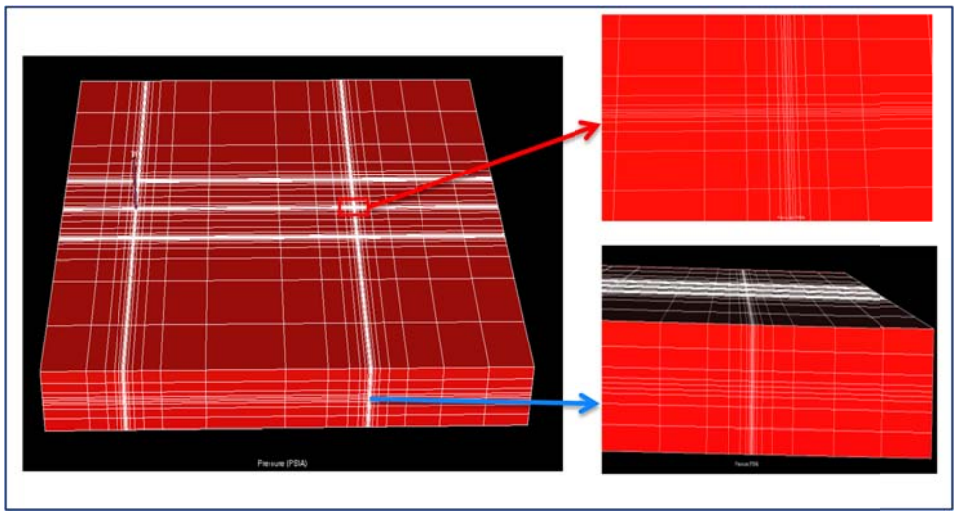

Figure 2.18 3D grid model showing the increased grid concentration along the locations of the wellbore and the plane of the fracture.

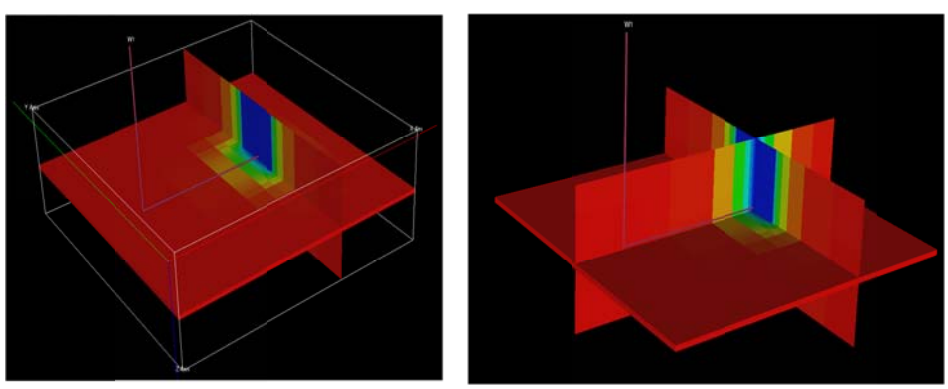

Figure 2.19 3D simulations including the wellbore, a fracture stage, and the associated depletion from a single fracture, during production, and including convergent flow at the wellbore.

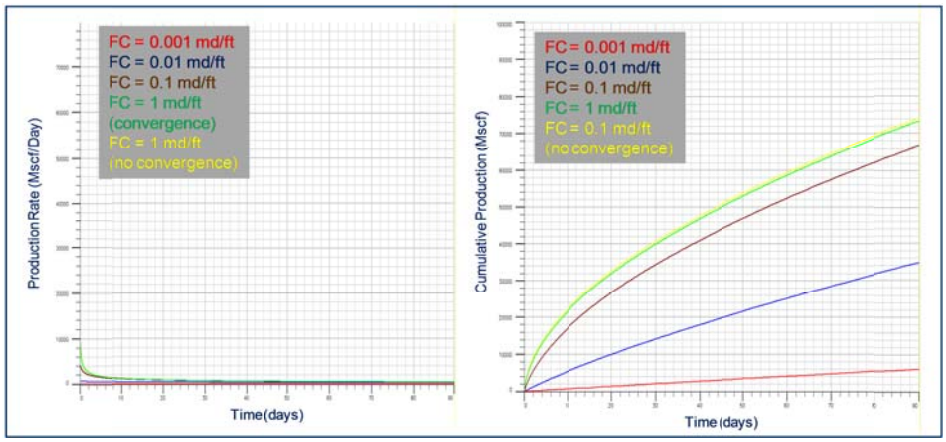

Figure 2.20 Results indicate that well cumulative production and production rate are more sensitive to the overall fracture conductivity than to flow restrictions associated to near-wellbore convergence. In the above, the green and yellow lines show comparisons with and without convergence flow. Differences between the two are small.

Figure 2.20 summarizes the results from numerical modeling. Results indicate that the cumulative production and production rate are more sensitive to changes in fracture conductivity than to flow restrictions associated to near-wellbore convergence. In the Figure, the green and yellow lines show the differences between identical simulations, except for a case where the convergent flow is eliminated (yellow). The differences between the two cases is negligibly small.

2.9 Summary

Typical fracture networks common to the Barnett, Marcellus and Haynesville plays were defined. Four types were selected, based on fracture geometries observed on core and published observations on mine back fracture experiments. One of these is representative of a "fish bone" fracture network, where the secondary fractures are distributed along the dominant fracture and oriented relatively perpendicular to this. The others are "fork" fracture networks with secondary fractures parallel to the dominant fracture and step overs creating the bifurcation of a main fracture into two separate fractures. Three realizations of "fork" fracture networks were proposed with small separation and large separation, and with small and large secondary fracture length. Third tier and fourth tier fractures are undoubtedly present. However, these were ignored in the model because of their negligibly small fracture conductivity and minor impact to production.

Numerical simulations of stage production using the four common types of fracture networks were conducted, using measured properties of matrix permeability and fracture conductivities and using field data for the Haynesville shale. The numerical software Eclipse was used for these evaluation. Results show that the fracture geometry (i.e., the

geometrical configuration of the effective surface area) makes a considerable difference to production. This is contrary to anticipated concepts, based on analytical models, indicating that production is primarily proportional to the square root of permeability and the surface area, and independent of fracture geometry.

Numerical modeling results provided input to evaluate the effect of surface area and fracture geometry on production characteristic of tight shale reservoir systems (Marcellus, Haynesville, Barnett). For example, results show that reservoirs that promote the preferential generation of "fish bone" fracture networks provide higher initial production but lower long-term production and lower total recovery. Conversely, reservoirs that promote the preferential generation of "fork" fracture networks with long secondary fractures and wide spacing, provide lower initial production and higher long-term production and higher total recovery.

3 FRACTURE CONDUCTIVITY OF UN-PROPPED FRATURES ON CORE

3.1 Introduction

The objective of this section is to evaluate theoretically and experimentally the conductivity of un-propped fractures of the representative shale lithotypes.

Components of this effort are as follows:

(i) Measure the fracture surface area, Brinell hardness, continuous scratch test, and fracture conductivity to water and gas, on fractured core samples without proppant, under reasonable conditions of shear displacement, and as a function of stress.

(ii) Measure the fracture surface area, Brinell hardness, continuous scratch test, and fracture conductivity to water and gas, on fractured core samples without proppant, under a given condition of shear displacement (obtained from the previous section - i), at in-situ stress and elevated temperature, and with prolonged loading and fluid exposure.

3.2 Testing Matrix

The matrix of testing carried out is shown in Table 3.1. The basic variables were:

- **Shale Play:** Barnett, Haynesville and Marcellus.
- **Reservoir Quality:** Samples were described as "best, good, fair, and poor," reservoir quality based on criteria defined in Section 1.
- **Surface Roughness:** Three qualitatively comparable surfaces were prepared. These included saw-cut, samples split by Brazilian loading (core loaded across its axis) and samples mechanically split by wedge loading.
- **Temperature:** Barnett samples were run at temperatures of 70°F. One Barnett sample with best reservoir quality was run at 120°F. All other samples from other formations were tested at nominally ambient temperature (~70°F). Also, additional three tests, one per formation, were performed at 240°F
- **Flowing Fluid:** Some samples were tested using nitrogen as the flowing fluid. Synthetic formation water was also used. The composition of this is shown in Table 3.2.
- **Fluid Exposure:** A restricted number of sample surfaces were exposed to water and conductivity testing was subsequently undertaken.
- **Long-Term Measurements:** One sample was allowed to creep at a closure stress of 5,000 psi. This implies that the closure stress was applied and held constant for an extended time with periodic flow measurements.

- **Shear Displacement:** A one-mm lateral displacement was made perpendicular to bedding planes and conductivity measurements were repeated. The motivation was to determine if asperity override had a substantial impact and - even more important - if the asperities hold up with increasing effective normal stress consistent with drawdown or depletion. In other words, can substantial and permanent conductivity result from self-propping?

Table 3.1 Testing Matrix for Un-propped Samples

Formation	Sample Identifier	Reservoir Quality	Surface [4]	Temperature (°)	Flowing Fluid	Exposure (No Data)	Creep
Barnett	01	Best	SC, NA	120	Water,N_2		5000 psi
	02	Good	SC,NA,BR	70	Water, N_2		-
	03	Fair	SC,NA	70	Water, N_2		-
	04	Poor	SC,NA	70,240	Water, N_2		-
Haynesville	05	Good	SC,NA	70	Water, N_2		-
	06	Fair	SC,NA	70,240	Water, N_2		-
	07	Poor	SC,NA	70	Water, N_2		-
Marcellus	09	Best	SC,NA	70,240	Water, N_2		-
	10	Good	SC,NA	70	Water, N_2		-

Table 3.2 Properties of Synthetic Water

Component	Concentration (mg/l)
Calcium Chloride Dihydrate	451.17
Magnesium Chloride Hexahydrate	175.63
Potassium Chloride	17.16
Sodium Sulphate	337.1
Sodium Bicarbonate	239.64

The data for the un-propped measurements are included in Appendix 2.

3.3 Observations on Experimental Protocol

- **Flow Direction:** The flow in the experiments is vertical. Thus, for the small pressure drops encountered, at least when water or oil is flowed, the transducers are tared. However, in the cases where reverse flow was carried out, the calibration to accommodate for the gravity effects is no longer needed.

[4] SC is saw cut, NA is natural asperity, BR is Brazilian

- **Calibration:** Calibration of the differential pressure transducers was carried out using pressure standards specific to the pressure range of the transducer being calibrated. Three separate differential pressure transducers with the following full scale pressure ranges, 0-3 psi, 0-20 psi and 0-200 psi, were used during the experiments. An inclined oil manometer standard (using Meriam oil), was used to calibrate the 0-3 psi transducer. An upright mercury manometer standard was used to calibrate the 0-20 psi transducer. And, a rotating hydraulic 'dead weight' standard was used to calibrate the 0-200 psi transducer. An example of typical calibration data are shown in Appendix 3. As a result the very small pressure drops, accurate calibration is essential for successful experimentation.
- **Resolution and Accuracy of Transducers:** Some measurements were found to be less than 0.5 percent of full scale of the differential pressure transducer used. Those data should be considered with caution.
- **Viscosity:** 1 cP was used for all water measurements. This was changed to 0.56 cP for measurements at 120°F.
- **Flow Length:** The sample flow length was usually less than the sample diameter. Entrance effects might be an issue. However, the particle Reynolds' numbers for the flow were verified to be small such that the end effects are also small.
- **Flow Rate and Flow Volume:** The flow rate for liquid was on the order of 0.1 ml/minute. The flow rate for gas measured was of the order of 27 cm^3/min to 15 cm^3/min. This was observed while testing Barnett good reservoir quality sample. Typical flow times at individual closure stresses were on the order of 5 minutes. For a liquid, this suggests 0.5 ml of flow at each stage.
- **Baseline Testing:** Flow through steel blanks was undertaken. The results for two smooth steel halves in contact (mimicking the saw cut situation) are shown in Figure 3.1. Figure 3.2 shows flow for a sample with shims to create a finite, open aperture. An analytical reality check on the calculated conductivity between the two steel billets was conducted. Appendix 4 shows the derivation for a lubrication theory relationship that gives the conductivity of two smooth, parallel plates with no flow alterations due to boundary conditions, for laminar flow of a Newtonian fluid like water. Figure 3.1 shows conductivity measured in the steel billets versus hydraulic aperture in mm, as well as predictions from lubrication theory. Any deviations suggest unaccounted friction or deviations from the simple calibration experiment.

$$kw = \frac{w^3}{12} m^3$$

$$kw = 2.79 \times 10^{14} w^3 \ md - ft$$

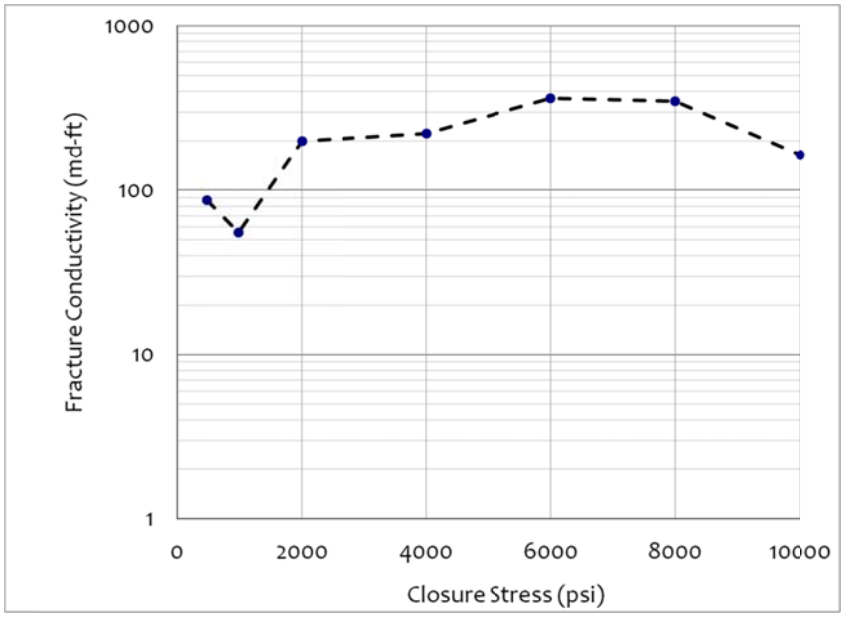

Figure 3.1 Conductivity data for flow through two steel halves in contact.

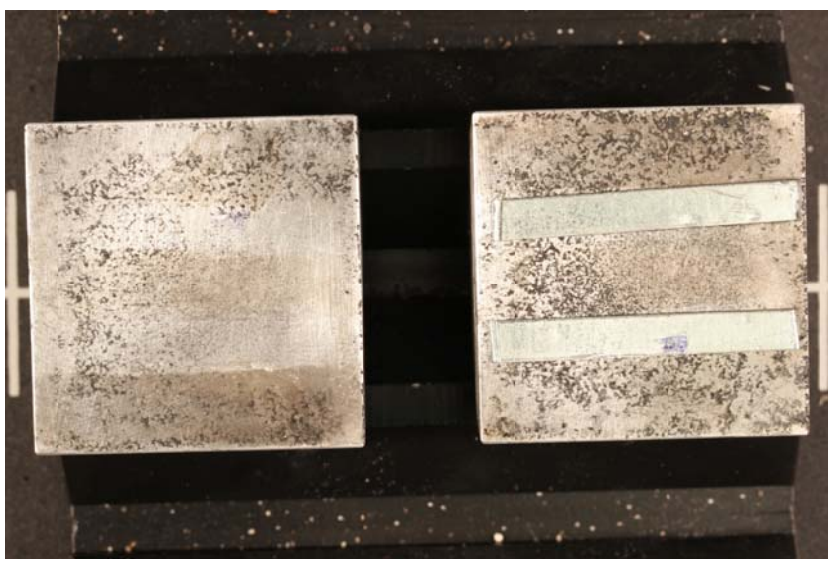

Figure 3.2 Baseline steel billets separated by two shims. The steel plates have some degree of roughness.

3.4 Comparisons

The mechanically split and Brazilian data are not sufficiently reliable to draw conclusions. There is substantial fluctuation at low confining pressure that can be directly correlated with sample quality. Figure 3.3 is a photograph of a typical split sample. Brazil tensile failure, and the fragile nature of the planes of weakness during handing and preparation, led to bedding plane parting (or other fracturing) that affected the measurements at low confining pressure. Sometimes even at high confining stress alternative flow paths were open. This problem was exacerbated by the small flow rates, which sought out these preferential, alternative flow paths. Figure 3.4 is a schematic illustrating how substantial conductivity correlates with bedding plane parting. Figure 3.5 through Figure 3.7 show annotated data for liquid as the flowing fluid. Figure 3.8 through Figure 3.10 are for gas.

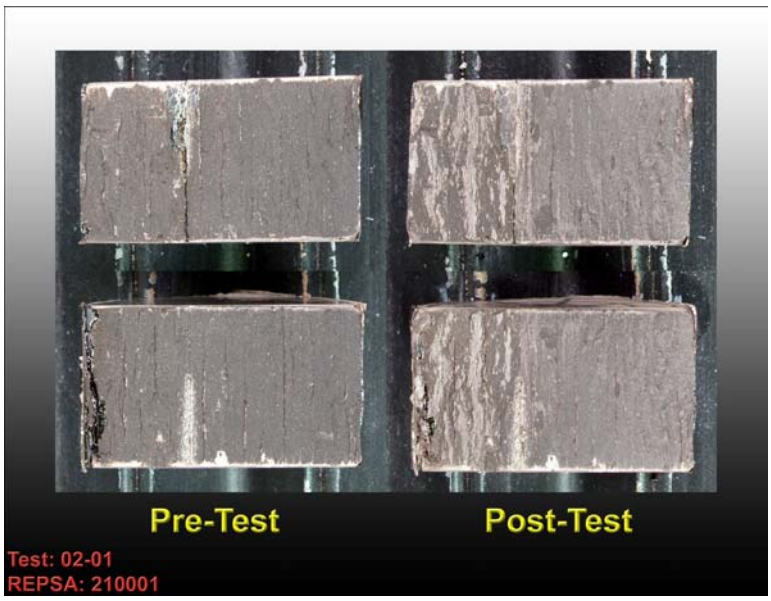

Figure 3.3 Photograph of a mechanically split sample showing bedding plane fractures that accepted the very small amounts of fluid injected at low rate and without backpressure. These fractures are usually a consequence of unloading during sample recovery and desiccation.

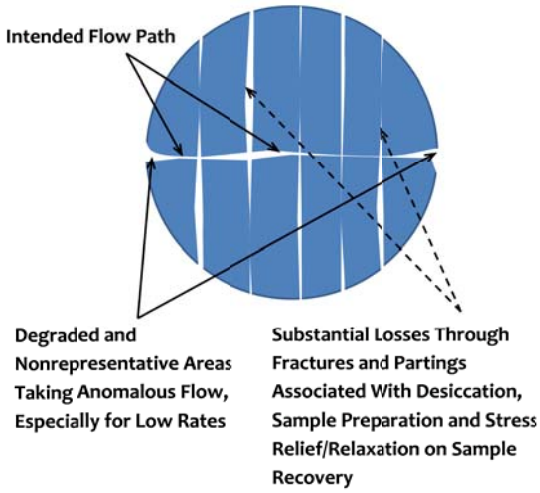

Figure 3.4 Schematic of laboratory flow paths showing the consequences of stress-relief and sample preparation difficulties.

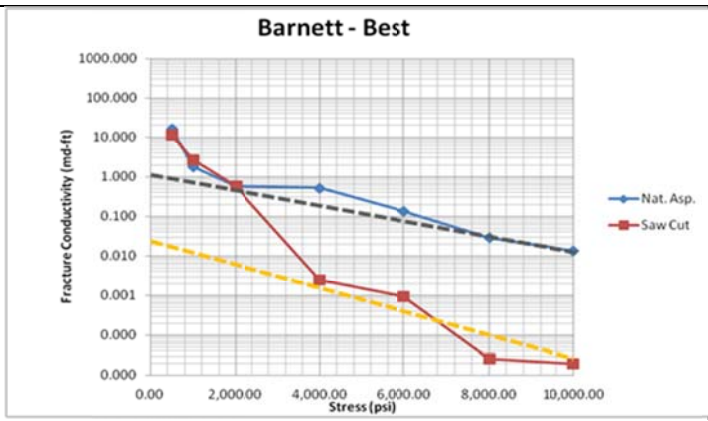

Figure 6.5a. This is a Barnett, best reservoir quality sample with water as the flowing fluid. The saw cut fracture conductivity decayed faster than the natural asperities fracture conductivity. Fracture conductivities for the natural asperities decreases by 2 decades and that for the smooth surfaces by 3 decades, for an increase in closure stress of 10,000 psi. Conductivities below 0.01 mD/ft may be too low to support flow

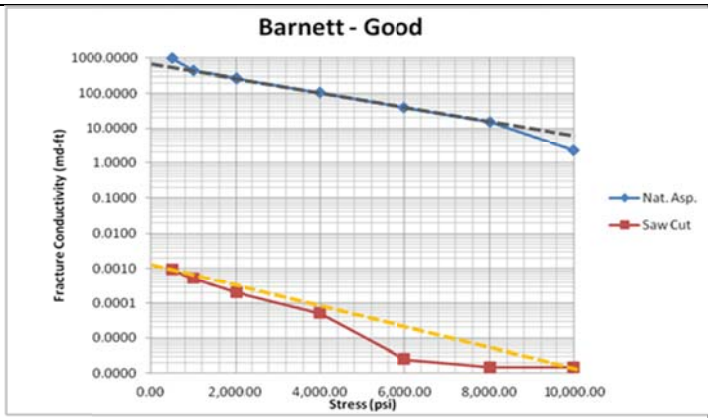

Figure 6.5b. This is a Barnett, good reservoir quality sample with water as the flowing fluid. The fracture conductivity for the natural asperities sample at 2000 psi is 300 times higher than that for the best Barnett sample, and the quality of the data is suspect. However, the relative trends are strongly related (i.e., 2 decades change for natural asperities and 3 decades change saw cut surfaces, for an increase in closure stress of 10,000 psi).

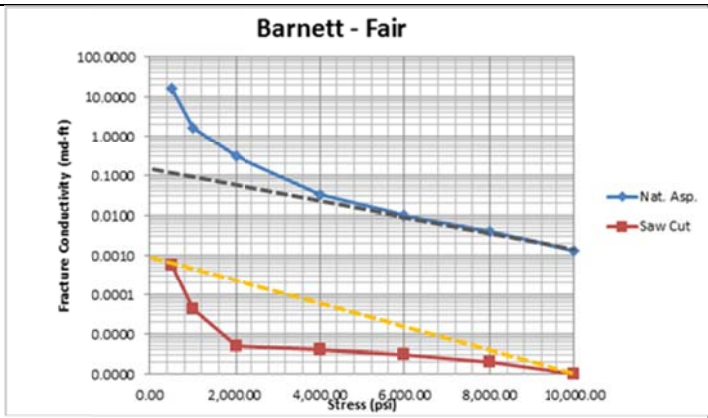

Figure 6.5c. This is a Barnett, fair reservoir quality sample with water as the flowing fluid. These are relatively similar to the data for the best and the poor reservoir qualities. As above, the straight lines represent changes in fracture conductivity by 2 decades (natural asperities) and 3 decades (saw cut surfaces), for an increase in closure stress of 10,000 psi. The overall range is similar, but large differences occur at low closure stress values

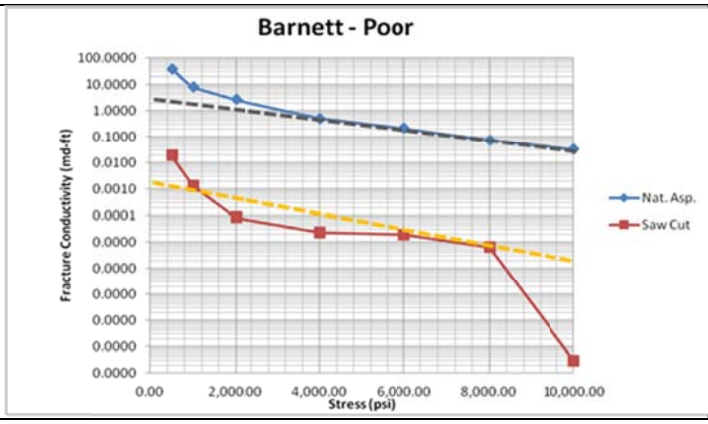

Figure 6.5d. This is a Barnett, poor reservoir quality sample with water as the flowing fluid. As above, the straight lines represent changes in fracture conductivity by 2 decades (natural asperities) and 3 decades (saw cut surfaces), for an increase in closure stress of 10,000 psi. This indicates high overall consistency in the measurements, with small changes at the low closure stress values.

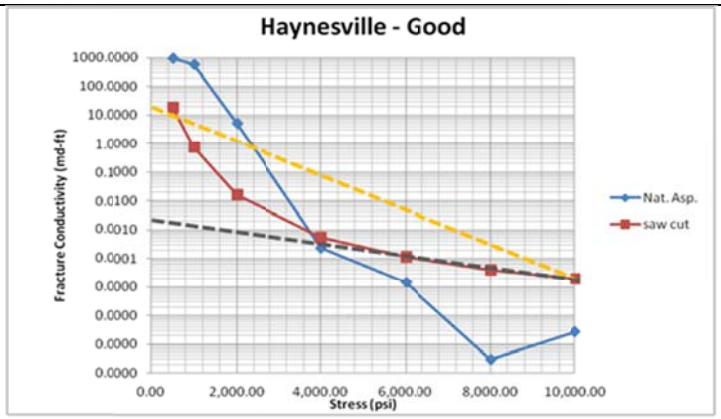	Figure 6.6a. This is a Haynesville, good reservoir quality sample with <u>water</u> as the flowing fluid. The high values of the low confining pressure data for the natural asperities sample are troubling and the data should be used with caution. As in the previous figures, the straight lines represent changes in fracture conductivity by 2 decades (natural asperities) and 3 decades (saw cut surfaces), for an increase in closure stress of 10,000 psi.
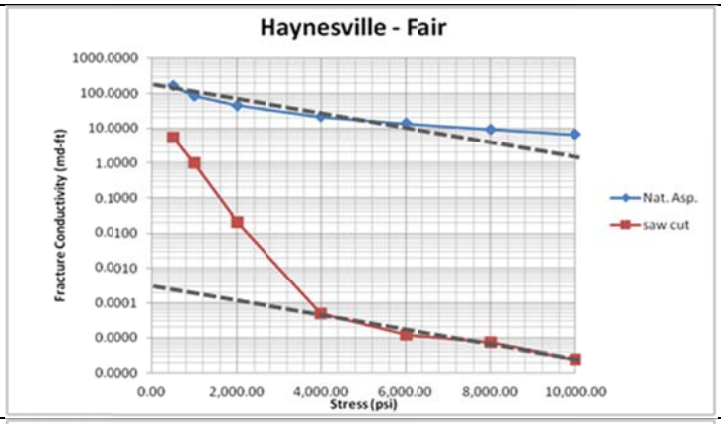	Figure 6.6b. This is a Haynesville, fair reservoir quality sample with <u>water</u> as the flowing fluid. The relatively constant apparent conductivity with confining pressure may suggest supplementary flow paths, other than the fracture, that are not sensitive to closure stress, Thus, the data for the natural asperities should be used with caution
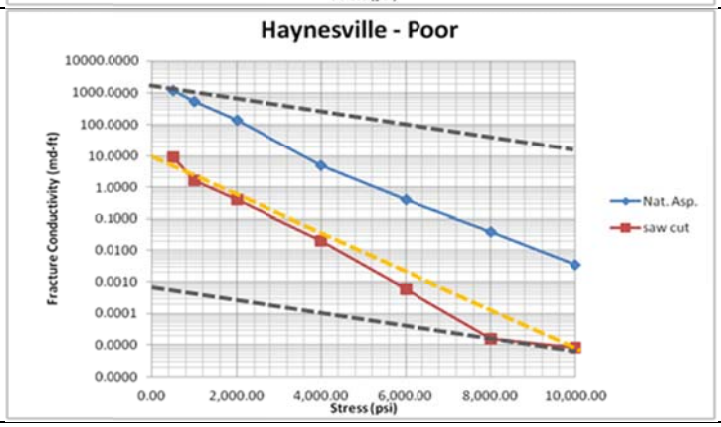	Figure 6.6c. This is a Haynesville, poor reservoir quality sample with <u>water</u> as the flowing fluid. The high values of the low confining pressure data for the natural asperities sample are troubling and the data should be used with caution. In relation to the straight line trend, the decrease in fracture conductivity with stress is considerably larger than that seen in the Barnett samples.

Figure 3.6 Haynesville test results with water.

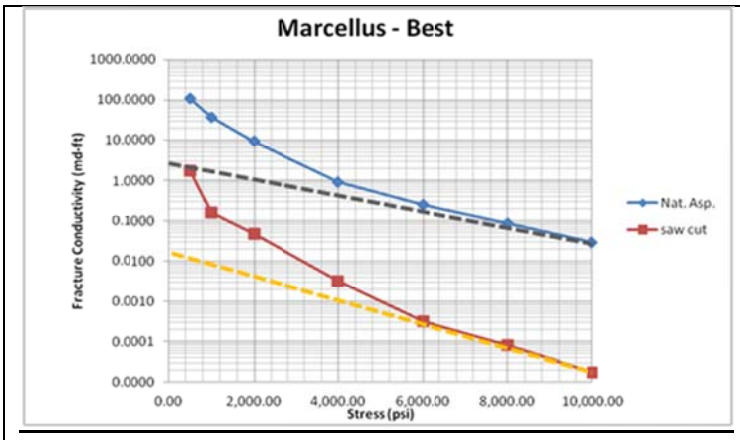

Figure 6.7a. This is a Marcellus, best reservoir quality sample with water as the flowing fluid. As in the previous figures, the straight lines represent changes in fracture conductivity by 2 decades (natural asperities) and 3 decades (saw cut surfaces), for an increase in closure stress of 10,000 psi. At high closure stress, the decrease in fracture conductivity is consistent with the Barnett data.

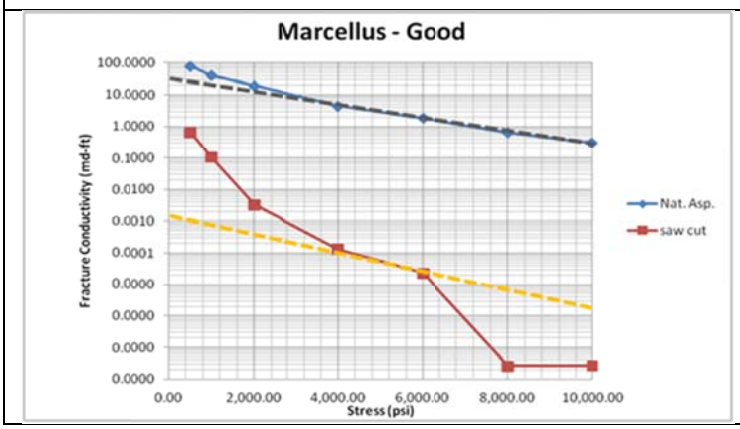

Figure 6.7b. This is a Marcellus, good reservoir quality sample with water as the flowing fluid. At high closure stress, the decrease in fracture conductivity is consistent with the Barnett data. For the saw cut measurements, the trend suggest that the last two points, measured at 8000 and 10,000 psi, may be affected by a sudden conformance between the two surfaces. A similar behavior is observed on other samples at high temperatures

Figure 3.7 Marcellus test results with water.

- **Fracture conductivity to water (Smooth surfaces):** Conductivities below 0.01mD/ft may be too low to support flow. If correct this means that for closure pressures above 2000 psi, smooth surfaces (saw cut) do not contribute to flow. For these surfaces, the rate of decrease in fracture conductivity with stress is 3 decades per 10,000 psi (or approximately 1 decade per 3,300 psi). This rate is consistent, at high closure stress, for all samples tested and is independent of rock type (Figure 3.11). The rock dependence becomes more evident at low closure stress. Here, the Haynesville is more stress sensitive than the Marcellus and the Barnett. These results indicate that un-propped secondary and tertiary fractures should be excluded from production calculations.
- **Fracture conductivity to water (Rough surfaces):** When the fractures are supported by their own asperities, the change of fracture conductivity with stress is reduced to approximately 2 decades per 10,000 psi (or approximately 1 decade per 5000 psi). This rate of decrease is reasonably consistent for all samples tested and is independent of rock type (Figure 6.12). This is particularly true at high closure stress. In most cases, the fracture conductivity remains above the limiting value of 0.01 mD/ft. This indicates that rough fractures can contribute to fluid flow even at high closure stress.

The data for gas flow are included in the following figures.

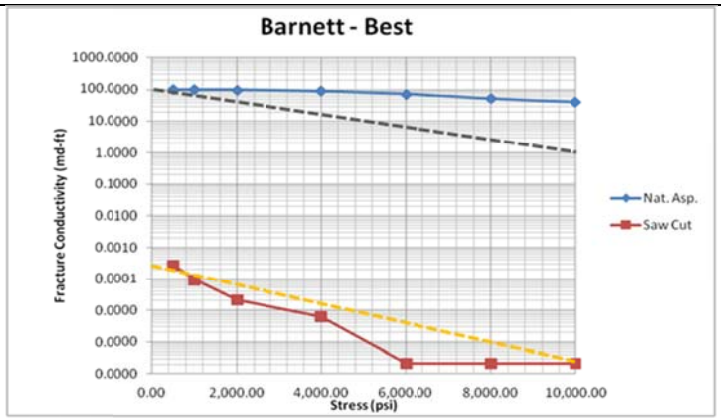	Figure 6.8a. This is a Barnett, best reservoir quality sample with gas as the flowing fluid. The lack of change in fracture conductivity with stress, for the Natural Asperities test, almost certainly suggests an open path that is not sensitive to confining pressure. These data should be ignored. The straight lines represent changes in fracture conductivity by 2 decades (natural asperities) and 3 decades (saw cut surfaces), over 10,000 psi.
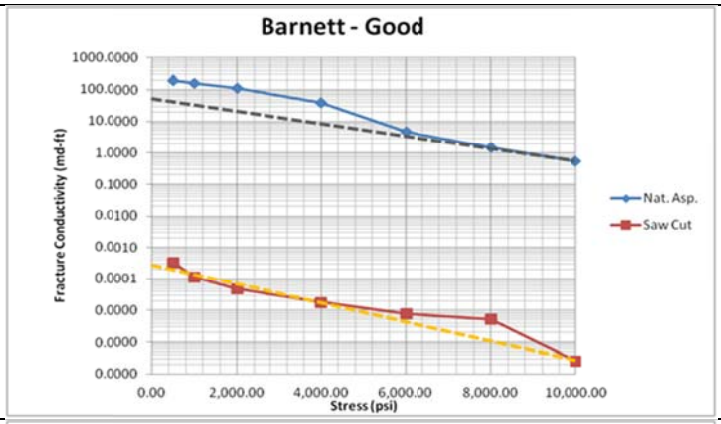	Figure 6.8b. This is a Barnett, good reservoir quality sample with gas as the flowing fluid. As in the previous, the straight lines represent changes in fracture conductivity by 2 decades (natural asperities) and 3 decades (saw cut surfaces), over 10,000 psi. A strong consistency in the overall results is noticed.
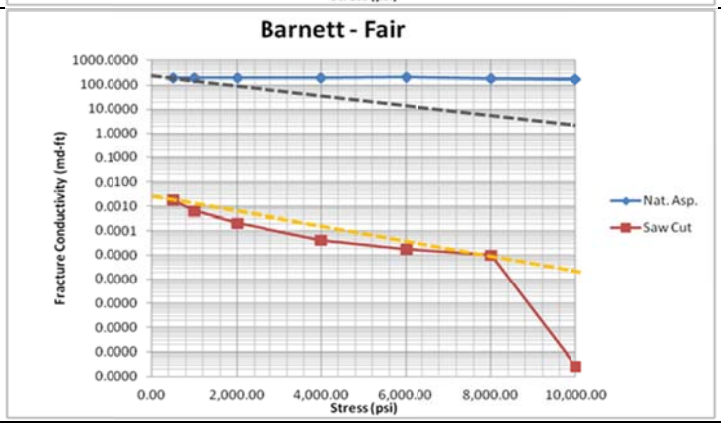	Figure 6.8c. This is a Barnett, fair reservoir quality sample with gas as the flowing fluid. The lack of change in fracture conductivity with stress, for the natural asperities test, almost certainly suggests an open path that is not sensitive to confining pressure. These data should be ignored. The saw cut data is consistent with the previous measurements.

Figure 3.8 Barnett test results with gas.

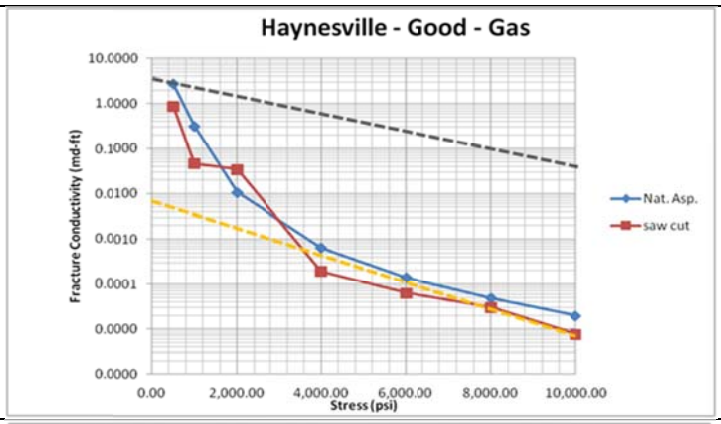

Figure 6.9a. This is a Haynesville, good reservoir quality sample with gas as the flowing fluid. These data seem reasonable in magnitude and decay. They are also similar to the data for liquid for the equivalent sample. The close agreement between the natural asperities and the saw cut is problematic and may require further verification. The 3 decade decay for the natural asperity surface is consistent with other samples.

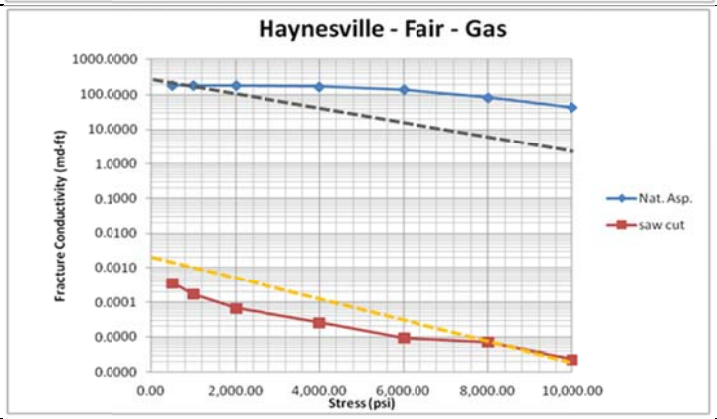

Figure 6.9b. This is a Haynesville, fair reservoir quality sample with gas as the flowing fluid. The lack of change in fracture conductivity with stress, for the natural asperities test, is problematic. These data should be ignored. The straight lines represent changes in fracture conductivity by 2 decades (natural asperities) and 3 decades (saw cut surfaces), over 10,000 psi.

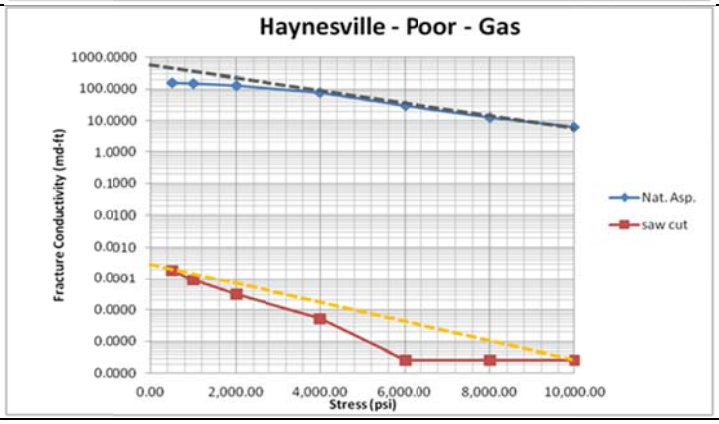

Figure 6.9c. This is a Haynesville, poor reservoir quality sample with gas as the flowing fluid. The change in fracture conductivity with stress, for the Natural asperities test and the saw cut surface is in line with other samples.

Figure 3.9 Haynesville test results with gas.

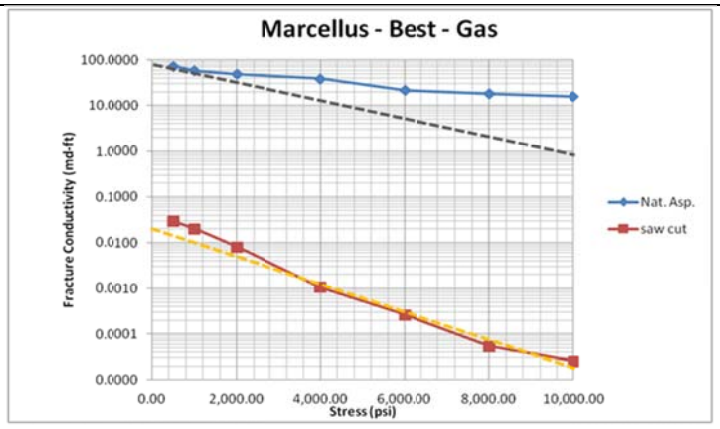

Figure 6.10a. This is a Marcellus, best reservoir quality sample with gas as the flowing fluid. The lack of change in fracture conductivity with stress, for the natural asperities test, is problematic. These data should be ignored. The straight lines represent changes in fracture conductivity by 2 decades (natural asperities) and 3 decades (saw cut surfaces), over 10,000 psi. The latter is consistent with previous results.

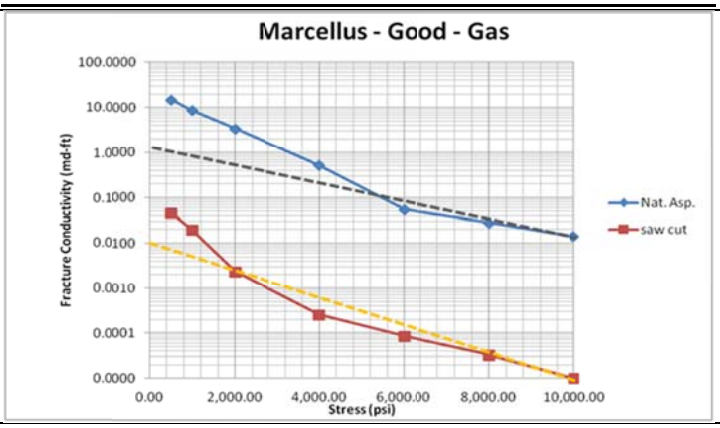

Figure 6.10b. This is a Marcellus, good reservoir quality sample with gas as the flowing fluid. The data is consistent with previous measurements on other samples.

Figure 3.10 Marcellus test results with gas.

- **Fracture conductivity to gas (Smooth surfaces):** Assuming the same limit of 0.01mD/ft, fracture conductivities to gas on smooth (saw cut) surfaces are too low for fluid flow at all stress levels. These results indicate that un-propped secondary and tertiary fractures should be excluded from production calculations. However, this limiting value of 0.01 mD/ft should be verified by comparison to field studies of numerical simulations. The change in fracture conductivity with stress is approximately 3 decades per 10,000 psi (or one decade per 3300 psi).
- **Fracture conductivity to gas (Rough surfaces):** When the fractures are supported by their own asperities, the change of fracture conductivity with stress is 2 decades per 10,000 psi (or approximately 1 decade per 5000 psi), and similar to that for water. However, only the Marcellus and Barnett good reservoir quality facies supported these observations. For all other samples, results were questionable and possibly affected by additional fractures associated to the surface preparation process.

- **Fracture conductivity to gas (Smooth surfaces):** Assuming the same limit of 0.01mD/ft, fracture conductivities to gas on smooth (saw cut) surfaces are too low for fluid flow at all stress levels. These results indicate that un-propped secondary and tertiary fractures should be excluded from production calculations. However, this limiting value of 0.01 mD/ft should be verified by comparison to field studies of numerical simulations. The change in fracture conductivity with stress is approximately 3 decades per 10,000 psi (or one decade per 3300 psi).
- **Fracture conductivity to gas (Rough surfaces):** When the fractures are supported by their own asperities, the change of fracture conductivity with stress is 2 decades per 10,000 psi (or approximately 1 decade per 5000 psi), and similar to that for water. However, only the Marcellus and Barnett good reservoir quality facies supported these observations. For all other samples, results were questionable and possibly affected by additional fractures associated to the surface preparation process.

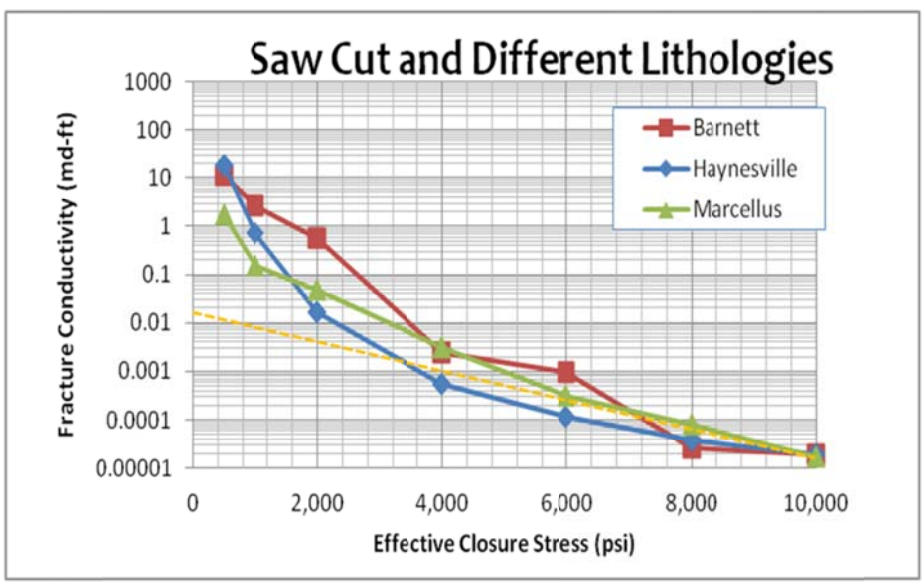

Figure 3.11 Composite of data for saw cut samples for water.

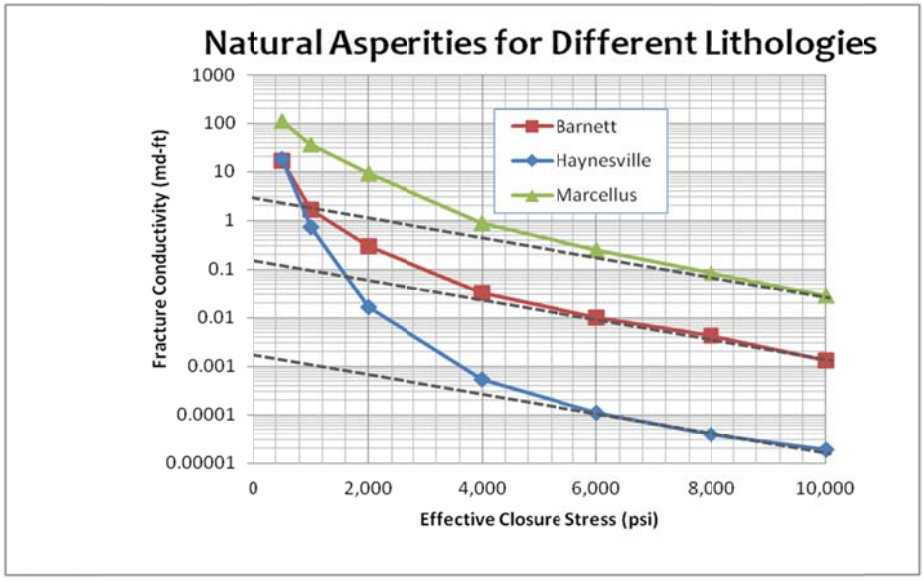

Figure 3.12 A common feature of the un-propped, mechanically split data is the loss of fracture conductivity to water with increasing stress, asperity failure at an effective confining pressure that is well within what would be encountered during depletion of the three characteristic plays.

The data for gas flow under temperature are included in the following figures.

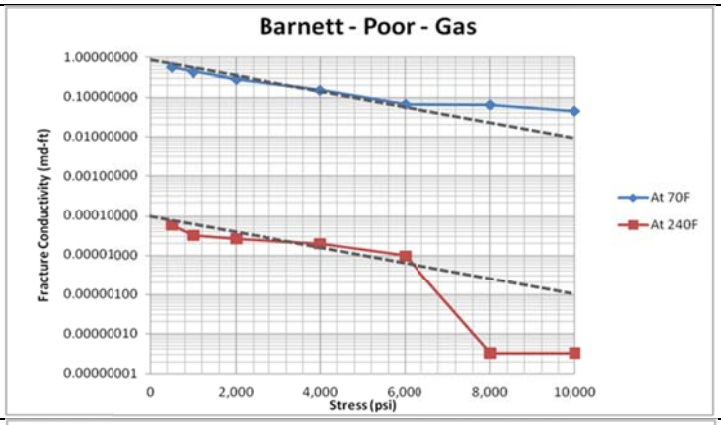

Figure 6.13a. This is a Barnett, poor reservoir quality sample with gas as the flowing fluid. These data represent the effect of temperature on the conductivities. As can be seen the conductivities at higher temperature 240°F are significantly lower than at 70°F. There is a sudden drop in conductivity at 6000 psi. The relative trend with stress is the same for the two, up to 6000 psi.

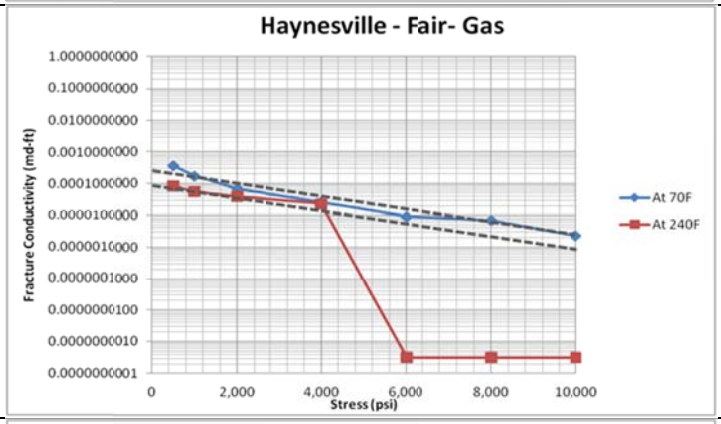

Figure 6.13b. This is a Haynesville, fair reservoir quality sample with gas as the flowing fluid. The initial conductivities are similar but at 4000 psi there is a sudden drop in conductivity at 240°F. The relative trend with stress is the same for the two, up to 4000 psi.

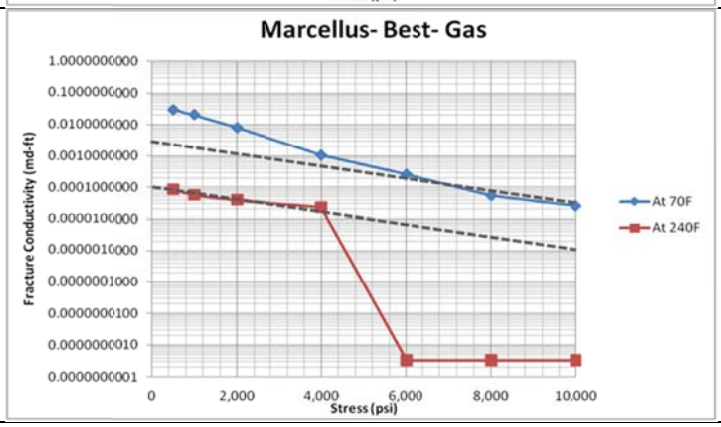

Figure 6.13c. This is a Marcellus, best reservoir quality sample with gas as the flowing fluid. Similar drop in conductivity is seen at 4000 psi as seen in the above Haynesville sample. The relative trend with stress is the same for the two, up to 4000 psi.

Figure 3.13 shows the results for high temperature conductivity tests for Barnett, Haynesville and Marcellus. The drop in conductivity at higher temperatures could be attributable to increasing viscosities of flowing fluid.

- **Temperature:** Three conductivity tests were performed at high temperature 240°F. When compared to the results obtained at 70°F, the conductivities observed at 240°F are much lower than those at 70°F. One of the possible reasons would be the increase in viscosity of gas at higher temperature. However, the relative trend of the decrease in fracture conductivity with stress is similar on all samples. A sudden decrease in fracture conductivity is seen in all samples at temperature. This occurs at 4000 psi in the Haynesville and Marcellus, and at 6000 psi in the Barnett.

Comparison between Water and Nitrogen:

Figure 3.14 through Figure 3.16 compares fracture conductivity tests on saw cut samples with nitrogen and water as the flowing fluids. Data from the Haynesville and the Marcellus overlie each other. The Barnett samples behave differently. However, the stress dependence of 3 decades per 10,000 psi appears consistent for all samples, particularly at high closure stress.

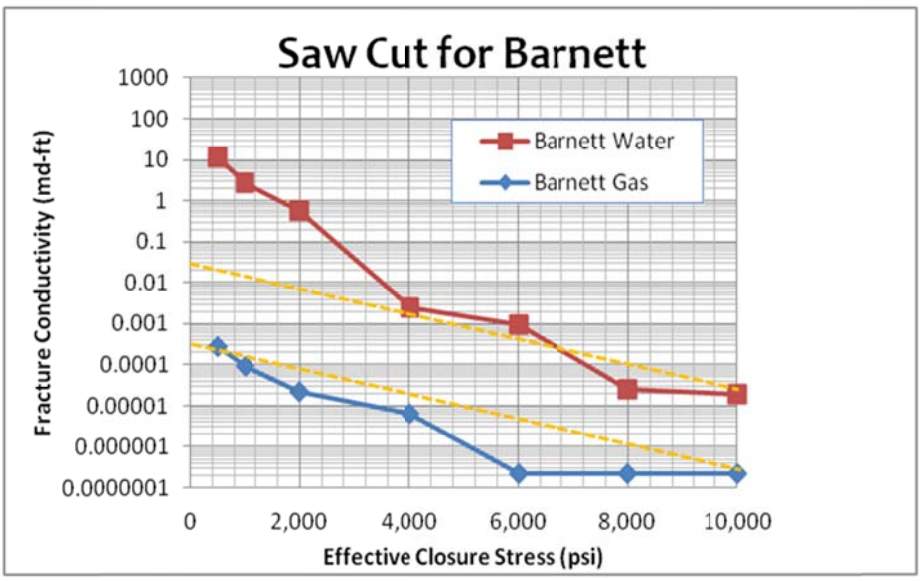

Figure 3.14 This is a comparison of fracture conductivity for two discrete Barnett (best reservoir quality) shale measurements, the relatively low values for the gas, in comparison with most other measurements made in the program, suggest that the data for gas in this plot may be unreliable.

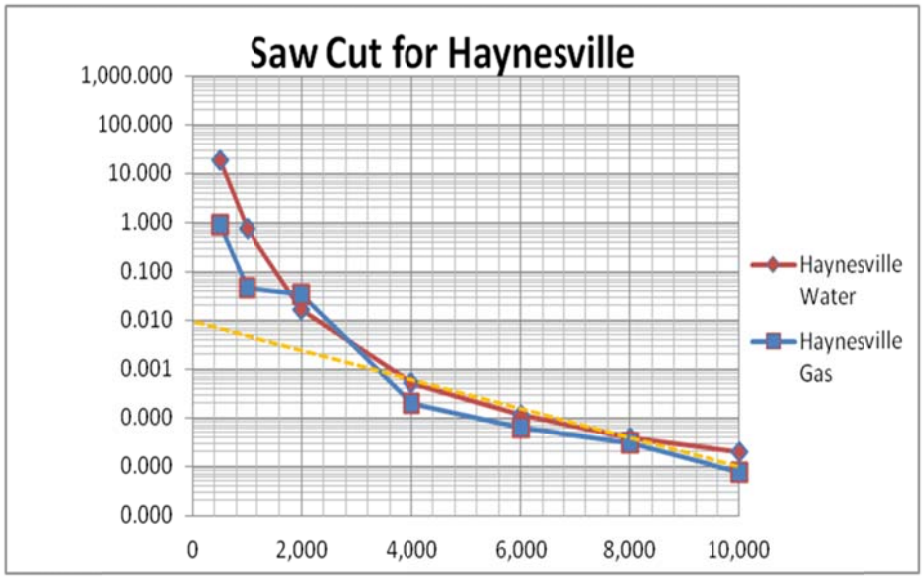

Figure 3.15 Within the range of reliable prediction, these two curves – absolute fracture conductivity for each fluid, are nominally the same. Differences will arise with more than one fluid in the fracture (relative permeability) and with Reynolds' numbers that are substantially greater than 1.

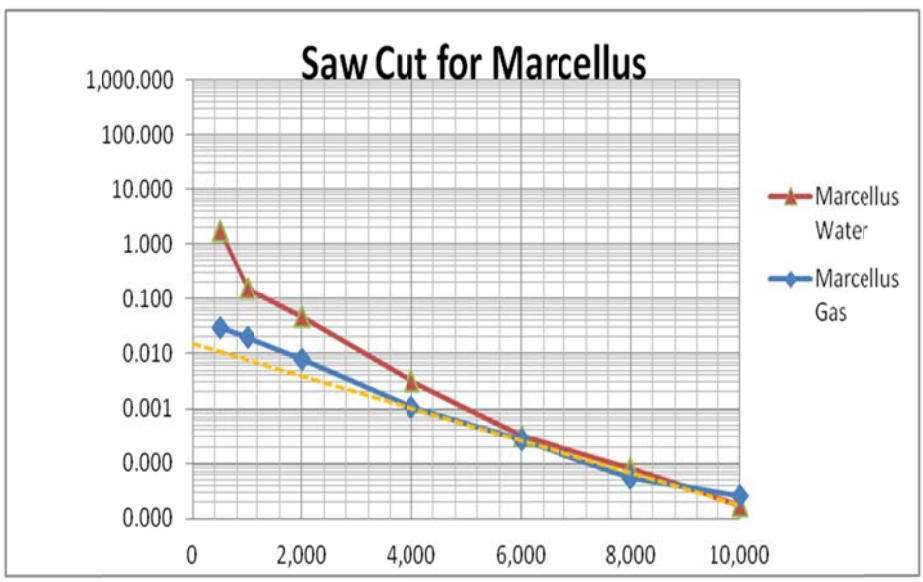

Figure 3.16 Within the range of reliable prediction, these two curves – absolute fracture conductivity for each fluid, are nominally the same. Differences will arise with more than one fluid in the fracture (relative permeability) and with Reynolds' numbers that are substantially greater than 1.

- **Fluid Exposure:** A number of sample surfaces were exposed to water prior to fracture conductivity measurements. Comparative data for propped fractures are provided in the next section. Further, the general observations from all saw cut samples, even without pre-treatment with a weakening fluid, is that un-propped conductivity will contribute little, particularly in distal parts of the reservoir where drawdown will be restricted.
- **Long-Term Creep Measurements:** One Barnett sample was allowed to creep at a closure stress of 5000 psi and a temperature of 120°F. This implies that the closure stress was applied and held constant at an effective stress of 5000 psi for an extended time, with periodic flow measurements. The results are quite definitive. Figure 3.177 shows the creep data on the one sample.

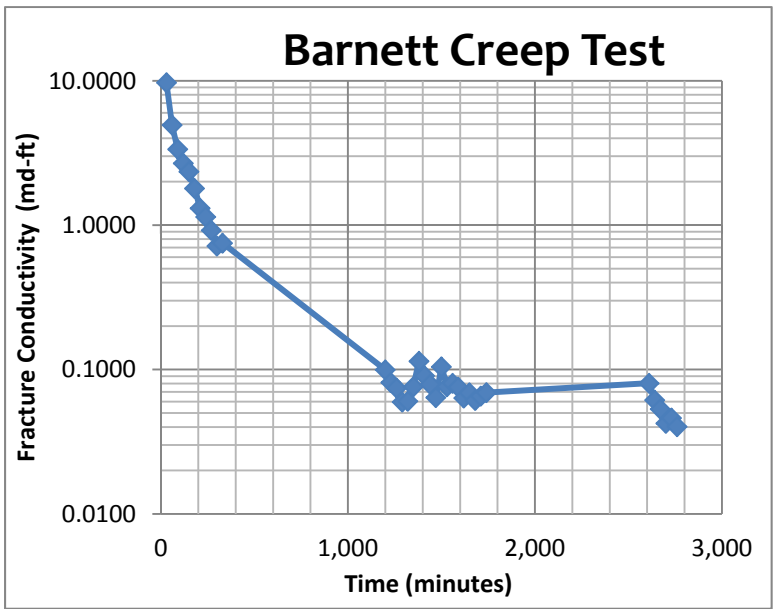

Figure 3.17 Creep data from one Barnett shale sample. All measurements were carried out at an effective closure stress of 5,000 psi. The reservoir quality was "best," and the flowing fluid was the synthetic water.

- **Shear Displacement:** In these experiments, a one-mm lateral displacement was imposed, perpendicular to bedding, and fracture conductivity measurements were repeated. The motivation was to determine if asperity override had a substantial impact on fracture conductivity, and even more important, if the asperities would hold up with increasing effective normal stress that is consistent with drawdown or depletion. These measurements were carried out on mechanically split samples without creep periods. Data from these tests are shown with commentary in Figure 3.18 through Figure 3.20.

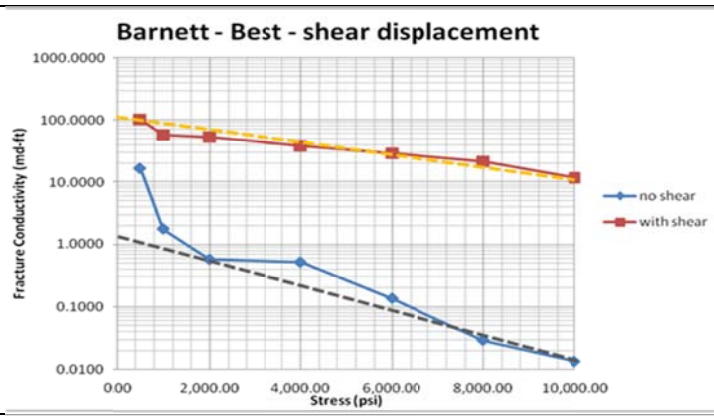	Figure 6.18a. This is shear displacement on a Barnett, best reservoir quality sample with water as the flowing fluid. The sheared sample has a consistent and relatively constant conductivity that is an order of magnitude larger than the unsheared sample. The native sample loses conductivity with stress at a rate of 2 decades per 10,000 psi. The sheared sample loses it at half this rate or 1 decade per 10,000 psi.
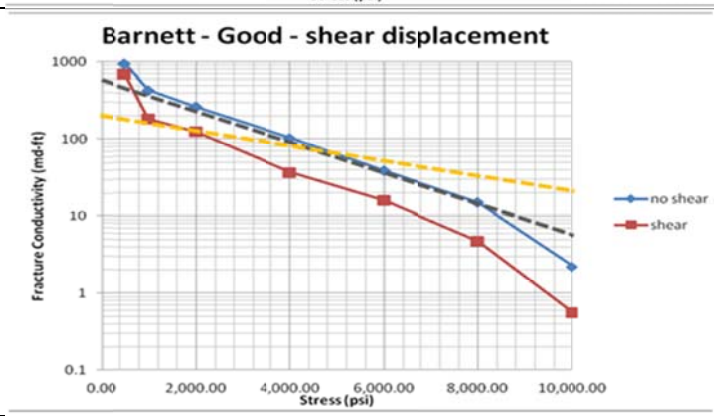	Figure 6.18b. There is little difference between sheared and unsheared conductivity, both in magnitude and in the rate of decline, which is very similar after 2000 psi. The initial conductivity at 1,000 psi is somewhat higher than for the best reservoir quality. This is a "good" reservoir sample and the flowing fluid was water. This sample was created with Brazilian loading (less roughness).
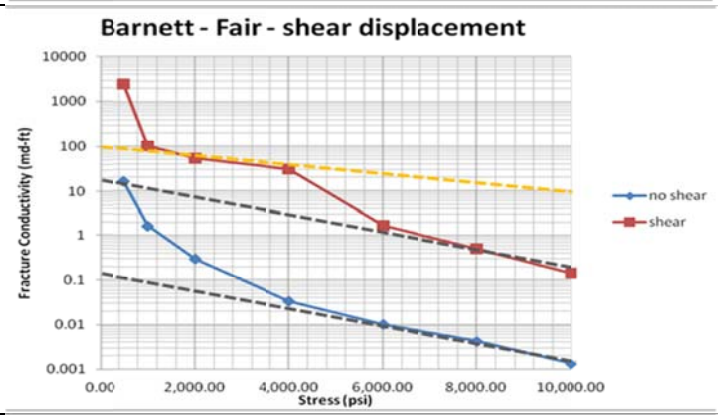	Figure 6.18c. This is shear displacement on a "fair" reservoir quality sample with water as the flowing fluid. The sheared sample has a fracture conductivity that is an order of magnitude larger than the unsheared sample. The native sample loses conductivity at a rate of 2 decades per 10,000 psi. The sheared sample loses it initially at half this rate (yellow line).
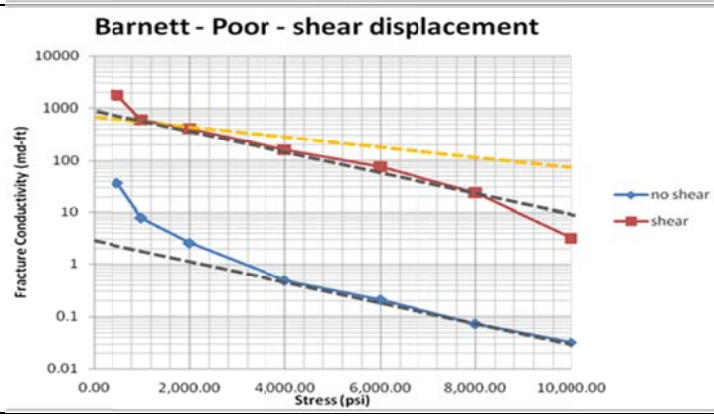	Figure 6.18d. This is shear displacement on a "poor" reservoir quality sample with water as the flowing fluid. The sheared sample has a consistent and relatively constant conductivity that is an order of magnitude larger than the unsheared sample. Both samples lose fracture conductivity at a rate of 2 decades per 10,000 psi. The difference occurs at lower closure stress, where the sheared sample is more resilient.

Figure 3.18 Barnett shear displacement test results.

Results for the **Haynesville samples** are less consistent (Figure 3.19) as for the Barnett. The surface hardness is considerably lower, and the sheared samples do not always exhibit higher fracture conductivity. Overall, it appears that there is no substantial improvement or degradation by shearing, taking into account performance of all three samples.

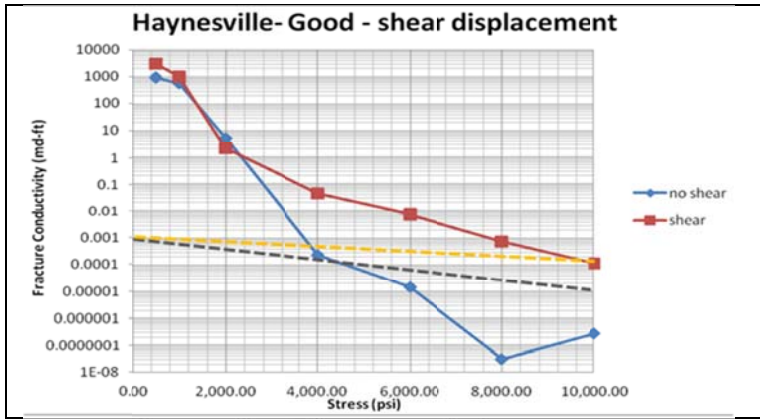

Figure 6.19a. This is shear displacement on a Haynesville good reservoir quality sample with water as the flowing fluid. Initially the conductivity is quite similar between samples. The sheared sample preserves conductivity to higher stresses. However, beyond 6000 psi, most values are below the limit of 0.01 md-ft – a value that seems to be below effective and economic deliverability.

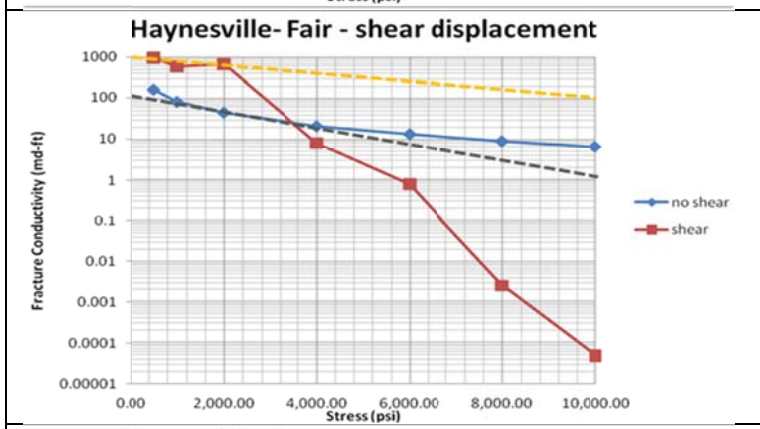

Figure 6.19b. This is shear displacement on a Haynesville fair reservoir quality sample with water as the flowing fluid. The behavior is the opposite than what is seen in the good reservoir quality sample (Figure 6.19a). The unsheared sample maintains conductivity over all loading, whereas the sheared sample loses conductivity quickly after a closure stress of 2000 psi.

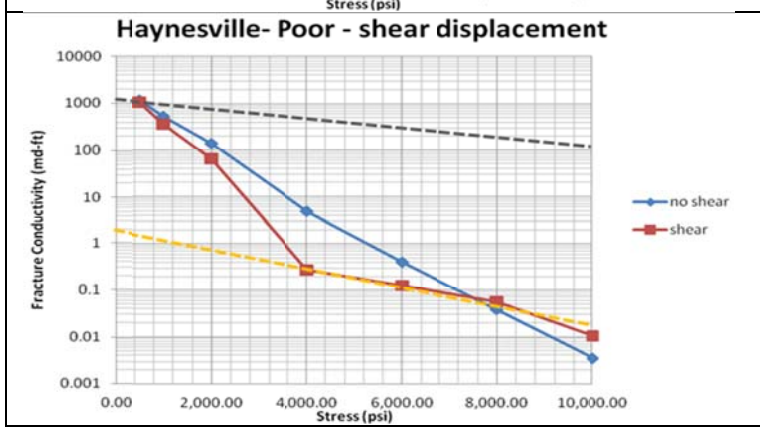

Figure 6.19c. This is shear displacement on a "poor" reservoir quality sample with water as the flowing fluid. There is little difference between either sample at low closure stress. At higher stress, the sheared sample retains more conductivity.

Figure 3.19 Haynesville shear displacement test results.

Performance of the Marcellus samples is less regular (Figure 3.20). Sheared samples generally have higher conductivities throughout the entire closure stress regime.

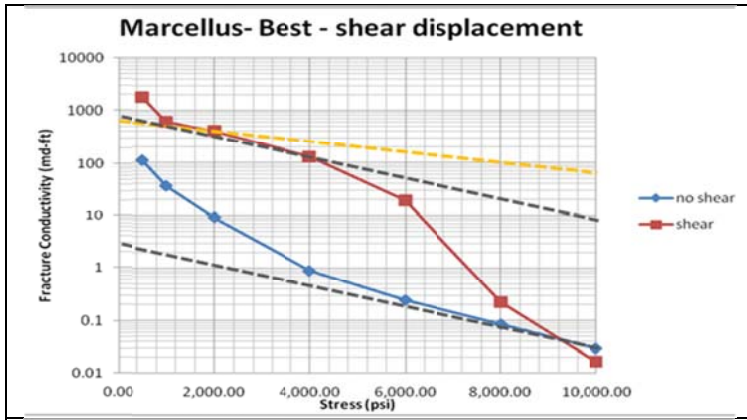

Figure 20a. This is shear displacement on a Marcellus best reservoir quality sample with water as the flowing fluid. The sheared sample shows higher permeability over most of the stress range, with some substantial degradation after 6,000 psi.

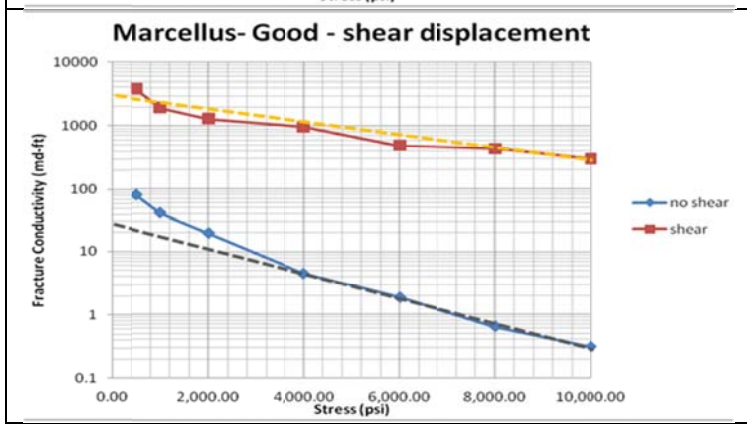

Figure 20b. This is shear displacement on a Marcellus good reservoir quality sample with water as the flowing fluid. The sheared sample performs substantially better than the unsheared sample. The change in fracture conductivity with stress is for these are 1 decade (sheared and 2 decades (not sheared) per 10,000 psi.

Figure 3.20 Marcellus shear displacement test results.

The following observations are noted.

- Unfortunately, the mechanically split data is in general of poorer quality, because of the conditions of fracture generation.
- By and large the shear-displaced samples tend to have higher conductivities.
- For the Barnett shale samples, the effects of shear displacement – if it can be achieved in situ –is very promising. In this rock, for three of the four reservoir qualities, the apparent values of fracture conductivity are improved by an order of magnitude above the baseline values, which were measured on samples without shear displacement.
- For the Haynesville shale samples, the effects of shear displacement are not promising. The rock hardness is low and there is no apparent improvement in fracture conductivity that is noticed.
- For the Marcellus shale samples, the effects of shear displacement – if it can be achieved in situ –are also very promising.

3.5 Summary

The conductivity of un-propped fractures of Barnett, Marcellus and Haynesville samples were measured. Three types of surface conditions were considered: Saw cut surfaces, representing smooth surfaces. Brazil loading tensile fractures, representative of intermediate roughness, and fractures with natural asperities, created by wedge loading on a notched sample were tested. In addition, similar measurements were conducted flowing nitrogen gas and flowing water. Few measurements were also conducted to understand the effect of temperature and time dependent creep. In addition, measurements were repeated with a shear displacement added, perpendicular to bedding, to investigate the effect of shear and overriding asperities on fracture conductivity. General results are as follows:

(i) Fracture conductivities of 0.01 mD-ft or lower were assumed to be too low for production. Thus fractures with conductivities below this level should be ignored for production assessment.

(ii) Smooth fractures without proppant do not retain sufficient conductivity to be of relevance to production. In practice, these are far-field second and third tier network fractures that are predominantly filled with water.

(iii) Fractures with natural asperities are important to production, and particularly so when the closure stress is below 6000 to 4000 psi. The sensitivity with stress for these is approximately 2 decades per 10,000 psi.

(iv) There is a great deal of consistency on the measured data between samples, and at high closure stress, there is no rock type differentiation. However, a strong differentiation by rock type occurs at low closure stress. Here, the Haynesville samples are the most sensitive to stress. The Barnett samples are the most resilient.

(v) The sensitivity to temperature and time dependence, creep, was also investigated. Temperature appears to introduce a dramatic decrease in fracture conductivity at some critical stress. This effect should be investigated further. Creep introduces high initial stress dependence (at low confining stress). Thus, laboratory conditions for fracture conductivity may need to include temperature and creep to be more representative of field conditions.

(vi) Comparisons between samples with and without shearing show that for the Barnett and the Marcellus shales, the effect of shearing is substantial and results in stress dependence that is approximately half of the rate of the unsheared sample. Because of the low surface hardness of the Haynesville shale, shearing these samples do not result in any improvement in fracture conductivity. Values of unconfined strength and Brinell hardness for these samples are reported in Section 1.

4 FRACTURE CONDUCTIVITY OF PROPPED FRACTURES ON CORE

4.1 Introduction

The objective of this section is to conduct a theoretical and laboratory evaluation of the fracture conductivity to gas and water, using the same representative material that was used in the previous section, under various conditions of proppant size, distribution and concentration.

Key components of this effort are as follows:

(i) Measure the fracture surface area, Brinell hardness, continuous scratch test, and fracture conductivity to water and gas, on saw-cut samples with different proppant sizes and concentration, as function of effective stress (proxy for depletion). This will lead us to investigate the fracture conductivity for flow of gas and water.

(ii) Measure the fracture surface area, Brinell hardness, continuous scratch test, and fracture conductivity on core samples exposed to water and oil under given conditions stress, and temperature. Basic evaluation to investigate the effect of sensitivity to fluids.

(iii) Measure the fluid production from water-exposed fractures, during gas flow and at in-situ stress conditions. This will lead us to investigate the water mobility (or retention) due to capillary forces induced by rock-water and rock-fluid interactions.

4.2 Testing Matrix

The matrix of testing carried out is shown in Table 4.1. The basic variables were:

- **Shale Play:** Barnett, Haynesville and Marcellus
- **Reservoir Quality:** Samples were described as "best, good, fair, and poor" reservoir quality, based on a criterion presented in Section 1.
- **Surface Roughness:** All samples were saw cut (i.e., representative of smooth surfaces).
- **Temperature:** Barnett samples were run at temperatures of 70°F. One Barnett sample with best reservoir quality was run at 120°F. All other samples from other formations were tested at nominally ambient temperature (~70°F).
- **Flowing Fluid:** Some samples were tested using nitrogen gas as the flowing fluid. Synthetic formation water was also used. The composition of that fluid is shown in Table 4.2.
- **Fluid Exposure:** A restricted number of sample surfaces were exposed to water for 18 hours prior to conducting fracture conductivity measurements.

- **Long-Term Measurements:** Four samples from each reservoir quality and two samples from Barnett best reservoir quality were allowed to creep at a closure stress of 5000 psi. This implies that the closure stress was applied and held constant for an extended time with periodic flow measurements.
- **Proppant Concentration and Size:** Experiments for all reservoir quality shales were performed using different sizes of proppants namely 40/70 sand, 80/100 sand and a mixture containing equal volumes of 40/70 sand and 80/100 sand. A restricted number of experiments were performed for different concentrations of proppant. The concentrations used were monolayer (1x) and three monolayers (3x) as shown in Table 7.1.

Table 4.1. Testing Matrix for Propped Samples

Formation	Sample Identifier	Reservoir Quality	Proppant Size	Proppant Concentration	Proppant Distribution	Exposure	Creep
Barnett	01	Best	40/70, 80/100 & mix	1x, 3x	-	Water, oil	@5000 psi
	02	Good	40/70, 80/100 & mix	1x	40/70, channel	Water, oil	@5000 psi
	03	Fair	40/70, 80/100 & mix	1x, 3x	-	Water, oil	@5000 psi
	04	Poor	40/70, 80/100 & mix	1x	-	Water, oil	@5000 psi
Haynesville	05	Good	40/70, 80/100 & mix	1x, 3x	40/70, channel	Water, oil	@5000 psi
	06	Fair	40/70, 80/100 & mix	1x	-	Water, oil	@5000 psi
	07	Poor	40/70, 80/100 & mix	1x	-	Water, oil	@5000 psi
Marcellus	09	Best	40/70, 80/100 & mix	1x, 3x	-	Water, oil	@5000 psi
	10	Good	40/70, 80/100 & mix	1x	40/70, channel	Water, oil	@5000 psi

Table 4.2. Properties of Synthetic Water

Component	Concentration (mg/l)
Calcium Chloride Dihydrate	451.17
Magnesium Chloride Hexahydrate	175.63
Potassium Chloride	17.16
Sodium Sulphate	337.1
Sodium Bicarbonate	239.64

The data for the propped measurements are included in Appendix 6.

4.3 Comparisons

4.3.1 Proppant Size and Distribution

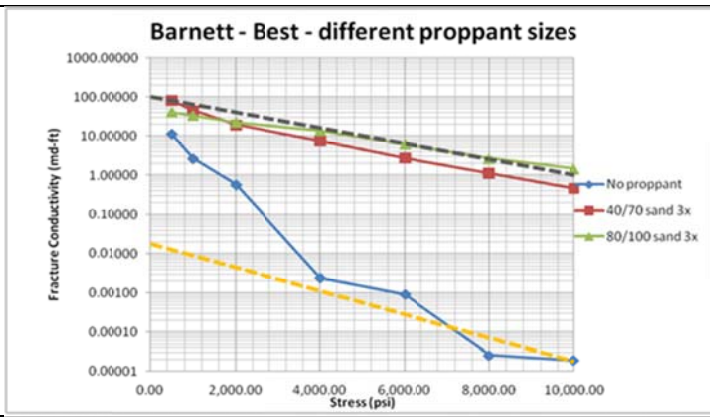	Figure 7.1a. This is a Barnett, best reservoir quality sample with water as the flowing fluid. This test shows 40/70 and 80/100 performance for a 3x layer. There is little discrimination between the conductivity. Because of the greater surface area the 80/100 mesh apparently held up better at higher closure stress. Since these are two different samples, conclusions are that the differences appear to be small.
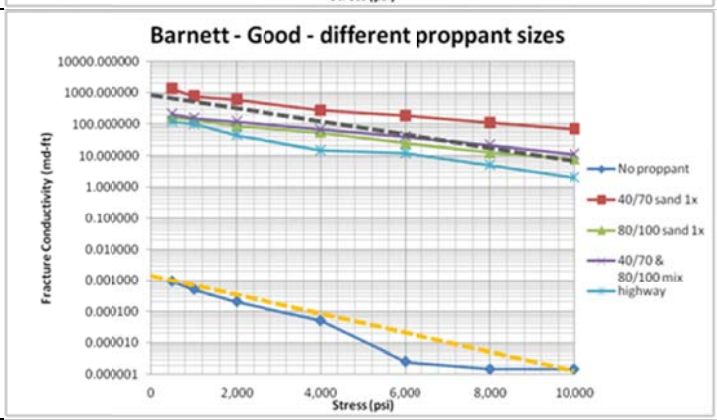	Figure 7.1b. This is a Barnett, good reservoir quality sample with water as the flowing fluid. The conductivity with 40/70 is higher than with 80/100. The conductivity for the mix proppant was intermediate, but the conductivity for Channel frac, particularly at low closure stress, was unexpectedly low. Possible reason for this may be higher proppant crushing.
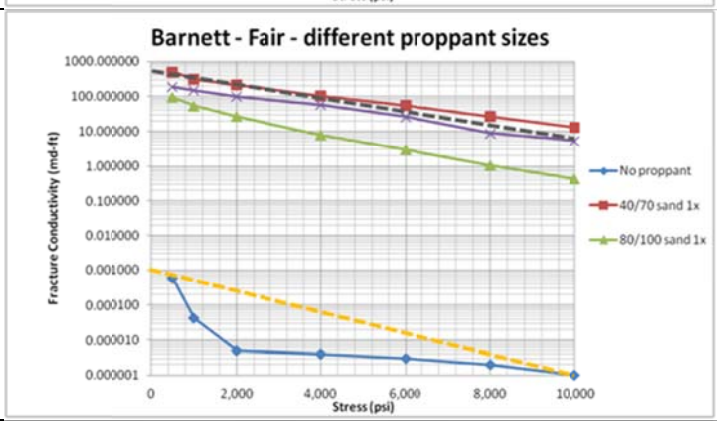	Figure 7.1c. This is a Barnett, fair reservoir quality sample with water as the flowing fluid. The conductivity with 40/70 is higher than with 80/100. The conductivity for the mix proppant was intermediate between the two.
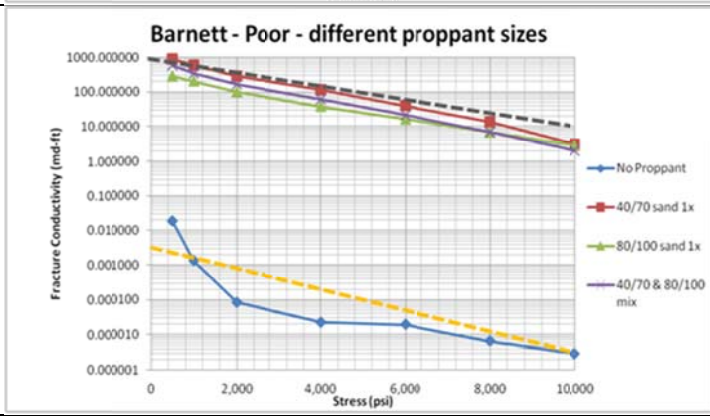	Figure 7.1d. This is a Barnett, poor reservoir quality sample with water as the flowing fluid. The general tends of this measurements with stress are similar to the previous. The slight increase in conductivity with decreasing reservoir quality does stand out. In addition, the difference between proppants types for this rock is smaller.

Figure 4.1 Barnett different proppant size tests with water.

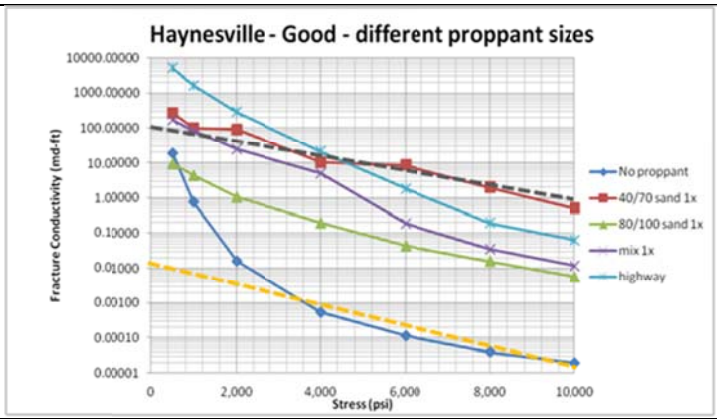	Figure 7.2a. This is a Haynesville, good reservoir quality sample with <u>water</u> as the flowing fluid. The partial monolayer (Channel) has the highest conductivity at low confining pressures but becomes less effective than the 40/70 sand at closure stresses above 4000 psi. The mix proppant has higher conductivity than the 80/100 sand. The slopes represent a 2 decade (black) and 3 decade (yellow) reduction with 10,000 psi.
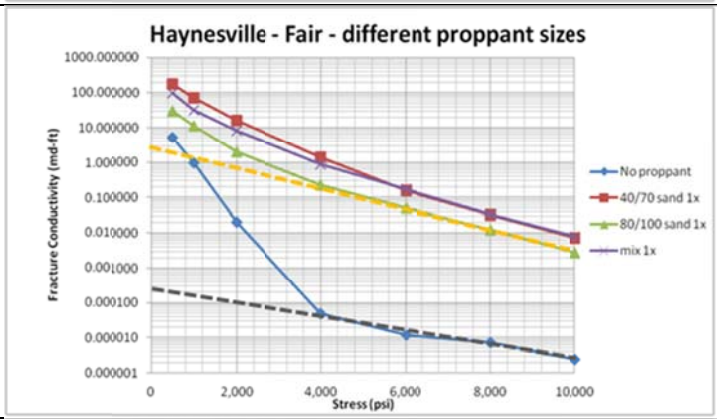	Figure 7.2b. This is a Haynesville, fair reservoir quality sample with <u>water</u> as the flowing fluid. There is a logical difference in conductivity based on grain size alone – small overall grain size gives small conductivity. The stress dependence for all proppant types is reasonably similar. The increase of stress sensitivity in this test with rock type is significant.
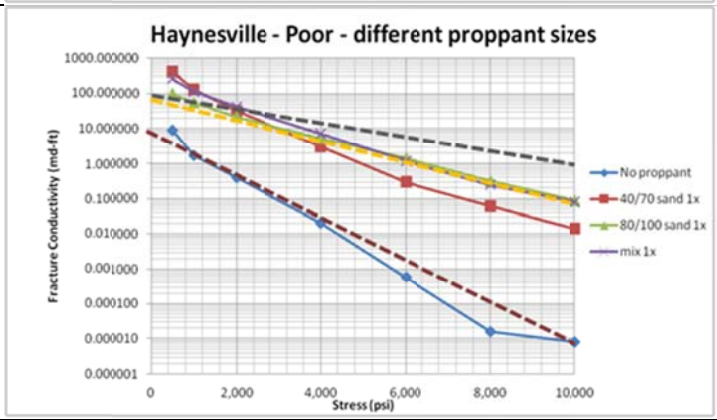	Figure 7.2c. This is a Haynesville, poor reservoir quality sample with <u>water</u> as the flowing fluid. 40/70 is the poorest performer at closure stresses greater than 2000 psi. However the measurement is consistent with the fair quality rock type. The difference is the decreased stress dependence of the 80/100 sand and the mix sand. For comparison to other tests, a brown line with slope of 6 decades per 10,000 psi is provided.

Figure 4.2 Haynesville different proppant size tests with water.

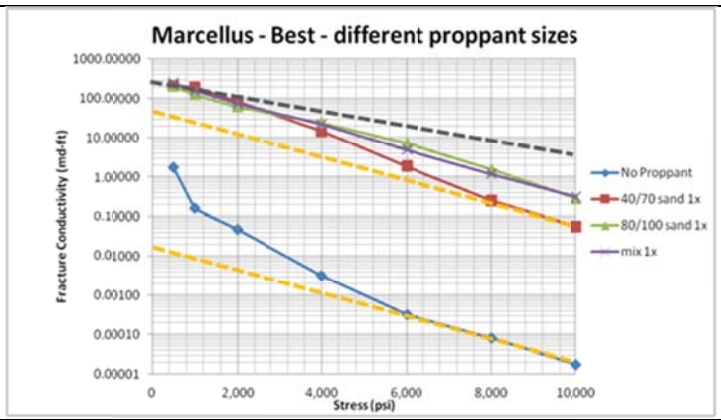

Figure 7.3a. This is a Marcellus, best reservoir quality sample with water as the flowing fluid. Note that this set of curves very nearly mirrors the Haynesville poor quality data. That is, the loss of conductivity with stress is included within the two slopes of 2 and 3 decades pert 10,000 psi. This reinforces the observation of small lithologic/reservoir quality dependency, for these short-term measurements.

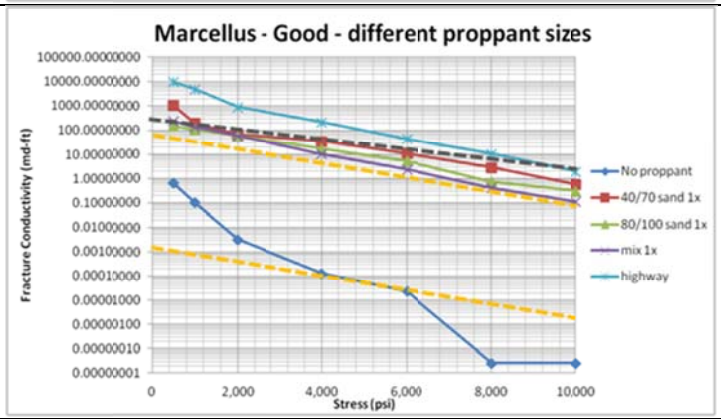

Figure 7.3b. This is a Marcellus, good reservoir quality sample with water as the flowing fluid. The partial monolayer (channel) is very successful in improving the overall conductivity and reducing the loss with stress. All other proppant blends perform better than for the other rocks tested. Their loss of conductivity with stress can be compared in reference to the two slopes of 2 and 3 decades per 10,000 psi.

Figure 4.3 Marcellus different proppant size tests with water.

Data for gas flow using propped and un-propped smooth fractures are included in the following figures. As discussed in the previous section, gas flow measurements on propped and un-propped data on smooth surfaces is problematic, less consistent, and less easy to interpret.

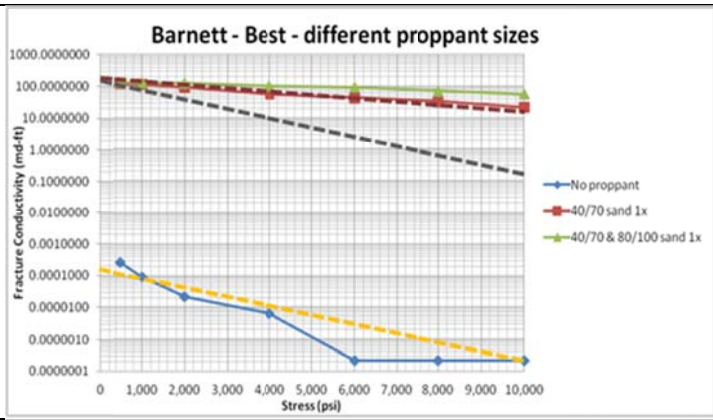	Figure 7.4a. This is a Barnett, best reservoir quality sample with gas as the flowing fluid. Characteristically, the decline in conductivity with closure stress, using gas, is apparently much smaller than with liquid. This might be an important consideration but cannot be confirmed because of the low reliability of the gas measurements in general – see Figures 7.4b and 7.4c.
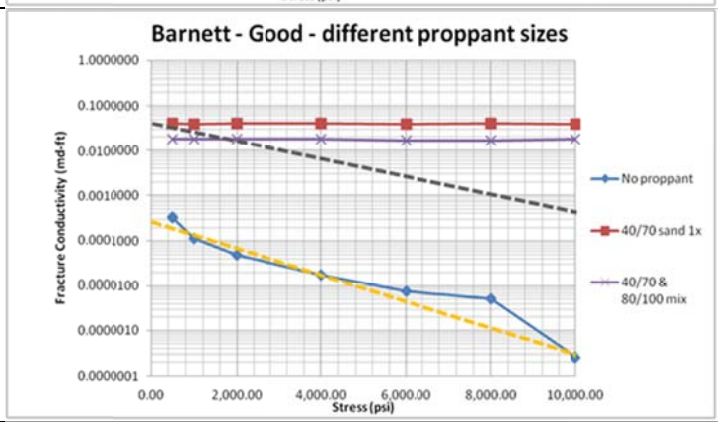	Figure 7.4b. This is a Barnett, good reservoir quality sample with gas as the flowing fluid. The lack of stress dependence is probelmatic and suggests lack of resolution. The proppant data should be ignored. The lines with constant slope are used as references for understanding the stress dependence. This is 2 decades (black) and 3 decades (yellow) per 10,000 psi
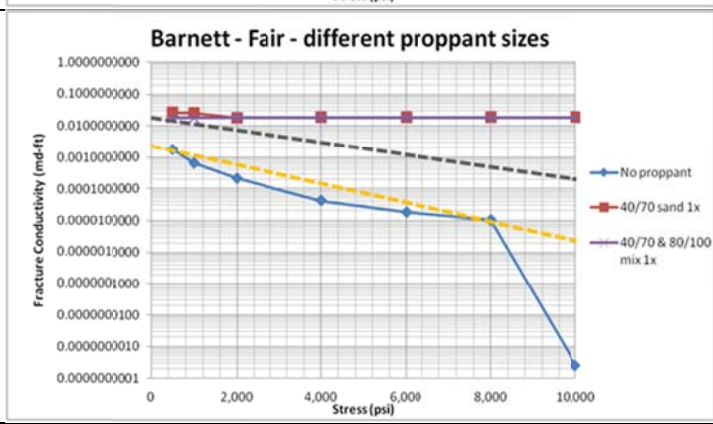	Figure 7.4c. This is a Barnett, fair reservoir quality sample with gas as the flowing fluid. The lack of stress dependence is probelmatic and suggests lack of resolution. The proppant data should be ignored.

Figure 4.4 Barnett different proppant size tests with gas.

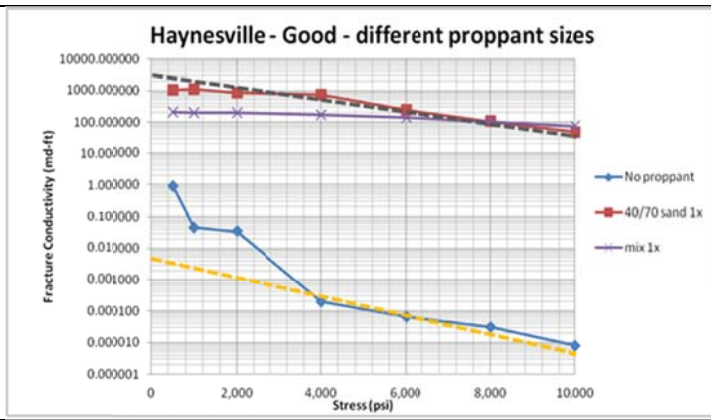	Figure 7.5a. This is a Haynesville, good reservoir quality sample with gas as the flowing fluid. The conductivity for the 40/70 proppant is initially constant and then it follows the standard 2 decade per 10,000 psi slope. This is consistent with the liquid conductivity. The relatively constant fracture conductivity for the mix proppant sample is problematic and possibly due to lack of appropriate resolution.
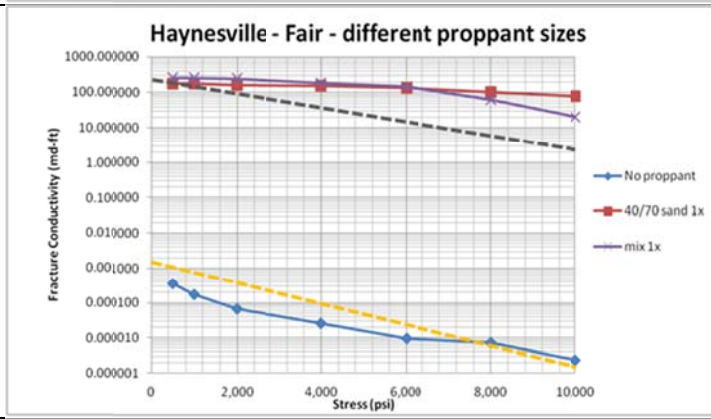	Figure 7.5b. This is a Haynesville, fair reservoir quality sample with gas as the flowing fluid. The relatively constant conductivity for the propped samples is problematic and possibly due to lack of appropriate resolution. Notice that at high closure stresses, the change in conductivity with stress for the mix proppant sample follows the standard 2 decades per 10,000 psi slope.
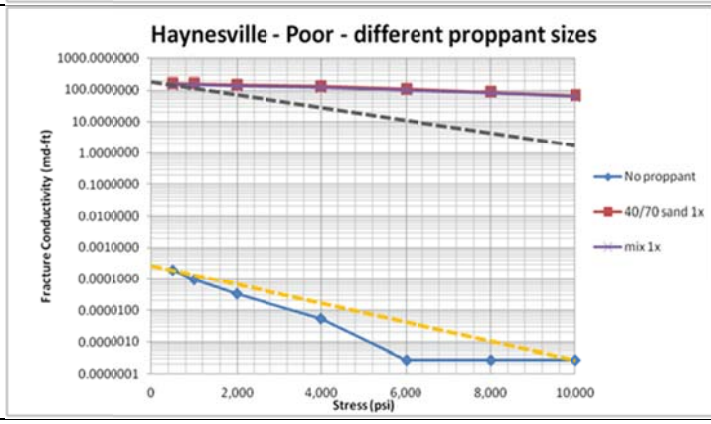	Figure 7.5c. This is a Haynesville, poor reservoir quality sample with gas as the flowing fluid. The relatively constant conductivity is problematic and possibly due to lack of appropriate resolution.

Figure 4.5 Haynesville different proppant size tests with gas.

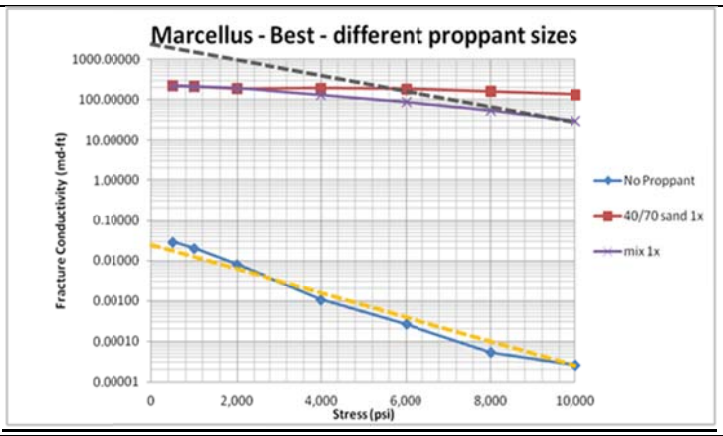

Figure 7.6a. This is a Marcellus, best reservoir quality sample with gas as the flowing fluid. The relatively constant conductivity is problematic and possibly due to lack of appropriate resolution.

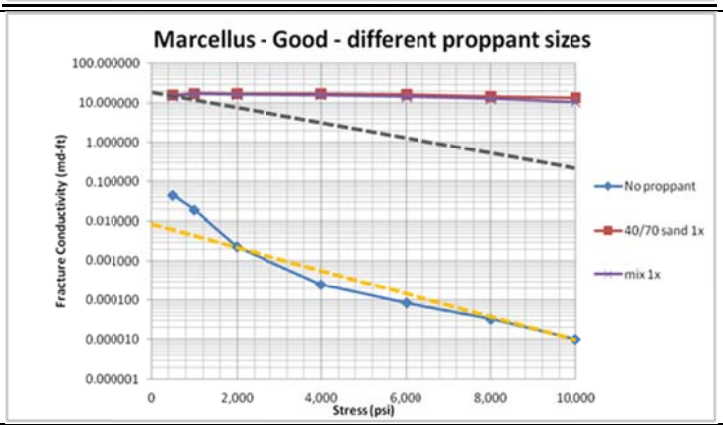

Figure 7.6b. This is a Marcellus, good reservoir quality sample with gas as the flowing fluid. The relatively constant conductivity is problematic and possibly due to lack of appropriate resolution.

Figure 4.6 Marcellus different proppant size tests with gas.

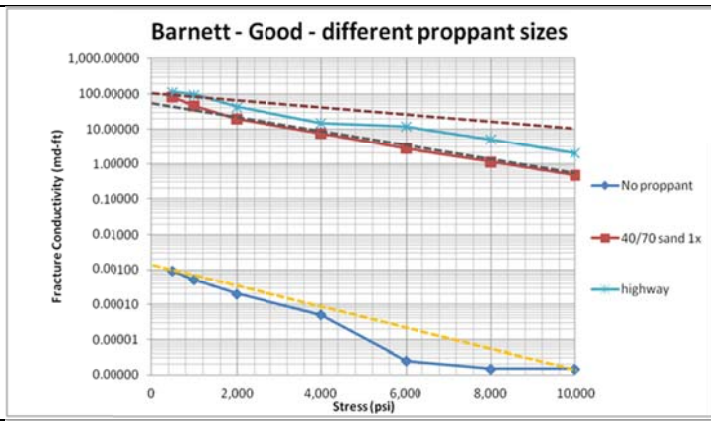

Figure 7.7a. These are Barnett, good reservoir quality samples with water as the flowing fluid and changing proppant sizes. The constant slope lines help us bound the stress dependence for these samples. Brown, black and orange correspond to 1, 2, and 3 decades per 10,000 psi. For Barnett samples at high closure stress, the stress sensitivity is 2 decades per 10,000 psi.

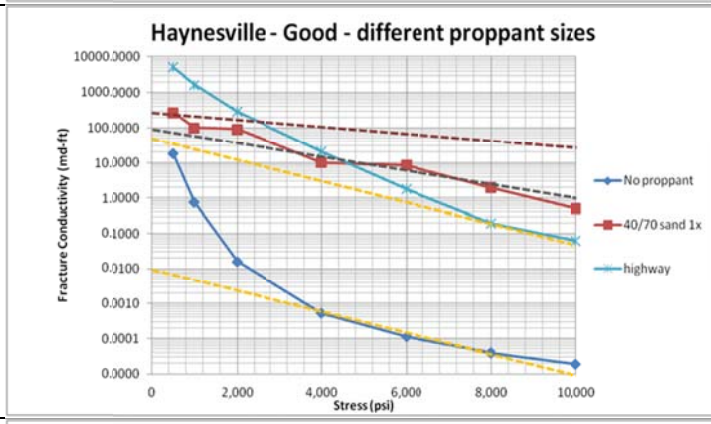

Figure 7.7b. These are Haynesville, good reservoir quality samples with water as the flowing fluid and changing proppant sizes. For Haynesville samples at high closure stress, the stress sensitivity is 3 decades per 10,000 psi. The stress dependence is considerably higher at lower fracture closure.

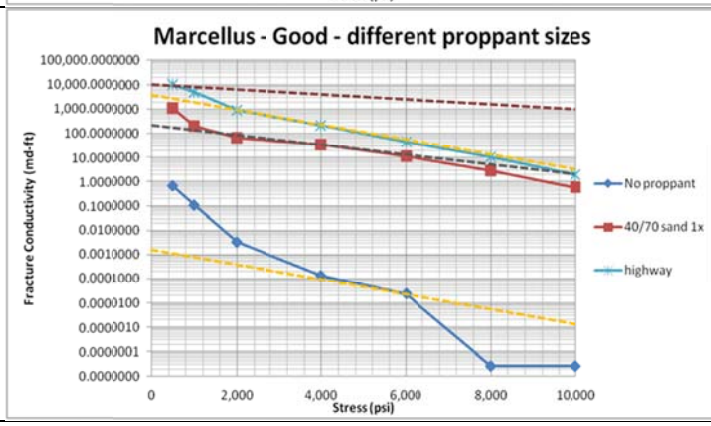

Figure 7.7c. These are Marcellus, good reservoir quality samples with water as the flowing fluid and changing proppant sizes. For Marcellus samples at high closure stress, the stress sensitivity is 3 decades per 10,000 psi. The stress dependence is between 2 and 3 decades per 10,000 psi at lower fracture closure.

Figure 4.7 Barnett, Haynesville and Marcellus samples for different proppant size tests with water.

4.3.2 Fluid Exposure

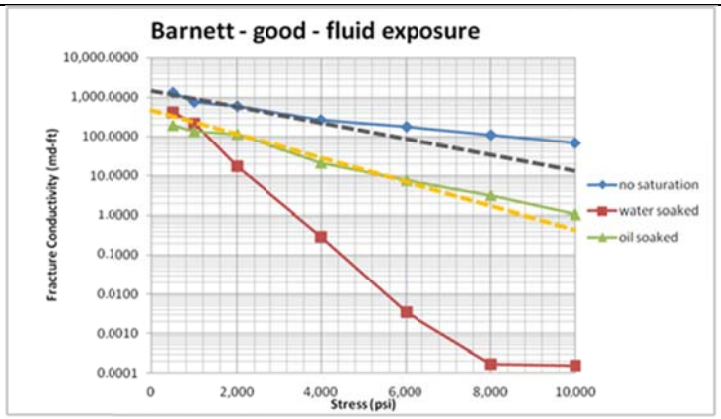

Figure 7.8a. Barentt shale, "good" reservoir quality. Sample was soaked in water for 18 hours prior to testing The flowing fluid is water. There is a rapid and substantial reduction in conductivity when the sample was exposed to water. The water used for saturation is same as the flowing fluid.

The lower conducitivities after oil soaking may relate to relative permeability considerations in a water-oil environment.

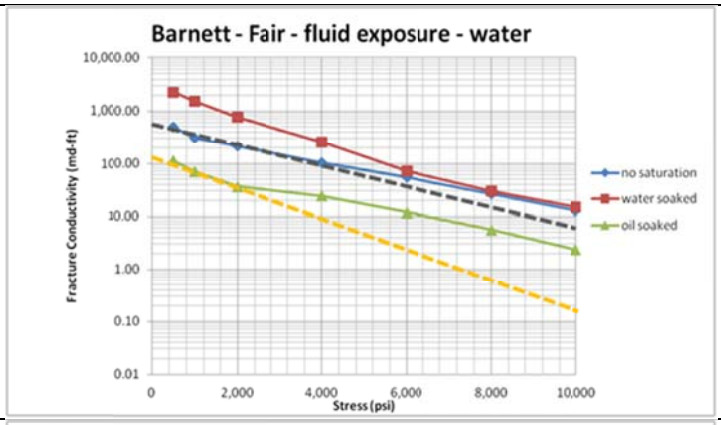

Figure 7.8b. Barnett shale, "fair" reservoir quality. Sample was soaked in water for 18 hours prior to testing The flowing fluid is water. Water soaking in this case did not have a substantial role in reducing conductivity. conductivity was higher. This may need to be validated with additional testing The lower conducitivities after oil soaking likely relate to relative permeability considerations.

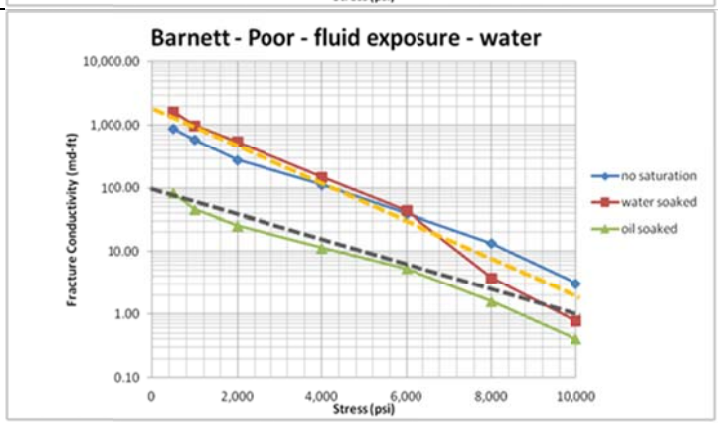

Figure 7.8c. Barnett shale, "fair" reservoir quality. The flowing fluid is water. Sample was soaked in water for 18 hours prior to testing Water soaking in this case did not have a substantial role in reducing conductivity. Water-saoked conductivity was higher suggesting experimental issues that may need to be validated with additional testing. The lower conducitivities after oil soaking likely relate to relative permeability considerations.

Figure 4.8 Barnett fluid exposure tests with water.

One sample was tested with prolonged exposure to water, followed by flow of gas.

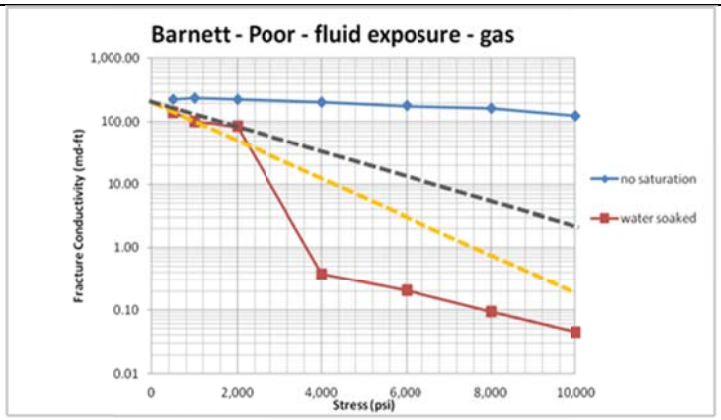

Figure 7.9a. Barentt shale, "poor" reservoir quality. The flowing fluid is gas. Sample was soaked in water for 18 hours prior to testing. The water-exposed sample showed a substantial reduction in permeability at about 2000 to 4000 psi. Causes of this could be embedment related to surface weakening or increased water saturation of the proppant pack with reduced aperture – or both. The non-water exposed sample exhibits an unusualy weak stress dependence.

Figure 4.9 Barnett fluid exposure with gas.

Figure 4.10 and Figure 4.11 demonstrate the response of Haynesville samples to fluid exposure, followed by flow of water and nitrogen, respectively.

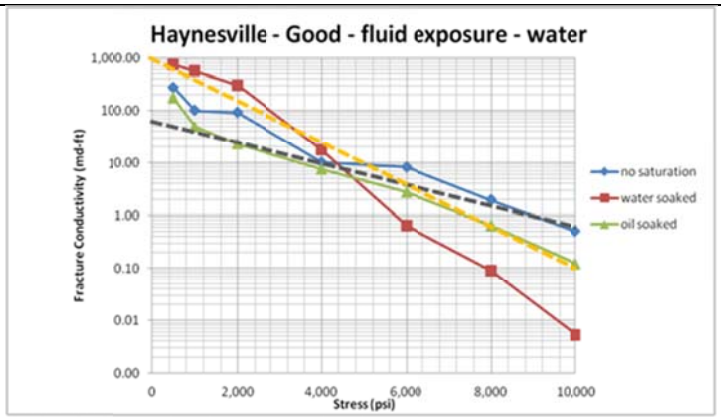	Figure 7.10a. Haynesville shale, "good" reservoir quality. The flowing fluid is water. Sample was soaked in water for 18 hours prior to testing There is a rapid and substantial reduction in conductivity when the sample was exposed to water. The water used for saturation is same as the flowing fluid. The lower conducitivities after oil soaking may relate to relative permeability considerations in a water-oil environment.
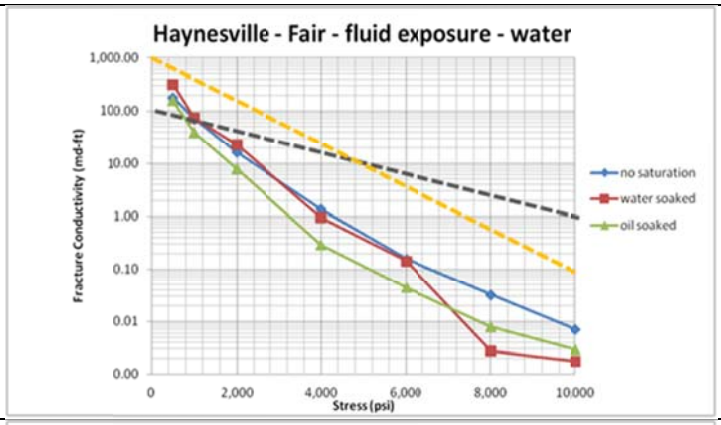	Figure 7.10b. Haynesville shale, "fair" reservoir quality. The flowing fluid is water. Sample was soaked in water for 18 hours prior to testing . Water in this case did not have a substantial role in reducing conductivity. Water-saoked conductivity was higher suggesting possibe issues in the experimental protocol. The lower conducitivities after oil soaking likely relate to relative permeability considerations.
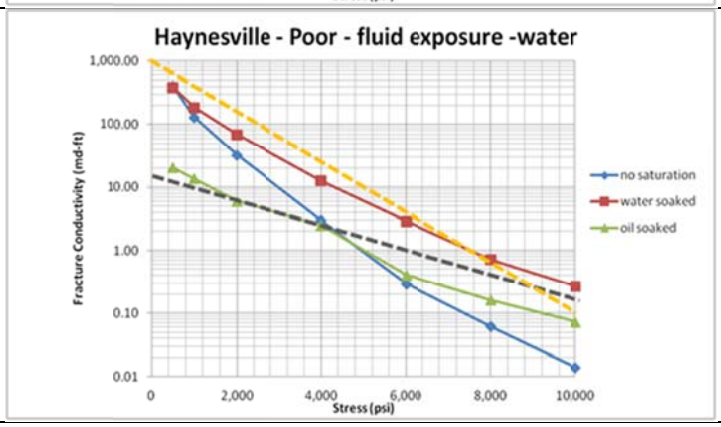	Figure 7.10c. Haynesville shale, "poor" reservoir quality. The flowing fluid is water. Sample was soaked in water for 18 hours prior to testing Water in this case did not have a substantial role in reducing conductivity. Water-saoked conductivity was higher suggsting possible issues in the experimental protocol. The lower conducitivities after oil soaking likely relate to relative permeability considerations.

Figure 4.10 Haynesville fluid exposure tests with water.

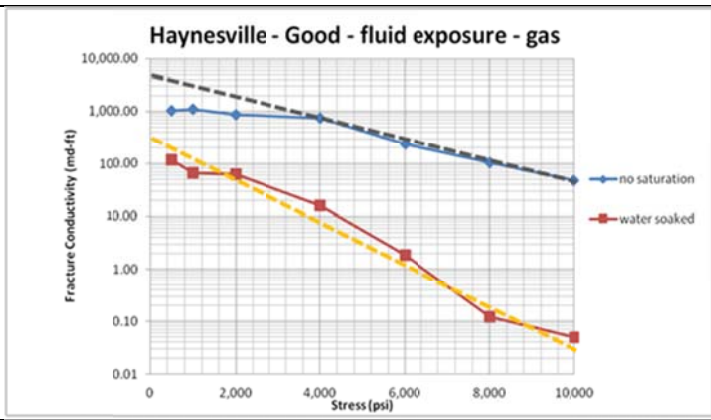	Figure 7.11a. Haynesville shale, "good" reservoir quality. The flowing fluid is gas. Sample was soaked in water for 18 hours prior to testing There is a definitive reduction in the magnitude of the fracture conductivity, either due to residual second phase or surface damage and embedment. Notice the consistent increase in stress sensitivity to 4 decades per 10,000 psi after soaking.
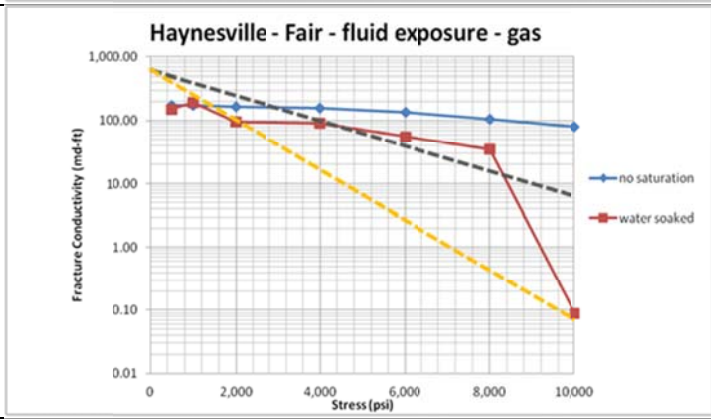	Figure 7.11b. Haynesville shale, "fair" reservoir quality. The flowing fluid is gas. Sample was soaked in water for 18 hours prior to testing. Water imbibition in this case did not have a substantial role in reducing conductivity. There was a dramatic change in fracture conductivity at high closure stress but it is difficult to attribute this to a specific mechanism. The final value, however, is consistent with the expected trend
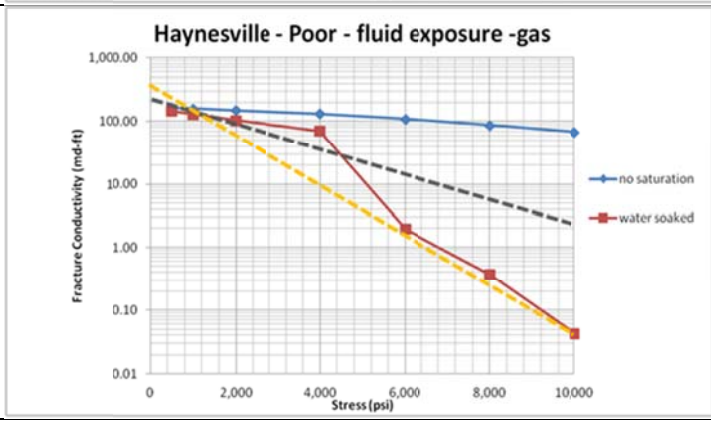	Figure 7.11c. Haynesville shale, "poor" reservoir quality. The flowing fluid is gas. Sample was soaked in water for 18 hours prior to testing Water imbibition in this case did not have a substantial role in reducing conductivity until the closure stress reached 4000 psi. Surface weakening may have been a relevant issue. The overall loss of fracture conductivity is consistent with the expected trend.

Figure 4.11 Haynesville Fluid exposure tests with gas.

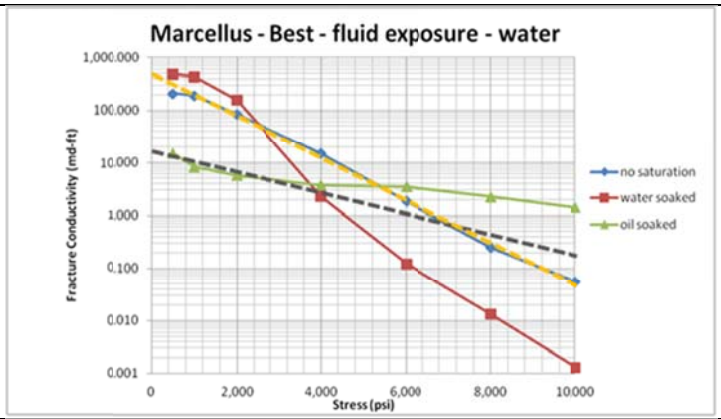

Figure 7.12a. Marcellus shale, "best" reservoir quality. The flowing fluid is water. Sample was soaked in water and oil for 18 hours prior to testing. The sample soaked in oil exhibits a low reduction in fracture conductivity with stress. The water soaked sample loses fracture conductivity at a much higher rate (i.e., larger than the expected 4 decades per 10,000 psi).

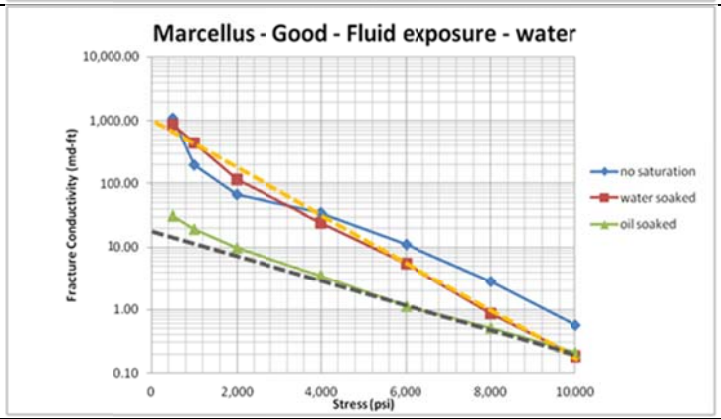

Figure 7.12b. Marcellus shale, "fair" reservoir quality. The flowing fluid is water. Sample was soaked in water and oil for 18 hours prior to testing. Water in this case did not have a substantial role in reducing conductivity. Oil reduced the loss of fracture conductivity with stress feom 4 decades to 2 decades per 10,000 psi. The initial values, however, were lower. This is possibly due to relative oil/water conductivity effects.

Figure 4.12 Marcellus fluid exposure tests with water.

4.3.3 Proppant Concentration

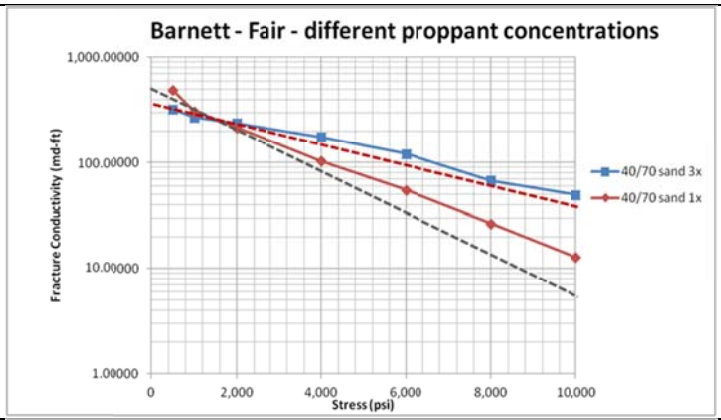

Figure 7.13a. Barnett shale, "fair" reservoir quality. The flowing fluid is water. The sample was run using 40/70 sand proppant with 1x and 3x monolayers. The conductivity observed for 3x is higher as compared to 1x. The stress dependence was reduced from 2 to 1 decade per 10,000 psi.

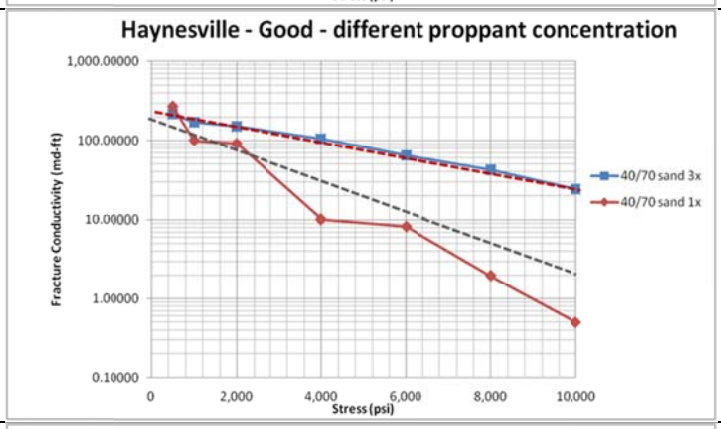

Figure 7.13b. Haynesville shale, "good" reservoir quality. The flowing fluid is water. The conductivities follow a similar trend as observed in Barnett with higher concentration. The conductivity is higher for high concentration and sustains at higher stresses when compared to lower concentrations. The stress dependence was reduced from 2 to 1 decade per 10,000 psi.

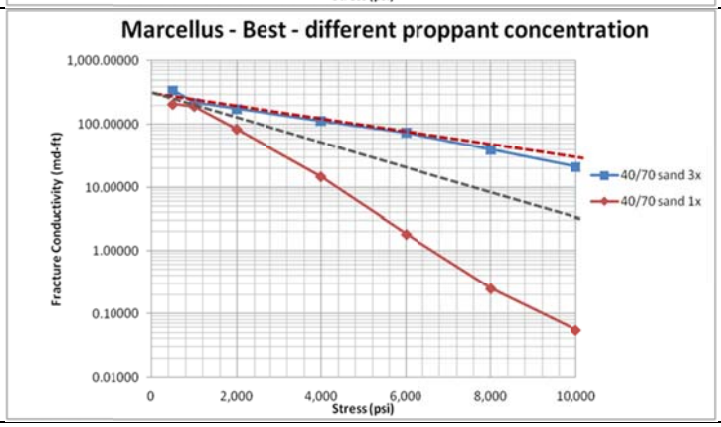

Figure 7.13c. Marcellus shale, "Best" reservoir quality. The flowing fluid is water. The conductivity is higher for higher concentration and remains higher even at higher stresses. The stress dependence was reduced from 4 to 1 decade per 10,000 psi.

Figure 4.13 Conductivity tests with higher proppant concentrations for Barnett, Haynesville and Marcellus shales.

4.4 Summary

The conductivity of propped fractures of Barnett, Marcellus and Haynesville samples were measured. Three types of proppant distributions were considered: uniform monolayer of 40/70 sand, uniform monolayer of 80/100 sand, uniform monolayer of a 50% mixture of 80/100 and 40/70 proppant, and a discontinuous, patchy, configuration of 40/70 proppant (Channel). These results were compared to a number of measurements using three monolayers of proppant, and also to tests where the samples were preconditioned by immersion in water for 18 hours prior to testing. This condition is intended to simulate the period of time that the fracture is in contact with the fracturing fluid prior to experiencing an increase in closure stress. Values of unconfined strength and Brinell hardness for these samples are reported in Section 1. These results show that the surface hardness for this samples increases in the following order: Haynesville, Marcellus and Barnett.

(i) Fracture conductivities of 0.01 mD-ft or lower are assumed to be too low for production. Thus, fractures with conductivities below this level should be ignored for production assessment.

(ii) All surfaces used in this comparative study are smooth (saw cut) and thus represent ideal and pessimistic conditions for fracture conductivity. In reality, fracture surfaces will have some asperities and these may help retaining additional conductivity.

(iii) In all cases, adding proppant to the fractures results in considerable increase in fracture conductivity, by several orders of magnitude, and a considerable reduction of the stress sensitivity. Typical reductions of fracture conductivity with stress for un-propped and propped fractures are 3 to 2 decades per 10,000 psi.

(iv) There is a great deal of consistency on the measured data between samples, and in general, there is no rock type differentiation. However, the rock type differentiation is present, and often is more apparent at low closure stress. The Haynesville samples are the most sensitive to stress. The Barnett samples are the most resilient.

(v) Mixed proppant and discontinuous proppant placement were tested for comparison with the standard uniform proppant experiments. Results indicate that the mixed proppant helps retaining fracture conductivity. However, it may also result in lower proppant pack permeability and thus increasing the plugging effect by debris, as a function of time. The effect of long term plugging by fines, produced solids, salt precipitation and others was not tested in this study and should be included for a proper appreciation of the various conditions of loss in fracture conductivity. Results also indicate that discontinuous proppant placement may results in increased fracture conductivity and increased retention of fracture conductivity with stress, if used in the appropriate rock.

(vi) The effect of water soaking the fracture surfaces prior to fracture conductivity testing shows a clear softening of the rock surface hardness and an associated loss in both fracture conductivity and fracture conductivity with stress. Surprisingly, the effect is stronger on the well cemented less clay-sensitive Barnett samples and less strong for the Haynesville and Marcellus samples. This may be so because the rock/proppant interaction for the latter are already strong and resulting is strong degradation of fracture conductivity even without fluid interaction.

(vii) Finally, results of tests with increased proppant concentration (3 monolayers instead of a single monolayer) show a consistent and strong increase in fracture conductivity and a reduction in stress sensitivity from 2 decades to 1 decade per 10,000 psi.

5 INTEGRATION OF THE LOSS OF EFFECTIVE SURFACE AREA AND CONNECTIVITY IN FRACTURE NETWORKS AND THE DEGRADATION OF FRACTURE CONDUCTIVITY

5.1 Introduction

The objective of this section is to integrate the results and concepts obtained from previous sections on fracture conductivity and fracture surface area into numerical models designed to demonstrate the impact of the measured properties on well production.

Key components of this effort are as follows:

(i) Evaluate numerically well production through fracture networks, with varying distributions of fracture conductivity within various branches. The simulations will be run with the results from un-propped and propped fractures.

(ii) Evaluate numerically well production through fracture networks using measured dependence of the conductivity with stress, under un-propped and propped conditions.

5.2 Background

In the discussion on the effect of fracture geometry and fracture conductivity, in Section 2.2, it was demonstrated via numerical models that the geometry and spatial variation of fracture conductivity within a hydraulic fracture has a significant impact on the production rate obtained from the fracture. In that work, several plausible fracture geometries were used to simulate production while assuming that the fracture conductivity remained constant throughout production. The laboratory conductivity tests discussed in Sections 3 and 4 demonstrated that fracture conductivity is a function of the closing stress acting normal to the fracture. Work conducted in Section 4 also demonstrated that the density and distribution of proppant within the fracture and the rock properties determine the degree to which the fracture conductivity decreases with stress. The objective of this section is to integrate via numerical modeling the combined effect that these conditions have on well productivity. To accomplish this, numerical simulations are presented that are similar to those discussed in Section 2, but with the additional feature of using the laboratory conductivity measurements defined in Sections 3 and 4, to determine how fracture conductivity and production potential vary as a result of increases in closure stress during production. Furthermore, to explore the effect of stress dependency of fracture conductivity, production simulations are presented with varying levels of horizontal stress contrast.

5.3 Methods

Well production is modeled using the equations of single-phase transient Darcy flow with the produced gas being modeled as an ideal gas. The rock matrix is modeled using linear

elasticity with a transversely isotropic vertical (TIV) stiffness tensor. The COMSOL finite-element package was used to solve these equations numerically. The parameters for these models, which are given in detail below, were measured in the material characterization tests discussed in Section 1.

The in-situ stress state for each play considered is estimated using measured transversely isotropic elastic properties and a passive basin approximation. Organic-rich mudstone reservoirs rocks have relatively low porosity (i.e. less than 10%) and exhibit a negligible amount of volumetric compaction. In addition, plastic dilation within the reservoir, during production, is also thought to be negligible. As a result, the coupling between the fluid transport and solid deformation is very weak and is neglected in this work. Therefore, the change in the effective stress at any point in the reservoir is only a function of the in-situ stress existing prior to production and the pore pressure at that point. This indicates that although a large uncertainty may exist in the absolute values of the in-situ stress at initial conditions, the relative change from this condition to the depleted condition, given the specified new reservoir pressure, will be well represented. Additionally, the effective closure pressure at a given point in the fracture network depends on the far-field total normal stress and the fluid pressure within the fracture:

$$P'_c = \sigma_h - \alpha P_f$$

where P_c' is the effective closure pressure, σ_h is the far-field total normal stress, α is the Biot coefficient for the *proppant pack* (here assumed to be 1.0), and P_f is the fluid pressure at a given point inside the fracture. As discussed above, the fracture conductivity decreases with effective closure stress, and as a result of the decrease in fluid pressure within the fracture during production. The conductivity at each point in the fracture is specified to be a piecewise linear interpolation of the values measured for each rock class as defined in Sections 3 and 4. Since the fluid pressure distribution within the fracture is non-uniform, so is the fracture conductivity.

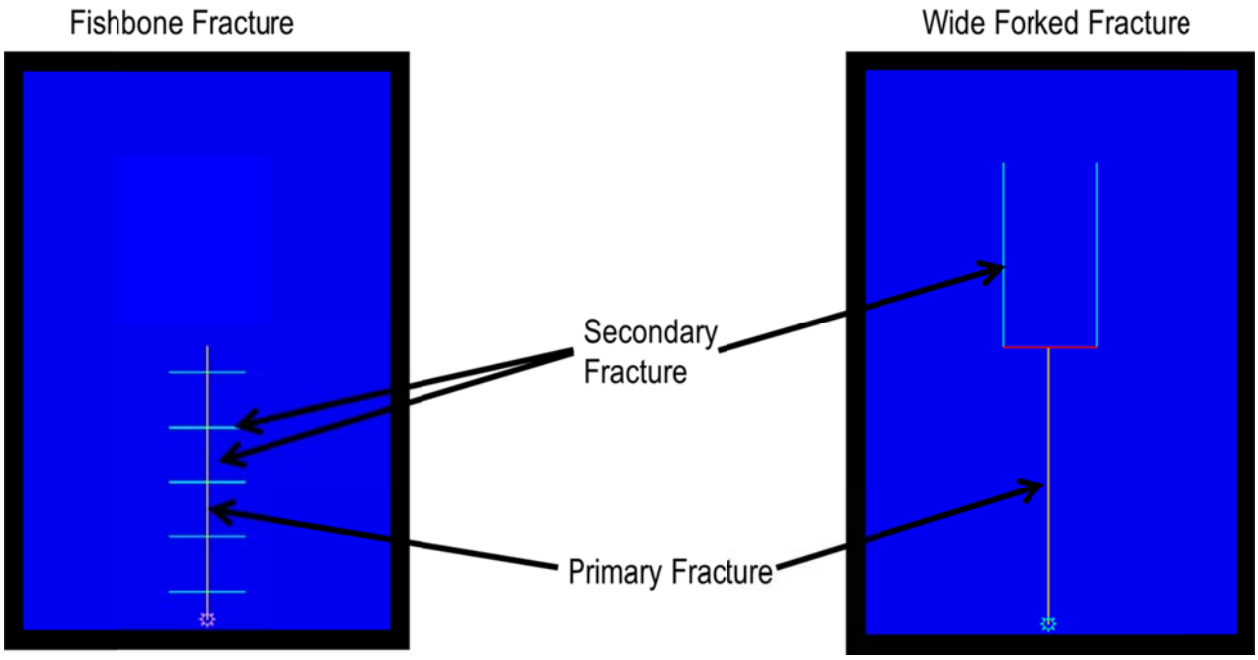

Figure 5.1 Fracture geometries used in the production simulations in this chapter.

Two different complex fracture geometries, which are shown in Figure 5.1, are used here. For the sake of comparison, the same primary and secondary fracture lengths and surface areas used in previous modeling, Section 2, will be specified for here as well. Specifically, the primary fracture, which is assumed to be well propped with multiple layers of proppant, is specified to have a half-length of 300 ft. With multiple layers of proppant the fracture conductivity is high and relatively insensitive to degradation with increases in closure stress. To model this situation the primary well-propped fracture is assumed to have a stress-insensitive fracture conductivity of 500 mD-ft. We understand, however, that a degradation of fracture conductivity over time will occur as a function of fines trapping, salt precipitation and the trapping of any type of debris that is transported from the far-field portion of the created fracture to the near-wellbore portion. This effect was not simulated here.

The secondary fractures, which are modeled using the stress-dependent propped or un-propped fracture conductivity data reported in Sections 3 and 4, have a total half-length of 400 ft. As defined previously (Section 2), the reservoir thickness is assumed to be 200 ft.

The Haynesville Light Blue rock class rock properties will be used in the simulations presented in this section. This rock class has the best reservoir quality in that play. The measured gas permeability of this rock class is 509 nD and the gas-filled porosity is 6.76%. A pore pressure gradient of 0.8 psi/ft. is assumed, which is reasonably representative of what is observed in the Haynesville play. Based on the geomechanical testing data and assuming a passive-basing approximation, the estimated horizontal stress gradient in this rock class is 0.96 psi/ft. This is also a reasonable approximation to minimum stress

measurements conducted in this play using D-FIT. Simulations will be presented with both zero horizontal stress difference and a stress difference of 500 psi (i.e. the maximum horizontal stress is 500 psi greater than the minimum in-situ stress). A typical reservoir depth of 12,500 ft. is assumed for the simulations presented.

Propped fracture conductivity was modeled using the 40/70 sand samples displayed at the top of Figure 4.2 and replicated below (Figure 5.2). Un-propped fracture conductivity was modeled using the un-propped data displayed in the same figure.

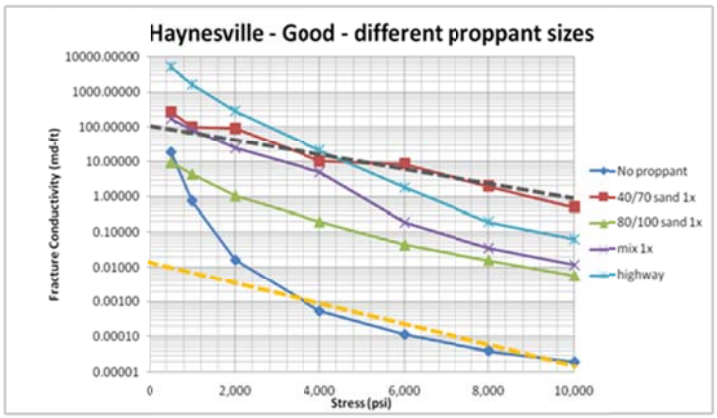

Figure 5.2 Fracture conductivity versus stress for Haynesville shale samples representative of a good reservoir quality facies. Changes in fracture conductivity with increasing stress and without proppant are compared to various proppant configurations, including discontinuous proppant placement (channel). The black and yellow dotted lines represent a reduction in fracture conductivity of 2 and 3 decades per 10,000 psi.

5.4 Results

5.4.1 Wide Forked Fracture Simulation Results

The pressure distribution within the reservoir at several points in time for the wide forked fracture with propped and un-propped secondary fractures is shown in Figure 5.3. The low pressure within the secondary fractures shows that the monolayer-propped secondary fractures have sufficient conductivity to significantly contribute to production. In contrast, the imperceptible change in pressure in the un-propped secondary fractures shown at the bottom of Figure 5.3 indicate that the un-propped secondary fractures do not have sufficient conductivity to contribute meaningfully to production.

Similar simulations were performed assuming constant fracture conductivity as well as assuming a 500 psi difference in the minimum and maximum horizontal stress. For the constant fracture conductivity case the propped fracture conductivity was as measured in Section 4 with the closure stress equal to the estimated in-situ effective stress of 2000 psi. For the case with horizontal stress anisotropy the primary fracture was assumed to be normal to the minimum horizontal stress, making the connectors between the primary and

secondary fractures normal to the maximum horizontal stress. The pressure distributions resulting from these two cases are indistinguishable from the propped conductivity simulation shown at the top of Figure 5.3.

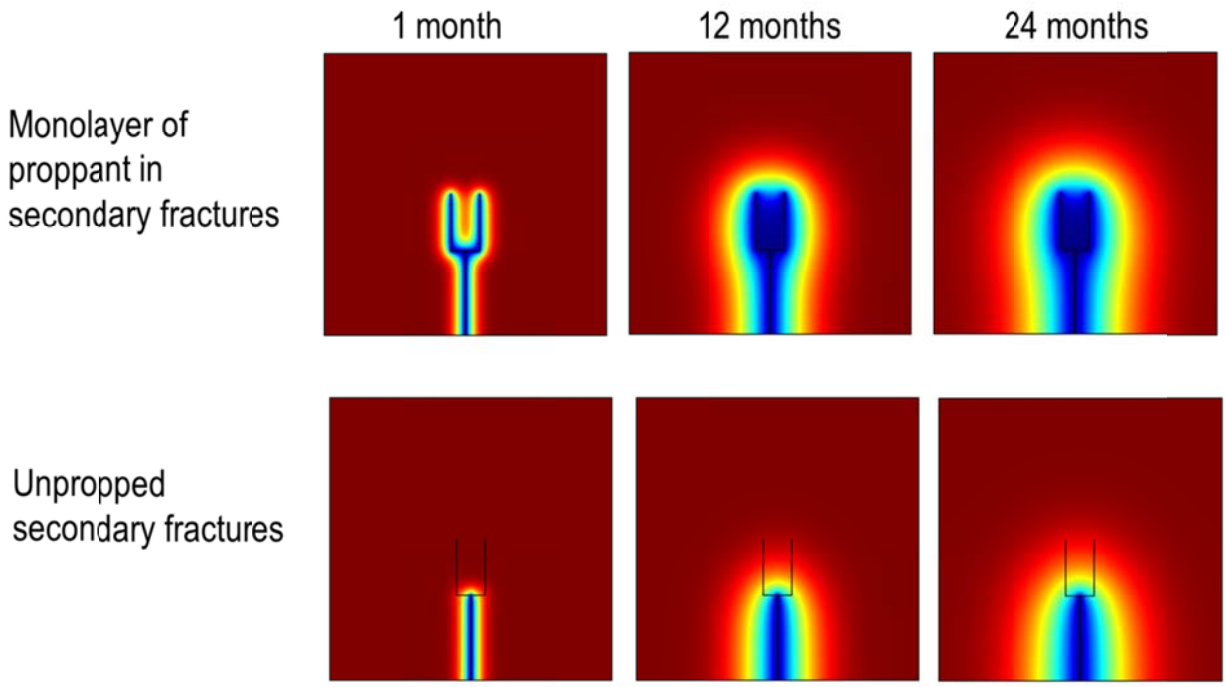

Figure 5.3. The pressure distribution within the reservoir for the wide forked fracture geometry after 1 month, 12 months, and 24 months of production. The top plots are for simulations with monolayer propped secondary fractures and the bottom plots are for simulations with un-propped secondary fractures. Red indicates high pore pressure and blue indicates low pore pressure.

Figure 5.4 is a plot of the production rate and cumulative gas production from the four simulations discussed above. As the plot illustrates, the predicted production from simulation with propped secondary fractures with constant conductivity, variable conductivity, and with horizontal stress anisotropy are indistinguishable from one another. The simulation with un-propped secondary fractures, on the other hand, shows a drastic reduction in the prediction production as compared to the propped cases.

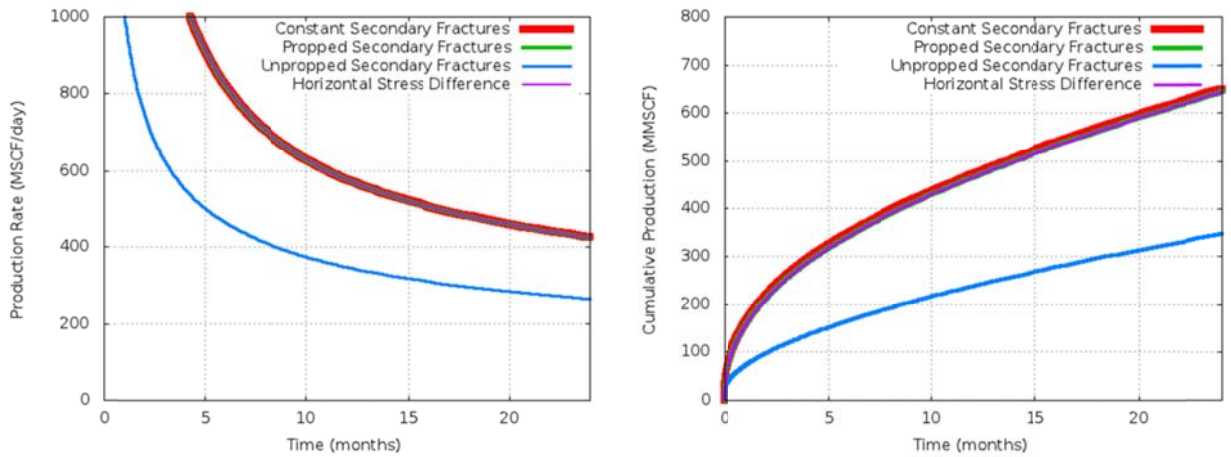

Figure 5.4. Production rate (left) and cumulative gas production (right) for various production simulations through the wide forked fracture geometry.

5.4.2 Fishbone Fracture Simulation Results

Figure 5.5 is a plot of the pressure distribution within the reservoir for the simulations with the fishbone fracture and monolayer propped and un-propped secondary fractures. As with the wide forked fracture geometry discussed above, the pressure distribution plots for the fishbone fracture reveal that the un-propped secondary fractures contribute little to production. A unique feature of the fishbone fracture geometry is that after approximately 12 months of production the reservoir is depleted nearly to the tips of the secondary fractures, after which point even the propped secondary fractures contribute little to production.

As with the wide forked fracture above, simulations were also performed with stress-insensitive propped fracture conductivity, and with a 500 psi contrast between the minimum and maximum horizontal stresses. For the fishbone fracture, all of the secondary fractures are aligned normal to the maximum horizontal stress. Nonetheless, as with the wide forked fracture geometry, the differences between all of the propped secondary fracture cases were negligible. This can be seen in the production rate and cumulative production plots for all of the fishbone fracture simulations shown in Figure 5.6. These plots show that the differences between the propped and un-propped cases, while still significant, are much less dramatic that they are with the wide forked fracture cases, shown in Figure 5.4. This is also the result of interference between the reservoir volume drained by the primary fracture and the secondary fractures.

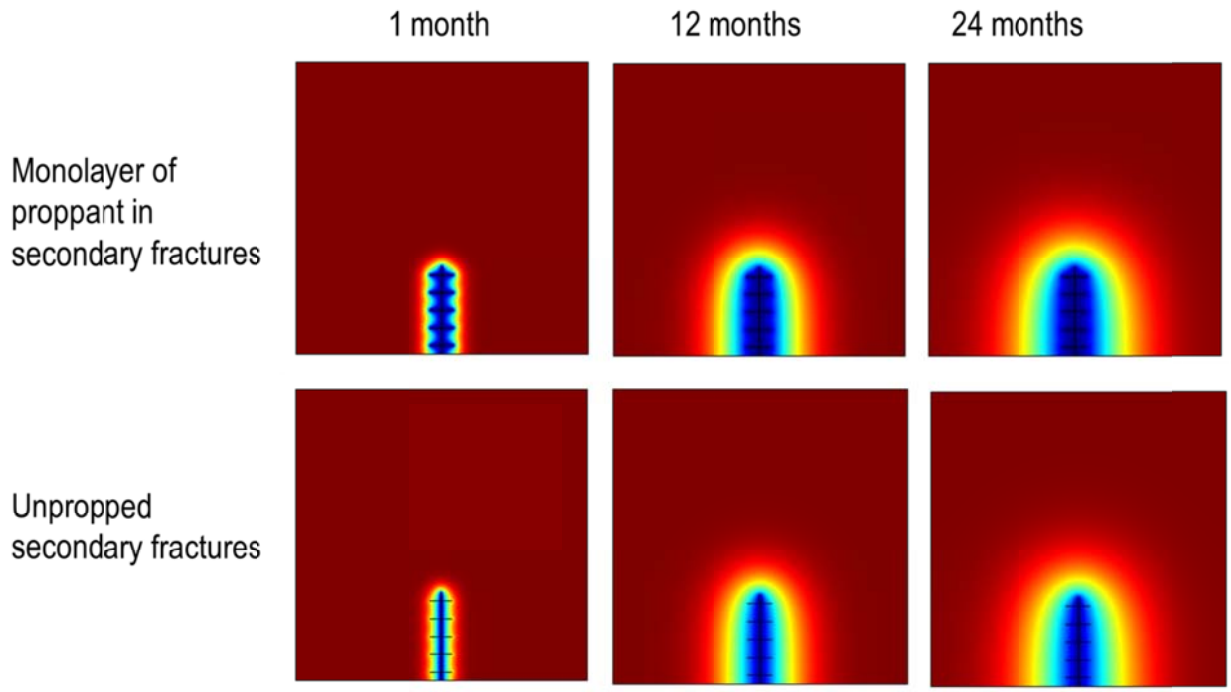

Figure 5.5. The pressure distribution within the reservoir for the fishbone fracture geometry after 1 month, 12 months, and 24 months of production. The top plots are for simulations with monolayer propped secondary fractures and the bottom plots are for simulations with un-propped secondary fractures. Red indicates high pore pressure and blue indicates low pore pressure.

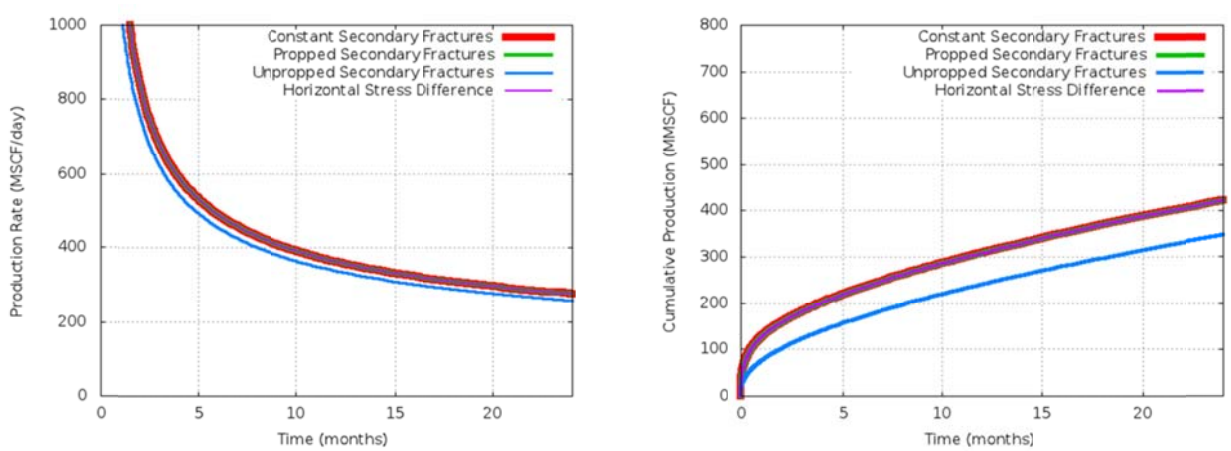

Figure 5.6. Production rate (left) and cumulative gas production (right) for various production simulations through the fishbone fracture geometry.

5.5 Discussion

In this chapter, we explored a range of possibilities existing in the primary and secondary fractures for enhancing or deteriorating productivity. In Section 2, we showed that convergence of flow from the far field fractures to the wellbore creates a substantial pressure difference that chokes production. Because the 2D nature of the simulations used in this chapter, this effect is not replicated here. Thus, the actual pressure drop is larger and the resulting fracture conductivity lower than simulated here. We argued that because the mode of proppant transport in slick water fracturing (dune effect), the primary, near-wellbore, fracture contains most of the proppant, and has more proppant concentration and more fracture conductivity than needed. We also argued that having multiple layers of proppant reduces the importance of the proppant-rock interaction and thus reduces the stress sensitivity of fracture conductivity, in this region. Under this conditions of constant primary fracture conductivity (500 mD-ft), we have compared the influence of the secondary and tertiary fractures to production.

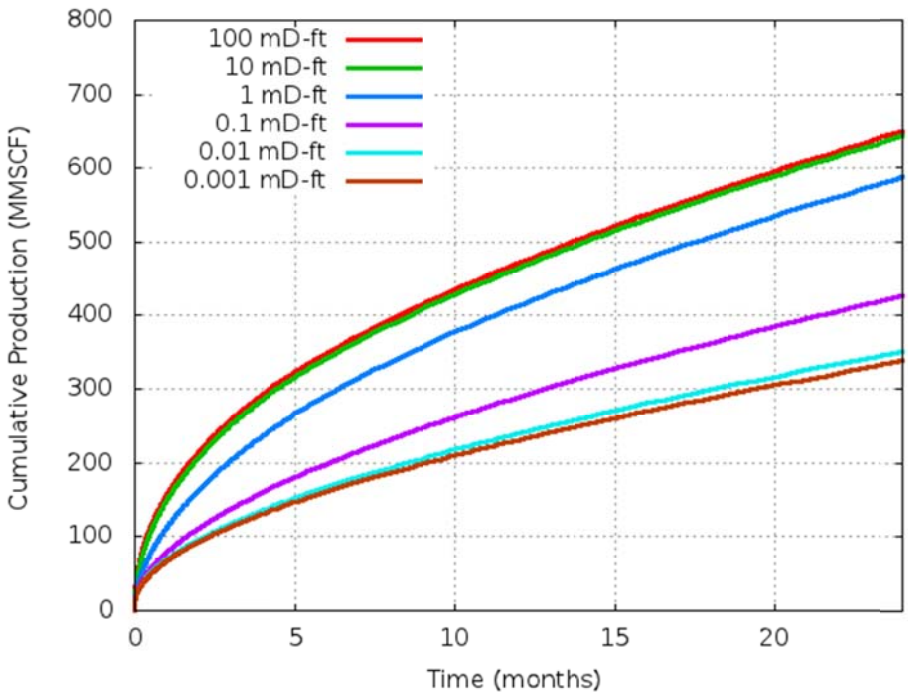

Figure 5.7. Cumulative gas production from the wide forked fracture with various values of secondary fracture conductivity.

To better understand how changes in the secondary fracture conductivity affects production, a series of simulations were performed using the forked fracture geometry and various values of secondary fracture conductivity. Figure 5.7 is a plot of the cumulative production from each of these simulations. The figure shows that fracture production with contribution from secondary fracture conductivity of 100 mD-ft and 10 mD-ft is nearly identical, and a secondary fracture conductivity of 1 mD-ft results in a relatively small

reduction in production. Thus, the two decade reduction in fracture conductivity, over 10, 000 psi, which is characteristic of the 40/70 proppant in the Haynesville shale, does not provide sufficient change as to affect the overall flow performance. Once the secondary fracture conductivity is reduced to 0.1 mD-ft., however, the production is reduced sharply. This would be the case for the other propped cases of 80/100, 50% mixtures of 40/70 and 80/100, and the discontinuous proppant configuration (channel).

In the simulations presented in Section 5.4, the well flowing pressure was set to be 2,000 psi less than the pore pressure. The resulting maximum possible closure pressure on any hydraulic fracture is then approximately 4,000 psi. With 4,000 psi closure pressure and a monolayer of 40/70 proppant the measured conductivity on the Haynesville Light Blue rock reported in Section 4 is 10.1 mD-ft. Therefore, even at the highest closure stress possible the secondary fractures with only a monolayer of proppant are still effectively infinite conductivity fractures. On the other hand, the un-propped fracture conductivity on this rock class at the same level of closure pressure is 0.0005 mD-ft. With this value of fracture conductivity the secondary fractures are not able to effectively drain the surrounding reservoir.

We understand that fracture conductivity of the primary fracture can decrease substantially in this region as a function of time due to plugging with fines, salt precipitation and debris arriving from the fracture far field boundaries. We have also argued that the permeability at the fracture face may change substantially (due to embedment and the uniformity of the pack on the near wellbore fracture). Thus, it seems reasonable to anticipate that as the fracture conductivity of the primary fracture decreases with time, the relative contribution of the secondary and tertiary fractures to production may also change with time and depletion. They may be less relevant initially and more important later on.

5.6 Summary

Production simulations were performed using the rock mechanical and reservoir properties for the Haynesville shale best reservoir quality rock (Light Blue rock class). For this rock class, a propped fracture with a monolayer of 40/70 sand has a fracture conductivity of 10.1 mD-ft at a closure stress of 4000 psi. Assuming fork fracture geometry, for the secondary fractures, and using the reservoir properties measured in Section 1, these propped fractures exhibit an effectively infinite conductivity and therefore contribute effectively to the production of hydrocarbons to the wellbore. For this reason, for this rock class, and the given proppant type and concentration, no significant reduction in well production would be expected as a result of depletion or changes in drawdown, and consequent increase in closure stress, during production.

Simulations performed with un-propped secondary fractures indicate a dramatic reduction in production as compared to the monolayer-propped secondary fracture simulations. This indicates that un-propped fractures do not significantly contribute to production at any conditions of fracture closure stress.

6 LARGE-SCALE SIMULATION OF FIELD PRODUCTION – BLOCK TESTING

6.1 Introduction

The objective of this section is to use fracture geometry characterization and fracture conductivity measurements on a large-scale shale block, to validate results obtained in previous sections. A Niobrara shale outcrop block (approximately 3 ft. x 3 ft. x 3ft.) and representative of the reservoir facies of the Niobrara formation was used.

Components of this effort are as follows:

(i) Induce a hydraulic fracture and measure its un-propped fracture conductivity at various levels of closure stress. After completion of the un-propped fracture conductivity, transport proppant into the fracture and evaluate fracture conductivity, finally, evaluate proppant embedment as a function of stress and time.

(ii) Monitor fracture propagation with acoustic emission and acoustic transmission measurements.

(iii) If possible, image the block using X-ray computer tomography before and after testing, to investigate the effect of the rock textural complexity on hydraulic fracture complexity.

(iv) Measure the surface area and surface roughness of the produced fracture. Measure the distribution of proppant on the created fracture surface. Measure the amount of proppant embedment and proppant crushing after the stress cycles.

Fracture conductivity, measured as a part of this large-block test, was compared to core-scale measurements, made in Sections 3 and 4. To understand the comparison, it is important to highlight several key differences between the large-block test conductivity and those on small samples, discussed as part of Sections 3 and 4. The large-block test offers an opportunity to understand differences associated with changes in scale.

Also, the large block offers an opportunity to evaluate surfaces that are created via hydraulic fracturing. These are strongly affected by the rock fabric effect. This is not the case on the small samples that were predominantly conducted on saw cut surfaces. Fabric complexity results in fracture complexity, complex flow paths, and heterogeneous distribution of proppant. Finally, in the large block test, proppant is transported and deposited by fluid flow. In the small samples, it is deposited manually, to produce uniform monolayer coverage across the surface.

The large-block fracture propagation and fracture conductivity test described in this section help us understand the relationship and representativeness of small sample testing to the larger-scale processes occurring in-situ.

6.2 Large-scale Simulation (Block Test) Methodology and Results

6.2.1 Objectives

The following were the objectives for this test:

1) Create a planar hydraulic fracture, with simple geometry, using Niobrara outcrop shale sample, and using Glycerol as the fracturing fluid.
2) Measure un-propped fracture conductivity at different levels of fracture closure stress.
3) Inject and transport 100 mesh proppant into the fracture.
4) Measure propped fracture conductivity at different levels of fracture closure stress.

6.2.2 Testing Equipment

6.2.2.1 Loading System

This test was performed in TerraTek's large block multi-axial stress frame. The stress frame makes it possible to apply unique stresses in three principal directions, North-South (N-S), East-West (E-W), and Top-Bottom (T-B). The stresses are generated using four flatjacks for the horizontal directions and actuators in the vertical direction. Flatjacks are planar steel bladders that are pressurized with fluid to expand and transmit loads to the sample inside the stress frame. The stress frame can apply a maximum vertical stress of 10,000 psi, and a maximum horizontal stress of 8000 psi. A photo of the large stress frame can be seen in Figure 6.1.

Three sets of continuous injection intensifier pumps were used to create and supply the pressure for the flatjacks. The continuous pumps are computer controlled and may be operated in either volume or pressure control. For this series of testing the pumps were run in constant pressure/stress control.

Figure 6.1. A photograph of TerraTek's large multi-axial stress frame is shown.

6.2.2.2 Injection System

A 40 hp hydraulic pump was used in-line with a pressure intensifier for the fluid injection during the testing. The intensifier was used to generate the bore pressure that was necessary to fracture the block sample. It can generate a maximum of 10,000 psi and has a volume capacity of 3.27 liters. The intensifier flow rate was computer controlled during the block testing.

For the proppant injection phase, a continuous displacement MOYNO pump was used. Lastly, a separate (TerraTek system) continuous injection system was used for fracture conductivity measurements.

6.2.3 Sample Preparation and Quality Control

The Niobrara shale outcrop used for this testing program was acquired from a quarry located in Colorado near the city of Denver. The approximate location of the quarry is shown on a regional map in Figure 6.2.

The boulder from which the rock was cut is shown in Figure 6.3. The block was cut with a large rotary impregnated diamond saw to the final dimensions of 27.25 in x 27.25 in x 32 in. An initial cut was made on the bottom of the sample. The sample was then placed bottom side down on this initial cut and the four vertical faces were cut, forming the sides of the block. Using the sides as a reference, the top face was cut perpendicular to the sides. The final face was cut from the bottom surface, parallel to the top face, completing the block. This process was done such that the bedding planes were oriented perpendicular to the longest axis of the block.

Figure 6.2. The approximate location of the Niobrara quarry is shown.

Figure 6.3. Niobrara boulder acquired from the quarry. The surfaces are painted for preventing changes in humidity during transport and storage.

A visual evaluation of the sample was conducted to characterize the rock fabric prior to testing, as shown in Figure 6.4. The photos show the bedding orientation, a large distribution of calcite inclusions predominantly oriented parallel to the bedding and the presence of partings along planes of weakness. The photos also show that the bottom section of the block represents a different geologic facies, which is more homogeneous and less laminated than the rest of the block.

To highlight the partings along planes of weakness, a second set of photographs were taken after dabbing the surfaces of the block surface with odorless mineral spirits (OMS). These are shown in Figure 6.5. OMS is a low viscosity hydrocarbon, inert to the rock chemistry, and one that imbibes easily into hairline fractures and then evaporates, making them temporarily more visible. The photographs show a large number of partings along the direction of bedding as well others that occur oblique to bedding. The presence of lithologic contacts, bedding planes with different degrees of weakness, parted interfaces, calcite interfaces, hairline mineralized fractures, and the various partings in directions oblique to bedding provide the rock with a large amount of textural complexity.

Understanding this fabric is fundamental for understanding the evolution hydraulic fracture propagation during testing. As it will become apparent in the subsequent section, the resulting hydraulic fracture was complex despite the fact that several design choices were taken to promote a simple fracture.

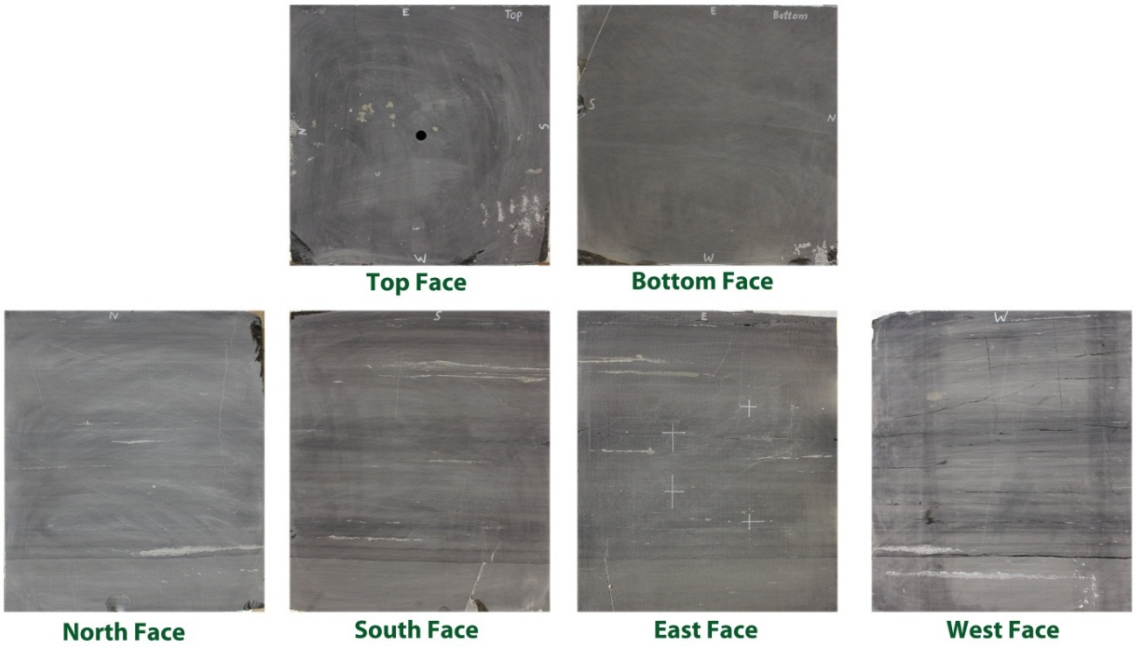

Figure 6.4. Photographs of all faces of the block showing calcite inclusions.

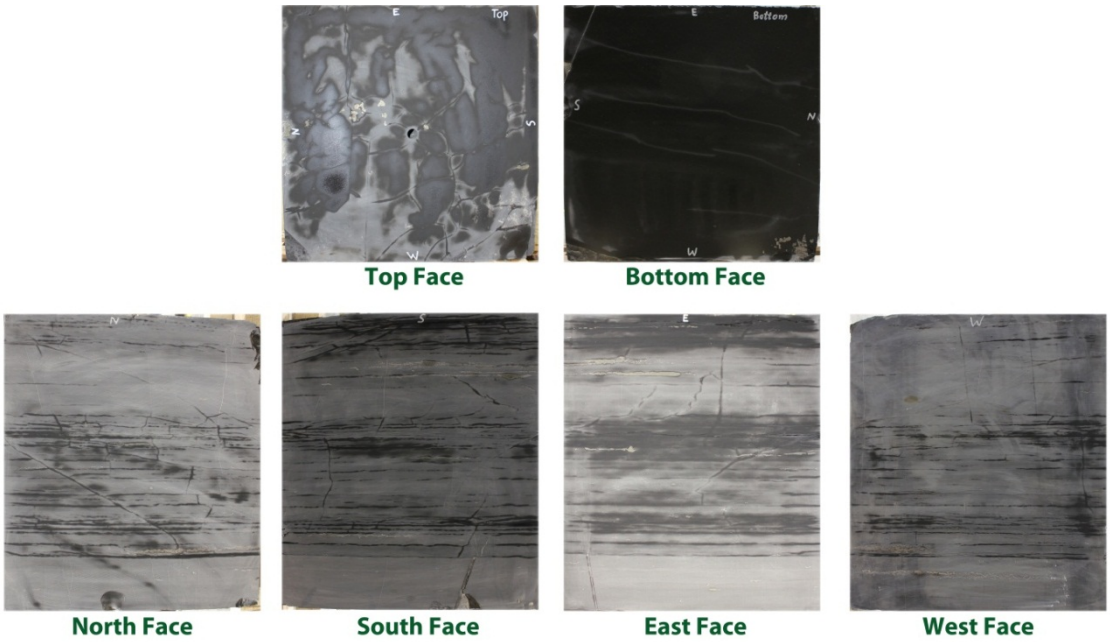

Figure 6.5. OMS dabbed on the block surfaces highlight the texture of the rock fabric.

6.2.4 Experimental Set-up and Procedures

After preparation of the block and successful quality assessment, a wellbore was drilled in the direction perpendicular to bedding. This is also the direction of the applied maximum stress during testing, to represent a vertical completion. The wellbore was a partially penetrating wellbore of 1.06 inches in diameter and 22 inches long, and was drilled vertically at the center of the top surface of the block. A stainless steel casing, 17 in long, with a 1.0 inch outside diameter and a 0.75 in inside diameter was fabricated and secured to the wellbore with epoxy. The position of wellbore and casing inside the block is shown in Figure 6.6. The steel casing extends 15 inches into the wellbore, leaving the last 7 inches open between 15 and 22 inches. Slots of 7 inch length and 12 mm penetration were sandblasted along the openhole section, to facilitate fracture initiation and breakdown.

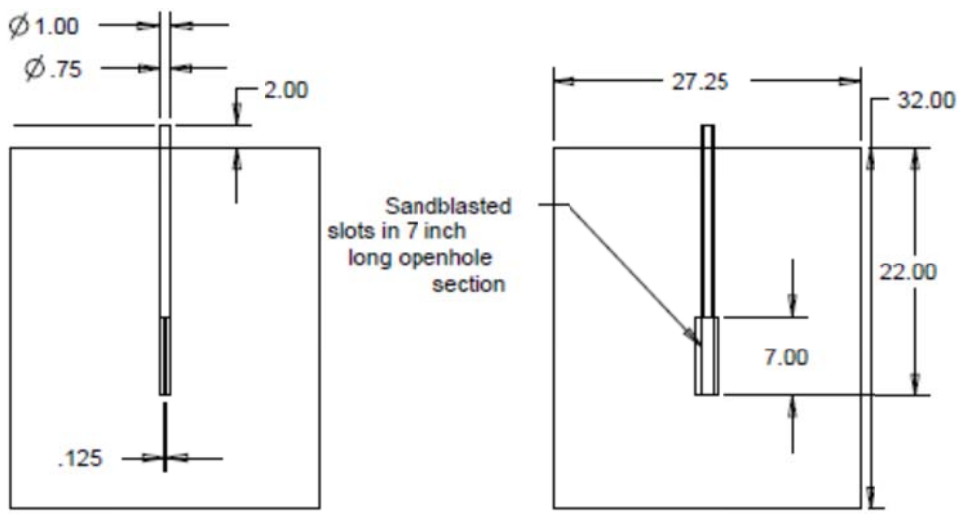

Figure 6.6. A drawing of the sample configuration is shown.

After preparation of the wellbore, multiple pockets were drilled along the sample surfaces to accommodate ultrasonic acoustic sensors, for evaluation of acoustic wave propagation and acoustic emissions localization during testing. This setup also required the creation of groves along the surfaces of the sample for accommodating the connecting cables. Figure 6.7 and Figure 6.8 show examples of this setup, along the south and west faces of the block. Quality control of acoustic sensor system was conducted multiple times: under bench conditions, prior to loading the sample to the loading frame, and at various stages during loading. These procedures and the results of these measurements are provided in the Acoustic Measurements section.

After installing the acoustic transducers and the connecting cables, these pockets and grooves were sealed with clay and then hydro stone. On completing this setup, the block was strapped with bands to secured and prevent the generation of additional partings during handling.

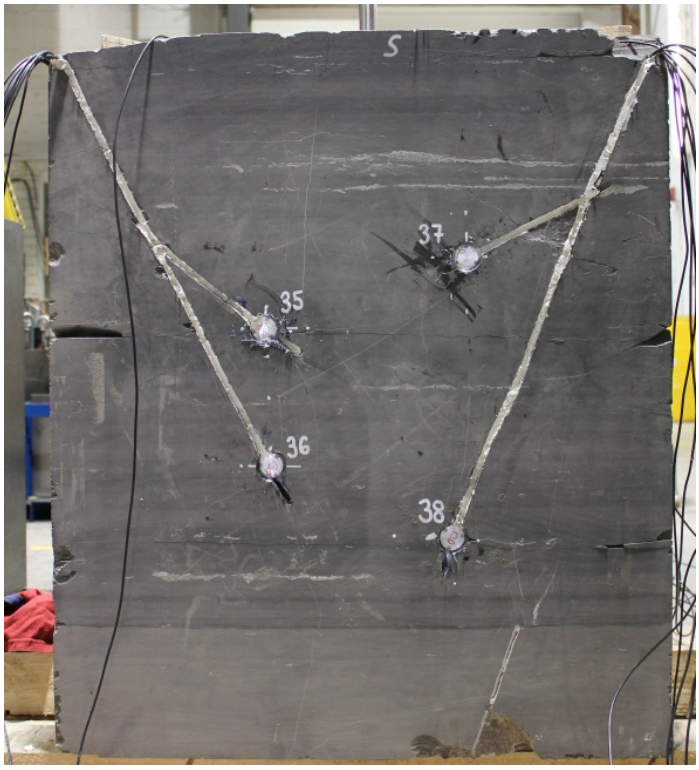

Figure 6.7. AE sensor pockets drilled on the south face of the block.

Figure 6.8. AE sensor pockets drilled on the west face of the block.

The hydraulic fracture was designed to propagate in the North and South direction and a 200 *u*m x 200 *u*m steel mesh was installed on the rock on the North and South faces, to collect proppant and fines during injection after the initial fracturing stage.

The important steps in the set-up process include:

- Placement of the block in a steel can and filling the annular gap between the rock and the can with a permeable layer of high strength 30/60 mesh proppant.
- Placement of two 0.25" flow tubes in the proppant pack along the North face of the block. These were placed 16 inches deep and were used to measure the pore pressure in the proppant and for fluid flow out of the can.
- Placement of a third flow tube in the proppant pack along the South face of the block and 2 inches deep. This was used to saturate the bead pack before the fracture conductivity measurements.
- Sealing the top section of the can with a precast polyurethane sheet 27.5 in. x 27.5 in. x 1in. with 5 in centered hole.
- Placement of the loading top plate, flat jacks, spacers and ancillary components of the axial loading system.
- Making the acoustic transducer cables accessible to the exterior of the block through the can corners and through the sealing plate.
- Bled air from the hydraulic system, including the flatjacks.
- Connect the flatjacks, actuators and wellbore to the corresponding components of the injection and injection control system

6.2.5 Test Results

The description of test results is divided into the following five sections:

1) Hydraulic Fracturing
2) Borehole Cleanout
3) Un-propped Fracture Conductivity Measurements
4) Proppant Transport
5) Propped Fracture Conductivity Measurements

6.2.5.1 Hydraulic Fracturing

As indicated in Section 9.1, the first objective in this test was to obtain a planar fracture, with reasonable width and simple fracture geometry, to allow proppant transport with slick water. To accomplish this, the initial fracture was conducted with 1000cp glycerol, at a constant injection rate of 1000 mL/min, and with the sample subjected to representative in-situ stress and with a significant stress contrast in the plane perpendicular to the plane of the fracture.

Given the presence of weak interfaces in this sample, prevention of shear failures during loading was critical to the success of the test. For this, we imposed a loading protocol that minimized the development of shear stress at low confining stress. A summary of the testing conditions are shown in Table 6.1. The details of the application of the applied external stresses to the rock are listed in Table 6.2.

The stress histories applied during this test are shown in Figure 6.9. These were increased to a maximum hydrostatic stress of 4000 psi on all sides and then reduced individually in each direction to obtain the desired final loading. The associated change in flatjack volumes during this same time period are shown in Figure 6.10. These measurements are best considered in a relative sense and not on their absolute values. Differences in the loading system (flatjacks versus actuators) and the associated compliances in the interfaces (including spacers, flatjacks, polyurethane pads, can, and proppant pack) complicate the evaluation of the absolute rock deformation. The intensifier and borehole pressurization history, injected borehole volume and the applied stresses are shown in graphical format in Figure 6.11.

Borehole fluid injection at 1000 mL/min started at approximately 138.42 minutes after the application of stress to the rock. The injection continued at a constant rate until borehole breakdown was observed, at a pressure of 4202 psi. Fluid injection was continued at the same rate, during fracture propagation, as the borehole pressure dropped continuously and stabilized at a pressure of 1585 psi.

Figure 6.12 shows the flatjack volumetric deformation, for the duration of the injection period. Figure 6.13 shows borehole pressure and flatjack volumetric deformation closer to the wellbore breakdown. At approximately 138.67 minutes, a reduction in East-West flatjack volumes was observed which is slightly before the wellbore breakdown was measured. This response suggests opening of a longitudinal fracture. The small volumetric deformation in the North-South flatjack volume suggests momentary opening of a fracture against the intermediate stress, which closes immediately after. Furthermore, the stabilized pressure response after 139 minutes indicates that the fracture geometry has stopped developing and that the fracture has reached the boundary of the rock.

Table 6.1. Test details and conditions for test

Test:	203871-RPSEA-Niobrara
Completion:	Vertical completion with a cased borehole and 7 inch long open hole section located 15 inches to 22 inches from the top face of the block. Two sandblasted slots in the north and south direction were created along the length of the open hole section
Block Size:	27.25 in x 27.25 in x 32 in
Rock Type:	Niobrara Shale
Fracturing Fluid:	Glycerol, 1000cP
Acoustic Emission Sensors:	37 P-wave sensors were installed in bored pockets, distributed on the five faces of the block.
Vertical Stress	σ_1 = 4500 psi (Top-Bottom
Maximum Horizontal Stress	σ_2 = 3000 psi (North-South)
Minimum Horizontal Stress	σ_3 = 1000 psi (East-West)

Table 6.2. Details of loading history for the lower completion are shown below

Loading State	Top-Bottom Stress (psi)	North-South Stress (psi)	East-West Stress (psi)	Ramp Rate (psi/min)
1	3000	3000	3000	200
2	4500	4500	4500	200
3	4500	3000	3000	200
4	4500	3000	1000	200

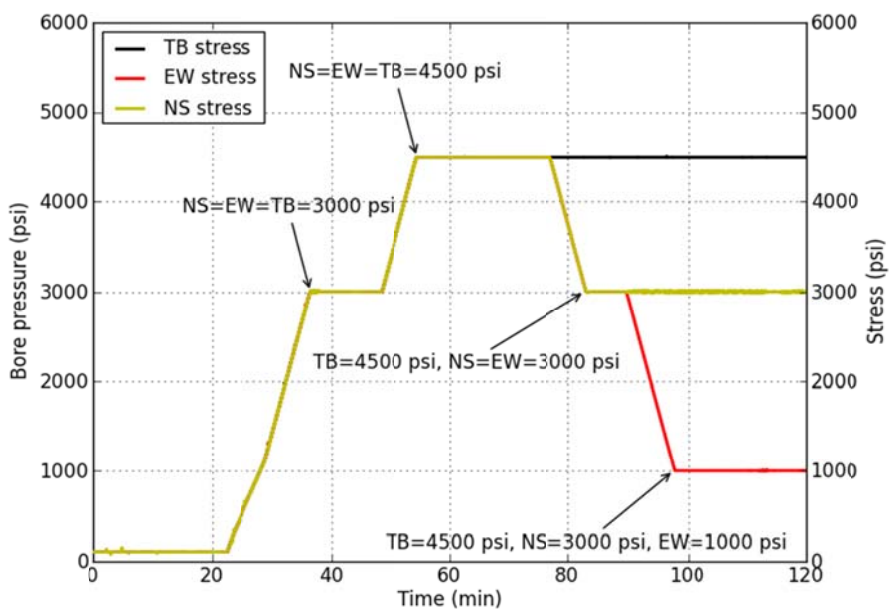

Figure 6.9. Block pressurization history prior to wellbore injection is shown in a graphical format.

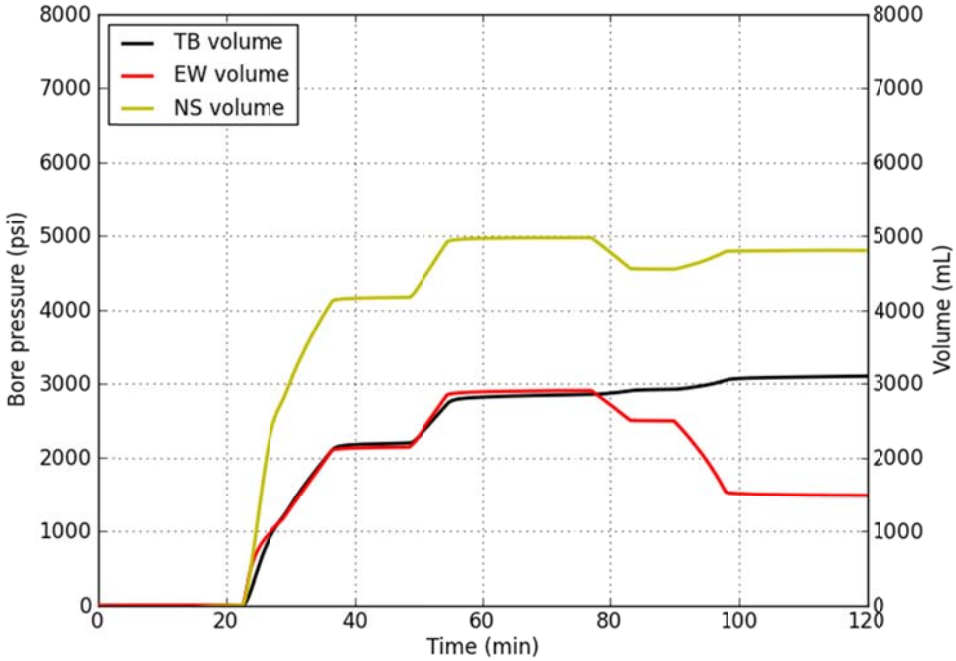

Figure 6.10. The change in flatjack volumes, as a function of applied stress, versus time is shown for the period preceding borehole fluid injection. The nonlinearities in the traces up to approximately 37 minutes reflect the stiffening up of the system as the flatjacks seat and the compliance of the system is reduced. Differing injected fluid volumes over each loading period are reflective of the rock anisotropy.

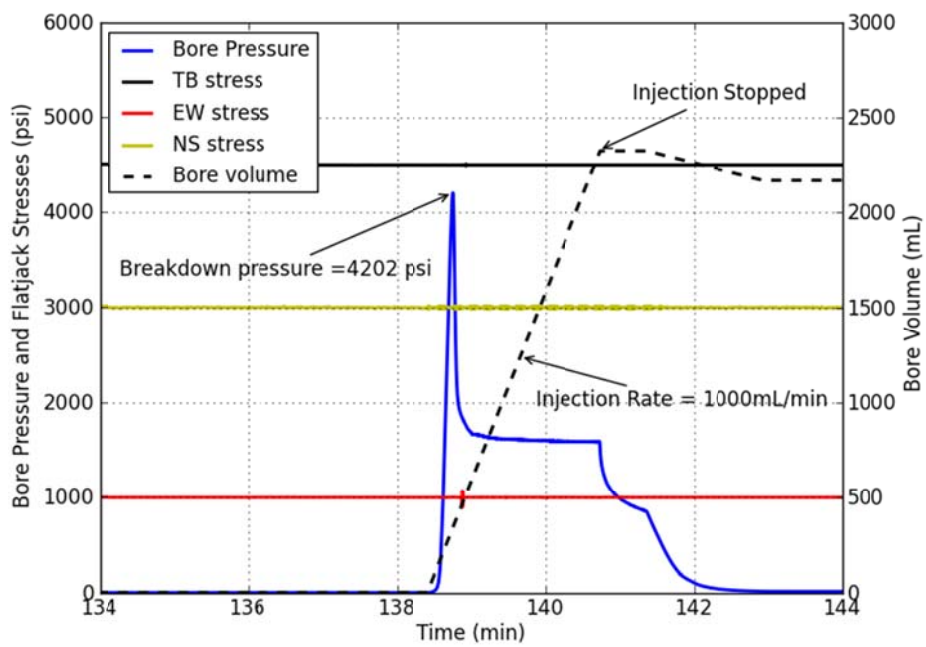

Figure 6.11. Bore pressure, bore volume and applied stresses versus time from the beginning of borehole fluid injection.

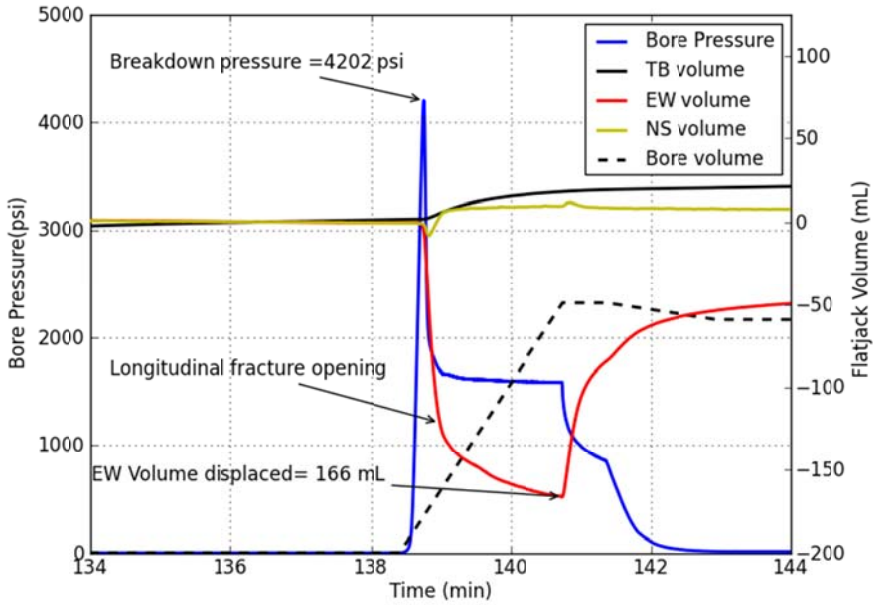

Figure 6.12. Bore pressure, and flatjack volumetric deformation versus time commencing with borehole fluid injection.

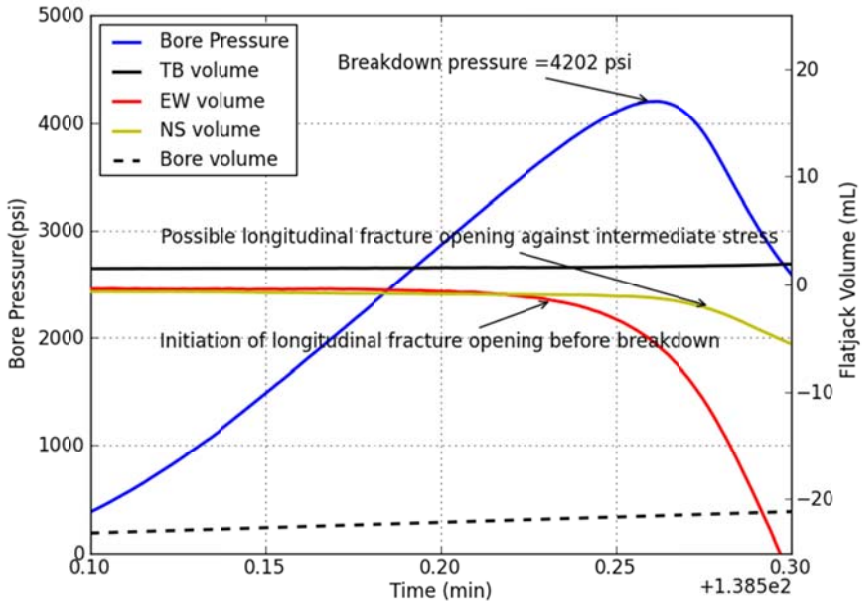

Figure 6.13. Borehole pressure and flatjack volumetric deformation measurements closer to the breakdown are shown.

6.2.5.2 Borehole Cleanout

After hydraulic fracturing, the applied stresses to the sample were reduced as shown in Figure 6.14, to facilitate the measurements of fracture conductivity and to develop sufficient width for proppant entry and transport. Figure 6.15 shows a diagram of the test setup for fracture conductivity measurements. The glycerol used for the fracturing stage was flushed by injecting water at approximately 6 liters/min for a period of 20 minutes. The borehole pressure was monitored during water injection to keep it below the maximum applied stress of 1000 psi and prevent re-fracturing. Figure 6.16 shows the applied stresses and the borehole pressure during the glycerol displacement. Three stages of injection were conducted. The first two stages of injection are shown in Figure 6.16. The initial high wellbore pressure and subsequent continuous decay results from the hydration and displacement of glycerol from the fracture. The stabilized pressure response at the end of the first cycle and identical pressure response during the second cycle indicates that the glycerol has been fully replaced with water. Figure 6.17 shows the minimum stress applied to the rock sample, the borehole pressure and the back pressure (pressure in the steel can) versus time during the third stage of injection. During the third stage of water injection, the fluid injection rate was kept constant at 6 l/min. The borehole pressure was constant between 182.5 and 185.75 minutes. At 187.75 minutes the borehole pressure started dropping and the back pressure (in the steel can) started increasing. The back pressure reached a maximum of 32 psi. At this point the injection rate was reduced to keep the back pressure below the minimum confining stress.

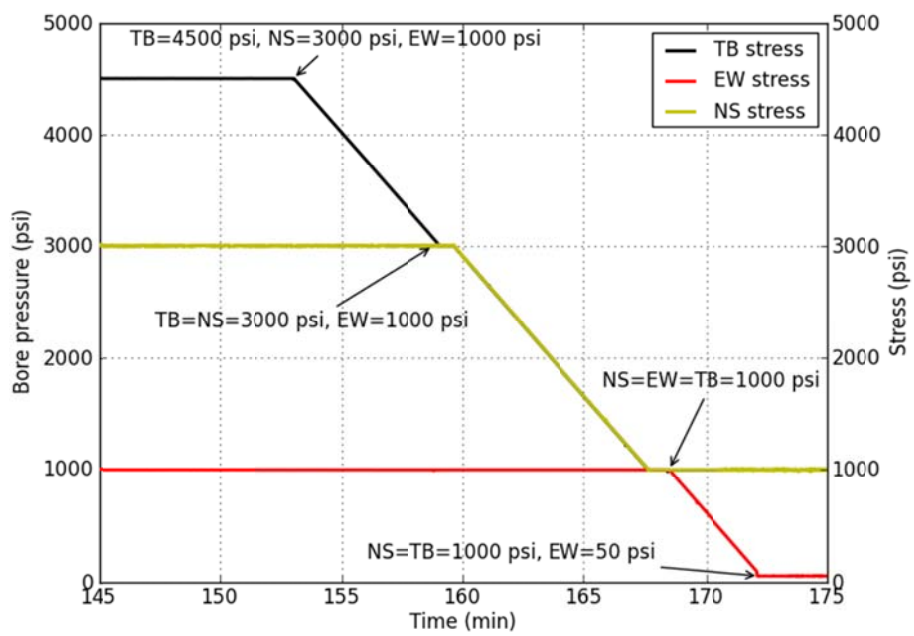

Figure 6.14. Post hydraulic fracturing stress down phase is shown.

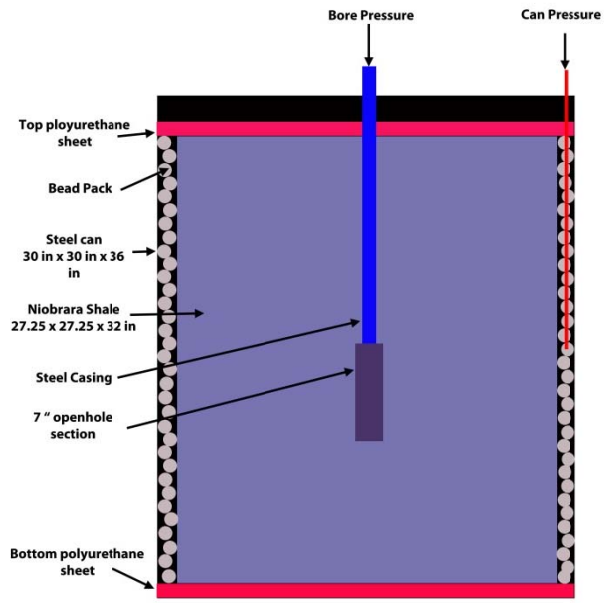

Figure 6.15. Diagram of the test setup is shown.

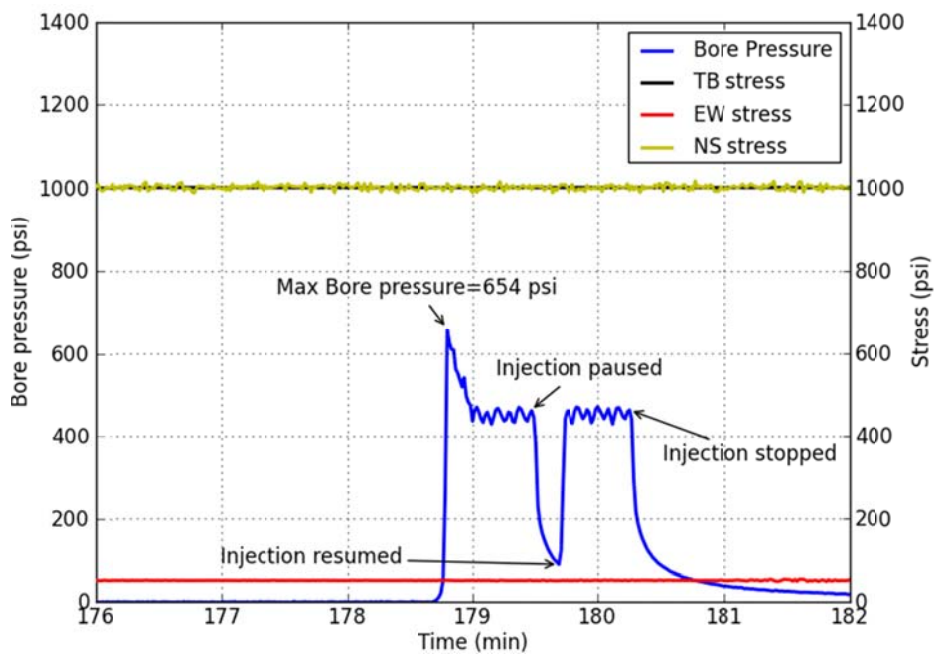

Figure 6.16. Borehole pressure and applied stresses during first two stages glycerol flushing phase are shown.

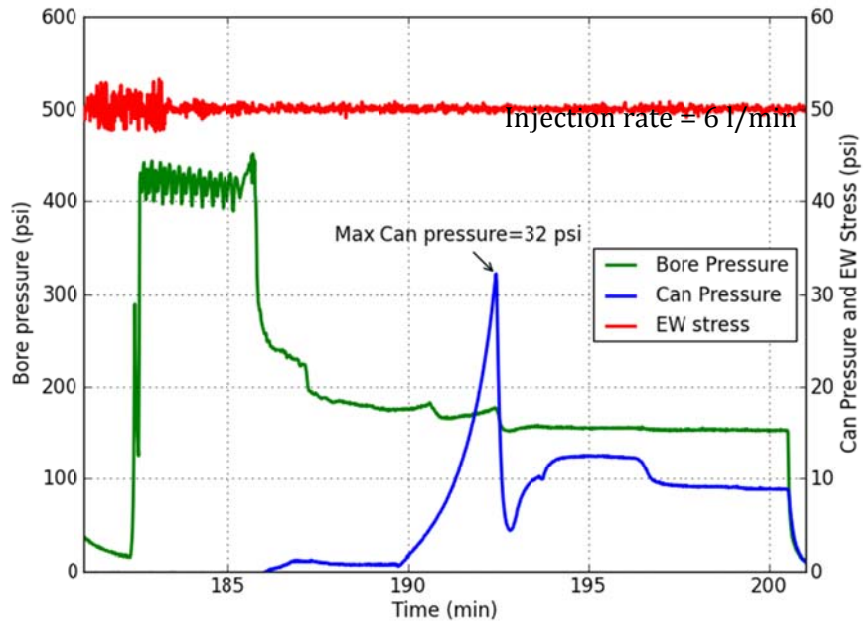

Figure 6.17. Borehole pressure, bead pack (pore) pressure and applied minimum stresses during the third stage of glycerol flushing phase are shown.

6.2.5.3 Un-propped Fracture Conductivity Measurements

After borehole cleanout, the borehole injection system was switched from the high-rate MOYNO pump to continuous intensifier system. The goal was to measure fracture conductivity at different levels of the fracture closure stress. To achieve this, the applied stresses were initially set to σ_v = 1000 psi, σ_H = 1000 psi and σ_h = 500 psi. The fluid injection control system was used to specify a pressure difference of 100 psi between the borehole and the bead pack surrounding the block. This differential pressure was maintained until the flow rate into the borehole required to maintain the specified differential pressure reached a steady-state value. The differential pressure was then increased to 200 psi, then 300 psi and the steady-state flow rate was measured in each case. Figure 6.18 shows a plot of the specified differential pressure and flow rate measurements for this case. These flow measurements were later used to calculate the effective fracture conductivity as described below. After the flow measurements were taken with σ_h = 500 psi, the normal load was increased to σ_h = 1000 psi, and three more flow measurements were made to compute the fracture conductivity with the increased closure stress. This process was repeated for a total of four closure stress values using the parameters shown in Table 6.3. Figure 6.18, Figure 6.20, Figure 6.22, and Figure 6.24 show plots of the pressure and flow rate measurements for each value of the closure stress.

For each value of the closure stress a linear regression curve was fit to these pressure/flow measurements. The data points and regression curves for each case are shown in Figure 6.19, Figure 6.21, Figure 6.23, and Figure 6.25. The slope of these regression curves was then used together with finite-element simulations of flow through the fracture, to numerically invert for the effective fracture conductivity. Figure 6.26 shows an example flow field from one of the numerical simulations used to perform this inversion. The calculated effective conductivity for each value of the closure stress is shown in Table 6.3.

Table 6.3. Applied stress conditions, measured differential pressure, an approximate flow rate and calculated Fracture conductivity at each stress state for un-propped fracture conductivity measurements are listed

	NS Stress psi	EW Stress psi	TB Stress psi	Estimated Fracture Delta P psi	Approximate Flow Rate mL/min	Best-Fit Fracture conductivity mD-ft
	1000	500	1000	5.8	25	
Stage 1	1000	500	1000	11.6	65	20.2
	1000	500	1000	17.4	117	
	1000	1000	1000	192	41	
	1000	1000	1000	321	75	0.7
Stage 2	1000	1000	1000	385	89	
	1000	1000	1000	481	94	
	2000	2000	2000	687	22	
Stage 3	2000	2000	2000	918	27	0.1
	2000	2000	2000	1377	45	
	2000	2000	2000	1606	60	
	4000	4000	4000	1702	11	
Stage 4	4000	4000	4000	2917	27	0.035
	4000	4000	4000	3160	39	
	4000	4000	4000	3404	41	

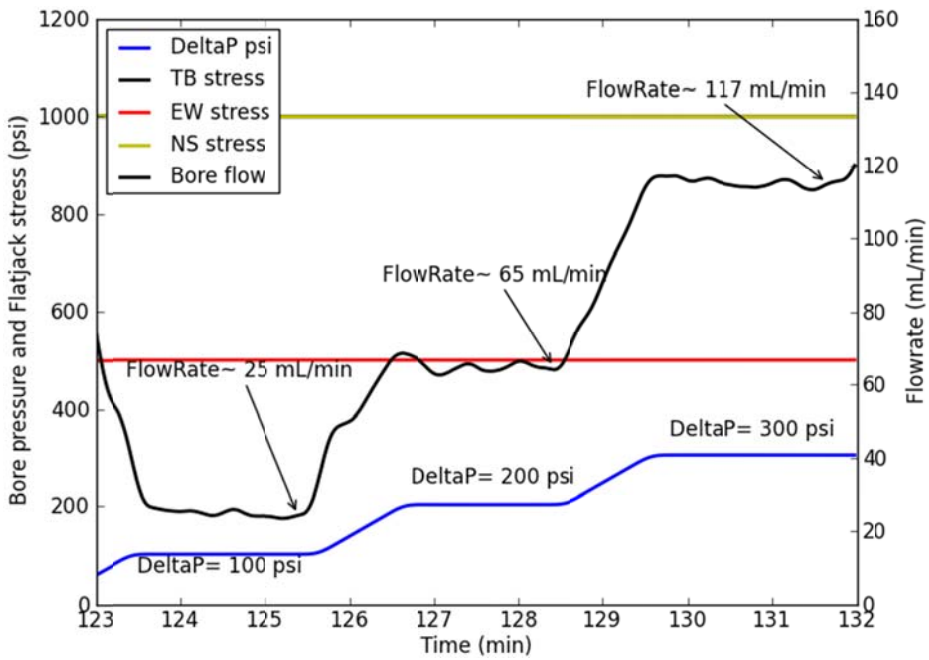

Figure 6.18. Pressure drop across the un-propped fracture (DeltaP), applied flatjack stresses and measured flow rate are shown for repeat of stage 1.

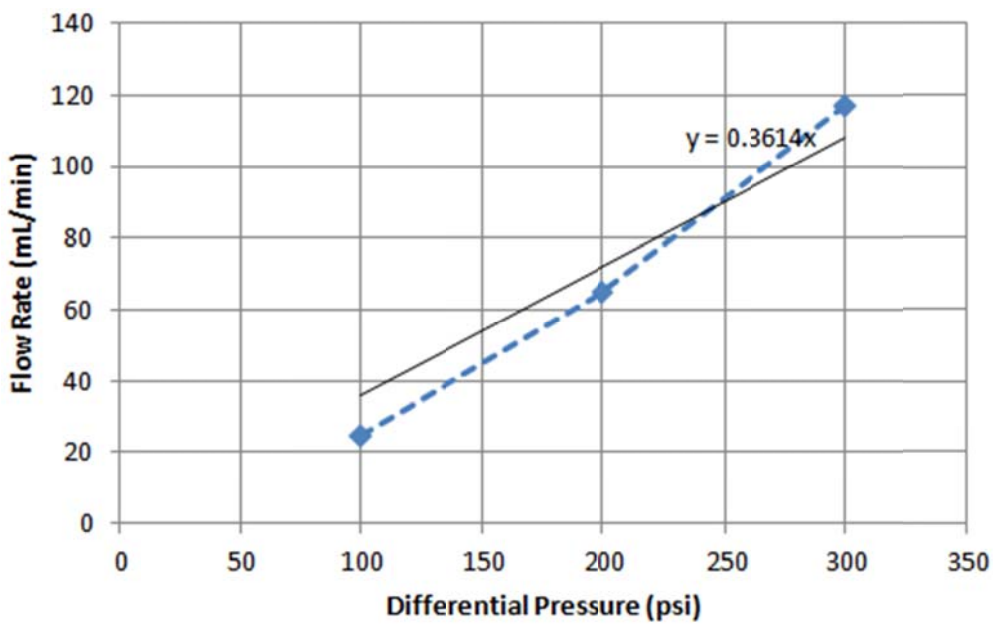

Figure 6.19. Flow rate vs. differential pressure across the fracture for the four measurements made during stage 1 of the un-propped fracture conductivity measurement. The slope of the linear regression curve was used to calculate the best-fit conductivity value at this value of closure stress.

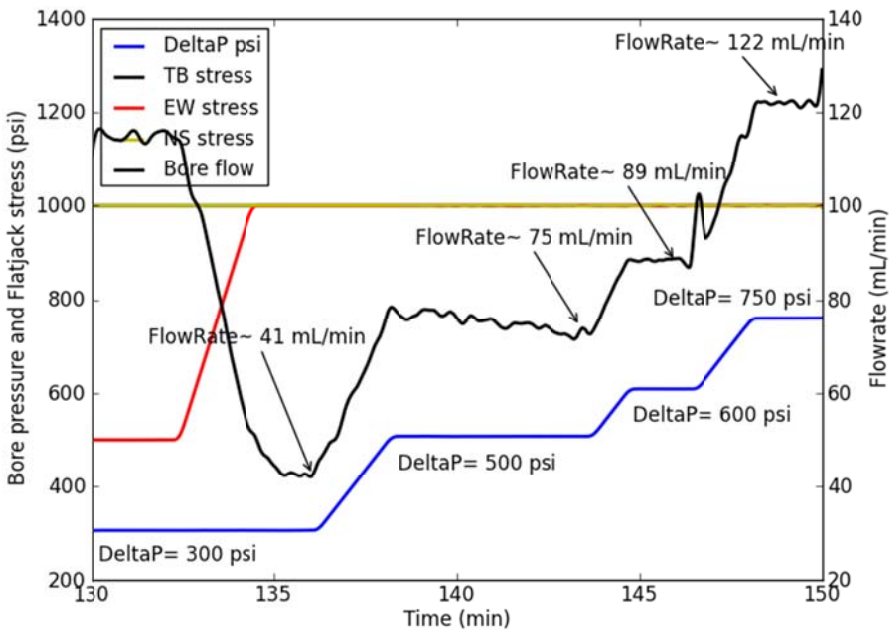

Figure 6.20. Pressure drop across the un-propped fracture (DeltaP), applied flatjack stresses and measured flow rate are shown for stage 2.

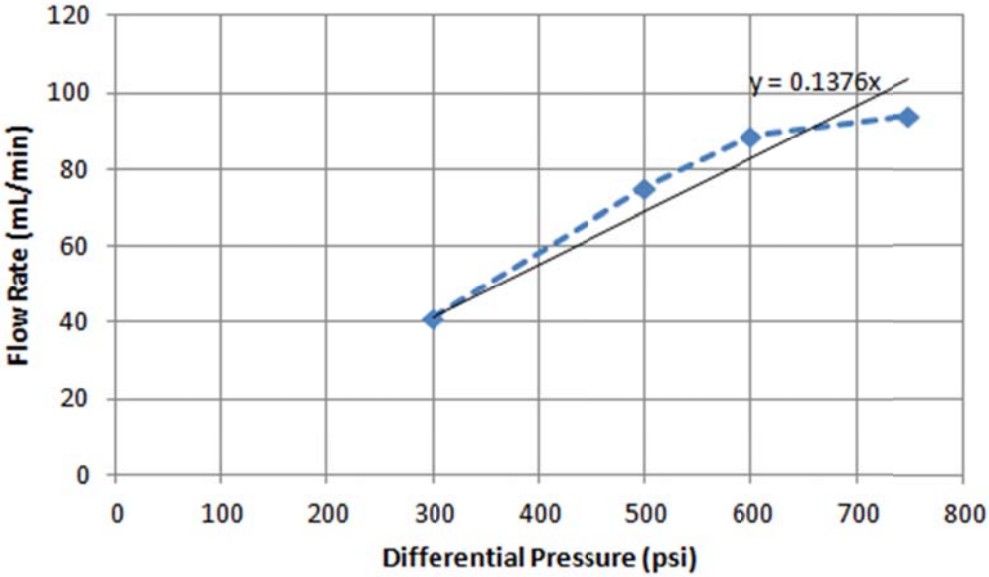

Figure 6.21. Flow rate vs. differential pressure across the fracture for the four measurements made during stage 2 of the un-propped fracture conductivity measurement. The slope of the linear regression curve was used to calculate the best-fit conductivity value at this value of closure stress.

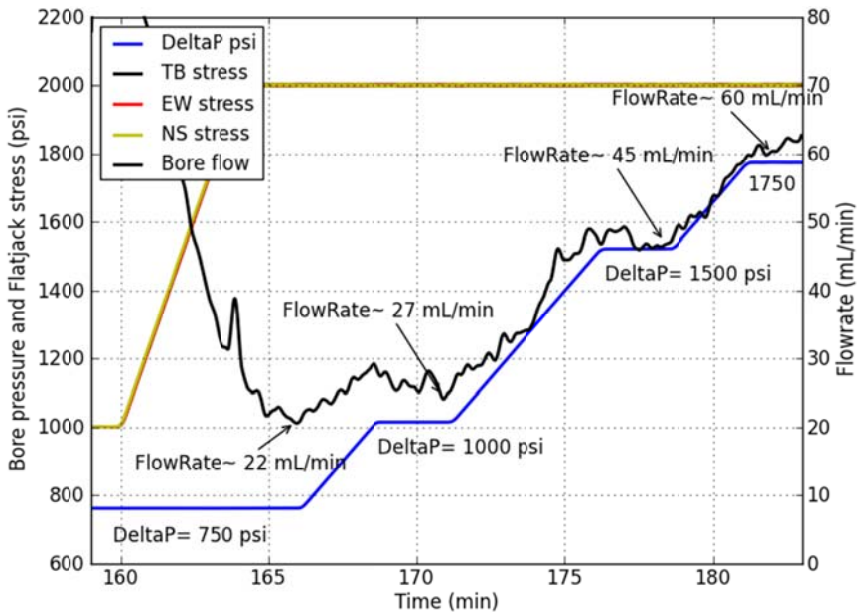

Figure 6.22. Pressure drop across the un-propped fracture (DeltaP), applied flatjack stresses and measured flow rate are shown for stage 3.

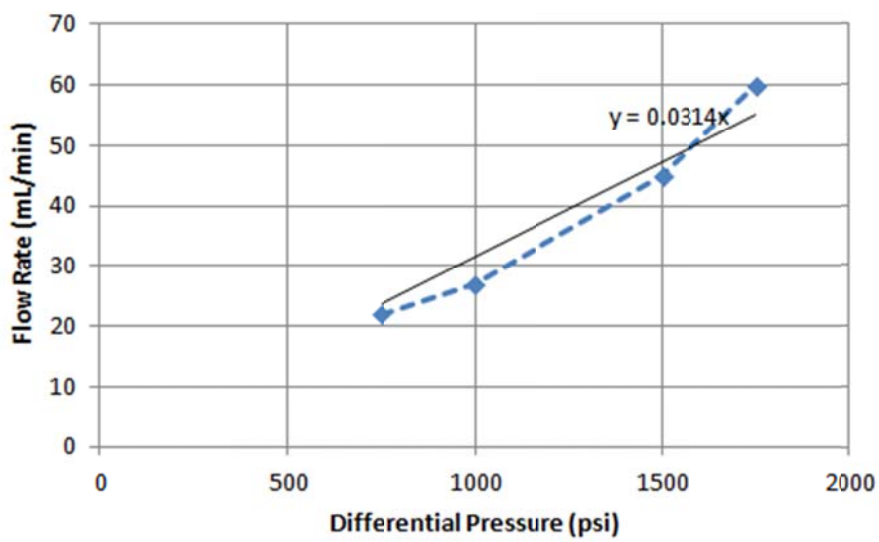

Figure 6.23. Flow rate vs. differential pressure across the fracture for the four measurements made during stage 3 of the un-propped fracture conductivity measurement. The slope of the linear regression curve was used to calculate the best-fit conductivity value at this value of closure stress.

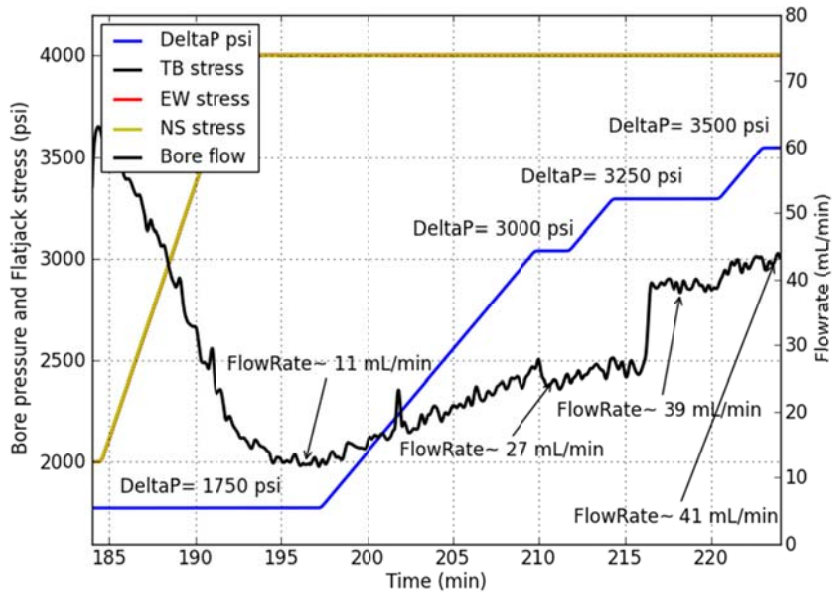

Figure 6.24. Pressure drop across the un-propped fracture (DeltaP), applied flatjack stresses and measured flow rate are shown for stage 4.

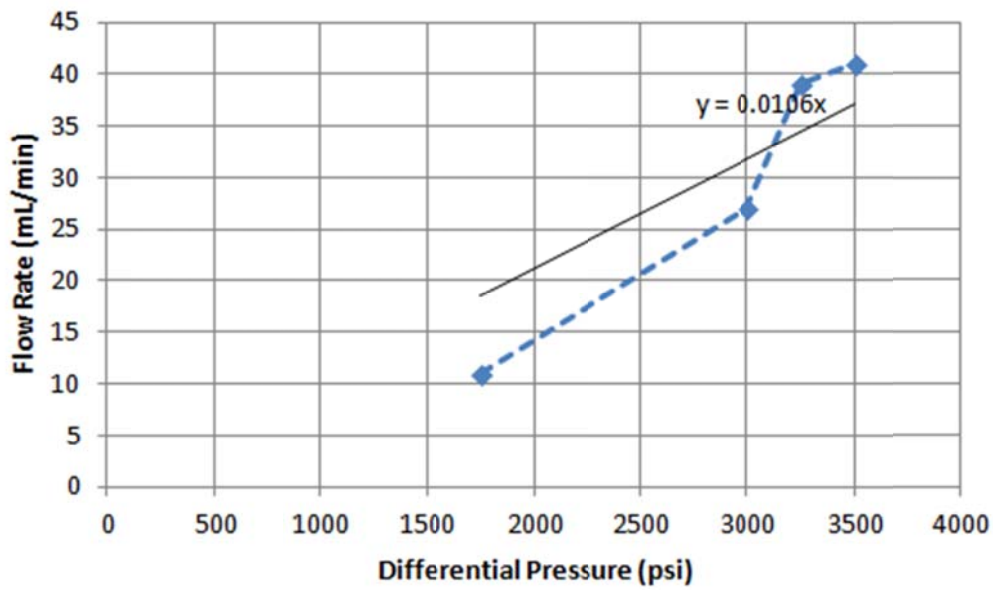

Figure 6.25. Flow rate vs. differential pressure across the fracture for the four measurements made during stage 4 of the un-propped fracture conductivity measurement. The slope of the linear regression curve was used to calculate the best-fit conductivity value at this value of closure stress.

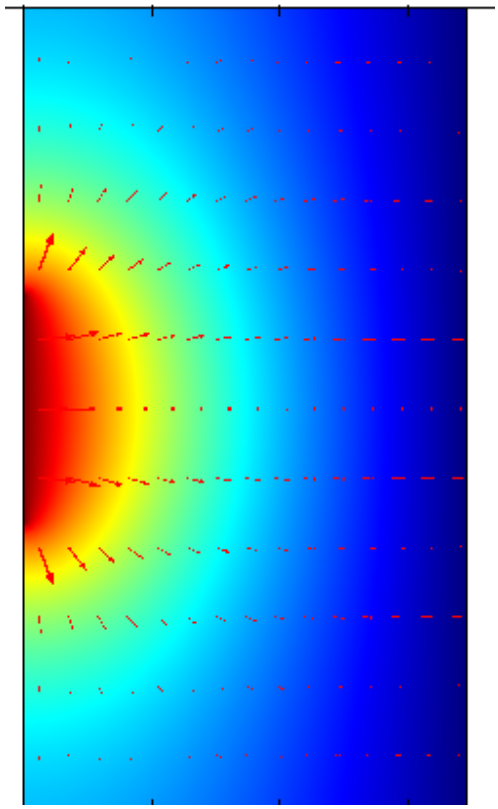

Figure 6.26. An example of the finite-element results that were used to invert for the effective conductivity from the block test measurements. Fluid flows from the 7" open-hole section of the wellbore (left-hand side of plot), through the fracture at out the edge of the block (right-hand side of plot). Red indicates high pressure and blue indicates low pressure and the red arrows are the fluid velocity vectors.

6.2.5.4 Proppant Transport

After un-propped conductivity measurements, the borehole injection system was switched from the continuous intensifier system to the high-rate MOYNO pump system. The goal was to inject 100 mesh proppant into the previously created hydraulic fracture. To achieve this goal following steps were taken:

1) The stresses on the Top-Bottom and North-South flatjacks were kept constant at a value of 1000 psi and the stress on the East-West flatjacks was reduced to 50 psi, as shown in Figure 6.27.
2) Water injection was started at a rate of approximately 6 l/min.
3) Once the bead pack (pore) pressure was stabilized, ¼ lb of 100 mesh sand was added to the flow approximately every 1.5 minutes as shown in Figure 6.28. The bead pack pressure was diligently observed in order to maintain it below the minimum confining stress of 50 psi.

Figure 6.28 shows the sequence of proppant injection, at a constant rate of 6 l/min, using water as the carrier fluid. The goal was to increase the total proppant content in the fracture in steps, while maintaining the pressure in the fracture below the reopening stress of 50 psi. The NS and top stress (1000 psi) and the EW stress (50 psi) are shown. The wellbore pressure (green) and the back-pressure (blue), measure at the point of exit of the fracture in the block, are also shown. The location of the bore pressure and back pressure measurements are shown in Figure 6.28. Adding proppant during injection caused a rapid increase in borehole pressure up to approximately 400 psi. During this time the back pressure increased to 35 psi. Continued injection without adding proppant increased the borehole pressure to 800 psi, while the back pressure gradually decreased to its original value.

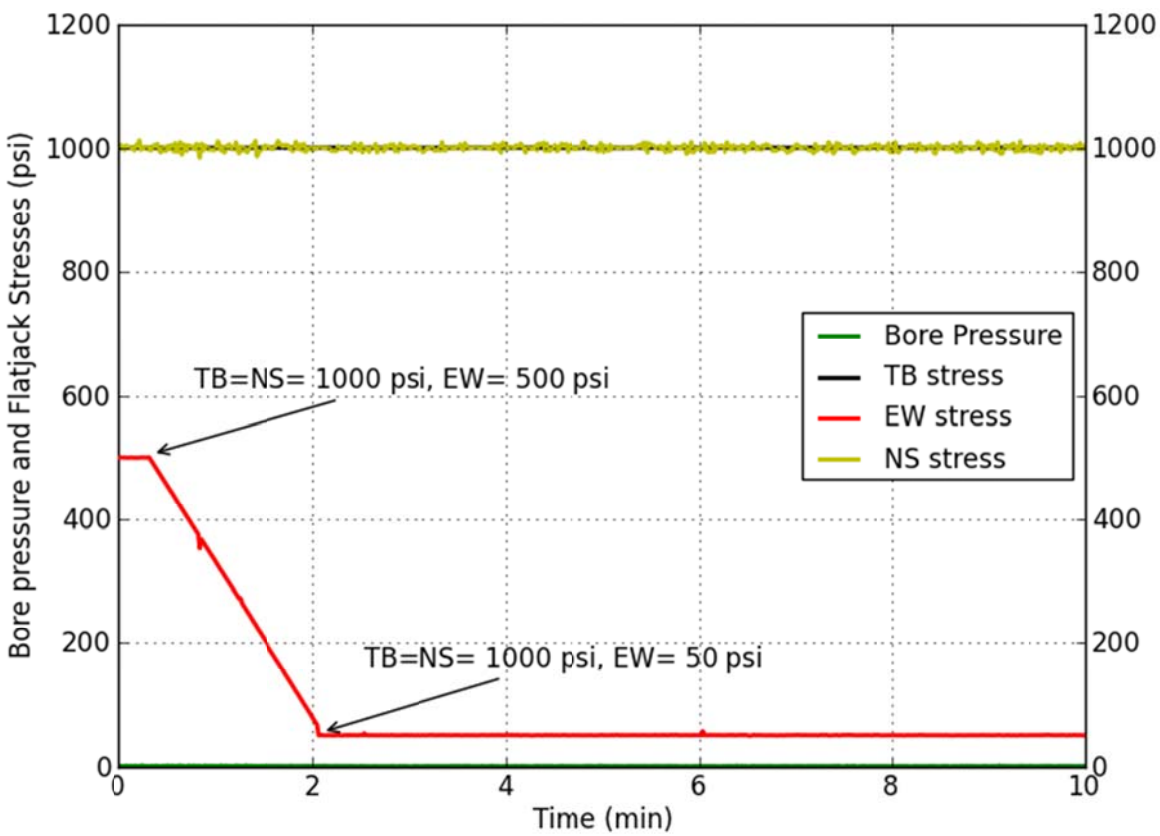

Figure 6.27. Stress ramp down phase after un-propped fracture conductivity measurements is shown.

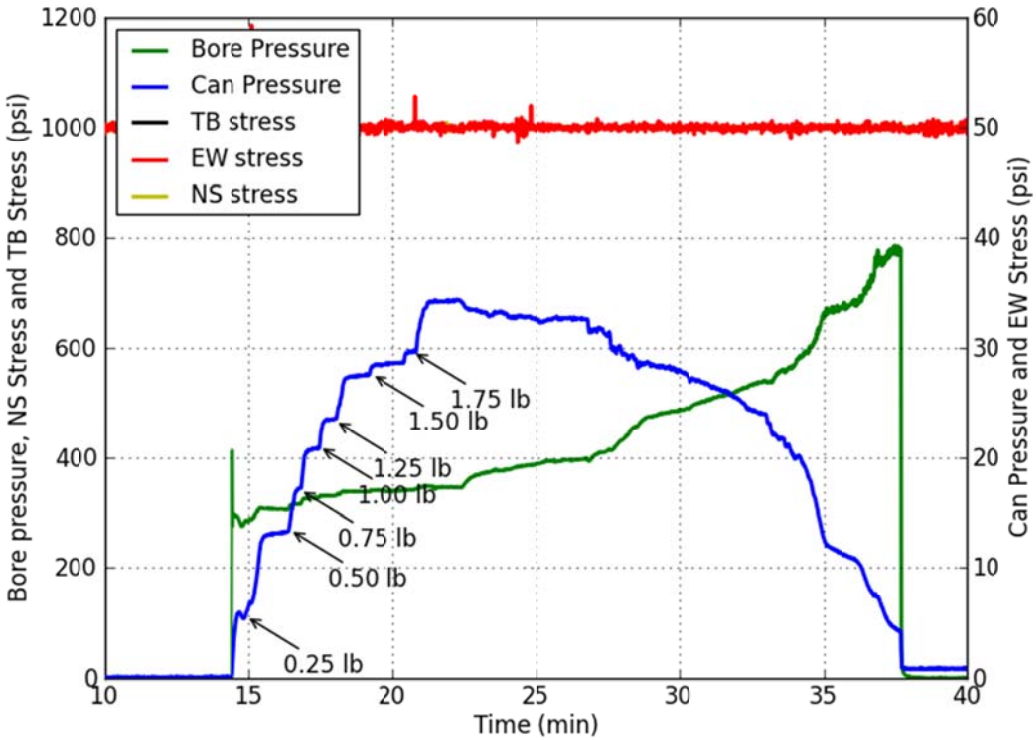

Figure 6.28. Bore Pressure, pressure in the bead pack (pore pressure) and applied flatjack stresses versus time are shown.

6.2.5.5 Propped Fracture Conductivity Measurements

After the proppant injection stage, the borehole injection system was switched from the MOYNO pump to continuous intensifier system to make propped fracture conductivity measurements. A similar procedure was used for the propped conductivity measurement as was described above for the un-propped conductivity measurements. Table 6.4 shows the values of closure stress, differential pressure, and measured flow rates for the propped fracture conductivity measurements. One difference in the un-propped and propped fracture conductivity measurements was the presence of a significant volume of sand in the wellbore that did not enter the fracture. Therefore, the pressure drop specified for each propped conductivity measurement included both the desired pressure drop across the fracture as well as the undesired pressure drop through the sand remaining in the wellbore.

To eliminate the undesired additional pressure drop the height of sand in the wellbore was measured immediately after the proppant transport phase of the test and prior to beginning the fracture conductivity measurements. After the test was completed an identical wellbore was measured and filled with sand to the same height measured during

the test. Water was then flowed through the sand-filled wellbore and the pressure drop was measured at several flow rates. This measured relationship between the flow rate through and the pressure drop across the sand-filled wellbore was used calculate the pressure drop across only the fracture during each stage of the propped conductivity test. The differential pressure value reported in Table 6.4 is the calculated pressure drop across only the fracture. Figure 6.29, Figure 6.31, Figure 6.33, and Figure 6.35 are plots of the pressure and flow measurements during each stage of the propped fracture conductivity measurements. Figure 6.30, Figure 6.32, Figure 6.34, and Figure 6.36, and plots of the pressure and flow measurements along with the linear regression curve used to calculate the effective propped fracture conductivity at each stage.

Table 6.4. Applied stress conditions, measured DeltaP, an approximate flow rate and calculated Fracture conductivity at each stress state for propped fracture conductivity measurements are listed

	NS Stress psi	EW Stress psi	TB Stress psi	Estimated Fracture Delta P psi	Flow Rate mL/min	Fracture Conductivity md-ft
	1000	500	1000	6.8	448	
Stage 1	1000	500	1000	15.0	697	153
	1000	500	1000	22.6	1040	
	1000	1000	1000	51.2	980	
Stage 2	1000	1000	1000	85.9	1600	49
	1000	1000	1000	104	1870	
	2000	2000	2000	219	1460	
Stage 3	2000	2000	2000	256	1685	22
	2000	2000	2000	292	1950	
	4000	4000	4000	478	1235	
Stage 4	4000	4000	4000	538	1375	8.4
	4000	4000	4000	597	1550	

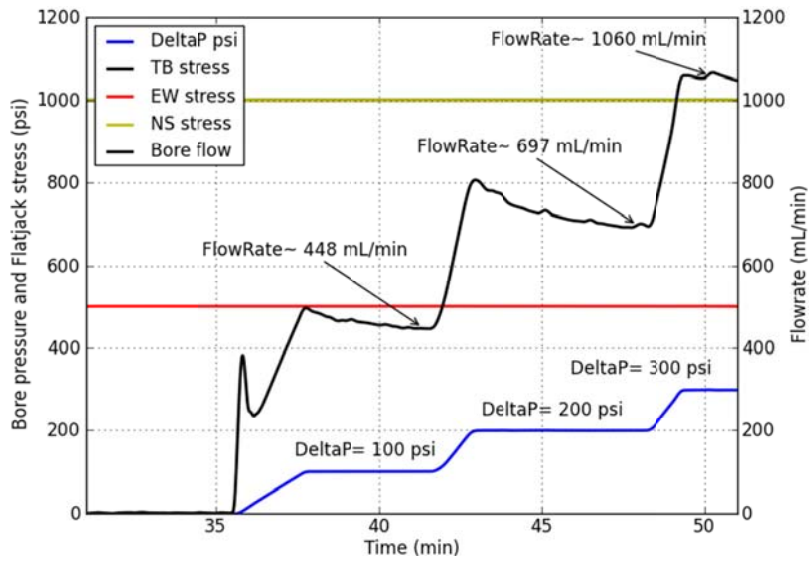

Figure 6.29. Pressure drop across the propped fracture (DeltaP), applied flatjack stresses and measured flow rate are shown for stage 1.

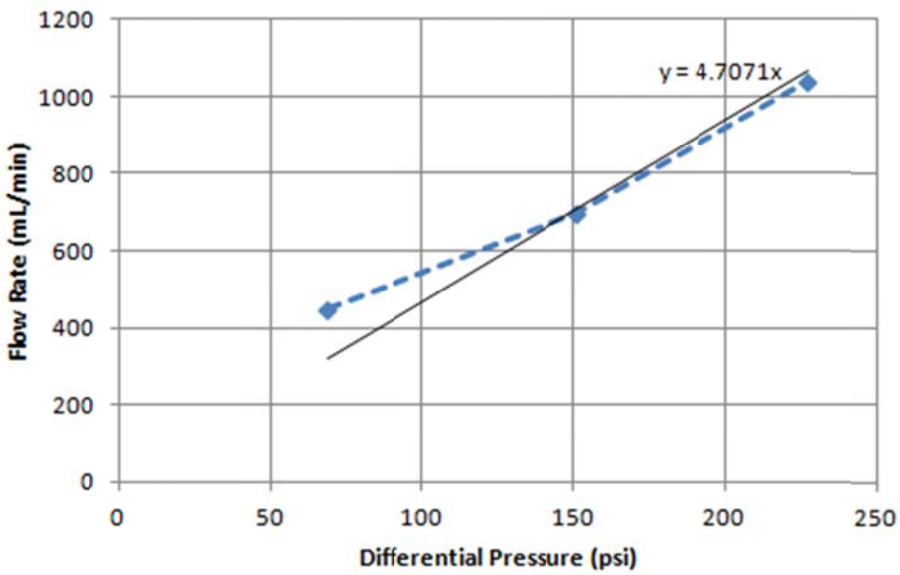

Figure 6.30. Flow rate vs. differential pressure across the fracture for the four measurements made during stage 1 of the propped fracture conductivity measurement. The slope of the linear regression curve was used to calculate the best-fit conductivity value at this value of closure stress.

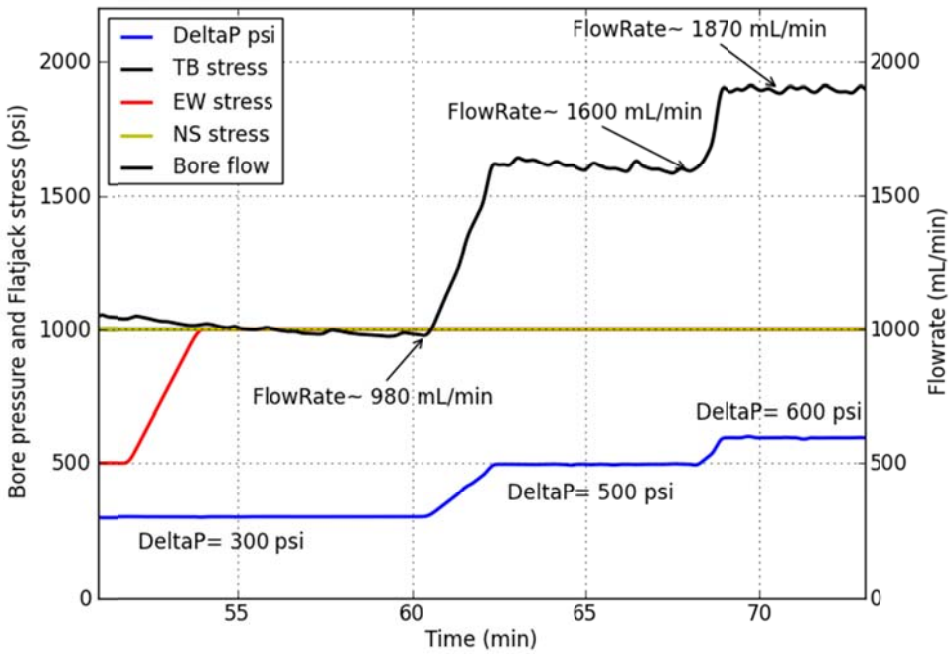

Figure 6.31. Pressure drop across the propped fracture (DeltaP), applied flatjack stresses and measured flow rate are shown for stage 2.

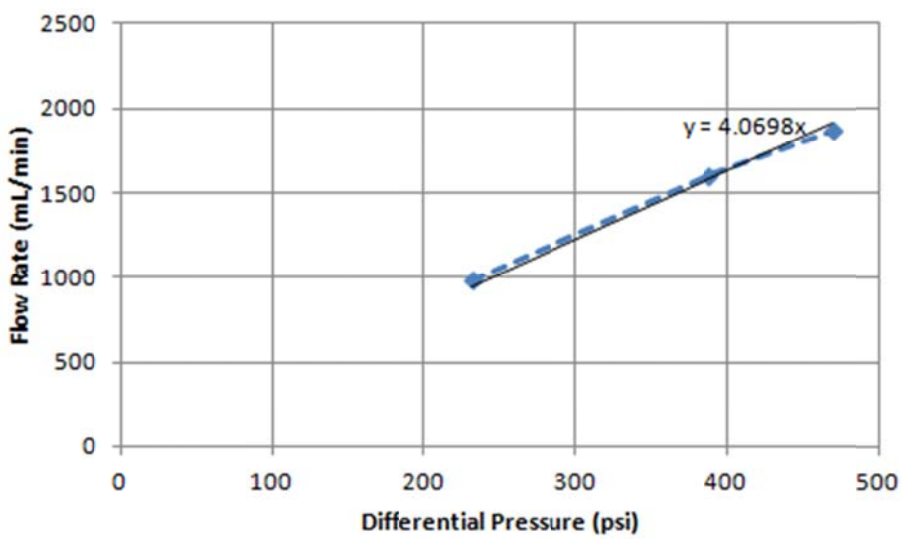

Figure 6.32. Flow rate vs. differential pressure across the fracture for the four measurements made during stage 2 of the propped fracture conductivity measurement. The slope of the linear regression curve was used to calculate the best-fit conductivity value at this value of closure stress.

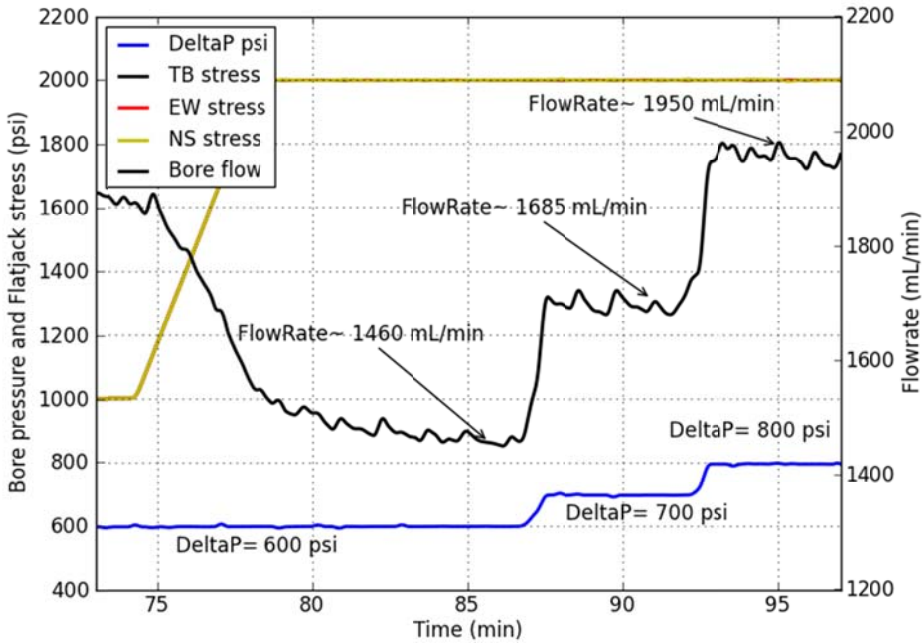

Figure 6.33. Pressure drop across the propped fracture (DeltaP), applied flatjack stresses and measured flow rate are shown for stage 3.

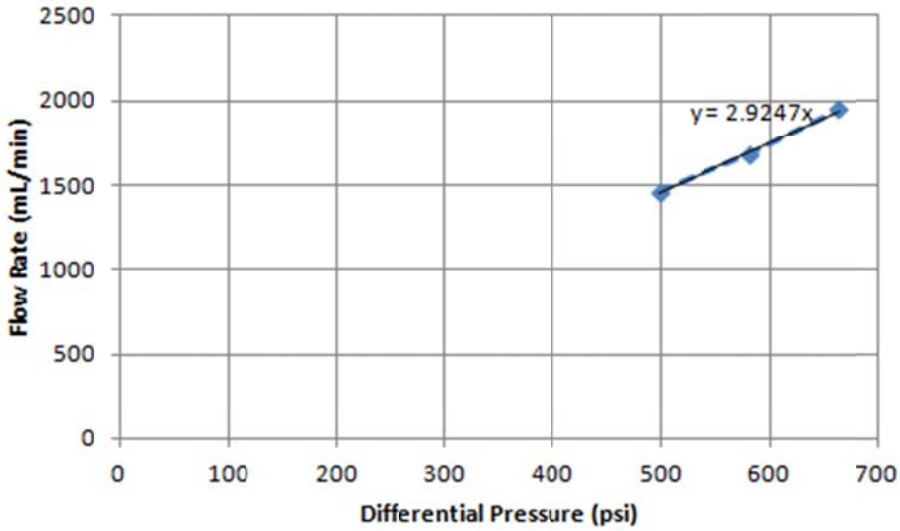

Figure 6.34. Flow rate vs. differential pressure across the fracture for the four measurements made during stage 3 of the propped fracture conductivity measurement. The slope of the linear regression curve was used to calculate the best-fit conductivity value at this value of closure stress.

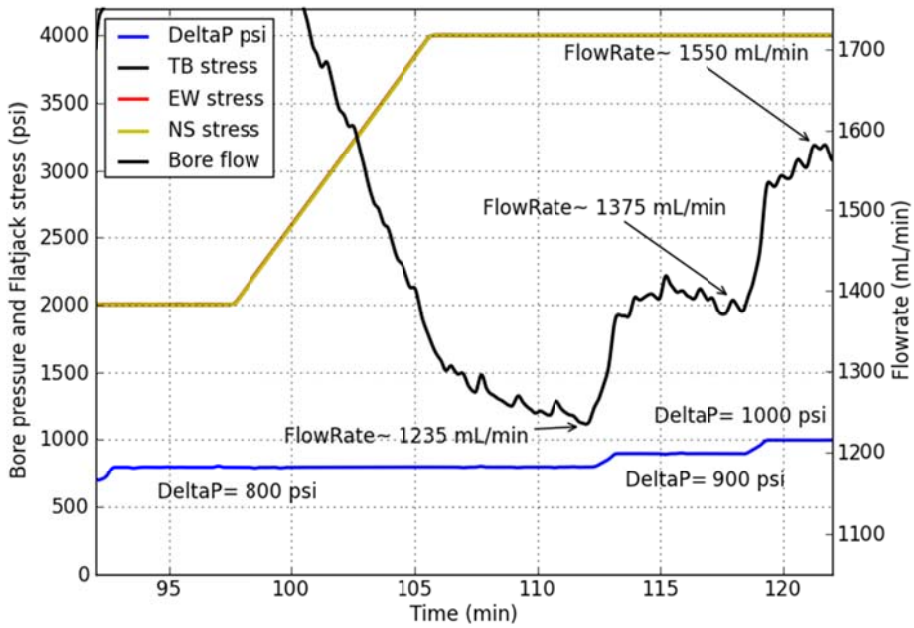

Figure 6.35. Pressure drop across the propped fracture (DeltaP), applied flatjack stresses and measured flow rate are shown for stage 4.

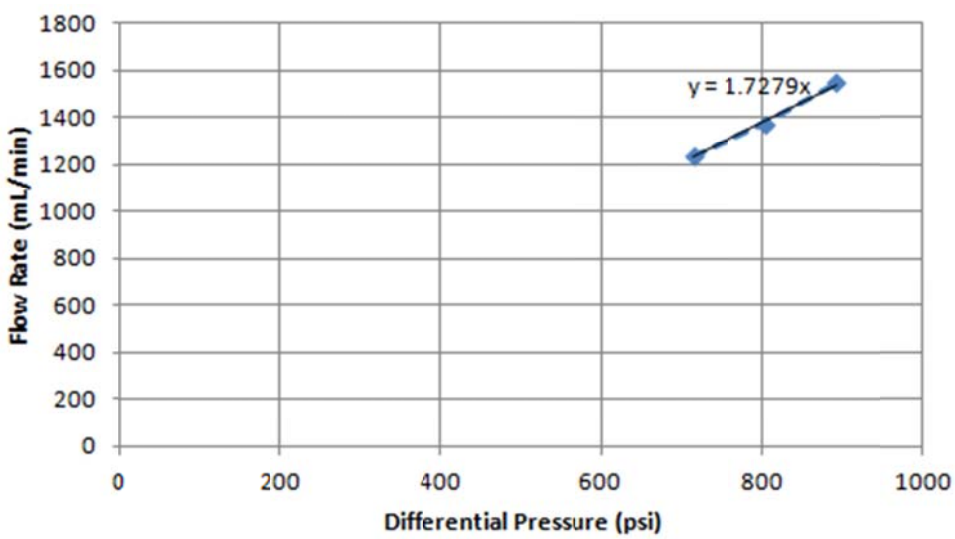

Figure 6.36. Flow rate vs. differential pressure across the fracture for the four measurements made during stage 4 of the propped fracture conductivity measurement. The slope of the linear regression curve was used to calculate the best-fit conductivity value at this value of closure stress.

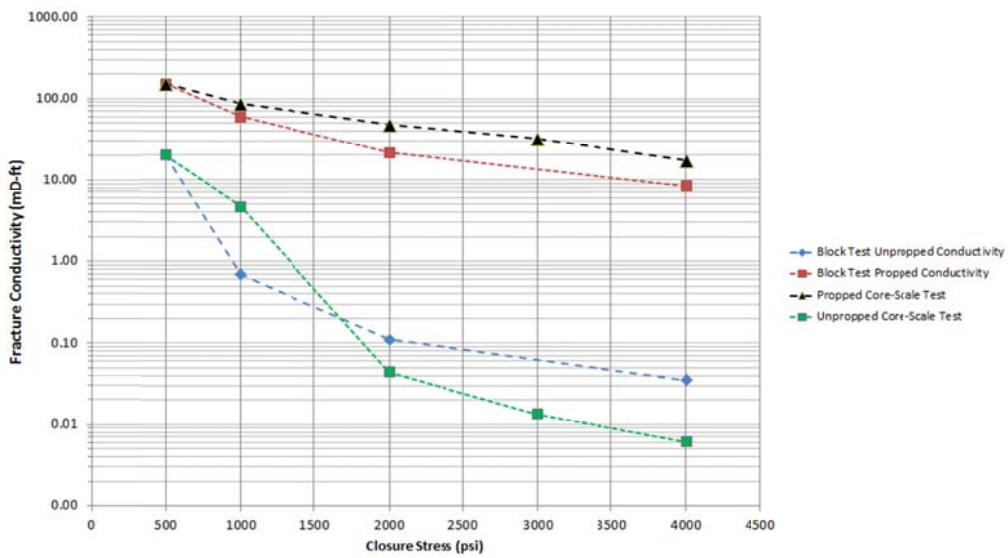

Figure 6.37. Un-propped and Propped fracture conductivity as a function of confining stress.

One of the goals of this program was to compare the un-propped and propped conductivity of this block test to the conductivities measured in the core. Figure 6.37 shows the calculated un-propped and propped conductivity as a function of applied stress for the block test as well as the core samples. The stress dependence on fracture conductivity of the un-propped core sample is similar to that for the Haynesville and slightly higher than that for the Marcellus sample, and spans approximately 4 decades over 4500 psi. The corresponding stress dependence of the propped core sample is representative of other core samples and particularly similar to the Macellus good reservoir quality rock and the Haynesville poor reservoir quality rock. In general, there is strong similarity between the measurements on core samples for the Niabrara shale and the other shales tested in this program.

The stress dependence on fracture conductivity of the un-propped and propped large fracture is substantially lower than in the small sample. This is expected given the surface roughness and the tortuous nature of the hydraulic fracture as compared to a saw cut (smooth) surface of the small sample. This indicates that the laboratory measurements on small samples are conservative estimates of fracture conductivity and that the real stress dependence is lower than predicted from lab experiments. The difference may be considerable for the un-propped surfaces and smaller for the propped surfaces.

The absolute magnitudes of fracture conductivity on the large block samples were smaller than that measured on the small samples. This was argued to be so because of an additional pressure drop between the tip of the fracture the screen on the fracture face that collected fines, and the pressure probe. Numerical modeling was used to evaluate the pressure drop between the pressure sensor and the end of the probe. The additional pressure drop was evaluated by equating the fracture conductivity of the two un-propped samples at the initial pressure step.

6.2.6 Block Fracture and Proppant Placement Evaluation

6.2.6.1 Fracture Traces on the Block External Faces

Once the fracture had been generated and the conductivity measurements were completed the block was removed from the vessel and the can. The bead pack surrounding the block was then cleaned from the surface of the sample to allow better viewing of the 200 mesh screen covering the fracture (Figure 6.38). When viewing the screens on the North and South faces of the block the trace of the hydraulic fracture is seen in the screen, as a result of fines collected during the various stages of flow. The fracture on the North face is oriented slightly off vertical, and the bottom of the screen is noted to have limiting staining, indicating limited conductivity from the fracture at the bottom of the block. Along the South face, we observe a continuous trace in the screen, indicating a vertically oriented fracture that experienced uniform flow through the entire fracture height. In this face, in addition to the vertical fracture, one observes two additional horizontal traces marked on the screen. Later analysis revealed that these were partings that resulted from two distinct lithologic transitions in the block. These are also apparent along the East and West faces of the block (without screens).

Figure 6.38: Large block faces North (left) and South (right) with screens still on.

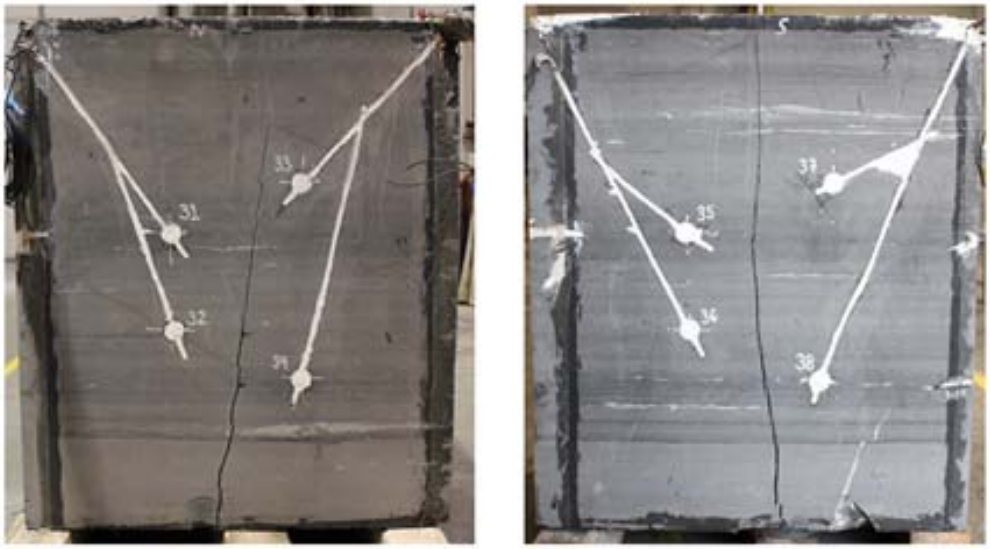

Figure 6.39: Block exterior with screens removed displaying the fracture face (North and South faces of the block respectively).

Once the screens were removed from the block faces, a direct observation of the fractures was possible. Figure 6.39 shows images of the same faces of the block after removal of the screens. Unfortunately, handling of the block to reposition it caused a slight opening of the fracture. This is particularly clear at the bottom of the sample, where the fracture is now seen clearly open. The direction of the fracture is also clearly seen. The fracture in the South face extends clearly from the bottom of the sample to the top following a general vertical orientation, and with a slight deviation of approximately 10 degrees from the middle of the sample downwards. The fracture on the North face was found to deviate by approximately 8 degrees along the entire length of the sample. In addition, in this view, it appears to be arrested approximately 8 to 10 inches from the top of the block. However, close examination shows the generation of complexity and en-echelon fracturing which occurred by branching and shear displacement. Figure 6.40 show a detail image of this region. The image was rotated sideways for convenience. Fracture complexity in this region is the result of mixed mode fracturing events converging to meet the centered fracture propagating across the top of the block. These fractures daylight on the North surface of the block with widths varying from 0.5 to 5.0 mm, and forming clear stacking patterns. Towards the interior of the block these coalesce together forming one predominant fracture.

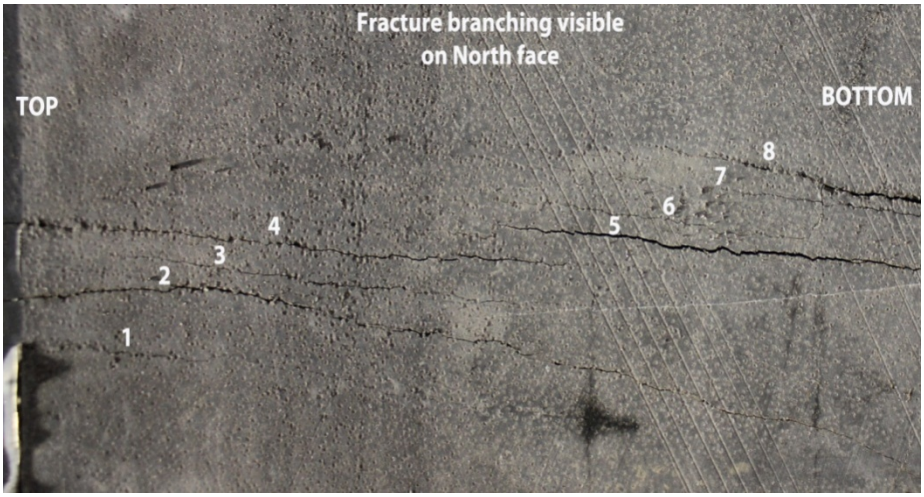

Figure 6.40: The en echelon fracture found on the North side of the block.

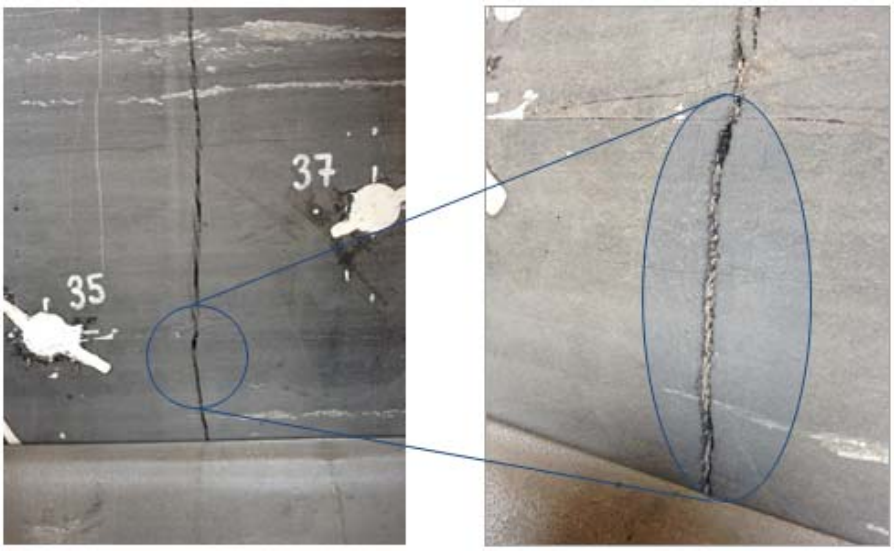

Figure 6.41: Exterior of the South face of the block displaying proppant bound to the fracture face.

Along the South face, the fracture looks more macroscopically uniform. However, close observation along its length demonstrates the presence of textural complexity and en-echelon min-mode fracture propagation. Figure 9.41 shows this pattern along the length of the fracture. It also shows a detail of the region towards the bottom of the sample showing the irregular distribution of proppant associated to the textural heterogeneity of the fracture.

Figure 6.42 shows the top view of the block and highlights important details of the fracturing process that shed additional information on the fracturing process. The blue arrows in this figure help identifying the trace of the macroscopic fracture on this face. The

trace of the half length fracture section growing from the wellbore towards the South face is relatively planar and simple, exhibiting minimal deviation. In contrast, the trace of the opposite half length fracture section growing from the wellbore towards the North face exhibits considerable complexity and en-echelon fracturing. These patterns are observed at a distance of 1 inch from wellbore and continued to the edge of the block. As shown in Figure 6.40, they also continue several inches down the North face of the block. Figure 6.43 shows a close-up image of the near wellbore region. The white arrows show the trace of the fractures. The left section (towards the North face of the block) clearly shows that significant branching has occurred in this region. This image also shows that the fracture trace on the top of the block was filled with proppant and this appears to be distributed uniformly along the fracture length (in the Top face of the block). Figure 6.44 shows a close-up view of this region. A ruler seen in this image shows a fracture approximately 0.8 mm wide. Given that 100 mesh proppant was used and that this has a mean diameter of 0.145 mm, one can calculate the presence of 5 to 6 proppant layers in the proppant pack. These observations correspond to the trace of the fracture on the external surface of the block and may not be representative the proppant distribution in the rest of the fracture (internal to the block).

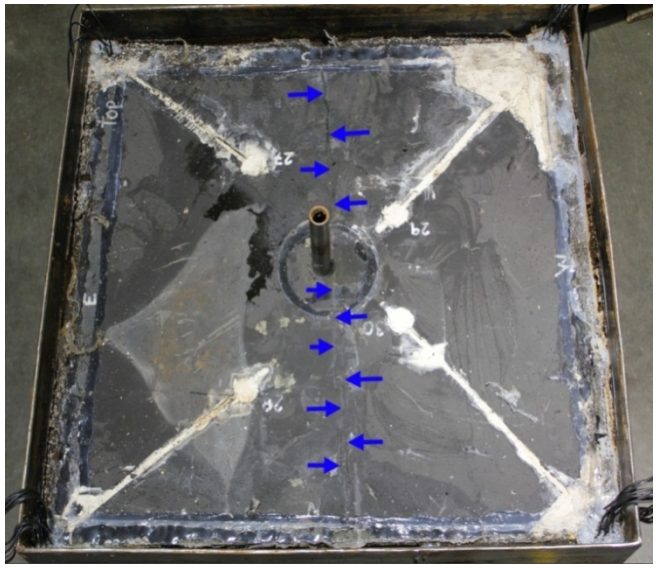

Figure 6.42: The top of the block displaying the fracture radiating from the wellbore. The South face of the block is at the top of the picture and the North is at the bottom. En echelon fractures are found along the fracture from the wellbore to the edge of the North face.

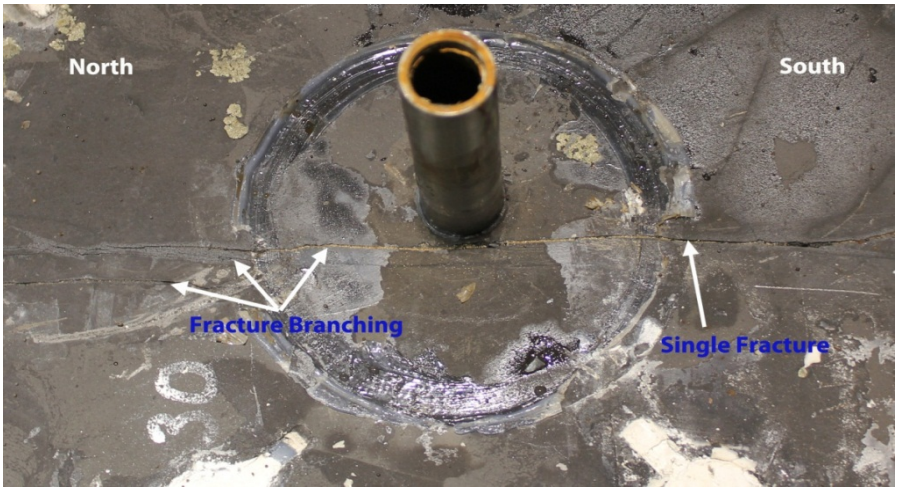

Figure 6.43: The top surface of the block displaying the wellbore and fracture. The North face of the block is to the left of the photo and to the right is the South face of the block.

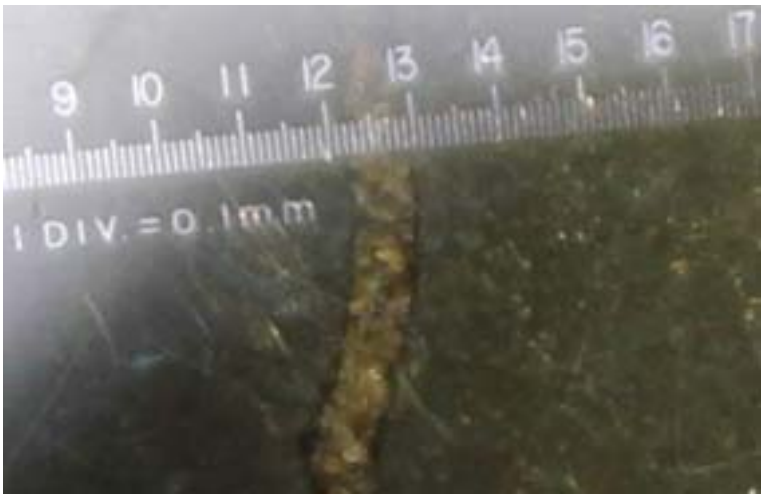

Figure 6.44: The fracture on the top of the block displaying 5-6 layers of proppant.

6.2.6.2 Fracture Geometry Inside the Block

After external inspection of the fracture traces on the block, the block was prepared for post-test CT scanning. First, the steel casing had to be removed by coring, to allow X-Ray imaging of the near wellbore region. Unfortunately, during this process, a large portion of the proppant in the fracture was washed away by the fluid circulation used during coring.

Subsequently, during handling, preparation and packaging to send the block to the CT-scanning facility, the block parted along the fracture plane, and along two additional planes of weakness that had not been previously noticed. As a result, the CT-scanning operation was aborted and the block was made available for internal inspection of the fracture face.

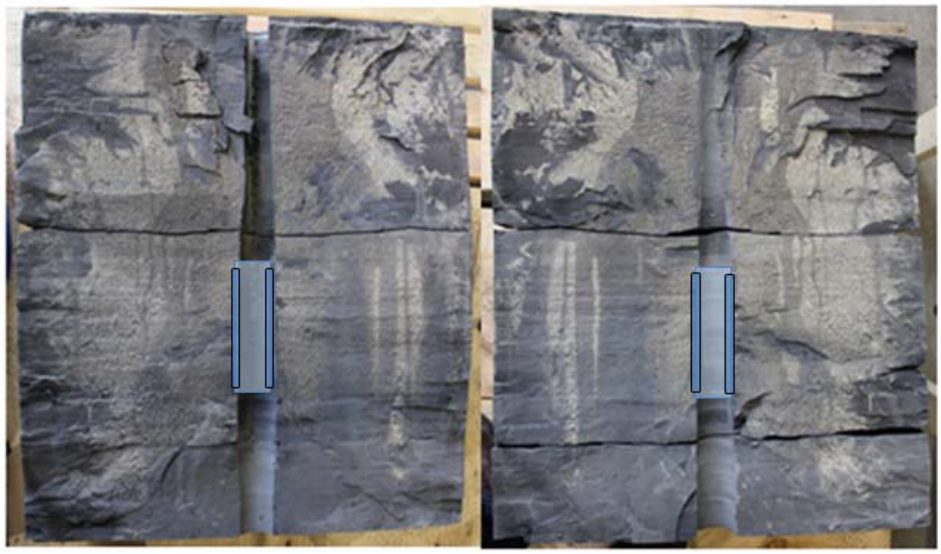

Figure 6.45: Images of the open fracture displaying the proppant placed on the fracture surface (East and West faces respectively). A representative drawing of the open hole section of the casing along with the stress concentrator is displayed towards the center of the block image.

Figure 6.45 show the two reconstructed sections of the block and the exposed surface generated by the hydraulic fracture. The parted horizontal planes of weakness are also seen. These partings occurred after the block was removed from the can. There is no indication of their opening during testing (e.g., by the fluid evacuation of the top actuator, by AE localization, or by the presence of proppant in these surfaces). These were closed during the fracturing process and did not affect the fracture conductivity measurements. Remnants of proppant placement and their distribution are easily identified along the periphery of the block. However, proppant in the near-wellbore region had been fully flushed out by the casing coring operation. In addition, this figure shows three distinct regions of fracturing: a wellbore region, connecting the wellbore to the fracture, which is characterized by some degree of complexity and tortuosity as the hydraulic fracture develops from the sand blasted slots; a near-wellbore region that is characterized by a reasonably planar and smooth fracture, and a far-wellbore fracture, near the edges of the block, that is associated with extensive branching and mix-mode fracture propagation.

Figure 6.46 highlights the presence of a calcite-filled fracture oriented parallel to the wellbore and perpendicular to the direction of fracture propagation. This fracture was observed to open and then close immediately after breakdown (Figure 6.13 in Section 6.2.5.1). The activation of this fracture during hydraulic fracturing was also detected via acoustic emission localization and is reported in the next section. Interestingly, there appears to be a strong relationship between the presence and activation of this fracture and the presence of mix-mode en-echelon fractures on this side of the block. The figure shows the vertical extent of the calcite-filled fracture and its orientation parallel to the wellbore (left side) and the relationship between the activation of these and the generation of branches on the hydraulic fracture (right side). Evidence that this transverse fracture

sealed itself after initial activation is found in the record of the displacement volume by the North-South flatjacks, and also in the absence of any proppant along this interface.

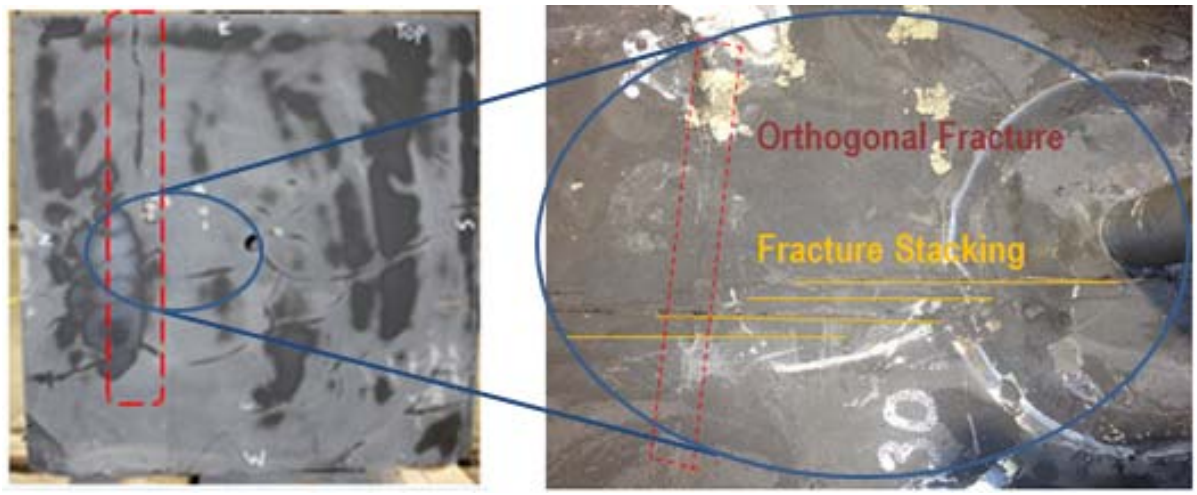

Figure 6.46: Top image of block (left) before casing and fracturing of the block. The pre-existing calcite healed fracture can be seen. The image on the right displays the post image of the hydraulic fracture (Yellow) interacting with a pre-existing fracture (Red).

Additional information on the origin and evolution of complex fracturing and branching on this section of the block is presented in Figure 6.47. In the left side of the figure two regions of the fracture face are bounded with red and blue rectangles. The portion of the fracture within the red rectangle is in direct contact with the calcite-filled natural fracture, and develops complexity by interaction with this interface. This region is also highlighted in the right side of the figure. Here, the red dotted line represents the direction of the natural fracture. A transition from few en-echelon factures, to the left of the interface, and more tightly spaced multilayer of fractures, to the right of the interface, is clearly apparent.

The blue rectangle in the left side of Figure 6.47 shows the presence of multiple fracture step-overs with one predominant one occurring along the North face of the block (mid section of the highlighted area). This fracture was further analyzed to assess the details of the stepover generation. When closely viewing this large stepover, it is observed that the hydraulic fracture does not simply stops at the calcite-filled interface, slides along it, creating the stepover, and propagates along a parallel direction. It also crosses the interface and continues propagating away of the interface for several inches before being arrested. Figure 6.48 shows the details of this complex interaction. Contact with the initial interface results in branching and each of the branches themselves interact independently with additional interfaces present in the rock to develop additional complexity.

Figure 6.47: Left image: En echelon fractures are observed along the top north section of the block (Red) and a large stepover, with other smaller stepovers, occurr on the north face (Blue). Right image: The Red line is used to delineate the location of the preexisting fracture and the Green arrows are used to display how the en echelon material broke in thin sheet along the rock surfaces.

Figure 6.48: A large stepover fracture on the North face of the block is observed to have continued on for several inches after passing a stepover fracture deviation.

In addition to the above analysis of the region with large fracture complexity, we analyzed the transitional region, which is defined by a gradual development of fracture branching and complexity. Figure 6.49 shows an example of a region along the middle of the block, near the perforation interval, and along the East section of the block. The figure shows the presence of fracture branching with three sub-millimeter thick stacked fractures of 7 to 8 inches in length. Each of these layers of fractures contains proppant in their first half inch. In addition, only the dominant fracture has proppant along the entire length of its surface.

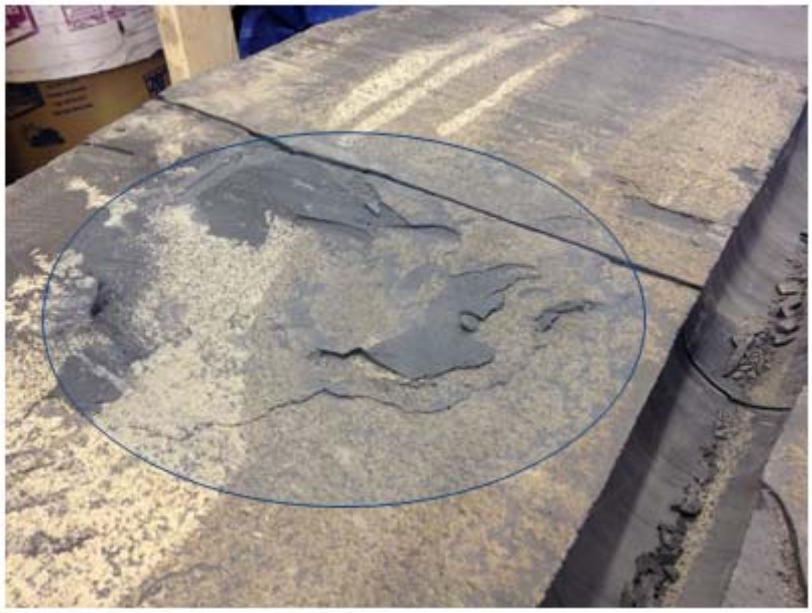

Figure 6.49: En echalon fracture stacking observed on the upper portion of the East face of the block. The material separating these factures from one another was less than 1.0mm thick.

After visual inspection of the fractures, these were mapped using a mechanical goniometer. This device uses a coordinate system and a mapping scribe to digitize the surface profile of the fracture and generate a XYZ file with location coordinates. This file is subsequently imported into a 3D visualization software to build a 3D digital image of the fracture surface. Figure 6.50 shows the equipment and the digital rendition of the fracture geometry.

Figure 6.50: A goniometer device used to map the fracture surface.

6.2.6.3 Proppant distribution and surface evaluation

To evaluate the proppant distribution on the fracture, several locations across the block were selected for proppant collection and analysis. These locations are shown in Figure 6.51 . A one inch diameter areal coverage was used for sampling the proppant and this was collected from eleven locations on the block. The proppant samples were subsequently inspected, using a digital microscope, to measure particle sizes and define the presence of grain crushing that may have occurred as a result of the increasing fracture closure stress. Table 6.5 shows the amount of proppant in the sampling site and its average proppant diameter.

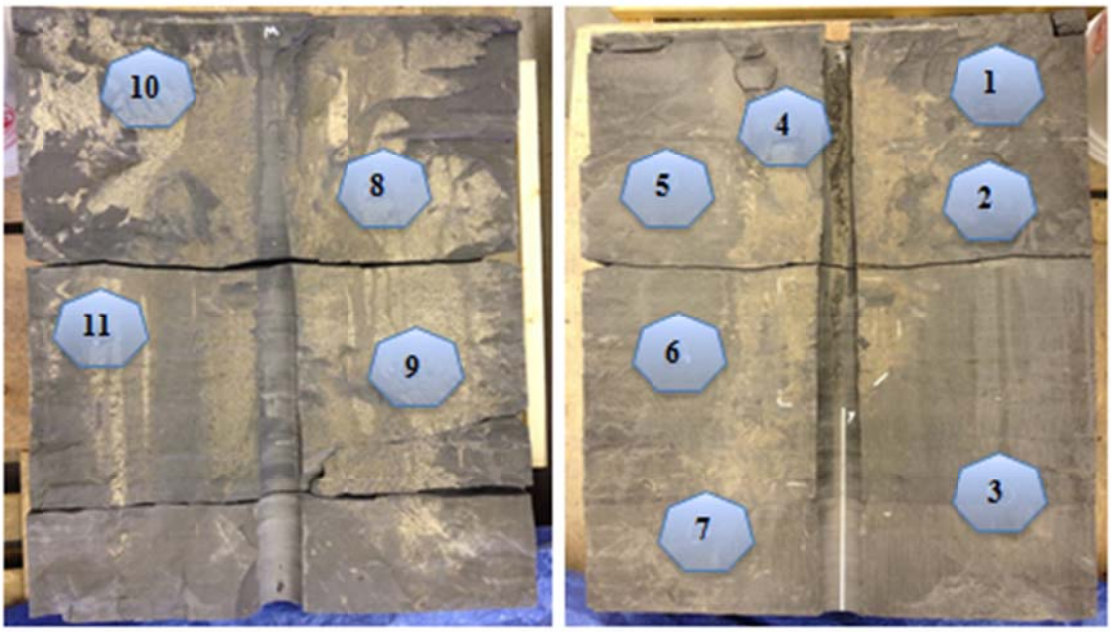

Figure 6.51: Images of the fracture surface and the locations where proppant samples were collected to evaluate particle grain size distribution and crushing.

Table 6.5: Distribution of proppant in grams, at defined locations on the fracture surface, and average proppant diameter at each of these locations

Location	Proppant (g)	Average Proppant Diameter (µm)
Wellbore	----	242.7
Site 1	0.134	198.1
Site 2	0.091	220.0
Site 3	0.169	216.6
Site 4	0.240	197.4
Site 5	0.137	213.2
Site 6	0.122	238.9
Site 7	0.058	219.1
Site 8	0.271	236.2
Site 9	0.159	219.6
Site 10	0.207	231.5
Site 11	0.107	242.7

Results show that the proppant left at the wellbore during injection have the largest average proppant diameter. In comparing the average proppant diameters to the location of the sampling sites (Figure 6.51), it is observed that the largest average proppant particle sizes are found nearest or just above the wellbore (sites 6, 8, 10, and 11), and these decrease as they move towards the outer corners of the block (sites 1 and 4). This occurrence can be attributed to the fracture width narrowing away from the wellbore.

When viewing the proppant under a digital microscope at 100X no clear signs of grain crushing were observed. Figure 6.52 shows an example of these observations. The image shows very little debris or visual information of crushing. Thus, either the crushed proppant developed fines that migrated to the screen on the exterior surface of the block, or very little to no proppant grain crushing occurred.

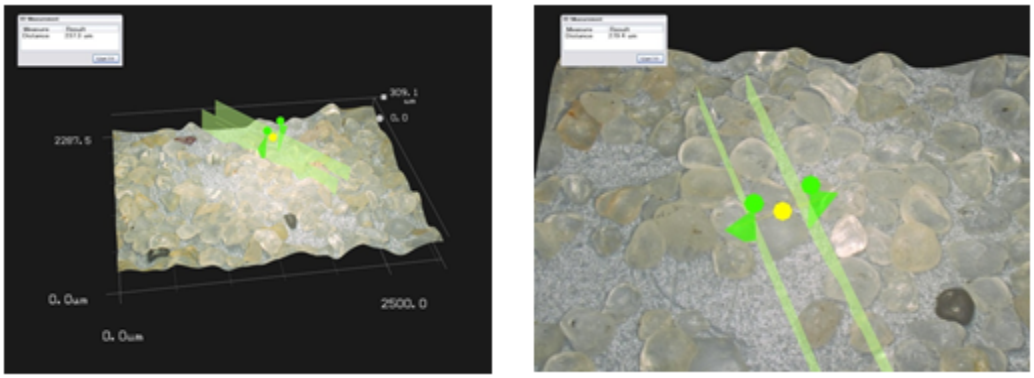

Figure 6.52: Digital microscope images of proppant grain quality and diameters being measured.

For each of the eleven locations on the block the overall proppant weight was also measured and compared to assess the uniformity of the proppant concentration transported along the length of the fracture (Table 6.5). Sites 4, 8, and 10 were found to contain the highest concentration of proppant and were located just above the wellbore casing. The sites found to contain the least proppant concentration (sites 2, 7, 11) were positioned below the fracture initiation region, or close to the edge of the block. Interestingly, we found a strong correlation between the distribution of regions with high proppant concentration and the distribution of acoustic emission (AE) events during fracture closure, after proppant transport. Here, the AE are generated by rock/proppant and proppant/proppant interactions as a function of the fracture closure stress. Thus, the regions found to contain the largest amounts of proppant also exhibited the highest number of AE events. These results are seen in Figure 6.53.

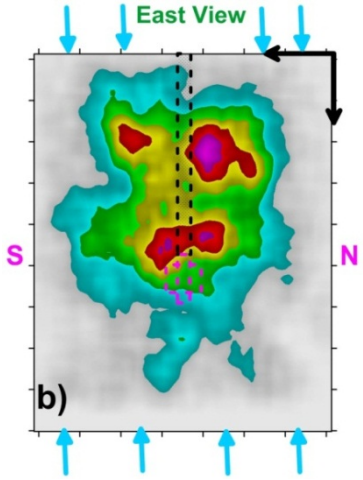

Figure 6.53: Acoustic emissions on the East/West face of the block at fracture closure following the placement of proppant. The image displays acoustic events of proppant embedding and consolidation around one another.

Once the distribution of proppant concentration was analyzed, we conducted an additional evaluation, using the digital microscope, to determine the degree of proppant embedment on the fracture surface. The same eleven locations used in the proppant concentration study were used for proppant embedment analysis. Results show that little to no embedment occurred on the sample. An example of the surface topography is shown in Figure 6.54.

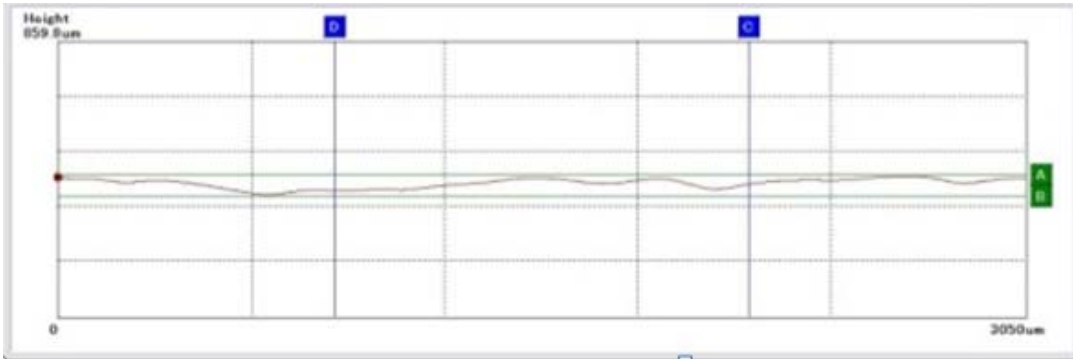

Figure 6.54: The embedment on the facture surface (Red) was measured using the Green lines to determine the overall surface height change. In this instance a total of 0.059 mm height change occurred. Additionally no clear signs of embedded particles were found.

In addition to proppant concentration, grain crushing and proppant embedment, we measured the degree of surface roughness generated during fracturing. Images at 200x and 300x magnification were used to evaluate the surface roughness, and this was calculated as the ratio of the measured surface area over the projected surface area.

Table 6.6 shows these results.

The areas with the highest roughness values (Site 3, 6, 9, and 11) were located directly opposite to the fracture initiation zone, and toward the edge of the block. The locations on the block with the lowest surface roughness where those located above and below the weak bedding interface (Sites 1, 5, 7, and 8).

Table 6.6: Surface area measurements using 200x and 300x for the eleven locations on the block

Location	Roughness Measurements (Magnification)	
	200x	300x
Site 1	1.26	2.66
Site 2	4.39	5.21
Site 3	7.07	9.01
Site 4	4.17	4.29
Site 5	3.83	3.66
Site 6	6.08	7.47
Site 7	2.23	3.78
Site 8	2.96	3.85
Site 9	5.09	5.12
Site 10	4.02	5.18
Site 11	5.75	6.04

6.2.7 AE Results During Hydraulic Fracturing of the Block

6.2.7.1 Post-Test Analysis of Acoustic Emission and Ultrasonic Transmission

For this project, 38 specialized, waterproofed sensors were designed, tested and manufactured in TerraTek, to perform acoustic emission and ultrasonic transmission measurements, under elevated fluid pressure. The following acoustic emission and ultrasonic transmission data processing were performed on the measured data:

(a) Real-time-data processing, using the Vallen GmbH acquisition system software, was used to evaluate sensor quality and analyze ultrasonic transmissions (amplitude and velocity).
(b) Post-test acoustic emission processing and data analysis was conducted based on proprietary statistical criteria of onset time determination, using time-dependent heterogeneous anisotropic velocity model for AE hypocenter determination.

6.2.7.2 Stressing-up the Rock Block

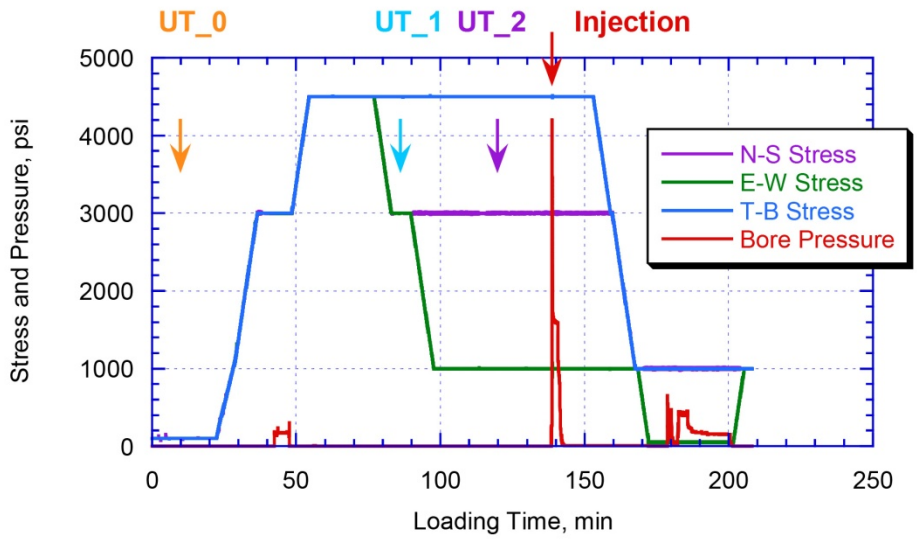

Figure 6.55. Variation of triaxial stresses (pink, green and blue curves) and bead pack (pore) pressure (red curve) applied to the block during testing. Labels UT_0, UT_1 and UT_2 indicate moments of auto-calibrations performed to estimate P-wave velocity of the rock.

Figure 6.55 shows the loading history of the block and time intervals of ultrasonic transmissions measurements, labeled as UT_ 0, UT_1 and UT_2, and marked by arrows in Figure 6.55. During the suite of acoustic transmissions events (called auto-calibration) each sensor operated as a sender of elastic waves, triggered by a 450 V electrical pulse provided by the Vallen System. All other sensors received the elastic wave signal. Measured Acoustic Emission (AE) and Ultrasonic Transmission (UT) signals were separated automatically. Evaluation of the P-wave velocities along different transmission traces was performed. Unfortunately, during pressurization of the block during the time between UT_0 and UT_1 measurements, the connection to 12 sensors was lost. Post-test analysis of the block indicated that these were sheared by an unexpected extrusion of polyurethane sealing (Figure 6.56[5]). For the current test, we analyzed acoustic emission and ultrasonic transmission data collected by the remaining 26 sensors of the original 38 sensors.

[5] We have now implemented a method with tension releasing loops, to minimize the risk of shearing cables in the future.

Figure 6.56. Photo of cables broken during block pressurization.

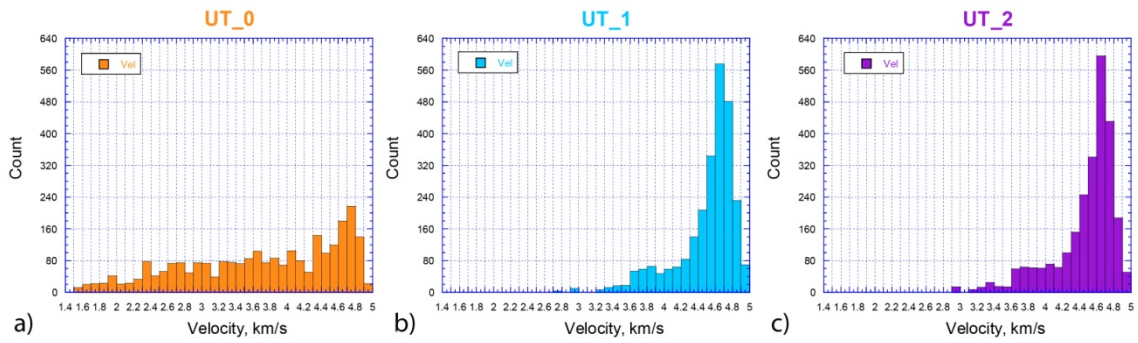

Figure 6.57. Velocity (km/s) of P-wave propagation along multiple paths inside the testing vessel. a) unstressed condition (UT_0); b) E-W Stress 2450 psi (UT_1); and c) E-W Stress 1000 psi (UT_2).

Figure 6.57 shows histograms of P-wave velocities of auto-calibration results measured by 26 sensors at the moments marked as UT_0, UT_1 and UT_2 in Figure 6.55. Results show an increase in the average P-wave velocity with stress. One of the main reasons of the measured stress dependence of velocity is the closure of the open fractures and the corresponding decrease in acoustic attenuation. Analysis of the waveforms recorded before application of stresses (moment UT_0) shows that because of high attenuation along the majority of ray-paths, it was not possible to detect the wave first motion or measure the P-wave velocity reliably, along many ray-paths. However, along some ray paths, successful picking of P-wave first motion was possible. Results of velocity measurements along 10 selected ray-passes crossing the block in horizontal direction, under unstressed and stressed conditions, are shown in Figure 6.58.

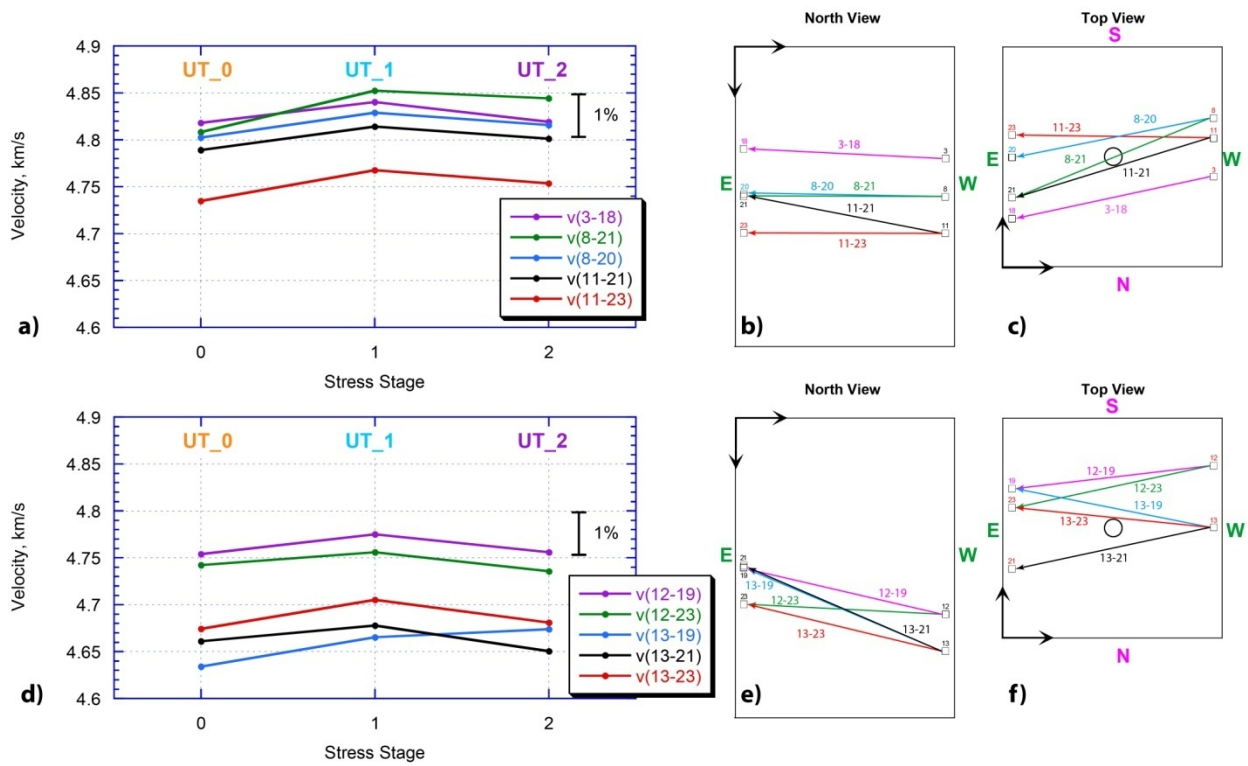

Figure 6.58. a) and d) Variation of P-wave velocities measured along 10 selected traces during the stressing of the block; b) and e) synoptic pictures demonstrating North View of selected traces; c) and f) synoptic pictures demonstrating Top View of selected traces. Upper row: sensors 3, 8 and 11 are transmitters; lower row: sensors 12 and 13 are transmitters of elastic waves.

Figure 6.58 shows that along a few ray-paths with low acoustic attenuation, mostly oriented parallel to bedding direction, stress sensitivity in this Niobrara Shale block is very small. All selected traces show velocity variations within 1%. This is only slightly above accuracy of the velocity measurements, estimated as 0.5%. In a summary, the following conclusions are noted.

(a) The stress sensitivity in velocity, measured along specific traces propagating through the unfractured rock matrix, is small. Velocity variations on the majority of the selected traces are within 1%.

(b) Stress sensitivity of acoustic velocity propagating through bedding planes is high. Effective velocities in the range of 2-5 km/s were observed in ambient conditions and in the range 3.6-5 km/s - after the stressing up the rock.

Using results of ultrasonic transmission measurements UT_2 obtained under final stress condition (T-B Stress = 4500 psi; N-S Stress = 3000 psi; E-W Stress = 1000 psi), and the analysis of 300 traces, results of the measured distance between sensors and the corresponding distance evaluated via the measured onset time, are shown in Figure 6.59.

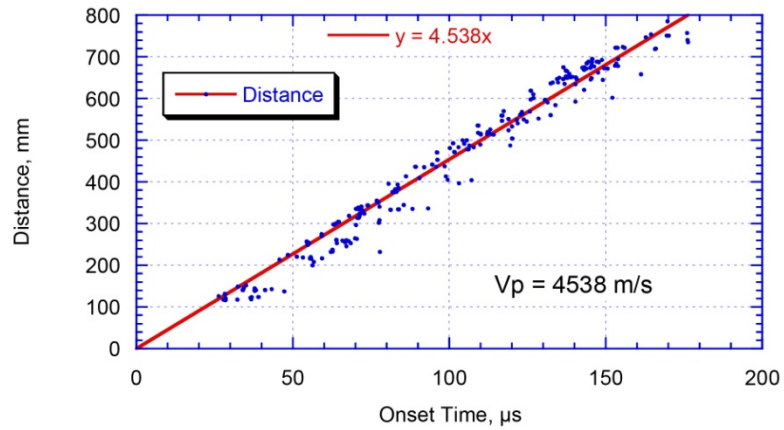

Figure 6.59. Distance between sensors versus observed onset time. The slope characterizes the mean value of homogenized velocity.

The slope of the best fit line of these data set provides the median homogenized velocity of the rock, which is equal to 4538 m/s. Since there was no AE sensors installed on the bottom of the block, it was not possible to measure vertical components of P-wave velocity. Therefore, we are forced to assume that velocity model is close to isotropic. As a consequence of this assumption, the error of AE hypocenter localization could be larger in vertical direction. However the distribution of AE events in horizontal direction was captured more accurately.

6.2.7.3 Analysis and Localization of Acoustic Events

Localization of acoustic emission events is based on the identification of P-wave onset times, using technique commonly applied in seismology (Akaike Information Criteria -- AIC technique[6], and then iteratively solving the equations, which find the common source of the events measured by multiple transducers. This is done by minimization of residuals of the time-distance relationship using SIMPLEX minimization technique[7]. The present solution is obtained using a homogeneous velocity model. The error associated with identifying each acoustic emission source location is given by a localization uncertainty parameter. This is equal to the remaining residual of hypocenter localization. In the current test only AE events satisfying a remaining residual less than 5 μs were used. This value roughly corresponds to 24 mm spatial accuracy of AE hypocenter localization (or ± 12 mm). All these AE events, localized with lower accuracy, were rejected. Thus, noisy sensors or sensors with weak signals are automatically excluded from the analysis. The minimum number of sensors required for localization is 8, though the larger the number of sensors, the larger accuracy and error quantification. After localization and analysis of the convergence of the solution, spatial locations (x, y, z) of the successful events are tabulated for subsequent analysis and visualization.

[6] http://en.wikipedia.org/wiki/Akaike_information_criterion)
[7] http://en.wikipedia.org/wiki/Simplex_algorithm

The time history of the applied bore pressure and the measured volumes of the East-West, North-South flat jacks and the Top-Bottom actuator, are presented in Figure 6.60.

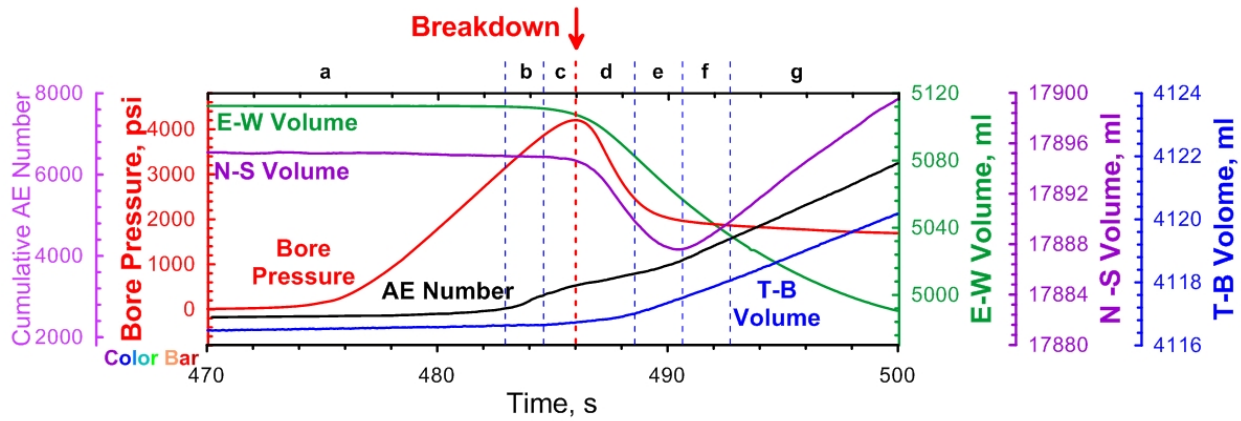

Figure 6.60. Bore pressure (red), cumulative number of localized AE (black), East-West flat jack volume (green), North-South flat jack volume (pink) and Top-Bottom Actuator volume (blue). All parameters are plotted versus loading time, separation of loading stages (a)-(e) is shown by vertical dash lines.

The cumulative number of localized AE is shown in Figure 6.60 (black). One can see the slight increase of AE activity, about 2 seconds before peak of borehole pressure (red). Based on the analysis of mechanical parameters, the loading process was divided into 7 stages labeled (a) – (g). Stage (a) characterizes the initial part of injection. Here we see no indication of fracturing. During the stage (b) we observe volumetric deformation of the rock in East-West direction, it coincides with increase of AE rate and with the onset of hydraulic fracture initiation. During the stage (c) we observe continuation of block dilatancy in East-West direction (green), indicating hydraulic fracture opening. The onset of block dilatancy in North-South direction (pink), is most likely related to the opening of some preexisting fractures oriented parallel to bedding planes (East-West direction). This may be caused by the application of bore pressure above the maximum horizontal stress of 3000 psi. The onset of Top-Bottom volumetric deformation (blue) during the stage (c) indicates block shortening in the vertical direction and is related to hydraulic fracture propagation and opening in the horizontal direction. After breakdown, during stages (d)-(e), we observed continuation of block shortening in vertical direction (blue) and extension in both horizontal directions, indicating opening of hydraulic fracture (green curve) and most likely, some orthogonally oriented preexisted fractures (pink curve). During the very last stages (f)-(g), we observed compaction of block in North-South direction, most likely indicating closure of preexisting fractures by maximum horizontal stress caused by decrease of bore pressure below 3000 psi level. It is worth mentioning that during stages (f)-(g) the bore pressure was above the minimum horizontal stress (1000 psi), and caused the continuation of hydraulic fracture opening indicated by the volumetric deformation observed in the East-West direction (green curve).

6.2.7.4 Acoustic Emission During Initial Stage of Fluid Injection (Stage a)

Figure 6.61 (a)-(c) show three orthogonal projections of AE hypocenters, and Figure 6.61(d) shows the time progression of the borehole pressure (red), the rate of acoustic emissions (pink) and the volumetric displacement along the EW direction (green). The highlighted portion of these curves (in colors violet to red) indicates the time interval of the stage. The color scheme is used to define the sequence of AE events in time: from violet (earliest) to red (latest). The AE hypocenters recorded before pressurization of the borehole lay almost uniformly distributed within the block, with a bit higher activity in the upper part of the block (pink – blue color of hypocenter dots). AE clusters near the top and North faces of the block may indicate the effect of the loading action on these surfaces.

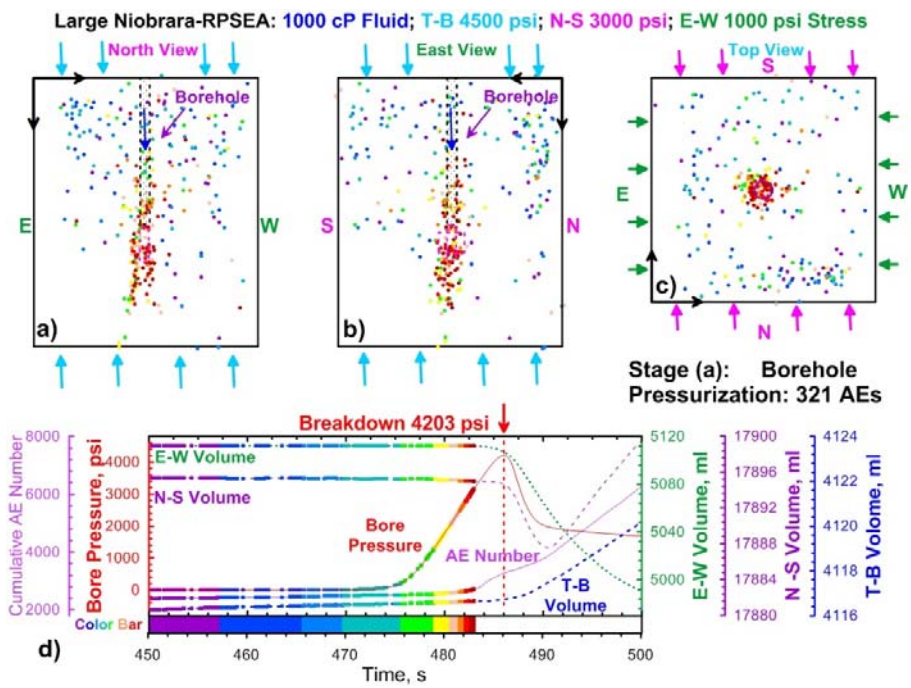

Figure 6.61. (a)-(c) Three orthogonal projections of AE hypocenters; d) Loading history recorded during Stage (a) of injection. The color of the dots corresponds to the time sequence of AE events appearance according to the color bar at the bottom of the figure.

To enhance the rendering of AE hypocenters, we calculated the density of these AEs within a sliding cube of dimensions 10 x 10 x 10 mm. These results are subsequently calculated as a normalized fraction of the maximum number of events counted per sliding cube, and then plotted on each orthogonal projection. The section of the borehole, where the perforations were located, is marked by a pink rectangle (dashed lines). Results are shown in Figure 6.62 and demonstrate the slightly higher AE density in the vicinity of the open hole section of the borehole. This is most likely related to the presence of perforations that create stress concentrators.

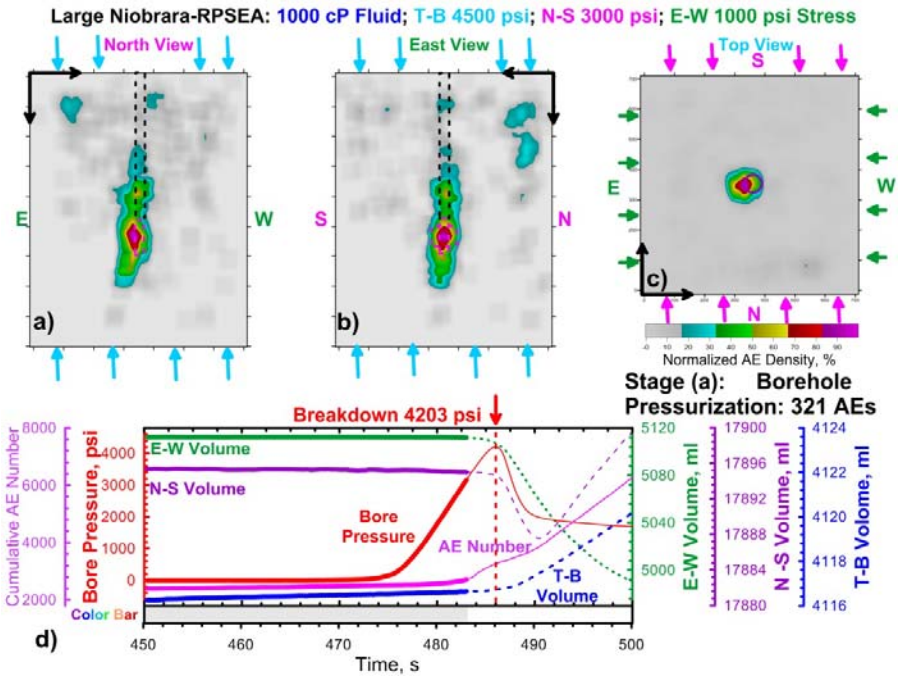

Figure 6.62. (a)-(c) Three orthogonal projections of AE hypocenters; d) Loading history recorded during Stage (a) of Injection. Original AE hypocenter data are the same as presented in Figure 6.61 (a)-(c).

6.2.7.5 Acoustic Emission During the Stage of Hydraulic Fracture Initiation (Stage b)

Similarly to the stage (a), Figure 6.63 (a)-(c) show three orthogonal projections of AE hypocenters, and Figure 6.63 (d) shows the time progression of the borehole pressure, the volumetric deformation along the EW direction, and the cumulative number of AE. In the selected time window (marked by the colors from violet to red), the borehole pressure data shows a slight deviation from a linear increase and the cumulative AE data shows a slightly higher density of AE hypocenters near the bottom of the borehole, where the perforations are located. This behavior coincides with the onset of East-West flat jack volume decrease, which indicates hydraulic fracture (HF) initiation and beginning of fracture opening.

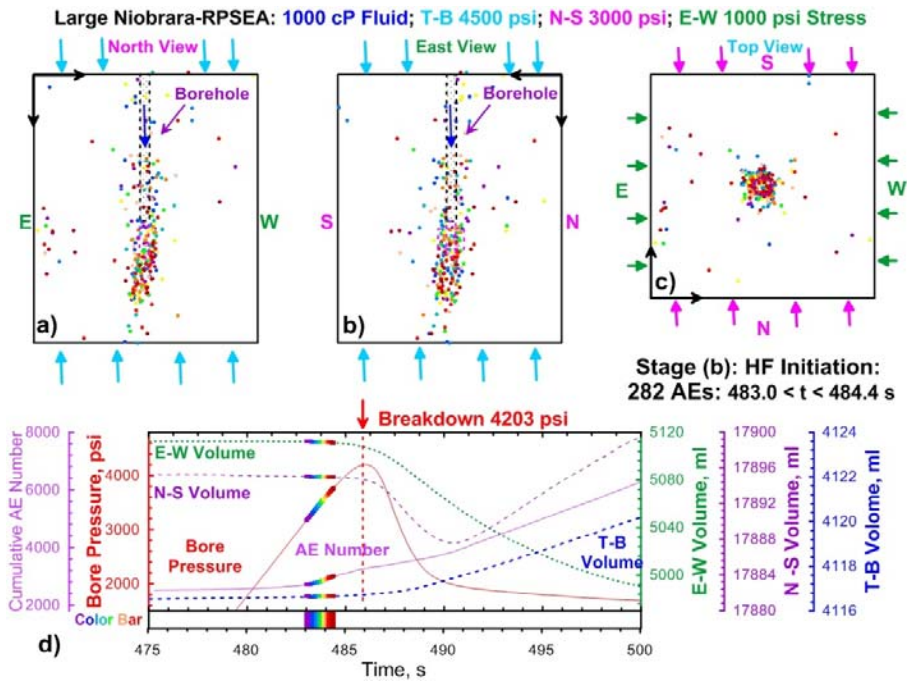

Figure 6.63. (a)-(c) Three orthogonal projections of AE hypocenters; d) Loading history recorded during stage (b) of injection. The color of the dots corresponds to the time sequence of AE events appearance according to the color bar at the bottom of the figure.

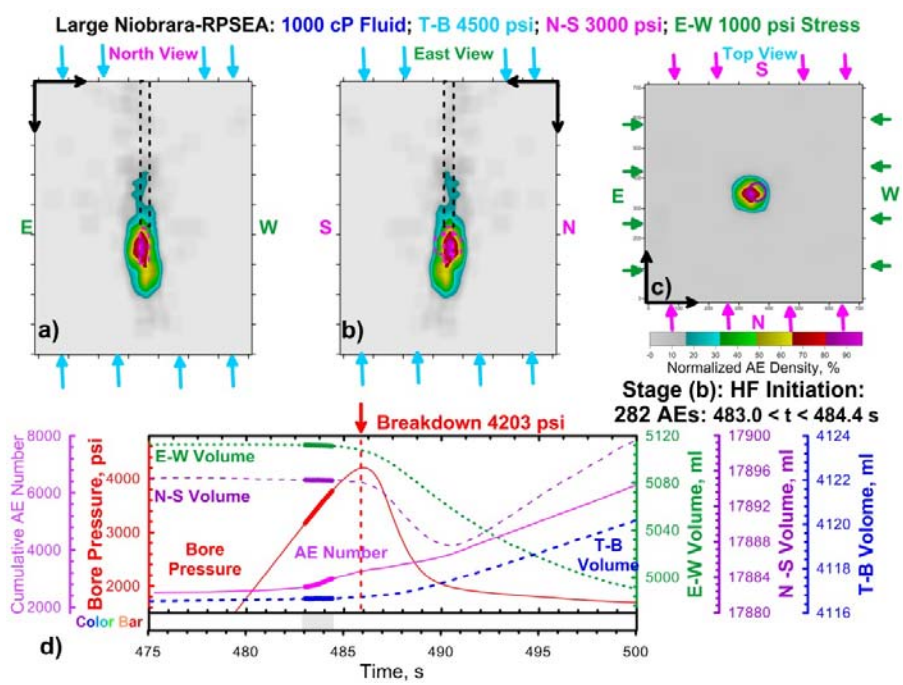

Figure 6.64. Three orthogonal projections of AE hypocenter normalized density calculated for the stage (b) of injection. Original AE hypocenter data are the same as presented in Figure 6.63 (a)-(c).

The AE density maps presented in Figure 6.64 confirm the appearance of AE clustering in the vicinity of perforation and fracture initiation during the stage (b).

6.2.7.6 Acoustic Emission During the Stage of Fracture Propagation (Stage c)

Similarly to the previous stages, Figure 6.65 (a)-(c) show three orthogonal projections of AE hypocenters, and Figure 6.65 (d) shows the time progression of the borehole pressure, the volumetric deformation along the EW direction, and the cumulative number of AE. In the selected time window (marked by the colors from violet to red), the data shows an additional increase of AE activity, indicating fracture propagation in the Top-Bottom and North-South directions. This process coincides with a decrease in East-West flat jack volume and with the onset of North-South flat jack volume decrease, indicating block dilatancy in both horizontal directions during the stage (c). Note that during this stage the value of bore pressure was above the maximum horizontal stress, therefore, the sample extension in North-South direction is most likely related to the fluid penetration into preexisting fractures oriented parallel to the bedding planes (East-West direction).

A map of AE hypocenter density (Figure 6.66) highlights the formation of a hydraulic fracture propagating in the North-South direction and having a pancake-like shape (East View, Figure 6.66b), parallel to the wellbore. AE analysis shows that at the moment of breakdown (at the end of stage (c)) the hydraulic fracture has almost reached the North and South faces of the block.

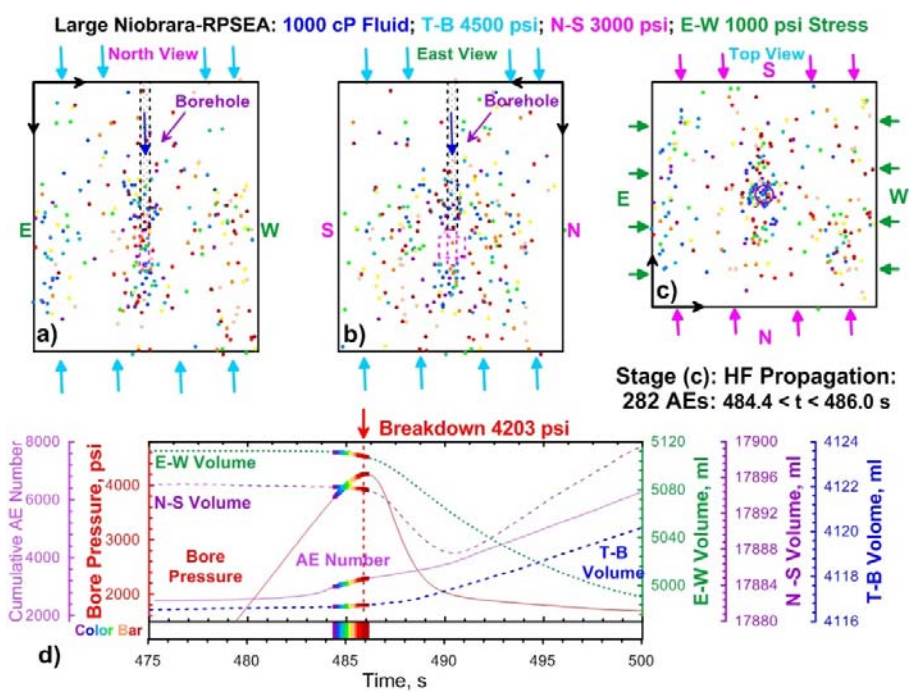

Figure 6.65. (a)-(c) Three orthogonal projections of AE hypocenters; d) Loading history recorded during Stage (c) of Injection. The color of the dots corresponds to the time sequence of AE events appearance according to the color bar at the bottom of the figure.

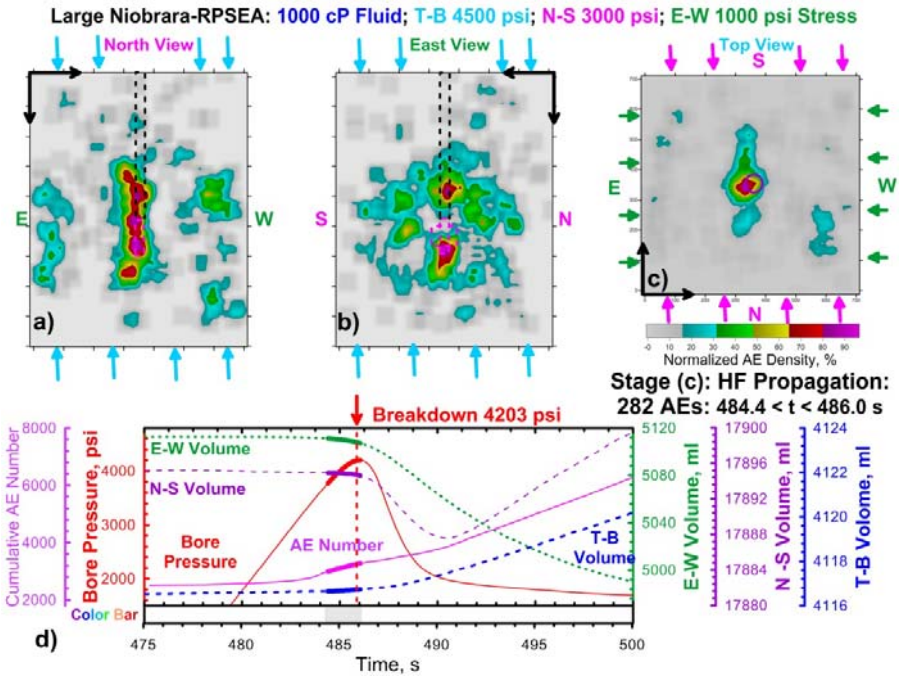

Figure 6.66. Three orthogonal projections of AE hypocenter normalized density calculated for the stage (b) of injection. Original AE hypocenter data are the same as presented in Figure 6.65 (a)-(c).

6.2.7.7 Acoustic Emission After Breakdown (Stages d-h)

Right after the breakdown moment during the stage (d) we observed the appearance of AE activity localized at the distance of about 70-90 mm from the North face of the block. These events extended slightly towards the West face of the block, as indicated in Figure 6.68, and also on the AE map of Figure 6.69. At the beginning of the stage (d) the bore pressure was above the intermediate stress, in the North-South direction. The, significant decrease of the North-South flat jack volume indicated sample extension in North-South direction, therefore, most likely, the AE activity localized near the North face of the block is related to the opening of preexisting fractures parallel to the bedding direction located nearby. This assumption also could be supported by analysis of post-test photos of the block, indicating branching of hydraulic fracture propagating northward, and also by the opening of some orthogonal fractures visible on the top face of the block (Figure 6.67).

Analysis of AE activity registered during the next stage (e) of injection indicates extension of this AE cloud eastwards, upwards and downwards (Figure 6.70 and Figure 6.71). At the end of stage (e), the AE cloud almost reached the bottom of the block and it coincided with the minimum value of the North-South flat jack volume, indicating highest extension of the block in the North-South direction. Note that after the end of stage (e), the bore pressure flattened at the level below the intermediate stress, and above the minimum stress. This behavior most likely indicates water seepage off the block at almost constant rate.

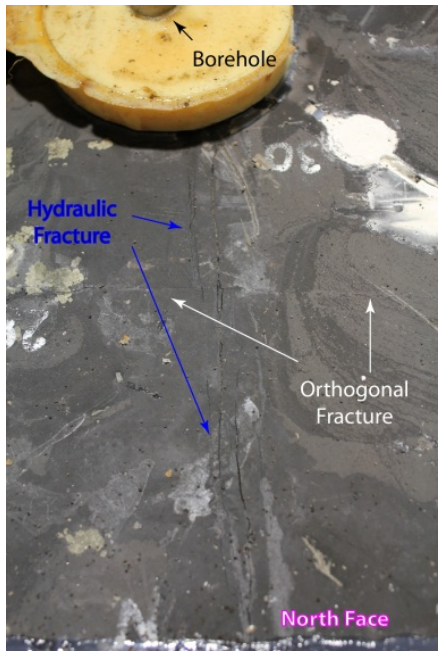

Figure 6.67. Top view photo of fractured sample.

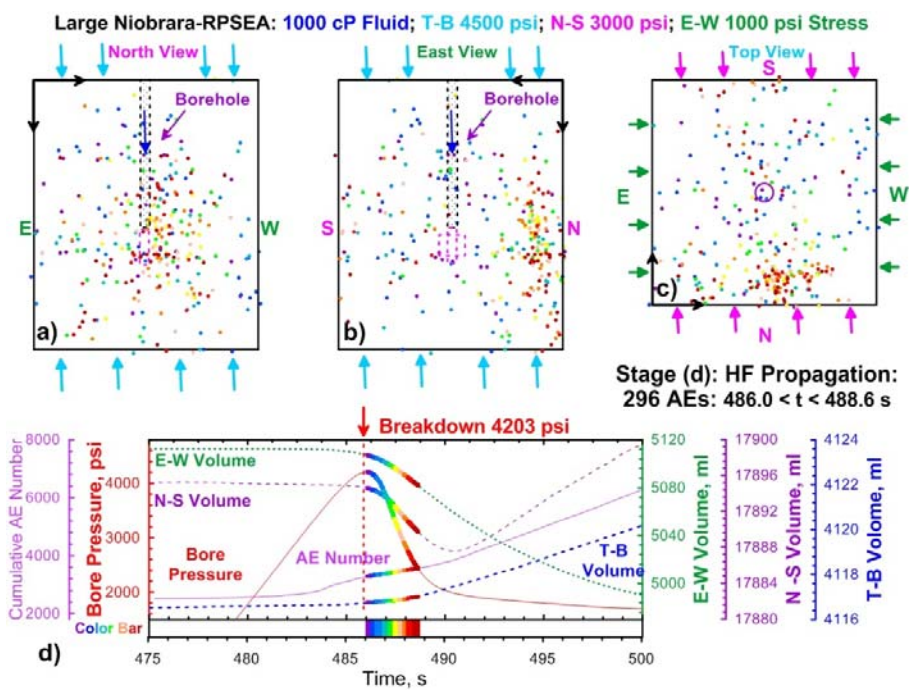

Figure 6.68. (a)-(c) Three orthogonal projections of AE hypocenters; d) Loading history recorded during Stage (d) of Injection. The color of the dots corresponds to the time sequence of AE events appearance according to the color bar at the bottom of the figure.

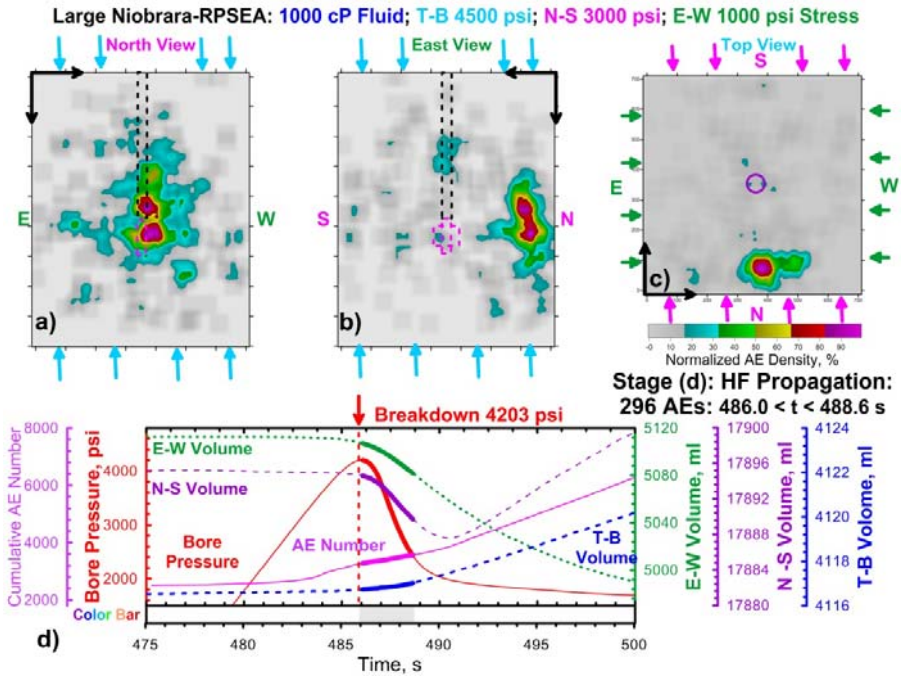

Figure 6.69. Three orthogonal projections of AE hypocenter normalized density calculated for stage (d) of injection. Original AE hypocenter data are the same as presented in Figure 6.68 (a)-(c).

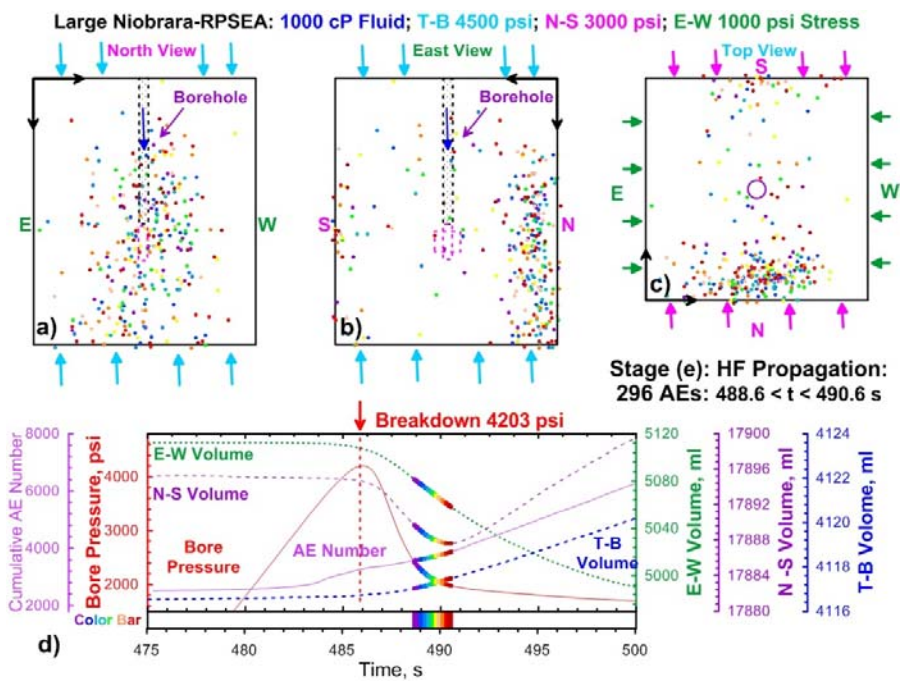

Figure 6.70. (a)-(c) Three orthogonal projections of AE hypocenters; d) Loading history recorded during Stage (e) of Injection. The color of the dots corresponds to the time sequence of AE events appearance according to the color bar at the bottom of the figure.

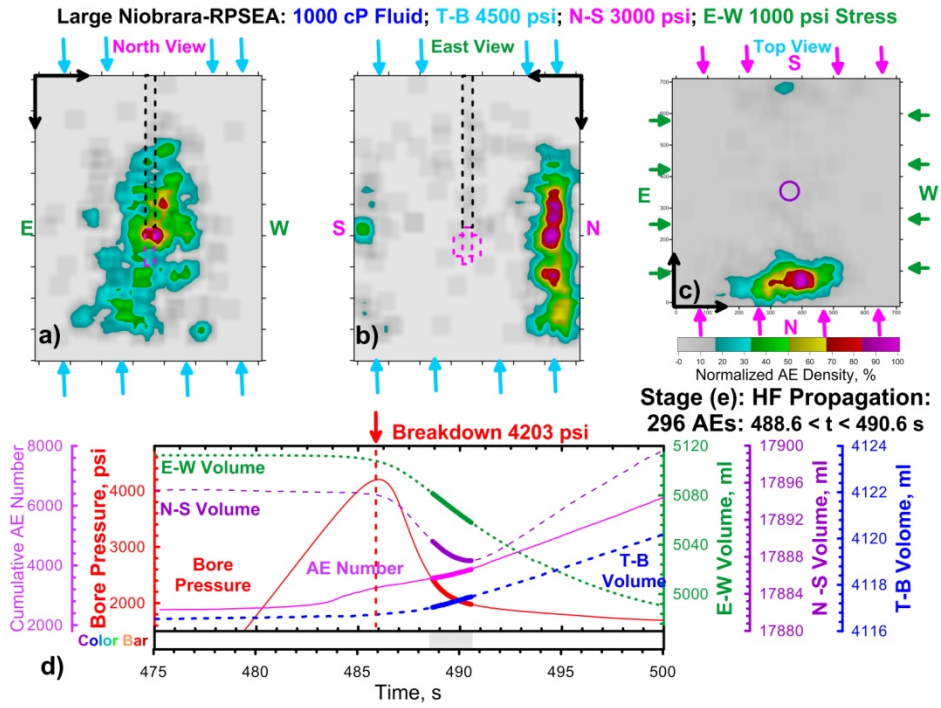

Figure 6.71. Three orthogonal projections of AE hypocenter normalized density calculated for stage (e) of injection. Original AE hypocenter data are the same as presented in Figure 6.70 (a)-(c).

During the next stage (f) we observed farther extension of the AE cloud eastwards and westwards (Figure 6.73a). The appearance of the AE cloud at the South face of the block (Figure 6.73b and Figure 6.73c) indicates that at the end of stage (f) the hydraulic fracture approached the South face of the block. Note that during the stage (f) we observed an increase of the North-South flat jack volume (Figure 6.73d, pink curve), indicating closure of preexisting cracks located near the North face of the block, and oriented parallel to the North face. At the same time we observed farther decrease of East-West flat jack volume (Figure 6.73d, green curve), indicating farther opening of hydraulic fracture. During the very last analyzed Stage (g) we observed farther spreading of AE clouds near the North and South faces of the block

Figure 6.74 and Figure 6.75), farther increase of North-South flat jack volume, and decrease of East-West flat jack volume (Figure 6.75d). This indicates the closure of a preexisting fracture and opening of a hydraulic fracture.

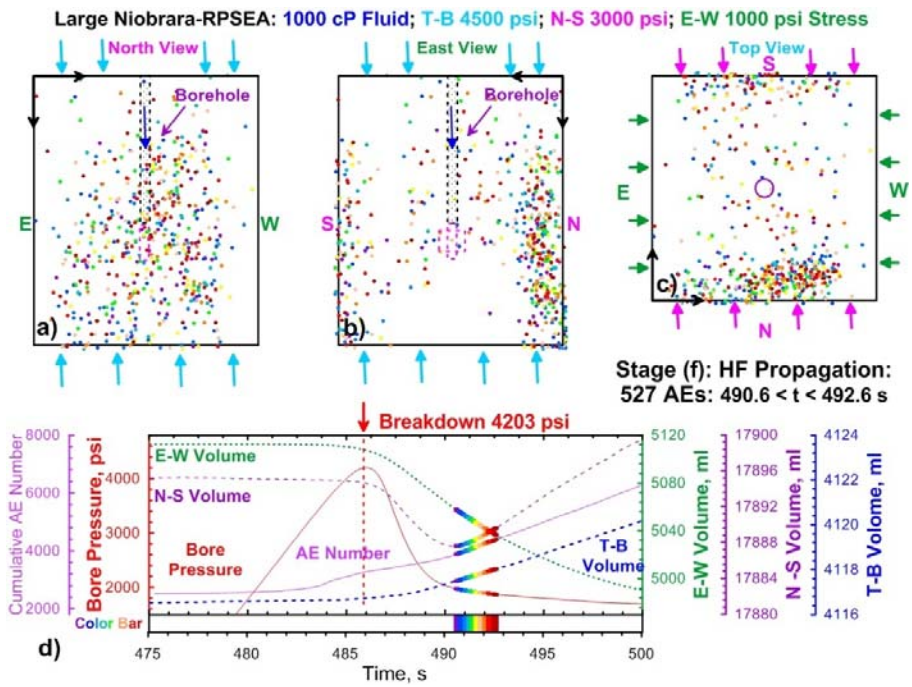

Figure 6.72. (a)-(c) Three orthogonal projections of AE hypocenters; d) Loading history recorded during Stage (f) of Injection. The color of the dots corresponds to the time sequence of AE events appearance according to the color bar at the bottom of the figure.

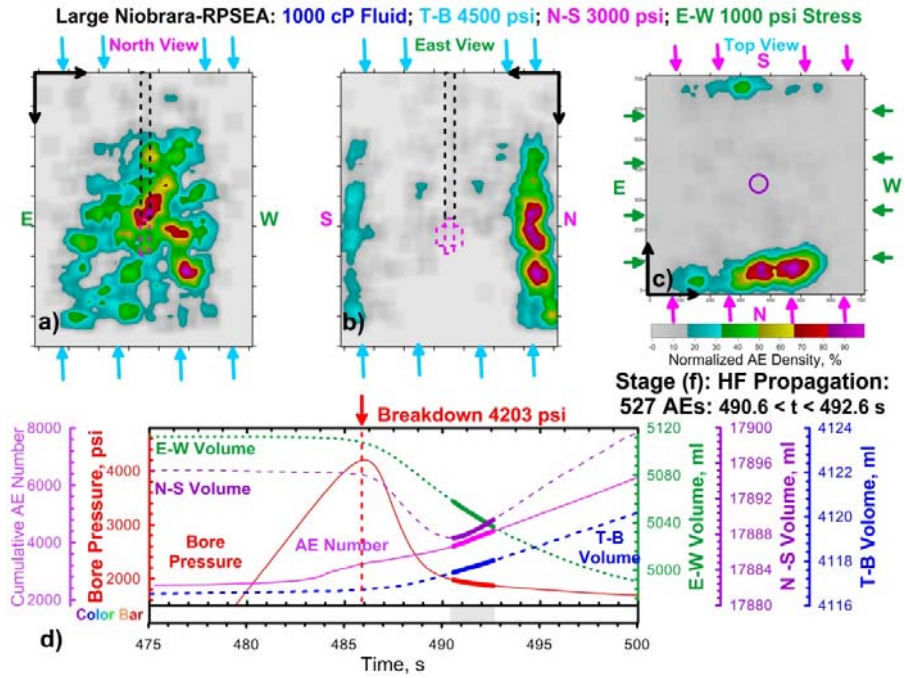

Figure 6.73. Three orthogonal projections of AE hypocenter normalized density calculated for the stage (f) of injection. Original AE hypocenter data are the same as presented in Figure 6.72 (a)-(c).

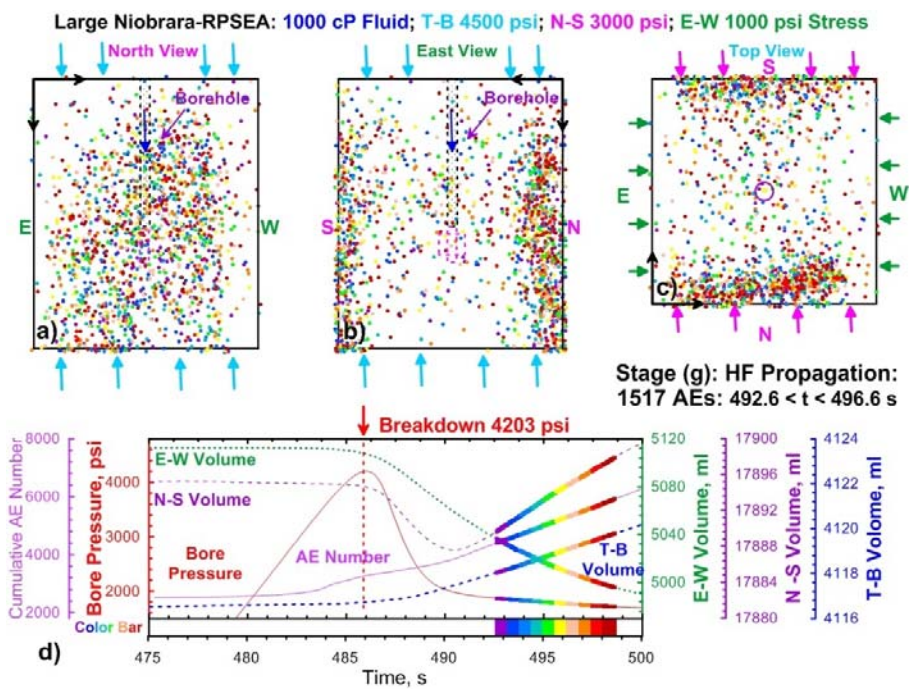

Figure 6.74. (a)-(c) Three orthogonal projections of AE hypocenters; d) Loading history recorded during Stage (g) of Injection. The color of the dots corresponds to the time sequence of AE events appearance according to the color bar at the bottom of the

figure.

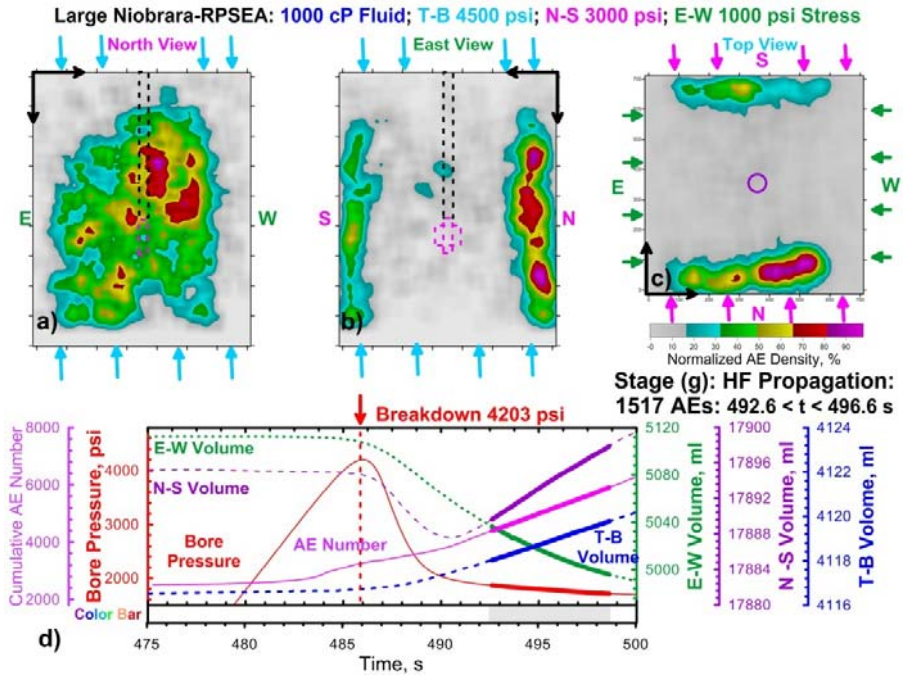

Figure 6.75. Three orthogonal projections of AE hypocenter normalized density calculated for the stage (g) of injection. Original AE hypocenter data are the same as presented in

Figure 6.74 (a)-(c).

6.2.7.8 Periodic Monitoring of P-wave Velocity and Amplitude during the Test

Additional information about the process of hydraulic fracturing could be obtained from the analysis of ultrasonic transmission. Acoustic transmissions were performed every 5 seconds during the initial stage of injection and every 2 seconds after the bore pressure approached 1000 psi. However, the very high injection rate of 1000ml/min caused a very high AE activity of approximately 240 localized AE events per second, after hydraulic fracture initiation. This value of AE activity is very close to the maximum rate of successful registration by the Vallen System. Such a high AE activity created problems in the acquisition and interpretation of ultrasonic transmission events, which overlapped with the high AE activity. Often, the Vallen system was triggered by AE signal and blocked during ultrasonic transmissions, in other cases the onset of ultrasonic transmission signals was hidden inside the high amplitude ringing of the block, caused by frequent AE signals.

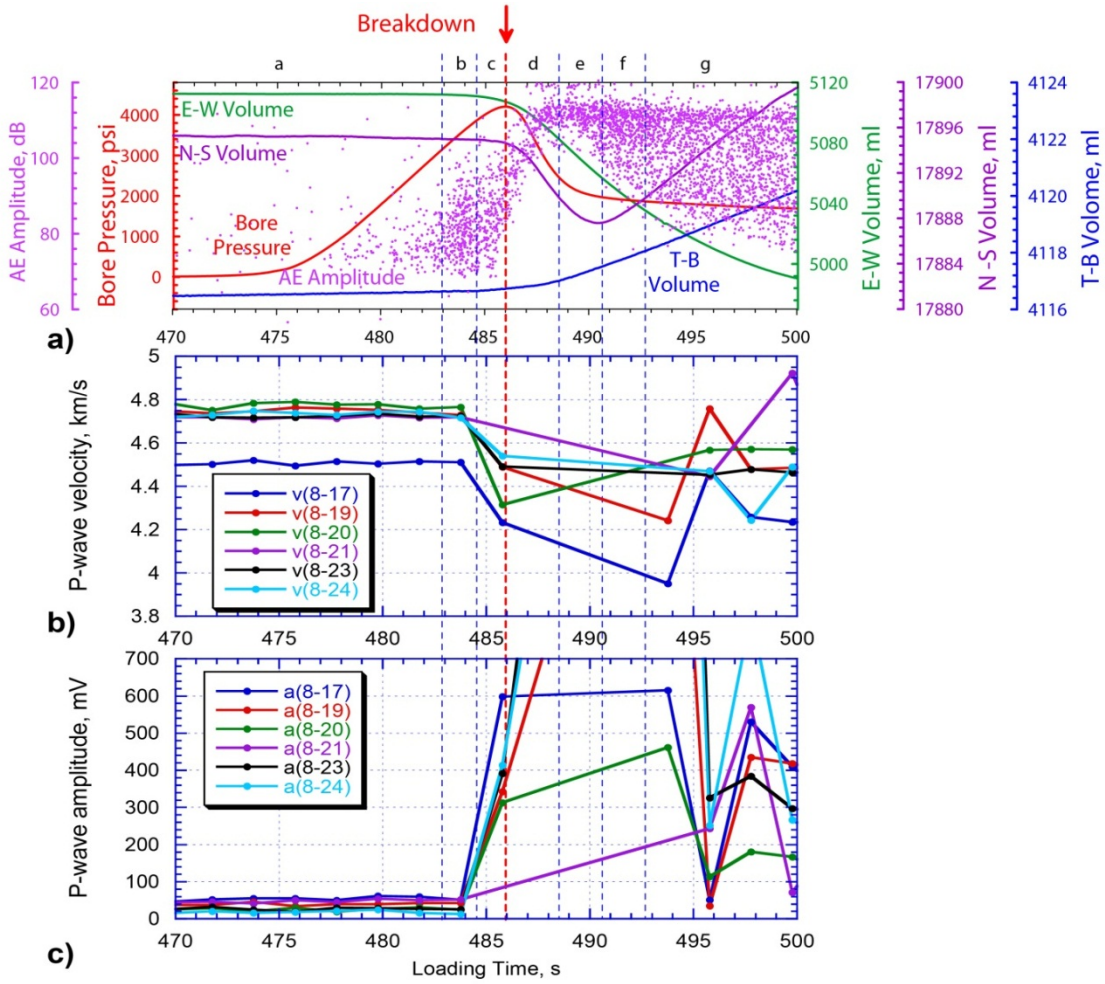

Figure 6.76. a) Time history of mechanical parameters and amplitude of localized AE events (pink color dots); b) P-wave velocity measured by using sensor 8 as transmitter and sensors 17, 19, 20, 21, 23 and 24 as receivers; c) P-wave first motion amplitude vs time.

Figure 6.76a shows a comparison of localized AE amplitude (pink color dots) and mechanical parameters, during the fluid injection stage that indicates significant increase of AE amplitude after the onset of hydraulic fracturing and also by the absence of localized low amplitude AE events during the fracture propagation stage. Ultrasonic transmissions were measured reliably every 2 seconds in numerous directions before the beginning of hydraulic fracture propagation (Figure 6.76 b and c). However, after the onset of high AE activity, successful ultrasonic transmission registration was significantly less frequent and less accurate, because of the often missing P-wave arrivals inside a high level background AE signals. Nonetheless, we observed a decrease of effective P-wave velocity during hydraulic fracture propagation (Figure 6.76 b), however this decrease was related to the missing of the very first P-wave arrival, within the high amplitude background noise, causing significant increase of the automatically picked P-wave amplitude (Figure 6.76c). Therefore and unfortunately, reliable ultrasonic measurements could not be performed during the time of very high AE activity, induced by fluid injection at a rate of 1000 ml/s.

6.2.7.9 Summary (Stages a through g)

In summary the AE measurements and localization analysis, during fluid injection, provided us with the following understanding:

- Before the beginning of borehole pressurization we observed AE activity spread in the upper part of the stressed block. These were not rock fracturing events but rock complaining events, associated to the contact between the rock external surfaces and the loading flatjacks After borehole pressurization we observed the appearance of AE activity localized in the vicinity of the perforations, as one would anticipate for a fracture initiation event.
- The onset of fracture initiation was detected by the AE analysis reasonably well, and occurred at a bore pressure below the breakdown. This onset of fracturing is consistent across the various measurements of volumetric deformation, cumulative AE and AE localization.
- AE analysis confirmed the formation of a planar hydraulic fracture, during about 2 seconds, with pancake-like shape oriented parallel to the wellbore, parallel to the maximum horizontal stress direction, and perpendicular to bedding, In this condition, and prior to breakdown, the fracture almost reached the North and South faces of the block.
- During the later stages of injection, AE analysis confirmed the formation of an AE cloud near the North face of the block, which coincided with the decrease in the flatjack volume indicating the opening of orthogonal fractures oriented in East-West direction.
- The moment, when AE activity indicated that the orthogonal fracture approached the bottom face of the block, coincides with the maximum extension of the block in North-South direction as indicated by volumetric deformation measurements. We assume that at this moment the fluid front approached the block boundaries and afterwards we observed seepage of the fracturing fluid through the opened hydraulic fracture.
- Reliable ultrasonic measurements could not be performed because of the very high rates of AE activity induced by rapid fluid injection at 1000 ml/s.

6.2.8 AE Results Registered during Proppant Injection

6.2.8.1 Stages of Proppant Injection

Time history of applied bore pressure, measured volumes of fluid inside East-West, North-South flat jacks, Top-Bottom actuator, as well as variation of AE event amplitudes are presented in Figure 6.77. Whole proppant injection interval was separated into 3 stages determined as follows: during stage (a) proppant was pumped using MOYNO pump with 6 l/min injection rate; during the stage (b) MOYNO pump was stopped and during the stage (c) East-West stress was increased from 50 up to 500 psi.

Volumetric deformation indicates that during the stage (a) the block extended in horizontal directions - East-West and North-South (green and pink curves in Figure 6.77.).

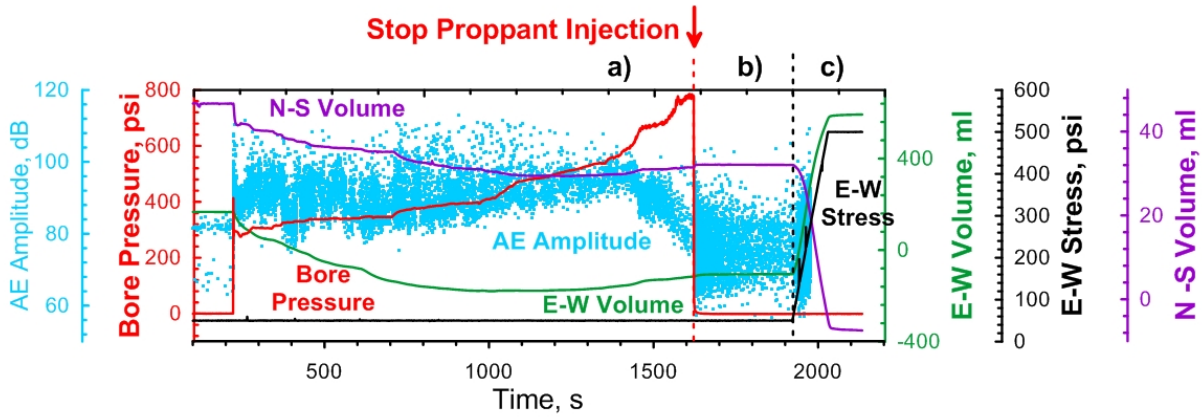

Figure 6.77. Bore pressure (red), amplitude of localized AE (blue), East-West flat jack volume (green), North-South flat jack volume (pink) and East-West stress (black). All parameters are plotted versus loading time, separation of loading stages (a)-(c) is shown by vertical dash lines.

During the stage (a) very high rate of Vallen System triggering was observed with high amplitude of recorded events (blue dots in Figure 6.77.), however post-test analysis of AE demonstrated that MOYNO pump produced very high amplitude background noise, making it difficult to localize AE events and to measure velocity and amplitude of ultrasonic transmissions reliably.

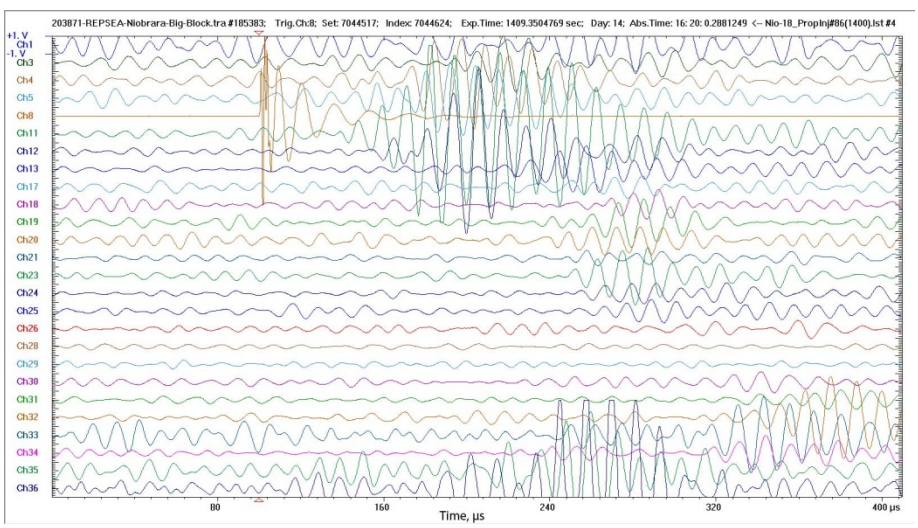

Figure 6.78. Representative example of waveforms recorded during the stage (a) at the moment of ultrasonic transmission by channel 8.

Waveforms presented in Figure 6.78 show that during the stage (a) very high amplitude non-stop vibrations were recorded by all channels, making difficult reliable estimation of onset time of elastic waves. Most likely these non-stop vibrations were related to very high

flow rate through the hydraulic fracture and bead pack. For that reason the stage (a) was excluded from AE analysis.

6.2.8.2 AE Results Registered during the Stage (b)

Right after interruption of MOYNO pump operation, high amplitude background noise disappeared, and successful AE localization became possible. Figure 6.79 shows localization of AE events and Figure 6.80 – mapping of AE activity, indicating clustering of AE events in the center and upper part of the block. Side view projections (Figure 6.79a and Figure 6.80a) show that AE events are localized in the plane, slightly tilted from vertical direction, position of orientation of this plane is in good agreement with actual hydraulic fracture surface captured by post-test photos. At the very beginning of the stage (b) bore pressure dropped to zero very fast and during the whole stage (b), all mechanical parameters (stresses and deformation) were almost constant. However, AE activity was very high for at least 5 minutes after the interruption of MOYNO pump, it was most likely related to the process of proppant readjustment and embedment into the rock. Note that AE activity is higher in the upper part of the rock, this is in a very good correspondence with post-test analysis of the fractured surface roughness. Also, Figure 6.79b shows that AE activity is higher in the vicinity of the borehole. Most likely, it is related to the thicker layer of proppant pack near the borehole, this assumption is supported by post-test measurements of the proppant weight measured in different zones of the fractured surface. Therefore, we can conclude that AE is very reliable tool to investigate a proppant placement process, it allows to highlight areas of the rock, where proppants are placed, and generate thousands of powerful signals by holding load.

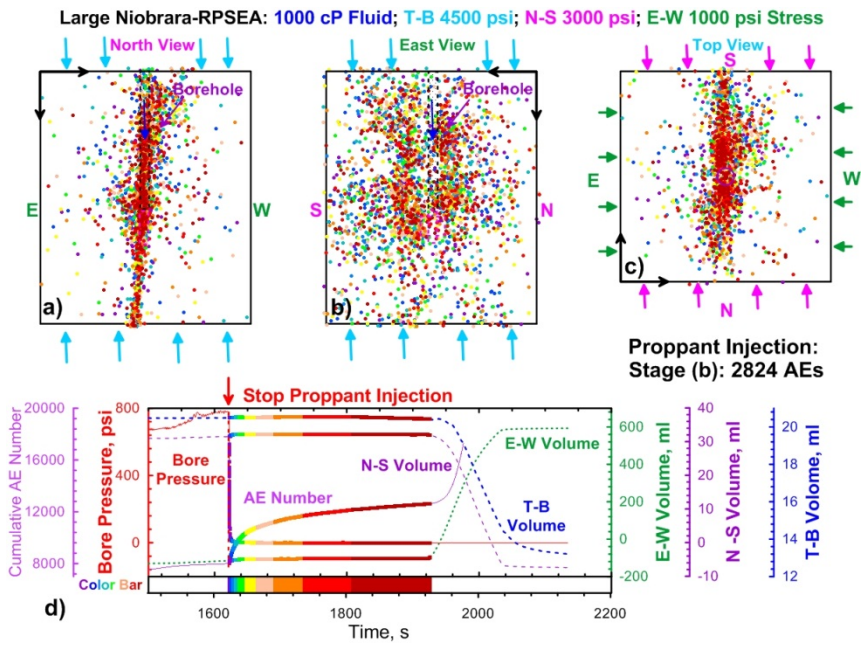

Figure 6.79. (a)-(c) Three orthogonal projections of AE hypocenters; d) Loading history recorded during Stage (b) of proppant injection. The color of the dots corresponds to the time sequence of AE event appearances according to the color bar at the bottom of the figure.

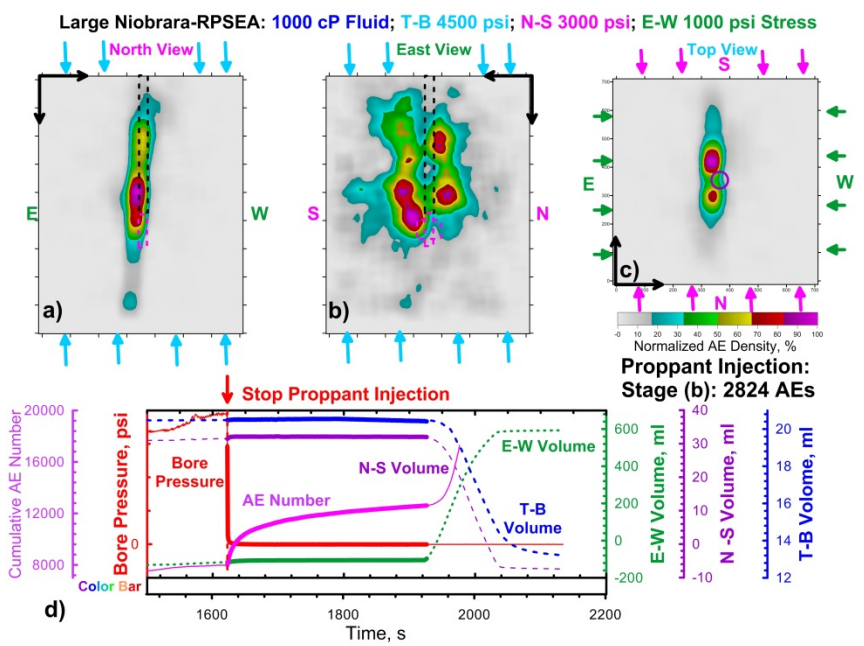

Figure 6.80. (a)-(c) Three orthogonal projections of AE hypocenters; d) Loading history recorded during Stage (b) of proppant injection. The color of the dots corresponds to the time sequence of AE event appearances according to the color bar at the bottom of the figure.

6.2.8.3 AE Results Registered during the Stage (c)

Right after beginning of East-West stress increase (in the direction orthogonal to hydraulic fracture plane), high increase of AE activity was observed. Figure 6.81 (a)-(c) show three orthogonal projection of AE events with the highest amplitude, and one can see that AE events are more uniformly distributed in the plane of hydraulic fracture (Figure 6.81b) than in the previous stage (Figure 6.79b). However, clustering of AE activity in few spots could be seen in Figure 6.81, most likely zones of increased AE activity could be related to the roughness of created hydraulic fracture surface and distribution of proppants in some patches holding the load orthogonal to the fractured surface.

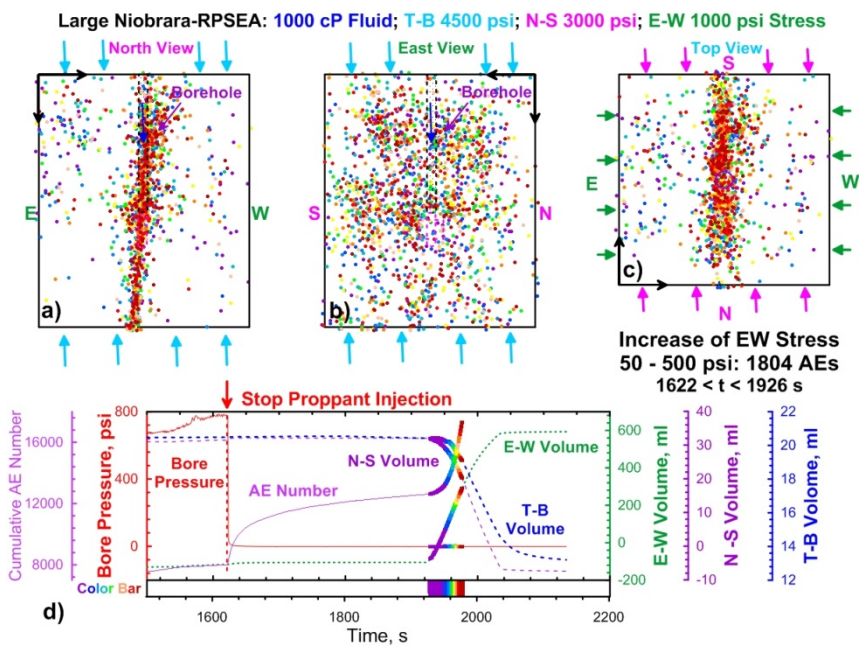

Figure 6.81. (a)-(c) Three orthogonal projections of AE hypocenters; d) Loading history recorded during Stage (c) of proppant injection. The color of the dots corresponds to the time sequence of AE event appearances according to the color bar at the bottom of the figure.

These clusters of AE activity could be seen in more details on the AE mapping presented in Figure 6.82b. North side view of AE activity in Figure 6.82a highlights the whole surface of hydraulic fracture, this image was found in a good agreement with the post-test photo of North face of the block, also demonstrating that orientation of fracture surface was not precisely vertical, but slightly tilted. Therefore, we can conclude that AE registration during the stressing of the block can provide very useful information about propant distribution over the whole fracture surface. We assume that clusters of AE activity could be related to the patches of proppant distribution.

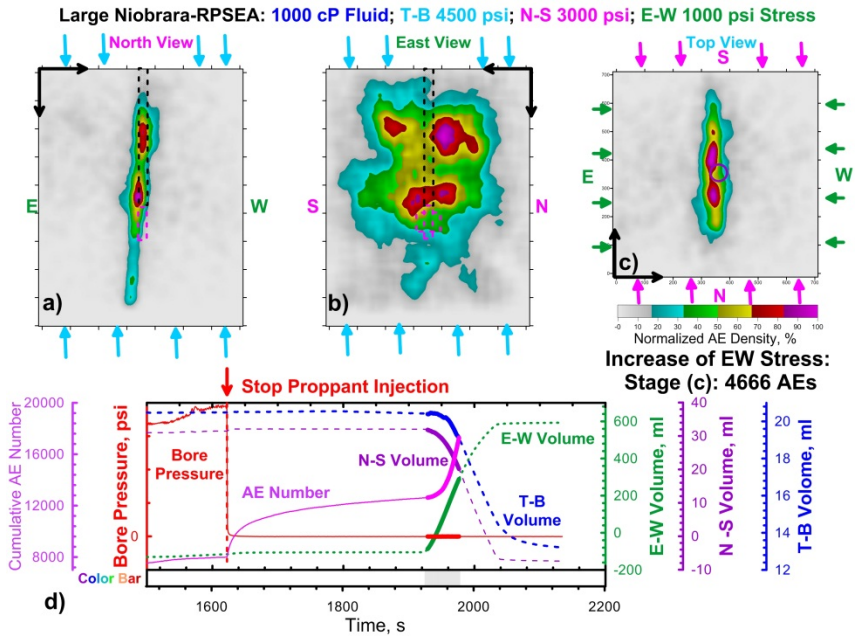

Figure 6.82. (a)-(c) Three orthogonal projections of AE hypocenters; d) Loading history recorded during Stage (c) of proppant injection. The color of the dots corresponds to the time sequence of AE event appearances according to the color bar at the bottom of the figure.

6.2.9 General Conclusions based on AE Analysis

- AE registration during hydraulic fracturing allows us to draw the following picture of hydraulic fracturing: hydraulic fracture was initiated in the vicinity of perforations, then very fast, during less than 2 seconds, propagated toward the North and South boundaries of the rock, causing activation of preexisting fracture located near the North face of the rock. After that we observed propagation of AE cloud at first toward East face of the rock, then westward and downward, most likely indicating position of the water front. At the very last stage we registered appearance and propagation of AE activity near the South face of the rock in all directions, indicating propagation of fluid front along beads surrounding the rock.
- AE registration after the cease of proppant pumping shows AE activity distributed in the upper part of the rock and in the vicinity of the borehole. It was most likely related to the process of proppant readjustment and embedment into the rock. AE activity distribution was found in a very good correspondence with post-test analysis of fractured surface roughness.
- AE registration during the stressing of the block orthogonally to the hydraulic fracture plane shows that AE events are more uniformly distributed in the plane of hydraulic fracture with some clustering of AE activity in few spots. These zones of increased AE activity could be related to the roughness of created hydraulic fracture surface and distribution of proppants in some patches holding the load orthogonal to the fractured surface.

6.3 Discussion and Summary

The objective of this section was to complete a large-scale laboratory test of hydraulic fracturing, proppant transport and fracture conductivity measurement, to validate results presented in previous sections, and have a better reference to extend these learnings to field operations. We used a Niobrara shale outcrop block (approximately 3 ft. x 3 ft. x 3ft.) representative of the Niobrara oil and gas producing formation to conduct the experiment. We also conducted additional measurements of fracture conductivity on small samples of Niobrara shale, and compared these to the measurements obtained in the large block.

Large block experiments that simulate hydraulic fracturing, proppant transport and fracture conductivity on heterogeneous tight shales are difficult to conduct and not common. The present effort represents a unique opportunity for understanding the various components of the process, and provides a better mental picture to the corresponding processes occurring at depth and at a field scale. The various components of the laboratory testing process are listed below:

1. Hydraulic fracturing of the block under realistic conditions of in-situ stress and pumping conditions. The fluid viscosity and pumping rates were scaled, using dimensionless numbers, to represent a viscosity dominated flow and thus facilitate the development of a planar, simple geometry fracture.
2. Measuring fracture conductivity to water on the un-propped fracture as a function of the fracture closure stress.
3. Fracture re-opening and proppant transport (100 mesh sand) using water at high pumping rates as the carrying fluid.
4. Measuring fracture conductivity to water on the propped fracture as a function of the fracture closure stress.
5. Supplementing these measurements with acoustic emission (AE) and acoustic transmission (AT) measurements, and with a comprehensive post-test characterization, including observations of proppant distribution, proppant embedment and created surface roughness.
6. Finally, the large-scale measurements were compared with small scale measurements, to evaluate the size effect and to better understand the processes at in-situ conditions.

The following summarizes key results from this effort.

- A high quality block sample, representative of an oil and gas producing, organic-rich, mudstone was prepared for this test. Pre-test observation of the external surfaces show a representative amount of textural complexity that includes well defined bedding, gradual lithologic transitions, presence of calcite-filled laminae

and calcite-filled hairline fractures, presence of organic-filled slickensides, and presence of partings oriented parallel and oblique to bedding. The latter occurring along planes of natural weakness (i.e., mineralized hairline fractures). Pre-test measurements of acoustic transmission along multiple directions show the velocity heterogeneity associated to the rock fabric. Unfortunately, during the initial loading the connection of 12 of the 36 acoustic sensors installed in the block were lost. Thus results had to be interpreted based on a homogenized velocity field, with the corresponding loss of detailed velocity resolution and highest accuracy localization.

- One of the main surprises during testing was the strong effect of the rock fabric on fracture propagation and their overriding control on local fracture propagation and complexity over the imposed boundary conditions of stress and flow. Large horizontal stress contrast, high viscosity, and high pumping rates were used to create a planar and simple geometry fracture. This was accomplished at a global scale. However, weak interfaces in the sample interacted strongly with the propagating hydraulic fracture and resulted in the development of a large amount of local fracture complexity, including the generation of multiple branching and stepovers. This resulted in a heterogeneous distribution of fracture apertures and proppant concentration. The interaction of the rock texture with the hydraulic fracture was observed via changes in the flatjack volumes during injection, acoustic emission localization during fracture closure, and detail post-test observations of the fracture geometry.
- An important element contributing to this complexity was the opening and subsequent closing of a mineralized fracture oriented perpendicular to the direction of the hydraulic fracture. This occurrence was clearly seen during testing. Its effect on the development of fracture branching, step-overs, and multi-layered fracture propagation was clearly seen and reported during post-test analysis. These interactions compounded the complexity of the AE localization and the understanding of the evolution of the fracture geometry.
- Re-fracturing and proppant transport with water at high pumping rates was completed successfully. This allowed us to inject a relatively large amount of proppant and observe the evolution of the net pressure as a function of proppant concentration in the fracture. Unfortunately, the proppant distribution in the fracture was altered during the subsequent coring operation for removing the casing. Thus observations of proppant distribution were only possible along the periphery of the block and along few locations in the near-wellbore region of the block where the proppant had been left unaltered.

- Fracture conductivity measurements were conducted under un-propped and propped conditions, and as a function of the fracture closure stress. Results show that the stress dependence on fracture conductivity of the un-propped and propped large fracture was substantially lower than that measured on the smaller core samples. This was expected given the surface roughness and tortuosity of the hydraulic fracture. The reduced stress dependence indicates that the laboratory measurements on small samples are conservative estimates of fracture conductivity on large scale samples and field-scale hydraulic fractures. This difference is higher for the un-propped fractures and smaller for the propped fractures.
- Post test analysis indicates the presence of three distinct regions of fracturing: a wellbore region, connecting the wellbore to the fracture, which is characterized by some degree of complexity and tortuosity as the hydraulic fracture develops from the sand blasted slots; a near-wellbore region that is characterized by a reasonably planar and smooth fracture, and a far-wellbore fracture, near the edges of the block, that is associated with extensive branching and mix-mode fracture propagation.
- Post test analysis indicates limited to negligible amount of proppant crushing or proppant embedment. This indicates that stress concentrations at the rock proppant interface did not exceed the hardness strength of the rock or the strength of the proppant.
- Post test analysis also indicates that there was a distribution of proppant concentration across the fracture that was in line with the distribution of acoustic emission events during fracture closure and after proppant transport. This indicates that regions with higher proppant concentration resulted in higher acoustic emission events during closure. Post-test observations showed that the propped fracture width was approximately 1mm; this is in line with calculation of maximum fracture width in the field. Given a nominal diameter of 0.149 mm for 100 mesh proppant, this means that the proppant pack in the large-block test can accommodate up to ten proppant layers. Along these paths, the proppant to proppant interaction becomes more dominant than the proppant-rock interaction, and the proppant conductivity is more resistant to changes in stress and to rock/fluid interactions with time.
- Post-test analysis, acoustic emission localization and volumetric deformation measurements converge in the detection of fracture complexity. This was observed to be related to the interaction of the hydraulic fracture with planes of weakness in the sample.

7 ROADMAP FOR RESERVOIR CHARACTERIZATION, AND PRODUCTION AND RECOVERY MAXIMIZATION

7.1 Introduction

The objective of this section is defining preferred practices for reservoir assessment to optimize hydraulic fracturing design and execution, and to encourage long-term deliverability. With this goal in mind, we reviewed input on field best practices provided by the industry participants to this program, and also conducted a comprehensive review of the broad industry current practices on reservoir characterization and completion design. The review includes material that was published by various technical communities, including geology, production engineering, drilling engineering and completion engineering. We also re-evaluated results from laboratory experiments, conducted at small and large scale, in light of the industry observations and present a brief review of them in a manner that addresses the industry needs. Analysis of these results was used to provide recommendations for reservoir characterization and fracture design that reduces the potential for loss of surface area and loss of fracture conductivity, improves the effectiveness of the hydraulic fracturing treatments, and increase production.

Heterogeneous tight shale systems exhibit strong rock fabric (representing a depositional and post depositional overprint), elevated pore pressure and volumetric variability in properties. As a result, the geometry of hydraulic fractures in tight shales are complex, typically consisting of multiple fracture branches that propagate in directions parallel, oblique or perpendicular to the original fracture, and that are connected to the original fracture branch via stepovers. These are connectors between branches that may or may not have sufficient width to allow proppant transport. A conceptual representation of these fractures was presented in Chapter 2, Figure 2.8 and is reproduced here in Figure 7.1.

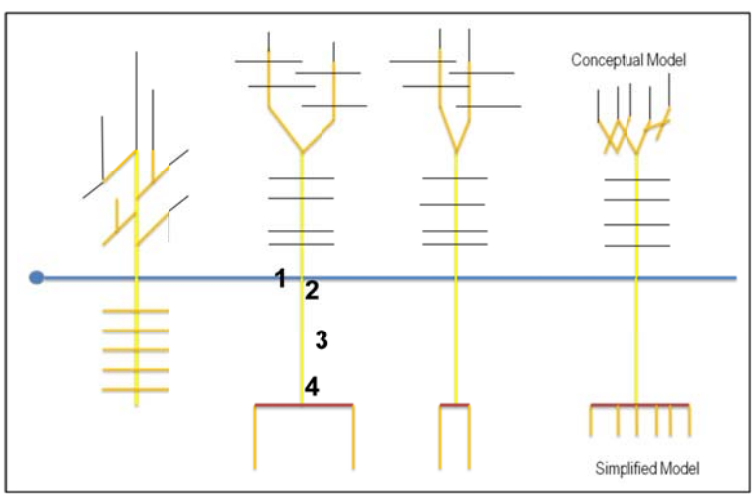

Figure 7.1 Conceptual fracture model (top), based on fracture observations on core, outcrops, and mine back experiments and simplified fracture model (bottom) for use in numerical simulations.

Regarding this conceptual hydraulic fracture system, four regions can be clearly identified: (1) the wellbore, (2) the connection between the wellbore and the fracture system, (3) the near-wellbore fracture, and (4) the far-wellbore fracture network. The particular nature of these regions may change depending on the play, the reservoir fabric, its relation to the in-situ stress, and the distribution of rock properties. However, these regions will always be well differentiated. Understanding the role of each of these components, to hydrocarbon production, is fundamental to understand the dominant sources of loss of production, and their associated drivers. For example, the far-wellbore region provides the highest surface area in contact with the reservoir, the lowest fracture conductivity, and offers the highest potential for improving productivity, by preserving surface area and improving fracture conductivity. Numerical simulations indicate that minor improvements in fracture conductivity in this region result in substantial improvements in production and total recovery. In contrast, the near-wellbore region provides limited surface area in contact with the reservoir. Because the majority of the proppant may reside in this region, this is a region of high conductivity and often controls the overall production of the stage. Numerical simulations suggest that changes in fracture conductivity in this near-wellbore region, even when substantial, do not produce significant changes in production. This is because it is already a region of high conductivity. The connection between the wellbore and the fracture system is a critical region and is highly susceptible of losing connectivity. It is also a region of convergence, and thus a choking point. In this region, the high fluid velocity, during fracturing, results in low proppant content, and this condition is further worsen by overflushing at the end of the treatment. Lack of sufficient proppant or poor selection of rock quality in this region significantly increases the risk of fracture closure and loss of stage production. This is so, independently of the conditions of the other two regions. The wellbore and the type of completion (e.g., cased, open hole, perforated, sand blasted) defines the condition of fracture initiation and influences the geometry of the connector between the wellbore and the near-wellbore fracture system. The wellbore location, type of completion, presence of fractures, type of perforations, use of cement dissolving acids, and even the time delay between perforating and fracturing, influence fracture initiation and its initial tortuosity. Ideally one would like to define the wellbore conditions of fracture initiation such that the fracture connector is simple, planar, wide, and provides a maximum connectivity between the wellbore and the near-wellbore fracture system. Unfortunately, current fracture design criteria are defined to address broad objectives that are assumed to improve production (e.g., rock properties, in-situ stress, percent clay, presence of fractures), while the different influences of these four fracturing regions to the overall success of the treatment is ignored.

7.2 Far-wellbore Region

Fracture containment is a dominant concern in the near-wellbore and the far-wellbore region, and is perhaps more important in the latter. Proppant transport to the far-wellbore region, and obtaining sufficient proppant concentration to maintain fractures in this region open, are of highest concern. Loss of surface area is possibly the dominant problem in this area. At low proppant concentrations, low fracture widths, and high stress concentrations, rock/proppant interactions are critical to define weather proppant embedment or

proppant crushing defines the potential for fracture closure. In addition rock-fluid interactions soften the rock and promote embedment; proppant-fluid interaction weakens sand, when used as proppant, and promotes proppant crushing. In either case the potential for loss of surface area is high.

Figure 7.2 shows a conceptual representation of the far-wellbore fractures (left). The Figure also shows examples from mineralized fractures in sandstone, located sufficiently far away from the source of hydro fracturing (center). In addition, the figure shows an example of closely spaced fracturing and propagation of secondary fractures in sub-parallel directions (right). The far-wellbore region is the fracture region that is primarily fluid filled and primarily devoid of proppant. Laboratory experiments have shown that fracturing with water results in highest fracture complexity, narrow widths, closely spaced fractures, and predominant propagation along planes of weakness. When these tests are conducted with proppant transport, one observes fracture networks with closely spaced fractures, some with narrow widths, and exhibiting a heterogeneous distribution of proppant. Examples of this are clearly seen in Figure 7.3. In addition, laboratory experiments of fracture conductivity on plugs, with un-propped fractures, indicate a high tendency of loosing conductivity with stress. In general, a 2000 psi closure stress is sufficient to eliminate fracture conductivity in un-propped samples from the Haynesville, Barnett, and Marcellus shales.

The far-wellbore region is also a region of salt dissolution, high salt concentration in the fracturing fluid, and potential precipitation during flowback. It is a region of high water imbibition, which results in water banking and fracture-face permeability impairment. Fracture-face permeability represents the magnitude of the matrix permeability at the fracture face. Because of the continuous capillary drive for imbibition by the rock away from the fracture, water banking spreads away with time, allowing the fracture face permeability to recover its original value.

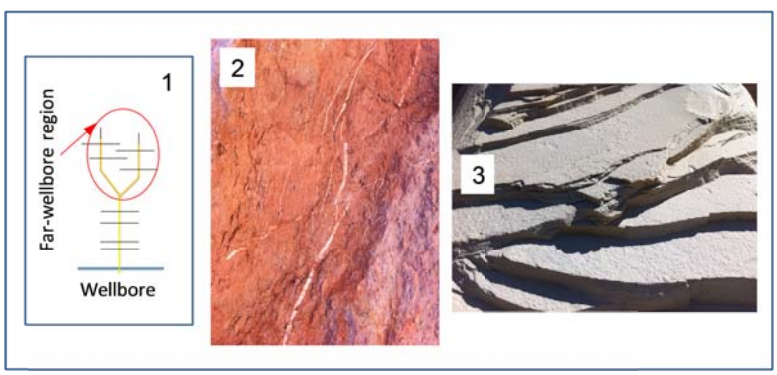

Figure 7.2 Typical morphology of far-wellbore fractures: (1) Conceptual model. (2) Mineralized fractures in sandstone away from the source. (3) Closely spaced fracturing in laminated sandstone. Fracture propagates in multiple sub-parallel directions and minimal width.

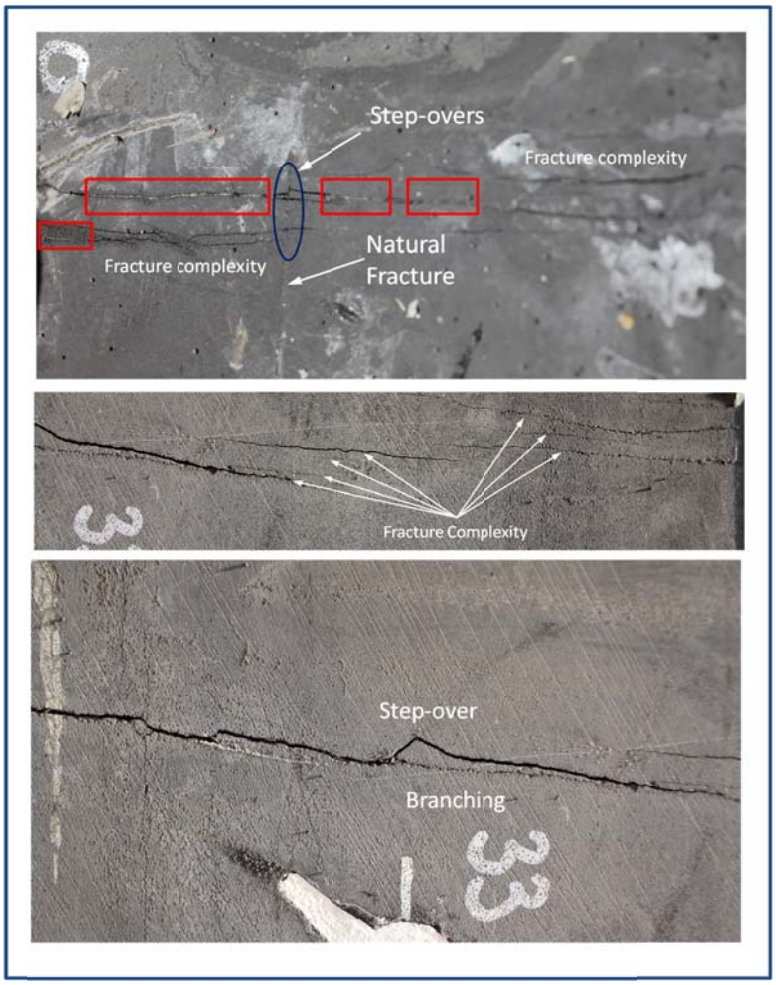

Figure 7.3 Fracture morphology and heterogeneous distribution of proppant transport during hydraulic fracturing in Niobrara shale. Regions with visual evidence of proppant in the fracture are highlighted with red rectangles (top). Closely spaced fracture branches and stepovers are commonly observed (center, bottom). These observations are recorded at the block surfaces, away from the wellbore and correspond to the far-wellbore region.

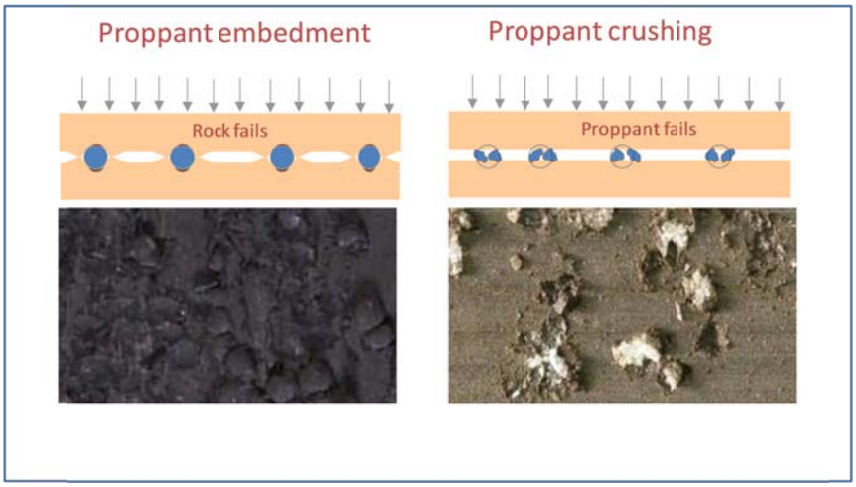

Figure 7.4 Proppant embedment results from rock failure due to stress concentrations and the proppant/rock interface. Proppant crushing results if the failure stress for embedment is higher than the crushing strength of the proppant. In both cases the result is fines generation, fracture closure and loss of fracture conductivity.

When low concentration proppant is transported to the far-wellbore fractures, the stress concentrations at the proppant/rock points of contact are high, and result of failure of the rock (proppant embedment) or failure of the proppant (proppant crushing), leading to loss of fracture conductivity. Figure 7.4 shows this effect. In addition, the displacement of formation fines, during proppant embedment, and creation of fragments, during proppant crushing, produces solids that will be transported to the near-wellbore fracture and possibly plug the near wellbore conductivity and the near-wellbore connector. Similarly, if produced, the high salt water content from far-wellbore fractures carries a high potential of salt precipitation. Laboratory testing of proppant embedment, proppant crushing and the closure of un-propped surfaces, provides important information on the potential loss of fracture conductivity on the far-wellbore fractures.

The potential of solids production due to excessive drawdown should not be overlooked. The industry has recognized that controlling drawdown improves production. It is not clear, however, if the source of the problem is well understood. Excessive drawdown pressure, typically during early production, results in tensile stresses at the fracture face that may exceed the tensile strength of the rock. When this happens, spalling and solid production is the result. The larger the surface area subjected to this action, the larger the amount of solid production and the bigger the damage to fracture conductivity.

Figure 7.5 shows the conceptual problem of applying excessive drawdown (left). It also shows a failure envelop for the drawdown problem (right). This Figure shows that spalling failure and loss of fracture conductivity from this mechanism is avoidable by maintaining the drawdown pressure within the safe zone. It also shows that the drawdown can be increased safely as a function of time. Evaluation of the failure envelope requires knowledge of the in-situ stress, reservoir pressure, matrix permeability, tensile strength, and the anisotropic elastic properties of the reservoir. Results from these predictions can

be validated or calibrated during early flowback studies. Among the multiple sources of loss of fracture conductivity, loss by solids production associated to excessive drawdown is the easier problem to evaluate and prevent.

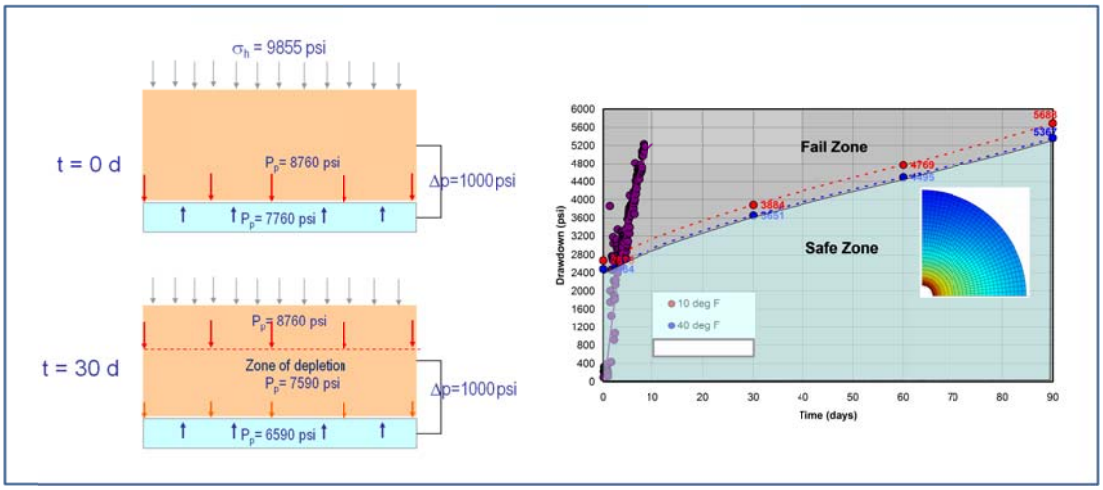

Figure 7.5 Tensile failure, at the unsupported fracture face, arises from high drawdown during production. This results in solids production (i.e., generation rock fragments and fines) that may enter the wellbore or plug the hydraulic fracture. The problem is controlled by understanding the failure envelope to drawdown, as a function of time.

7.3 Near-wellbore Region

The near-fracture region is most likely the dominant region of production. It is also the region with highest proppant concentration. Figure 7.6 shows a conceptual representation of this region. Similar to the far-wellbore region, the near-wellbore region is susceptible to solids production by high drawdown, salt dissolution and potential salt precipitation, mobilization of fines from proppant embedment and associated rock extrusion, and vulnerable to the associated loss of fracture conductivity resulting from all these factors. It is also susceptible to imbibition and loss of fracture-face permeability. The main difference between the near-wellbore and the far-wellbore region, however, is the high proppant concentration in the former and the potential problems, and benefits, associated to this. High proppant concentration and high proppant surface area may result in high capillary forces for water retention. This may be harder to overcome within the sections of the fracture below the wellbore, because of gravity. Under some conditions of proppant surface properties (e.g., resin coated proppant), the proppant pack may retain fines and contribute to the local degradation of conductivity. Resin coated surfaces may also retain liquid hydrocarbons and create blockages.

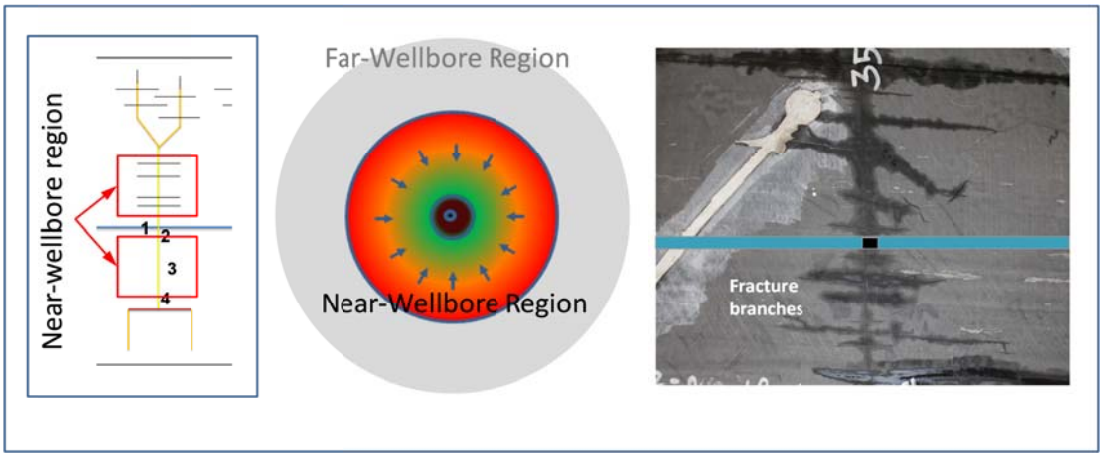

Figure 7.6 Conceptual morphology of the near-wellbore fracture region (left, center). Experimental results show the fracture face arises from high drawdown during production. This results in solid production (i.e., generation rock fragments and fines) that may enter the wellbore or plug the hydraulic fracture. The problem is controlled by understanding the failure envelope to drawdown, as a function of time.

Rock-proppant interaction, during embedment, results in local plastic deformation and may lead to dramatic changes in fracture-face permeability at the rock/proppant interface. Unfortunately, the higher the proppant concentration and the more uniform the proppant coverage, the bigger and more uniform the damage at the fracture face. Figure 7.7 shows experimental measurements of embedment and rock extrusion, during fracture conductivity experiments on Haynesville shale. The insert, in the Figure, provides a visual representation of the preserved surface area (shown in blue) due to embedment and rock plastic flow. Fortunately, however, the distribution of proppant in real fractures is hardly uniform, and the problem is less extensive. In addition to rock-proppant interaction, in the near-wellbore region the proppant pack may be multilayered, and thus proppant-proppant interactions are also of concern. Exposure to water base fluids, time and temperature affect the stability of sand based proppants. This exposure promotes grain crushing, with an associated degradation in fracture width and increase of fine materials.

Closer the wellbore, the near-wellbore region is a potential zone for retention and trapping of fines, fragments, precipitants, and all other plugging constituents that are mobilized from the farther regions of the fracture (Figure 7.6 - center). Thus, the gradual loss of fracture conductivity in this region is possibly inevitable, and this effect is a dominant source in the abnormally high loss in productivity.

Key considerations for the near-wellbore region is to reduce the damage of fracture face permeability due to embedment, improve water production from the proppant pack, and prevent the filtering action and resulting plugging of the near region. Laboratory experiments for evaluation of fracture-face permeability impairment, by proppant embedment, as a function of closure stress and proppant concentration and size, were not part of this program. However, these measurements are of high importance for evaluating

this problem in the near-wellbore region. Fluid selection and additive selection that considers the wettability and imbibition potential of the reservoir, as well as the wettability and capillary forces of the proppant is of high importance for facilitating the de-watering from this region without negatively altering the reservoir. A new technique of pillar proppant distribution (or Channel Fracturing) has been recently introduced to the industry by Schlumberger (Figure 7.8). Channel Fracturing has demonstrated to be highly effective in creating high conductivity channels, while preserving fracture aperture. This is accomplished by controlling the injection of proppant laden and non-proppant laden fluids in cycles during fracturing, and by minimizing the dispersion of the proppant using fibers. This solution proposes to control the distribution of proppant, create proppant pillars and high conductive channels and as a consequence facilitates the passage of solids and precipitants from the far-wellbore region. It also proposes to reduce the area of contact and thus the damage to the fracture-face permeability.

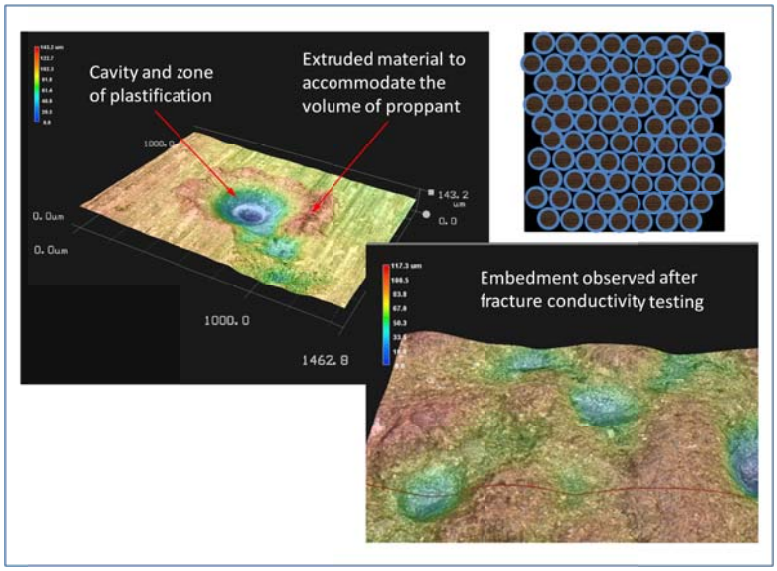

Figure 7.7 Microscope images of proppant embedment, plastic flow at the rock/proppant interface and associated extrusion of the surface around the proppant. The bulged region may be dispersed and mobilized by the flow. The surface of the rock in contact with the proppant is a plastified surface of highly reduced permeability.

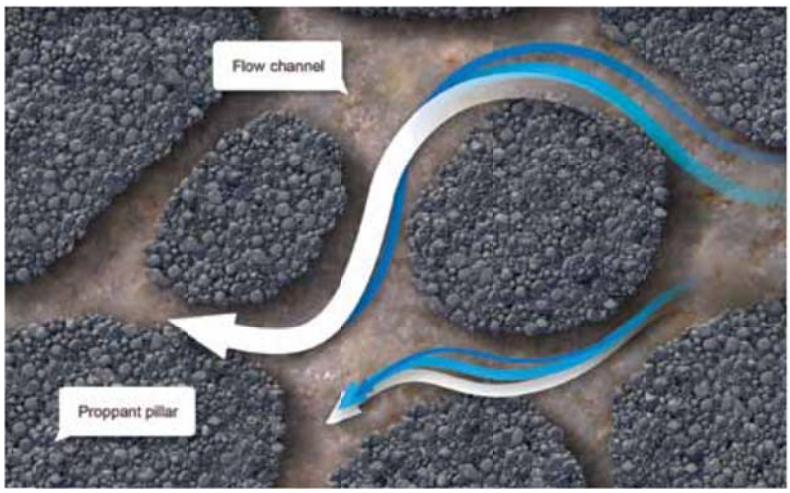

Figure 7.8 Schlumberger's HiWAY*[8] fracturing proposes to control the distribution of proppant, create proppant pillars and high conductive channels and as a consequence facilitate the passage of solids and precipitants from the far-wellbore region. It also proposes to reduce the area of contact and thus the damage to the fracture-face permeability.

7.4 The Connection between the Wellbore and Fracture System

The connection between the wellbore and the near-wellbore fracture system is a region of limited extent but of unordinary importance. This is a region where the wellbore stress concentrations, the regional stress concentrations, the perforations (or any other method used for facilitating fracture initiation), the choice of fluid properties, fluid rates, the pumping schedule and others strongly influence the way fractures initiate and develop. The desirable result is to create a conduit that maximizes connectivity between the wellbore and the near-wellbore fracture system and that minimizes any potential restrictions of flow. This means, obtaining a wide conduit with simple planar geometry, high fracture conductivity, minimal fracture tortuosity, limited changes in direction during propagation, limited generation of fracture branches of smaller widths, and maximum fracture conductivity, among others.

Some of these conditions are defined by the rock properties, the actual perforation geometry, and by the procedures leading to breakdown, including the pumping rate schedule from initiation to stabilization. For example, the rock hardness, rock stiffness, rock toughness and rock fabric play a strong role on the penetration and blunting of the perforations, the fracture aperture, and the generation of fracture branches. The presence of fractures or planes of weakness intersecting the wellbore, facilitate fracture initiation and the development of a simple connecting conduit. Fracture initiation procedures also play an important role. When fracture initiation is done from multiple perforations and different orientations, using low rates and low viscosity fluids, the result is typically multiple fractures and narrow fracture widths. There is a large collection of laboratory experiments on large blocks outcrop samples, representative of tight shale plays in North

[8] Mark of Schlumberger.

America, that support these comments. A key observation, in this regard, is that low viscosity fluids injected at low pumping rates create fractures that propagate preferentially along existing planes of weakness, while developing minimal fracture width. Depending on the rock fabric (including the presence of natural or drilling-induced fractures, mineralized or non-mineralized) the resulting geometry may be of simple fractures or closely spaced fracture networks.

The development of longitudinal fractures and orthogonal transverse fractures, resembling a manifold configuration, has also been a common observation in laboratory testing, in this connecting region. The presence or absence of these appears to be strongly dependent on the effectiveness of the perforations. Short perforation depths with multiple entry points support the generation of fractures that initiate longitudinal to the wellbore, as dictated by the local stress concentrations. Laboratory experiments show that these do not turn into the preferential transverse direction. Instead, they appear to be arrested at some distance from the wellbore and be intersected by one or many transverse fractures. In contrast, laboratory results show that oriented perforations with high flow capacity and adequate penetration depth generate transverse fractures without the presence of longitudinal fractures.

Under poor conditions of connectivity, including the presence of multiple fractures of small width, high tortuosity and high degree of interaction between fractures, the development of fracture width is restricted and proppant screenouts may occur during fracturing. In contrast, under favorable conditions of fracture initiation, the fracture width development is unrestricted, channels of adequate width are created, and proppant transport is possible with limited restrictions. This is the desired outcome during fracturing.

The connection between the wellbore and the near-wellbore fracture system, however, is also a region of high fluid velocity and limited proppant deposition. As a result, the proppant concentration in this region is possibly very low, during the duration of the treatment. Unfortunately, the low proppant retention in this region is further exacerbated by overflushing at the end of the treatment. This may create the closure of the critical connecting path between the wellbore and the created fractured system, and eliminate the potential of production, from a specific stage. It is possible that the large variability in stage production and the current inefficiency of the stimulation process is controlled primarily by this region of connectivity. This may be the weakest link of the hydraulic fracturing concept.

Figure 7.9 shows the conceptual representation of the complex fracture system and the region associated to the connection between the wellbore and fracture system (Region 2). It also shows laboratory results from perforations and hydraulic fracturing in North American organic-rich mudstones. The figure of the perforation, at the center, suggests that planes of weakness also play a role in the continuity and preservation of the perforation tunnel. The other figures provide examples of the degree of fracture complexity that occurs when fracturing with slick water, given the textural complexity of the rock.

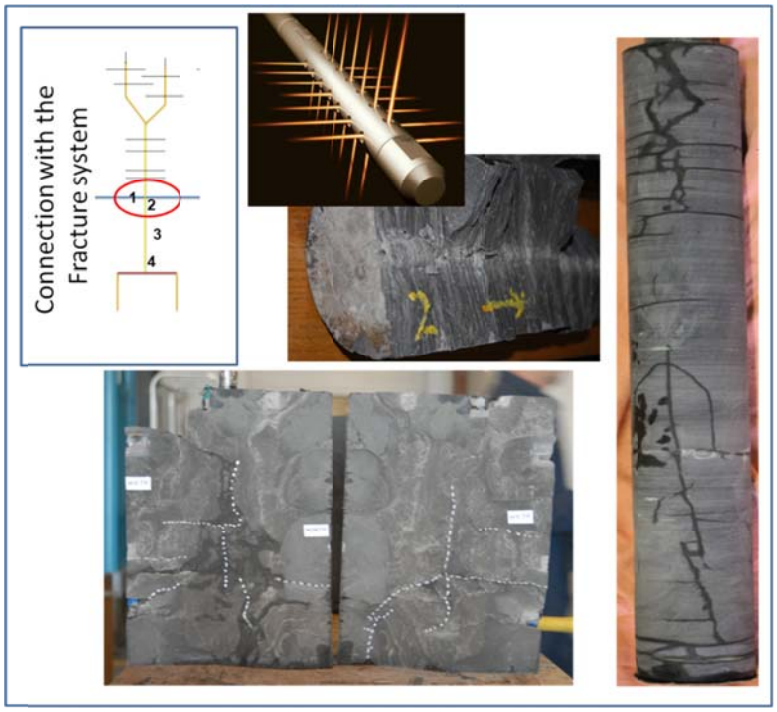

Figure 7.9 Examples of connectivity between the wellbore and the near-wellbore fracture. The conceptual representation of this region and the frequent use of perforations to facilitate fracture initiation are shown in the upper section. Photographs of this region from real experiments on tight shales are shown below. The fracture complexity in this region could be high. The opposite is the desired outcome.

Laboratory characterization to improve the conditions of this region include understanding mechanical properties (strength, stiffness, hardness, rock compatibility with the perforating system), and understanding of the rock fabric, including the presence of planes of weakness and fractures. The desired outcome is to create and preserve a geometrically simple conduit of high conductivity. This may require modifying the perforating techniques (e.g., using oriented and focused perforating charges), changing the fracture initiation protocols (e.g., using high viscosity fluids and high rates, fracturing immediately after perforating), and changing the fracture termination protocols (e.g., promoting screenouts at the end of the treatment, to maximize the proppant concentration and fracture conductivity of this region).

7.5 The Wellbore

The main concern in considering the wellbore is to decide the landing depth, its trajectory and azimuth, and whether it would be an open hole or cased completion. The wellbore and the type of completion (e.g., cased, open hole, perforated, sand blasted) defines the condition of fracture initiation and influences the geometry of the connector between the wellbore and the near-wellbore fracture system. The presence of weak interfaces that may open during drilling may facilitate fracture breakdown and connectivity to the near

wellbore fractures. However, this process may depend on the wellbore orientation. As discussed in the previous section, use of compliant cements, use of cement dissolving acids, and even the time delay between perforating and fracturing, influences fracture initiation and fracture tortuosity. The distinction between the wellbore and the connection between the wellbore and fracture system is one of convenience. It allows us to separate the effects of wellbore trajectories and orientations under the same conditions of perforating, pumping schedules, fracture initiation procedures, and others. It also allows us to compare cased completions versus openhole completions, and other conditions that are exclusively dependent on the wellbore configuration.

Figure 7.10 shows the potential consequences of creep on the hoop stress distribution along the wellbore, and on breakdown pressures. Numerical simulation, based on laboratory measurements of rock strength, elastic stiffness and creep indicate that the creep relaxation may considerably change the stress concentrations around the wellbore. This depends strongly on the completion configuration, open hole, cased, and the distribution and properties of the cement sheath around the casing. Results show the importance of understanding the time dependence of this process and conducting operations at the time that is more convenient for maximizing the connectivity between the wellbore and the near-wellbore.

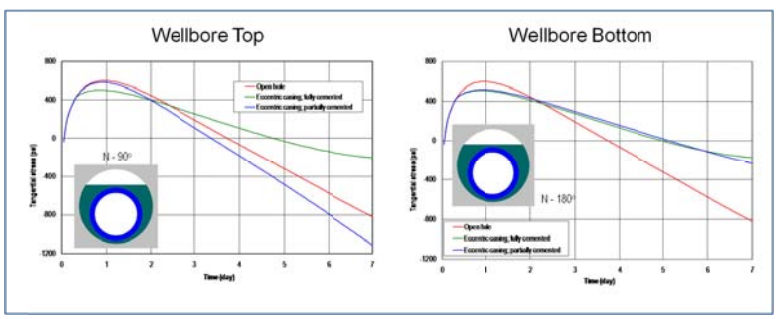

Figure 7.10 Effect of creep deformation (i.e., time dependence) on the stress concentrations around the wellbore. The hoop stress and fracture initiation pressure decrease considerably as a function of time.

Critical concerns for landing and for selecting the wellbore azimuth are mechanical stability, creep, good understanding of the in-situ stress (magnitude and orientation), rock competence to maintain strong connectivity with the fracture system over time, understanding of the potential for upper and downward fracture containment, and strong understanding the distribution of pore pressure, organic content and reservoir quality. These properties can be measured. The problem, however, is that the information is needed prior to defining the well trajectory and prior to conducting measurements. Seismic data, integrated to log measurements and integrated with core measurements provides a strong potential for providing this information prior to drilling.

7.6 Summary

In unconventional tight shale systems, well production depends of reservoir quality and completion quality. Each of these properties is multivariate. Reservoir quality (RQ) is defined by the combined contribution of hydrocarbon filled porosity, matrix permeability, organic content and maturation, and pore pressure, among others. In addition, for liquid plays, fluid properties of composition and phase transformations are essential. Completion quality (CQ) is defined by the combined contribution of fracture containment, fracture surface area and fracture complexity, retention of fracture surface area and fracture conductivity, and the effects of rock/fluid and proppant/fluid interactions on the previous. It turns out however, that these contributions of RQ and CQ have different importance and sensitivity along the four critical regions of the stimulated wellbore: the wellbore, the connector between the wellbore and the hydraulic fracture system, the near-wellbore fracture region and the far-wellbore fracture region. For example, the presence of high reservoir quality may not be of high importance to the wellbore. Furthermore, properties associated to fracture containment, fracture complexity and others, are also not relevant to the wellbore. In contrast, high reservoir quality is critical at the near-wellbore and far-wellbore fracture regions. Fracture containment and complexity are also critical here.

Understanding the properties (or measurements) required for successful well (or stage) production is complicated because of the complex interrelations between the multiple properties and their varied influences along the length of fractures. This effort can be greatly facilitated by providing a breakdown of the dominant dependence of critical properties along the various stages of the fracture. Figure 7.11 shows a possible representation of this concept. In this Figure, Red= bad, Yellow = intermediate, Green = Neutral, White = No dependence. This is done for the various regions of a fracture: NWC = near wellbore connectivity, NWF=near wellbore fracture; FWF = far wellbore fracture.

Problems / What it affects?	Surface Area			Fracture Conductivity			Fracture Face Permeability		
	NWC	NWF	FWF	NWC	NWF	FWF	NWC	NWF	FWF
Proppant embedment									
Proppant crushing									
Poor propant transport									
Proppant flowback									
Rock/fluid Interaction (softening)									
Rock/fluid Interaction (imbibition)									
Rock/proppant interaction (embedment)									
Pilar proppant distribution									
Uniform proppant distribution									
Degradation of proppant with time									
Water retention in proppant									
Solid retention in proppant									
Hydrocarbon retention in proppant									
Fines and solids migration									
Salt precipitation									
Filtering/Choking									
High Drawdown									
Fracture complexity									
High No. of fracture connectors									
Tortuosity									
Plastic rock deformation									
Overflushing									
Narrow fracture width									
Lack of fracture containment									
Complex rock fabric									
Landing point and trajectory									
Perforation procedures									
Breakdown procedures									
Presence of fractures (wellbore)									
Wellbore stability									

Figure 7.11 List of dominant dependence (Red= Bad, Yellow = Intermediate, Green = Neutral, White = No dependence) of critical properties along the various regions of a fracture.

7.7 Current Industry Practices and Concerns

Keeping the above review as a background, and with the gained understanding of the multiple conditions that affect loss of productivity in wells, on a stage by stage basis, during fracture initiation, propagation and termination, and including flowback procedures, we conducted a comprehensive industry review of current practices and concerns, to see the industry perception of this problem. We also requested additional input from the industry participants to this program, and summarized their input. Having these inputs and integrating these with the results of this program allowed us to produce a summary and recommendation of possible best practices to control production decline and increase production rates.

The following is an executive summary of a comprehensive industry review on current practices for controlling loss of well production. The study was conducted by Mike Vincent at our request. The full body of the document, including references is provided in Appendix 7.

7.7.1 Introduction

The ability to initiate multiple transverse hydraulic fractures from horizontal wellbores has allowed economic development of numerous resource plays, including the Barnett, Bakken, Marcellus, Haynesville, the Eagle Ford and numerous additional evolving plays. Although advances in this technology have dramatically increased the economically recoverable reserves in these plays, there is a growing awareness that the fracture treatments are not optimized, and that further innovation is necessary to make the fracture treatments more effective and durable.

The purpose of this review of industry practices and concerns is to identify mechanisms believed to be responsible for loss of fracture effectiveness, and discuss industry practices that have been implemented in various reservoirs to combat these problems. The full report, provided as an appendix, reviews field evidence, using refereed publications, that hydraulic fractures fail to provide durable or effective conductivity, throughout the created extent of their surface area. A large number of suspected damage mechanisms perceived to cause loss of fracture effectiveness were reported and discussed. Industry "best practices" that emerged in specific resource plays and appear to have proved beneficial in combating specific damage mechanisms are reviewed and discussed. Furthermore, the emerging consensus on data collection requirements, research needs, and other efforts (e.g., field studies) necessary to identify or develop best practices, on a play by play basis is reviewed. In the following sections, the main conclusions are reviewed.

7.7.2 Evidence that fractures are losing conductivity and/or surface area

While many production trends fail to yield a unique interpretation as to the damage mechanism, there are a number of observations that, when considered in conjunction, compellingly demonstrate that fractures are not recovering the hydrocarbon resource as effectively as commonly anticipated:

- **Infill drilling evidence** – New wells drilled through a microseismic swarm are encountering near-virgin reservoir pressure and appear to recover more than 80% of the EUR of parent wells drilled in the virgin rock. This indicates that the original "parent" wells have not depleted the rock volume, which is apparently covered with microseismic events.
- **Restimulation evidence** – Horizontal wells in most resource plays have been successfully restimulated, indicating that the initial fracture treatments were insufficient to drain the recoverable reserves accessible from the wellbore.
- **Steep decline evidence** – Steep decline curves may be attributed to collapse of fracture conductivity and/or loss of surface area.

- **Drawdown management evidence** – Evidence that in some reservoirs managing the drawdown seems to extend EUR, suggests that typical operational practices may accelerate fracture degradation. This observation suggests that traditional hydraulic fracture treatments are insufficiently durable to withstand traditional drawdown or standard operating practices (multiple shut-ins, cyclic stress, liquid loading, and others).
- **Laboratory testing evidence** – Laboratory measurements shows that even in "ideal" conditions in which proppant is arranged in multilayered packs with optimal packing arrangements, tremendous degradation of conductivity over time is measured. This effect has been noted in every published extended duration test. In the laboratory, proppants continue to crush and compact over time. Unless something magical happens in the field, when we pump proppant down a mile of pipe, it should be logically anticipated that actual fractures will similarly lose conductivity over time.
- **Fracture complexity evidence**. In numerous mine-back and core-through studies it has been apparent that fractures are not simple, wide, or planar. The industry should recognize that it is challenging to place a uniformly wide fracture and that will retain hydraulic continuity through highly heterogeneous or laminated intervals.
- **Hydraulic connectivity evidence** – This evidence refers to cases in which hydraulic fractures connect two wellbores. In a number of reservoirs, proppant has been pumped to the surface of adjacent wells completed at exactly the same depth, irrefutably indicating that a fracture was created between the two wells and proppant was transported through the entire hydraulic fracture length. However, subsequent diagnostic tests during production (pulse tests, interference tests, PBUs, calculation of EUR) typically indicate ineffective retained hydraulic continuity, and often zero sustained hydraulic connection. This indicates that hydraulic fractures are either not sustaining sufficient conductivity or are collapsing at some point between the wellbores.

7.7.3 Potential mechanisms responsible for loss of fracture effectiveness

To identify best practices, and improve fracture effectiveness and durability, it is necessary to review some of the mechanisms which may be responsible for fracture collapse. The following were reported:

- Degradation of proppant over time
- Overflushing of proppant from the near-wellbore area in transverse hydraulic fractures
- Flowback of proppant from near-wellbore area in transverse hydraulic fractures
- Failure to place sufficient proppant concentrations throughout the created network (in both lateral and vertical completions)
- Insufficient fracture conductivity to accommodate high velocity hydrocarbon flow due to near-wellbore convergence, especially in liquid-rich formations
- Proppant embedment
- Thermal degradation of sand-based proppants
- The appearance of extremely low quality sand and low quality ceramic proppants during the past decade
- Complex hydraulic fracture geometries requiring stronger or more conductive proppant in the fracture turns and "pinch points"
- Insufficient proppant concentrations, resulting in discontinuous proppant packs after fracture closure. This problem is compounded when operators specify intermediate or high density ceramics but pump the same mass concentration, resulting in reduced fracture width and 20% to 30% smaller areal extent
- Because of rock/fluid sensitivity, some fracturing fluids "soften" the formation, allowing more significant embedment and/or spalling (tensile failure)
- Durable gel filtercakes, deposited using crosslinked fluids, may completely occlude narrow propped fractures
- Precipitation of salt, asphaltenes, barium sulfate and calcium carbonate scales results on severe loss of fracture conductivity
- There appears to be a potential for chemical diagenesis of proppant (e.g., precipitation of zeolites and reduction of proppant pack permeabilityy). This concept, however, is still controversial given the existence of conflicting laboratory results. To date, proppant samples recovered from wells do not appear to indicate formation of zeolite precipitants. It appears that zeolite precipitation can be encouraged in laboratory tests under specific conditions.
- Failure to recover water from liquid-submerged portions of the fracture below the wellbore elevation

- The industry rush to secure acreage to "hold acreage by production" has reduced attention to completion effectiveness or optimization. Frenetic development pace has created an environment with focus on scheduling, logistics and assuring materials availability, and not with a focus to optimizing well productivity.
- Other unrecognized mechanisms

7.7.4 Best field practices currently implemented to combat loss of fracture area and fracture conductivity

There is a growing awareness that fractures fail to provide durable, infinitely conductive pathways to successfully recover all reserves within the "stimulated reservoir volume". Although hydraulic fracturing with current techniques provides imperfect connections, hydraulic stimulation remains the most cost-effective way to contact the reservoir rock and bring the massive resource plays into economic production.

It is evident that there is no single recipe or ideal hydraulic fracturing design that can be optimal for all resource plays. "Changes in kerogen content, total organic content, rock brittleness, thermal maturity, in situ pressure, formation thickness, permeability, porosity, degree and variability of natural fracturing; all influenced well spacing, lateral lengths and hydraulic fracturing design." (Fisher, 2012[9]). However, there are a number of common observations that appear to apply broadly to resource plays developed with transversely fractured horizontal wells:

- Increased number of stages
- Dividing a treatment into more stages increases production in most plays developed with multiple transverse hydraulic fractures. This is in contrast to what is predicted with most models, which incorrectly indicate that placing more, but smaller stages (of reduced fracture length) would hurt long-term productivity. This evidence strongly suggests that at least one of the following factors is true:
    - Pressure losses are high within transverse fractures, and dividing the hydrocarbons between multiple entry points is advantageous
    - Fractures lose hydraulic continuity at some location within the fracture, so increasing the number of stages increases the proportion that remains productive over time
    - The connection between the wellbore and fracture is tenuous and increasing the number of connections (or number of fractures) increases the durability
    - The overflushing of proppant, or flowback of proppant is challenging well productivity, and therefore increasing the number of stages somewhat compensates for our completion practices

[9] Fisher, K: Trends Take Fracturing 'Back to the Future'. *AOGR* Aug 2012.

- Some reservoirs appear to be tolerant of overflushing and can be economically developed with industry-standard practices that require flushing the wellbore of proppant between stages. This results in overflushing proppant in some number of the created fractures. Other formation types appear to be damaged with overflushing. Field studies have led several operators to publically disclose their efforts to reduce and/or eliminate overflushing, and some operators are choosing to screenout some stages to ensure good connection between the wellbore and fractures.
- In some plays with wells susceptible to proppant flowback, the use of curable resins near the wellbore have been beneficial, while the use of uncoated ceramic proppants has eliminated proppant flowback in others.
- There is growing recognition that placing proppants in diffuse concentrations in crosslinked fluids is yielding discontinuous proppant packs after closure. There are two potential solutions that are being pursued. Some operators are switching to low viscosity banking fluids (slickwater) that build a continuous proppant bank via the mechanism of saltation. Other operators are trying to improve continuity by specifying high proppant concentrations (often exceeding 6 to 9 ppa) in crosslinked fluids. The goal here is to place a sufficient number of proppant grains, to improve and sustain hydraulic continuity. Given an "industry standard" of approximately 4 ppa in many resource plays, it appears that either approach (slickwater at any concentration, or increasing to 8 ppa or larger in crosslinked fluids) is improving continuity.
- A growing number of operators are reporting using detectable proppants (radioactive or non-radioactive materials that can be identified with logging tools) to evaluate which fracturing stages contact offset wells. Additionally, the use of oil-soluble and water-soluble chemical tracers can indicate which injected fluids contact adjacent wells. The relative productivity of stages is then evaluated using recovery of water-soluble and oil-soluble tracers as proxies for load recovery and hydrocarbon productivity. Efforts to integrate the interpretation of these diagnostics with other data such as seismic attributes, microseismic frac mapping, mud logging, wellbore depth, production logs, DTS/DAS data from fiber optic monitoring and other data are improving the understanding of which parameters most directly correlate with sustained fracture productivity
- Several industry-leading operators are recognizing that proppants are not equivalent. There are more than 60 mines supplying fracturing sand, over 70 plants supplying ceramic and over 18 plants supplying resin coated proppant. Vast variation in quality and durability of these proppants has been documented (SPE 84304, 101821, and 119242). Industry-leading companies are beginning to specify exactly which material and which quality of proppant they will accept, and keeping

careful records such that wells stimulated with lower quality proppants can be identified for restimulation.

- This current reduced activity associated to lower gas prices has given some operators their first opportunity to consider the use of more time-consuming isolation procedures. These were previously unavailable or not feasible given the required development pace.
- In some reservoirs, compelling data is available suggesting that aggressive drawdown results in premature damage to the completion and/or reservoir resulting in loss of reserves. In other reservoirs, it appears that aggressive drawdown can only be pursued with specific completion types. In yet other reservoirs, drawdown procedures have not yet been proven to affect EUR. However, industry efforts to determine the best operational practices are ongoing in all resource plays.
- Refracs appear to be required and profitable in most resource plays, again indicating the opportunity to improve the quality and durability of initial stimulation treatments. It would be much cheaper and more profitable to improve the initial treatment, if possible, to avoid the need for subsequent restimulation.

7.8 Participants Current Practices

The following is a summary of answers to specific questions we asked to the industry participants of this program, regarding the Marcellus and Haynesville plays. Because of the public nature of this investigation, we have requested them to only provide information that can be made available to others and do not represent proprietary operational practices. We also indicated that their responses will be identified by play name rather than by company name. The following are the collection of questions and answers:

1. What is the extent of the loss in fracture conductivity and fracture surface area during production over time? How is this measured? How does one differentiate the effects of fracture conductivity and surface area?

   (Marcellus): There is significant loss of accessibility to created fractures early in the life of the well. Evidence of this is the loss of pressure communication between wells. This is observed during stimulation but goes away soon after the wells are placed on production. It is anticipated that this is a strong function of un-propped sections of the fracture that close during production.

   (Haynesville-1): Loss of fracture conductivity has been noted in the fields based on relative drawdown and performance of wells. Over time wells that have maintained back pressure outperform wells that have not been restricted. The restricted wells maintain higher pressure at a given cumulative production and outperform their counterparts on a rate versus cumulative production basis. Further, EUR predictions have been consistently higher. Damage has also been noted by drawing

down wells too rapidly. One cannot differentiate diagnostically the difference in conductivity loss versus the loss of fracture area. In modeling efforts, the two variables can be shifted and consistently it appears that loss of surface area is the greater driver.

(Haynesville-2): Analyses of production performance data seem to indicate a deterioration of network "conductivity" over time as a result, presumably, of gas pressure depletion and the consequential incremental stresses induced in the rock fabric. Further, there appear to be a characteristic response that is not uniform with time, with deterioration occurring in a "step-wise" fashion. This appears as a succession of "events" that diminish well production performance. Frequently, there are clearly "step" changes in well production performance most likely associated with a pinch-off of a major production network or perforations. Since this trend is quite correlatable across the Hayneville, suspicions are that it relates to the limitation of the rock fabric to retain the fracture network conductivity with the increased rock face stress that occurs because of pressure depletion.

2. What is the extent of the loss in fracture-face-permeability[10] and matrix permeability over time? How do we know? How does one discriminate between the two?

(Marcellus): There is no evidence to support either of these perceptions.

(Haynesville-1): In modeling it is necessary to impose pressure dependent permeability as well as conductivity loss to achieve history match. It is unknown whether this parameter could be an effect of fracture face permeability loss.

(Haynesville-2): Loss in matrix permeability is certainly a consideration, but it currently appears to be a minor consideration in comparison to other mechanisms that principally control production performance. There should be encouragement to quantify the reduced matrix permeability/diffusion characteristics that occur with pressure depletion, and to develop/apply simulation tools that consider such effects.

3. What are the best practices implemented to minimize these effects? To what extent are these beneficial? How do you know?

(Marcellus): By limiting early drawdown we have seen improved projected EUR's. Wells where the early drawdown has been restricted commonly surpass wells in daily production within 90 days and cumulative recovery in 6-9 months.

[10] Fracture-face permeability is the value of the matrix permeability at the face of the fracture. This may be substantially reduced because of a number of factors (e.g., imbibition, surface damage by proppant embedment).

(Haynesville-1): Current practice is to restrict flowback/keep pressure on the well. We have seen improvement to EUR predictions employing this method, hence we believe it is currently aiding in prevention of conductivity loss. It is important to note that the drivers on stress in the plays within the study (HSVL/BSSR) are related mostly to a loading model with minimum tectonic influence. Hence the impact of back pressure could be less in more tectonically active plays.

(Haynesville-2): Initially, Choke Management was the tool best employed to defer the damage that appeared to be occurring when high initial net stresses were placed on the rock fabric during initial completion of the well. Some companies have developed rather elaborate calculation methodologies to determine the optimum configuration of the well to maximize value by deferring the onset of fracture conductivity degradation. Other tools included the avoidance of flow back until water production was expected to be minimal.

4. Are the best practices providing the desired results?

(Marcellus): They are yielding improved results but we think they could be even better.

(Haynesville-1): Yes, as best as we can tell.

(Haynesville-2): There is no clear indication that the production performance is any more improved because of introducing these conductivity preservation techniques. On cross plots of Pressure Normalize Rates vs. EUR, the characteristic trends appear consistent across all areas of the field, and across all operating companies. It has not yet been proven/disproven, but there have been suggestions that such trends are consequential to the non-uniformity of completion effectiveness when using multiple perforation clusters in the staging of these horizontal well completions. Most of the public "published" Pressure Transient Analyses to date fail to warn the reader that irregularity in the effectiveness of cluster-to-cluster treatments within a stage (and from stage to stage) may significantly affect the interpretation of results. There should be encouragement to study this effect. It may very well be that what is presumed to be deterioration in well production performance may in large part be consequential to highly variable completion effectiveness from cluster to cluster, and from stage to stage.

5. Are there new industry procedures or products that could mitigate the above losses in fracture conductivity and fracture surface area? If so, what are these?

(Marcellus) I think that by utilizing new completion products that would allow more access points to the reservoir (more stages/perf clusters) and spreading the production over a larger area we can reduce the effects of high drawdown.

(Haynesville-1) No.

(Haynesville-2) The introduction and use of diverters (bio-balls, and such) may promote more uniform completion effectiveness, but it has yet to be clearly demonstrated that this has been effective. The innovative use of the "Channel Frac" seems to respect the expectation that the conduits to production are the defects that exist within the proppant packs, and that promoting the creation of these flow channels my promote a more effective proppant placement while minimizing the possibility of experiencing a pre-mature screen out during the frac job. Expanded use of distributed temperature (DTS) and distributed acoustical sonic (DAS) will better help to quantify both stimulation and production performance effectiveness.

6. Please summarize recommendations for fracture design (including comments on proppant selection, concentration, and scheduling, treating fluids and additives, staging, clustering, perforation design, horizontal well landing considerations, flow-back procedures, early production procedures). Please also indicate how these recommendations may vary from field to field?

(Marcellus): Limiting drawdown during both flowback and early production is preferable. Landing point and target zone is reservoir specific. For economic reasons we are trying to cram as much sand in as possible with as little water as possible (sand=good water=bad). Proppant selection is more of a reservoir fluid decision (how fine of a proppant pack will my reservoir fluid flow through).

(Haynesville-1): In terms of proppant selection, we currently believe conductivity testing to aid in selecting the optimal mesh size, material, and to a lesser extent treatment fluid. We also employ geomechanical testing and understanding of rock strength to better understand the selection for a relative formation. For example, the formations within the study have relatively low UCS values and it is believed the driver on conductivity loss is embedment and failure of the formation rather than proppant grain crushing. This was noted to be the case with both sand and ceramic and it was difficult to differentiate improvement of conductivity retention with ceramic. Hence we feel more comfortable using a sand rather than a ceramic as a cost saving tool. This may not/has not been the case in other plays. Treating fluids are based on understanding of the response of the formation (clay swelling) and cost saving /performance. We have seen in most shale gas plays performance enhancement and cost savings associated with thin fluids over viscous gel systems (this learning is fairly ubiquitous in the industry). We are currently assessing and testing the proper fluid type to employ in oil shales. We have noticed consistent improvement with tighter cluster spacing. Perforation design is limited entry and we have seen diminishing returns in over perforating a given stage. The current practice is to balance cost savings and performance by employing the maximum number of clusters per stage we can efficiently break down and stimulate. Horizontal well landing has been analyzed via production comparisons, fracture modeling, and reservoir simulation to attempt and determine the best zones and landing strategy. Flowback has been an iterative procedure to avoid well damage.

We generally employ a conservative strategy for both flowback and early time production until performance and lab data indicate a more aggressive strategy is acceptable. We have noted in certain fields (such as the ones within the study) that a conservative method is preferred, whereas other fields appear to accommodate higher rates.

(Haynesville-2): Clearly, the industry has not developed adequate analytical tools necessary to understand the important mechanisms at play during the fracture stimulation of Shale Plays. These tools, however, are rapidly evolving. The Schlumberger Mangrove Project was one of the first to demonstrate that relatively poor transport of proppants within the fracture networks created by the fracture and by the initial fracture system of the rock fabric. Similar work was performed internal to Shell with the use of commercially available CPFD-Software "Barracuda" simulations of proppant flow in wellbores and in fractures. Earlier prejudices demanding the use of high strength proppants have been discredited (Haynesville specific) when improved production performance is gained by the use of lower density lower strength and smaller proppants that result in significantly improved proppant transport. Recent simulation work with tiered thresholds for fluid and proppants (i.e. threshold dilation aperture for water, for 100 mesh, for main proppant) has shown that significant improvements in contacted stimulated reservoir volume can be achieved with higher rate fracture stimulations. This learning appears to be supported by empirical data from many unconventional plays.

7.9 Integration

Results of this program indicate that there is no simple solution for alleviating the loss of surface area and fracture conductivity during production, and consequently there is no simple solution for alleviating the loss of productivity with time. The solution is complex. It requires understanding of multiple reservoir and completion quality properties affecting the characteristic regions of the fracturing system. These are the wellbore, wellbore/fracture connector, near wellbore fracture region and far-wellbore fracture region. Because each of these regions may require different conditions of optimization, the solution also requires understanding the conflicting requirements and needed compromises to obtain an optimum overall solution. Unconventional tight shale reservoirs are geologic plays and understanding their geologic complexity is a fundamental prerequisite. The observed heterogeneous distribution of rock properties and in-situ stress are a direct reflection of their geologic complexity. Because of their low permeability, production depends on the creation of surface area in contact with the high reservoir quality sections of the play, and on the long-term retention of surface area and fracture conductivity. As indicated, however, it also depends on selecting the adequate landing point for improving the conditions of fracture initiation and depends critical on the wellbore/fracture connectivity. Although this report and the experimental effort addressed primarily the loss of fracture surface area and loss of fracture conductivity in the

far-wellbore region (i.e., region with no proppant or low proppant concentration), it is clear from the discussion that defining a workflow for improving well productivity requires the integration and optimization of the various components of the fracturing system. This includes:

- Understanding the geologic system
- Understanding the distribution of material properties in the system
- Understanding the combination of these rock properties, to define critical conditions of reservoir quality and completion quality,
- Understanding the implication of the distribution of reservoir quality and completion quality properties latter on the four fracture regions of: wellbore, wellbore fracture connector, near wellbore region and far-wellbore region, and
- Understanding the combined contribution of these regions to well production.

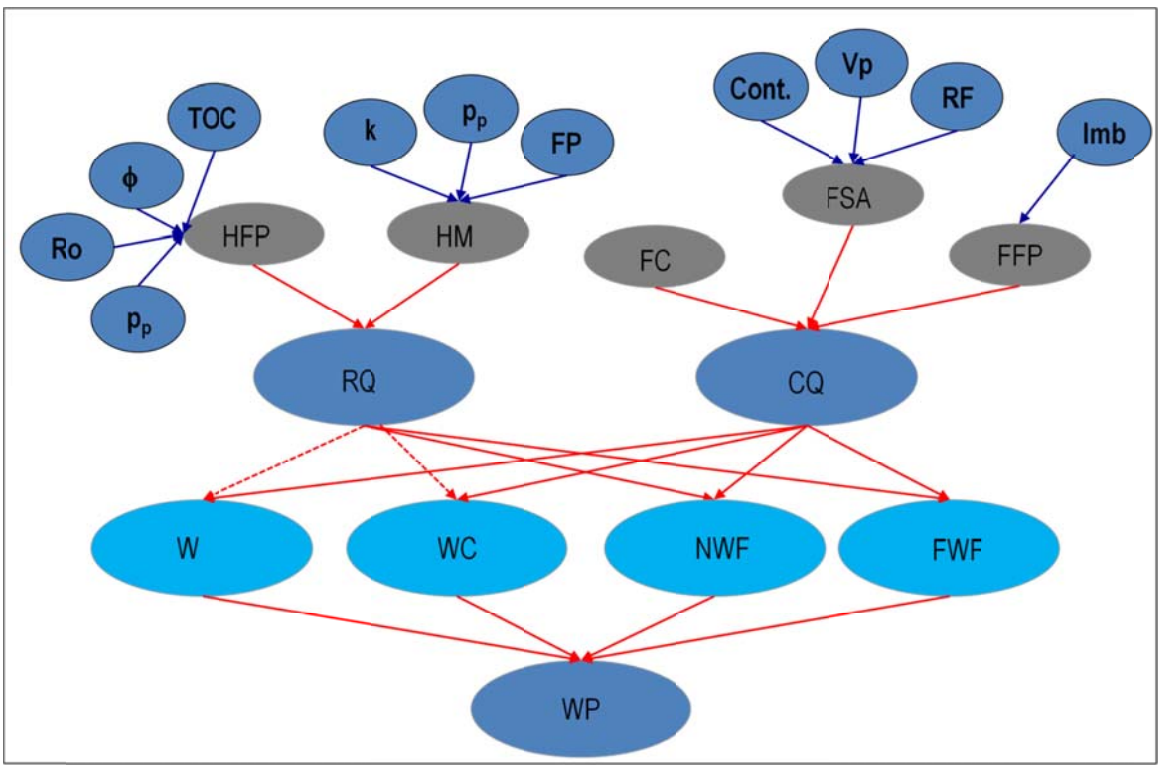

Figure 7.12 Graphical representation of the various contribution to the preservation of fracture surface area and fracture conductivity, and to the preservation of well production.

Figure 7.12 provides a graphical representation of the above concept. It shows that well production (WP) depends on the combined contribution of the four regions of the fracturing system: wellbore (W), the wellbore connector (WC), the near-wellbore fracture system (NWF), and the far-wellbore fracture system (FWF). These, in turn, depend on the

distribution of reservoir quality (RQ) and completion quality (CQ) in these regions. Reservoir quality is evaluated by a combination of properties that define hydrocarbon filled porosity (HFP) and hydrocarbon mobility (HM). Completion quality is evaluated by a combination of properties that define fracture conductivity (FC), fracture surface area (FSA), and fracture face permeability (FFP). Examples of the various properties that define these conditions are shown in the figure.

7.10 Recommendations

Recommendations for developing a workflow that improves the conditions of well productivity and decreases the loss of production over time, include the following:

- Characterization of the geologic system
- Classification of rock type units with similar texture and composition and corresponding similar material properties within the geologic system
- Evaluation of comprehensive material properties representative of each rock type.
- Evaluation of the fundamental properties of reservoir quality and completion quality and their variability along the reservoir
- Selection of the landing location and wellbore orientation based on the distribution of completion quality properties
- Design of a completion strategy (e.g., casing, open hole, type of perforations or sand blasted groves, number and orientation of perforations and others) based on the understanding of near-wellbore rock completion quality
- Design of a fracture initiation strategy for maximizing the connectivity between the wellbore and the fracture system.
- Design fracture propagation in the near-wellbore fracture region for limiting fluid leak off, reducing embedment, limiting the loss of fracture face permeability, and preventing the long term plugging by debris of the near-wellbore fracture. This should be in contact with the good reservoir quality rock.
- Design fracture propagation in the far-wellbore fracture region for proppant transport, preservation of surface area and fracture conductivity. This should be in contact with the good reservoir quality rock.
- Control the fracture termination process to limit or eliminate the overflush and for maximizing the chances for building high proppant concentration in the wellbore/fracture connector region.
- Control the initial flow back to maintain the surface area at a drawdown that does not exceed the tensile strength of the rock and prevent the generation of fines.
- Understand the potential sources of solid production, including the precipitation of salts.

7.11 Summary

In summary, this section provides a good discussion of the multiple conditions required for defining preferred practices for reservoir assessment and optimization of hydraulic fracturing design and execution, and to encourage long-term deliverability. The discussion and associated industry survey clearly indicates that there is no simple solution to this problem. The solution consists in integrating key understandings of heterogeneity, distributions of rock properties and understanding the role of these on alleviating the various challenges associated to four critical regions of the hydraulic fracturing system: the wellbore, the wellbore/fracture connector, the near-wellbore fracture and the far-field fracture. These concepts were integrated to provide recommendations for reservoir characterization and fracture design that reduces the potential for loss of surface area and loss of fracture conductivity, improves the effectiveness of the hydraulic fracturing treatments, and increase well production.

As a reference to the above concept, we conducted an extensive summary of the current industry best practices provided, including best practices by operator participants of this program. It appears that, in general, the industry is still searching for a single solution, and becoming confused with the results. Individually, operators are effectively adapting their practices to respond to the few parameters that give them good results in their particular plays. As a community, however, it is clear that the number of properties affecting production is very numerous and should be more broadly understood.

8 REFERENCES

Brannon, H.D. and Starks, T.R. 2008. The Effects of Effective Fracture Area and Conductivity on Fracture Deliverability and Stimulation Value. Paper presented at the SPE Annual Technical Conference and Exhibition, Denver, Colorado, USA. Society of Petroleum Engineers 116057-MS.

Bruner, K.R. and Smosna R. 2011. A Comparative Study of the Mississippian Barnett Shale, Fort Worth Basin and Devonian Marcellus Shale, Appalachian Basin. U.S. Department of Energy DOE/NETL-2011/1478.

Chipperfield, S.T., Wong, J.R., Warner, D.S. et al. 2007. Shear Dilation Diagnostics: A New Approach for Evaluating Tight Gas Stimulation Treatments. Paper presented at the SPE Hydraulic Fracturing Technology Conference, College Station, Texas USA. Society of Petroleum Engineers 106.

Cikes, M. 2000. Long-Term Hydraulic-Fracture Conductivities under Extreme Conditions. *SPE Production & Operations* **15** (4): 255-261. DOI: 10.2118/66549-pa

Cipolla, C.L., Warpinski, N.R., Mayerhofer, M.J. et al. 2008. The Relationship between Fracture Complexity, Reservoir Properties, and Fracture Treatment Design. Paper presented at the SPE Annual Technical Conference and Exhibition, Denver, Colorado, USA. Society of Petroleum Engineers 115.

Ghassemi, A., Tarasovs, A. and Cheng, A.D.-H. 2005. Integral equation solution of heat extraction induced thermal stress in enhanced geothermal reservoirs. *Int. J. Num. & Anal. Methods in Geomechanics*, 29, 829-844.

LOWE, D.K. and HUITT, J.L. 1966. Propping Agent Transport in Horizontal Fractures. *SPE Journal of Petroleum Technology* **18** (6): 753-764. DOI: 10.2118/1285-pa

Luna, J.B., Soriano, J.E., Garcia, R. et al. 2008. Sustaining Fracture Conductivity Increases Cumulative Production in Tight-Gas Reservoir: Case History. Paper presented at the SPE North Africa Technical Conference & Exhibition, Marrakech, Morocco. Society of Petroleum Engineers 111992-MS.

Palmer, I. D., Moschovidis, Z. A., and Cameron, J. R.: "Coal Failure and Consequences for Coalbed Methane Wells", SPE 96872, ATCE, Dallas, 9-12 Oct 2005.

Tronvoll, J., Larsen, I., Li, L. et al. 2004. Rock Mechanics Aspects of Well Productivity in Marginal Sandstone Reservoirs: Problems, Analysis Methods, and Remedial Actions. Paper presented at the SPE International Symposium and Exhibition on Formation Damage Control, Lafayette, Louisiana. Society of Petroleum Engineers 86468-MS.

Weaver, J.D., Nguyen, P.D., Parker, M.A. et al. 2005. Sustaining Fracture Conductivity. Paper presented at the SPE European Formation Damage Conference, Sheveningen, The Netherlands. Society of Petroleum Engineers 94666-MS.

Weaver, J.D., Parker, M., Batenburg, D.W.v. et al. 2007. Fracture-Related Diagenesis May Impact Conductivity. *SPE Journal* **12** (3): pp. 272-281. DOI: 10.2118/98236-pa

Weaver, J.D. and Rickman, R.D. 2010. Productivity Impact from Geochemical Degradation of Hydraulic Fractures. Paper presented at the SPE Deep Gas Conference and Exhibition, Manama, Bahrain. Society of Petroleum Engineers 130641-MS.

Weaver, J.D., Rickman, R.D., and Luo, H. 2008. Fracture-Conductivity Loss Caused by Geochemical Interactions between Man-Made Proppants and Formations. *SPE Journal* **15** (1): pp. 116-124. DOI: 10.2118/118174-pa

9 BIBLIOGRAPHY

Abass, H.H., Al-Mulhem, A.A., Alqam, M.H. et al. 2006. Acid Fracturing or Proppant Fracturing in Carbonate Formation? A Rock Mechanics View. Paper presented at the SPE Annual Technical Conference and Exhibition, San Antonio, Texas, USA. Society of Petroleum Engineers 102590-MS.

Abbas, H., Meadows, D. L., Brumley, J. L., Hedayati, S. and Venditto, J. J.:"Oriented Perforations – A Rock Mechanics View" SPE 28555 presented at the 1994 SPE Annual Technical Meeting, New Orleans, Louisiana, September 25-28.

Abass, H., Sierra, L., and Tahini, A. 2009. Optimizing Proppant Conductivity and Number of Hydraulic Fractures in Tight Gas Sand Wells. Paper presented at the SPE Saudi Arabia Section Technical Symposium, AlKhobar, Saudi Arabia. Society of Petroleum Engineers 126159-MS. DOI: 10.2118/126159-ms.

Anderson, D.M., Nobakht, M., Moghadam, S. et al. 2010. Analysis of Production Data from Fractured Shale Gas Wells. Paper presented at the SPE Unconventional Gas Conference, Pittsburgh, Pennsylvania, USA. Society of Petroleum Engineers 131787-MS.

Arthur, J.D., Bohm, B.K., Coughlin, B.J. et al. 2009. Evaluating the Environmental Implications of Hydraulic Fracturing in Shale Gas Reservoirs. Paper presented at the SPE Americas E&P Environmental and Safety Conference, San Antonio, Texas. Society of Petroleum Engineers.

Atkinson, B.K.(editor): Fracture Mechanics of Rocks. Academic Press, 1989.

Bagherian, B., Ghalambor, A., Sarmadivaleh, M. et al. 2010. Optimization of Multiple-Fractured Horizontal Tight Gas Well. Paper presented at the SPE International Symposium and Exhibiton on Formation Damage Control, Lafayette, Louisiana, USA. Society of Petroleum Engineers 127899-MS.

Barree R.D. Horizontal Well Stimulation Optimization. Presentation 2009

Behrmann, L. A. and Elbel, J. L.: "Effect of Perforations on Fracture Initiation," paper SPE 20661 presented at the 1990 SPE Annual Technical Conference and Exhibition, New Orleans, September 23-26.

Biot, M.A., 1941. General Theory of Three-dimensional Consolidation. *Journal of Applied Physics*, vol. 12, pp. 155-164

Brannon, H.D. and Starks, T.R. 2009. Maximizing Return-on-Fracturing-Investment by Using Ultra-Lightweight Proppants to Optimize Effective Fracture Area: Can Less Be More? Paper presented at the SPE Hydraulic Fracturing Technology Conference, The Woodlands, Texas. Society of Petroleum Engineers 119385-MS.

Bukovac, T., Belhaouas, R., Perez, D.R. et al. 2009. Successful Multistage Hydraulic Fracturing Treatments Using a Seawater-Based Polymer-Free Fluid System Executed from a Supply Vessel;

Lebada Vest Field, Black Sea Offshore Romania. Paper presented at the EUROPEC/EAGE Conference and Exhibition, Amsterdam, The Netherlands. Society of Petroleum Engineers 121204-MS.

Casero, A., Tealdi, L., Ceccarelli, R.L. et al. 2009. Multiple Transverse Fracturing in Horizontal Open Hole Allows Development of a Low-Permeability Reservoir in the Foukanda Field, Offshore Congo. Paper presented at the SPE Hydraulic Fracturing Technology Conference, The Woodlands, Texas. Society of Petroleum Engineers 119140-MS.

Cheng, Y. 2009. Boundary Element Analysis of the Stress Distribution around Multiple Fractures: Implications for the Spacing of Perforation Clusters of Hydraulically Fractured Horizontal Wells. Paper presented at the SPE Eastern Regional Meeting, Charleston, West Virginia, USA. Society of Petroleum Engineers 125769-MS.

Cipolla, C.L., Lolon, E., Erdle, J.C. et al. 2009. Reservoir Modeling in Shale-Gas Reservoirs. Paper presented at the SPE Eastern Regional Meeting, Charleston, West Virginia, USA. Society of Petroleum Engineers 125530-MS.

Cipolla, C.L., Lolon, E., Erdle, J. et al. 2009. Modeling Well Performance in Shale-Gas Reservoirs. Paper presented at the SPE/EAGE Reservoir Characterization and Simulation Conference, Abu Dhabi, UAE. Society of Petroleum Engineers 125532-MS.

Contreras, J.D., Durst, D.G., Harris, J.T. et al. 2008. High-Impact Techniques and Technology Increase Ultimate Recovery in Tight Gas Formations. Paper presented at the SPE Annual Technical Conference and Exhibition, Denver, Colorado, USA. Society of Petroleum Engineers.

Cooper, R.E. and Troncoso, J.C. 1988. An Overview of Horizontal Well Completion Technology. Paper presented at the International Meeting on Petroleum Engineering, Tianjin, China. 1988 Copyright 1988 Society of Petroleum Engineers 17582-MS.

Cramer, D.D. 2008. Stimulating Unconventional Reservoirs: Lessons Learned, Successful Practices, Areas for Improvement. Paper presented at the SPE Unconventional Reservoirs Conference, Keystone, Colorado, USA. Society of Petroleum Engineers 114172.

Daneshy, A. A. On the Design of Vertical Hydraulic Fractures. *JPT* (January 1973) 83-93; T*rans.*, AIME, 255.

Daneshy, A.A. 2004. Proppant Distribution and Flowback in Off-Balance Hydraulic Fractures. Paper presented at the SPE Annual Technical Conference and Exhibition, Houston, Texas. Society of Petroleum Engineers 89889-MS.

Economides, M.J. and K.G. Nolte., 2000. Reservoir stimulation. 3rd Edition, *John Wiley & Sons,LTD*, 2000.

Economides, M.J., Oligney, R.E., and Valkó, P.P. 2002. *Unified Fracture Design*. Houston: Orsa Press.

EPA-U.S. Environmental Protection Agency. August, 2004. Evaluation of Impacts to Underground Sources of Drinking Water by Hydraulic Fracturing of Coalbed Methane Reservoirs. EPA 816-R-04-003.

Evers, R., Young, D.A., Vargus, G.W. et al. 2009. Design Methodology for Swellable Elastomer Packers in Fracturing Operations.

Fisher, M. K., Heinze, J. R., Harris, C. D., Wright C. A. and Dunn, K. P.:"Optimizing Horizontal Completion Techniques in the Barnett Shale Using Microseismic Fracture Mapping", SPE 90051 presented at the SPE Annual Conference and Exhibition held in Houston, Texas U.S.A., 26-29 September 2004.

Ge, J., Ghassemi, A. 2007. Pore pressure and stress distributions around an injection-induced fracture. Transactions, Geothermal Res. Coun., Reno.

Ge, J., Ghassemi, A. 2008. Analysis of failure potential around a hydraulic fracture in jointed rock. Proc. 42nd U.S. Rock Mechanics Symposium, June 29 – July 2, San Francisco.

Geertsma, J., 1957. The Effect of Fluid Pressure Decline on the Volumetric Changes of Porous Rocks. *Journal of Applied Mechanics*, vol. 24, pp. 594-601

Geertsma, J. and de Klerk, F.A. 1969. Rapid Method of Predicting Width and Extent of Hydraulically Induced Fractures. *JPT* 21 (12): 1571-81. SPE-2458-PA DOI: 10.2118/2458-PA

Gidley, J.L., Penny, G.S., and McDaniel, R.R. 1995. Effect of Proppant Failure and Fines Migration on Conductivity of Propped Fractures. *SPE Production & Operations* **10** (1): 20-25. DOI: 10.2118/24008-pa.

Goodman, R.E., : Introduction to Rock Mechanics. 1989.

Hoek, E., and Brown, E.T., : Underground Excavations in Rock. 1980.

Holditch, S.A. 2006. Tight Gas Sands. *SPE Journal of Petroleum Technology* **58** (6): 86-93. DOI: 10.2118/103356-ms

Hossain, M.M., Rahman, M.K., and Rahman, S.S. 2000. Application of Hdr Stimulation Technology to Develop Tight Gas Reservoirs. SPE-64484, Paper presented at the SPE Asia Pacific Oil and Gas Conference and Exhibition, Brisbane, Australia. Copyright 2000, Society of Petroleum Engineers Inc.

Jaeger, J.C., and Cook N.G.W.: Fundamentals of Rock Mechanics. 1979.

Jaeger, J. C., and Rosengren, K. J. (1969). Friction and Sliding of Joints. Proc. Aust. Inst. Min. Meta. No.229, 93–104.

Jaripatke, O.A., Grieser, W.V., and Chong, K.K. 2010. A Review of Successful Approach Towards Shale Play Stimulation in the Last Two Decades - a Completions Road Map to Shale

Play Development. Paper presented at the SPE Deep Gas Conference and Exhibition, Manama, Bahrain. Society of Petroleum Engineers 130369-MS.

Jiang, T., Wang, X., Shan, W. et al. 2003. A New Comprehensive Hydraulic Fracturing Technology to Minimize Formation Damage in Low Permeability Reservoirs. Paper presented at the SPE European Formation Damage Conference, The Hague, Netherlands. Society of Petroleum Engineers 82222-MS.

Ketter, A. A., Heinze, J. R., Daniels, J. L. and Waters, G.:"A Field Study in Optimizing Completion Strategies for Fracture Initiation in Barnett Shale Horizontal Wells", SPE-103232-PA presented at the 2006 SPE ATCE, San Antonio, TX, USA, 24-27 September 2006.

Kim, C.M. and Losacano, J.A. 1985. Fracture Conductivity Damage Due to Crosslinked Gel Residue and Closure Stress on Propped 20/40 Mesh Sand. Paper presented at the SPE Annual Technical Conference and Exhibition, Las Vegas, Nevada. 1985 Copyright 1985, Society of Petroleum Engineers 14436-MS.

Koshelev, V. & Ghassemi, A. 2003 Numerical Modeling of Stress Distribution and Crack Trajectory near a Fault or a Natural Fracture. *Soil-Rock America Symp*., Boston.

Layne, A.W. and Siriwardane, H.J. 1988. Insights into Hydraulic Fracturing of a Horizontal Well in a Naturally Fractured Formation. Paper presented at the SPE Annual Technical Conference and Exhibition, Houston, Texas. Not subject to copyright. This document was prepared by government employees or with government funding that places it in the public domain. 18255-MS.

LeCompte, B., Franquet, J.A., and Jacobi, D. 2009. Evaluation of Haynesville Shale Vertical Well Completions with a Mineralogy Based Approach to Reservoir Geomechanics. Paper presented at the SPE Annual Technical Conference and Exhibition, New Orleans, Louisiana. Society of Petroleum Engineers 124227-MS.

Lewis, A.M. and Hughes, R.G. 2008. Production Data Analysis of Shale Gas Reservoirs. Paper presented at the SPE Annual Technical Conference and Exhibition, Denver, Colorado, USA. Society of Petroleum Engineers 116688-MS.

Li, Y., Wang, Y., Cheng, X. et al. 2010. Case Study of Multistage Isolating Stimulation in High Temperature Deep Carbonate Horizontal Wells. Paper presented at the SPE Oil and Gas India Conference and Exhibition, Mumbai, India. Society of Petroleum Engineers 125854-MS.

Lolon, E., cipolla, c., Weijers, L. et al. 2009. Evaluating Horizontal Well Placement and Hydraulic Fracture Spacing/ Conductivity in the Bakken Formation, North Dakota. Paper presented at the SPE Annual Technical Conference and Exhibition, New Orleans, Louisiana. Society of Petroleum Engineers 124905-MS.

Magalhaes, F.V., Zhu, D., Amini, S. et al. 2007. Optimization of Fractured Well Performance of Horizontal Gas Wells. Paper presented at the International Oil Conference and Exhibition in Mexico, Veracruz, Mexico. Society of Petroleum Engineers 108779-M.

Martocchia Francesco. Hydraulic Fracturing Optimization in Multi-Layered Heterogeneous Oil Field. Presentation in *Master in Petroleum Engineering 2008-09*, 2009.

Matthews, H. L.: "Overview of Shale Gas Stimulation Techniques" Adapted from oral presentation at AAPG Annual Convention, San Antonio, Texas, April 20-23, 2008.

Matthews, H.L., Schein, G.W., and Malone, M.R. 2007. Stimulation of Gas Shales: They're All the Same—Right? Paper presented at the SPE Hydraulic Fracturing Technology Conference, College Station, Texas USA. Society of Petroleum Engineers.

Mayerhofer, M.J., Lolon, E., Warpinski, N.R. et al. 2008. What Is Stimulated Rock Volume? Paper presented at the SPE Shale Gas Production Conference, Fort Worth, Texas, USA. Society of Petroleum Engineers. SPE-119890.

McDaniel, B.W., East, L., and Hazzard, V. 2002. Overview of Stimulation Technology for Horizontal Completions without Cemented Casing in the Lateral. Paper presented at the SPE Asia Pacific Oil and Gas Conference and Exhibition, Melbourne, Australia. Copyright 2002, Society of Petroleum Engineers Inc. 77825.

McDaniel, B.W., East, L.E., and Surjaatmadja, J.B. 2008. Use of Hydrajet Perforating to Improve Fracturing Success Sees Global Expansion. Paper presented at the CIPC/SPE Gas Technology Symposium 2008 Joint Conference, Calgary, Alberta, Canada. Society of Petroleum Engineers 114695-MS.

McDaniel, B.W. and Surjaatmadja, J.B. 2007. Horizontal Wellbore Placement Can Significantly Impact Hydraulic Fracturing Stimulation Results. Paper presented at the SPE Hydraulic Fracturing Technology Conference, College Station, Texas, U.S.A. Society of Petroleum Engineers. SPE-77825.

Meyer, B.R., Bazan, L.W., Jacot, R.H. et al. 2010. Optimization of Multiple Transverse Hydraulic Fractures in Horizontal Wellbores. Paper presented at the SPE Unconventional Gas Conference, Pittsburgh, Pennsylvania, USA. Society of Petroleum Engineers 131732-MS.

Mildren, S.D., Hillis, R.R. & Kaldi, J. 2002. Calibrating predictions of fault seal reactivation in the Timor Sea. Australian Petroleum Production and Exploration Association Journal, 42, 187–202.

Muskat, M.: The flow of homogeneous fluids through porous media, first edition, J.W. Edwards Inc., Ann Arbor, MI(1946).

Nelson, E.J., et al., 2007. Using geological information to fracture optimize stimulation practices in the Cooper Basin, Australia. Petroleum Geoscience, Vol. 13. 2007, 3–16.

Nguyen, P.D., Weaver, J.D., Dewprashad, B.T. et al. 1998. Enhancing Fracture Conductivity through Surface Modification of Proppant. Paper presented at the SPE Formation Damage Control Conference, Lafayette, Louisiana. 1998 Copyright 1998, Society of Petroleum Engineers, Inc. 39428-MS.

Nguyen, P.D., Weaver, J.D., and Rickman, R.D. 2008. Prevention of Geochemical Scaling in Hydraulically Created Fractures: Laboratory and Field Studies. Paper presented at the SPE Eastern Regional/AAPG Eastern Section Joint Meeting, Pittsburgh, Pennsylvania, USA. Society of Petroleum Engineers 118175-MS.

Nordgren, R.P. 1972. Propagation of a Vertical Hydraulic Fracture. SPEJ 12 (8): 306-314; *Trans*., AIME, 253, 1972.

Nygren, A. and Ghassemi, A. 2005. Poroelastic and Thermoelastic Effects of Injection into a Geothermal Reservoir. *The 41st U.S. Symposium on Rock Mechanics*. June 17-21, 2006.

Olson, J.E. and Taleghani, A.D. 2009. Modeling Simultaneous Growth of Multiple Hydraulic Fractures and Their Interaction with Natural Fractures. Paper presented at the SPE Hydraulic Fracturing Technology Conference, The Woodlands, Texas. Society of Petroleum Engineers.

Pace, G., Casero, A., Tealdi, L. et al. 2008. Transverse Multi-Fracture Technique in Kitina Highly Deviated Off-Shore Wells. Paper presented at the Europec/EAGE Conference and Exhibition, Rome, Italy. Society of Petroleum Engineers 113894-MS.

Palisch, T.T., Duenckel, R.J., Bazan, L.W. et al. 2007. Determining Realistic Fracture Conductivity and Understanding Its Impact on Well Performance - Theory and Field Examples. Paper presented at the SPE Hydraulic Fracturing Technology Conference, College Station, Texas, U.S.A. Society of Petroleum Engineers 106301-MS.

Palisch, T.T., Vincent, M.C. and Handren, P.J. Slickwater Fracturing – Food for Thought. 2008. Paper SPE 115766 presented at the 2008 SPE Annual Technical Conference and Exhibition, Denver, Colorado, 21-24 September. SPE-10.2118/115766-MS DOI: 10.2118/115766-MS

Palmer, I. Modeling Shear Failure and Stimulation of the Barnett Shale after Hydraulic Fracturing. 2007. Paper SPE 106113 presented at the 2007 SPE Hydraulic Fracturing Technology Conference held in College Station, Texas, U.S.A., 29–31 January 2007. SPE-10.2118/106113 -MS DOI: 10.2118/106113 –MS

Pearson, C. Dimensionless Fracture Conductivity: Better Input Values Make Better Wells. 2001, Journal of Petroleum Technology, Vol. 53, No. 1

Pollard, D.D. and Segall, P., 1987, Theoretical displacement and stresses near fractures in rock: with applications to faults, joints, veins, dikes, and solution surfaces. In B.K. Atkinson, ed., Fracture Mechanics of Rock, Academic Press, Inc., pp. 277-349.

Pope, D.S., Leung, L.K.-W., Gulbis, J. et al. 1996. Effects of Viscous Fingering on Fracture Conductivity. *SPE Production & Operations* **11** (4): 230-237. DOI: 10.2118/28511-pa

Pye, D.S. and Smith, W.A. 1973. Fluid Loss Additive Seriously Reduces Fracture Proppant Conductivity and Formation Permeability. Paper presented at the Fall Meeting of the Society of Petroleum Engineers of AIME, Las Vegas, Nevada. 1973 Copyright 1973, American Institute of Mining, Metallurgical, and Petroleum Engineers, Inc. 4680-MS.

Rahman, M.M., Rahman, M.K., and Rahman, S.S.: An Analytical Model for Production Estimation From Hydraulically Fractured Tight-Gas Reservoirs. 2002. Paper SPE 77901 presented at the 2002 SPE Asia Pacific Oil and Gas Conference and Exhibition, Melbourne, Australia, 8-10 October. SPE-77901-MS DOI: 10.2118/77901-MS

Rebbins, R.E., Chen, S., and Lemp S.P. Design Consideration for Fracturing Job Sizing of Low-Permeability Gas Reservoirs of the Arkoma Basin. 1991. Paper SPE 21718 presented at the 1991 SPE Production Operations Symposium, Oklahoma City, Oklahoma, 7-9 April. 10.2118/21718-MS

Rodrigues, V.F., Neumann, L.F., Torres, D.S. et al. 2007. Horizontal Well Completion and Stimulation Techniques--a Review with Emphasis on Low-Permeability Carbonates. Paper presented at the Latin American & Caribbean Petroleum Engineering Conference, Buenos Aires, Argentina. Society of Petroleum Engineers 108075-MS.

Romero, D.J., Valko, P.P., and Economides, M.J. 2003. Optimization of the Productivity Index and the Fracture Geometry of a Stimulated Well with Fracture Face and Choke Skins. *SPE Production & Operations* **18** (1): 57-64. DOI: 10.2118/81908-pa

Shaari, N.A.E., Swint, A., and Kalfayan, L.J. 2008. Utilizing Organosilane with Hydraulic Fracturing Treatments to Minimize Fines Migration into the Proppant Pack: A Field Application. Paper presented at the SPE Western Regional and Pacific Section AAPG Joint Meeting, Bakersfield, California, USA. Society of Petroleum Engineers 114220-MS.

Soliman, M.Y. and Boonen, P. 1996. Review of Fractured Horizontal Wells Technology. Paper presented at the Abu Dhabi International Petroleum Exhibition and Conference, Abu Dhabi, United Arab Emirates. Copyright 1997, Society of Petroleum Engineers Inc. 36289-MS.

Soliman, M.Y. and Boonen, P. 2000. Rock Mechanics and Stimulation Aspects of Horizontal Wells. Journal of Petroleum Science and Engineering. P: 187-204.

Surjaatmadja, J.B., McDaniel, B.W., Case, L. et al. 2006. Horizontal Well Drilling and Completion Schemes Consider Future Stimulation to Optimize Production. Paper presented at the International Oil & Gas Conference and Exhibition in China, Beijing, China. Society of Petroleum Engineers 103772-MS.

Surjaatmadja, J. B., McDaniel, B. W., Case, L. R., East, L. E. and Pyecroft, J. F.:"Consideration for Future Stimulation Options Is Vital in Deceding Horizontal Well Drilling and Completion Schemes for Production Optimization" SPE 103774 presented at the 2006 SPE International Oil Conference and Exhibition in Mexico, Monterrey, Mexico, 27-31 May 2006.

Vincent, M.C. 2009. Examining Our Assumptions -- Have Oversimplifications Jeopardized Our Ability to Design Optimal Fracture Treatments? Paper presented at the SPE Hydraulic Fracturing Technology Conference, The Woodlands, Texas. Society of Petroleum Engineers 119143-MS.

Vulgamore, T., Clawson, T., Pope, C., Wolhart, S., Mayerhofer, M., Machovoe, S. and Waltman, C.:"Applying hydraulic fracture diagnostics to optimize stimulations in the Woodford Shale"

SPE 110029 presented at the 2007 SPE Annual Technical Conference and Exhibition held in Anaheim, California, USA, 11-14 November 2007.

Wahl, H.A. 1965. Horizontal Fracture Design Based on Propped Fracture Area. *SPE Journal of Petroleum Technology* **17** (6): 723-730. DOI: 10.2118/976-pa

Warpinski, N.R. and Branagan, P.T. 1989. Altered-Stress Fracturing. JPT 1989.

Warpinski, N.R., Mayerhofer, M.J., Vincent, M.C. et al. 2008. Stimulating Unconventional Reservoirs: Maximizing Network Growth While Optimizing Fracture Conductivity. Paper presented at the SPE Unconventional Reservoirs Conference, Keystone, Colorado, USA. Society of Petroleum Engineers 11.

Warpinski, N.R. 2009. Integrating Microseismic Monitoring with Well Completions, Reservoir Behavior, and Rock Mechanics. Paper presented at the SPE Tight Gas Completions Conference, San Antonio, Texas, USA. Society of Petroleum Engineers 125239-MS.

Warpinski, N.R., Wolhart, S.L., and Wright, C.A. 2001. Analysis and Prediction of Microseismicity Induced by Hydraulic Fracturing. Paper presented at the SPE Annual Technical Conference and Exhibition, New Orleans, Louisiana. Copyright 2001, Society of Petroleum Engineers Inc. 71649-MS.

Waters, G.A., Heinze, J.R., Jackson, R. et al. 2006. Use of Horizontal Well Image Tools to Optimize Barnett Shale Reservoir Exploitation. Paper presented at the SPE Annual Technical Conference and Exhibition, San Antonio, Texas, USA. Society of Petroleum Engineers.

Watson, D.R., Durst, D.G., Harris, J.T. et al. 2008. One-Trip Multistage Completion Technology for Unconventional Gas Formations. Paper presented at the CIPC/SPE Gas Technology Symposium 2008 Joint Conference, Calgary, Alberta, Canada. Society of Petroleum Engineers 114973-MS.

Weaver, J.D., Rickman, R.D., Luo, H. et al. 2009. A Study of Proppant Formation Reactions. Paper presented at the SPE International Symposium on Oilfield Chemistry, The Woodlands. Texas. Society of Petroleum Engineers 121465.

Zahid, S., Bhatti, A.A., Khan, H.A. et al. 2007. Development of Unconventional Gas Resources: Stimulation Perspective. Paper presented at the Production and Operations Symposium, Oklahoma City, Oklahoma, U.S.A. Society of Petroleum Engineers.

10 LIST OF ACRONYMS AND ABBREVIATIONS

AAPG	American Association of Petroleum Geologists
AGU	American Geophysical Union
ARMA	American Rock Mechanics Association
CQI	Completion Quality Index
DAS	Distributed Acoustical Sonic
DTS	Distributed Temperature Sensing
EUR	Estimated Ultimate Recovery
FMI	Formation Micro-imaging
GFP	Gas Filled Porosity
HRA	Heterogeneous Rock Analysis
IP	Initial Production
PBU	Pressure Build-up
Perm	Permeability
RPSEA	Research Partnership to Secure Energy for America
RQI	Reservoir Quality Index
SEM	Scanning Electron Microscope
SPE	Society of Petroleum Engineers
TIV	Transversely Isotropic Vertical
TOC	Total Organic Carbon
TRA	Tight Rock Analysis
XRD	X-ray Diffraction

11 APPENDICES

Appendix 1 Creep Behavior of Barnett, Haynesville and Marcellus Shale

Appendix 2 Un-propped Fractures_ Raw Data and Sample Photographs

Appendix 3 Instrumentation Calibration

Appendix 4 Rudimentary Slot Flow Derivations

Appendix 5 Proppant Embedment Testing Procedure

Appendix 6 Propped Fractures_ Raw Data and Sample Photographs

Appendix 7 Review of Best Field Practices